Title	Development of Hydrogenation of N-Heteroaromatics with Triarylborane Catalysts under Crude or Pure H2 Conditions
Author(s)	橋本, 大輝
Citation	大阪大学, 2025, 博士論文
Version Type	VoR
URL	https://doi.org/10.18910/101633
rights	
Note	

Doctoral Dissertation

Development of Hydrogenation of *N*-Heteroaromatics with Triarylborane Catalysts under Crude or Pure H_2 Conditions

Taiki Hashimoto

January 2025

Graduate School of Engineering
Osaka University

Preface and Acknowledgements

This study in this thesis has been carried out under the direction of Emeritus Professor Dr. Sensuke Ogoshi and Associate Professor Dr. Yoichi Hoshimoto at the Department of Applied Chemistry, Faculty of Engineering, Osaka University from April 2019 to March 2025. This thesis describes the developments of hydrogenation of *N*-heteroaromatics with triarylborane catalysts under crude or pure H_2 conditions.

First of all, I would like to express my heartfelt gratitude to Associate Professor Dr. Yoichi Hoshimoto for a large number of invaluable suggestions, discussions, heartful encouragement, and inspiring leadership, which have profoundly enriched all of my entire Ph.D. study, related research, and my life. I would like to thank the rest of my thesis committee: Professor Dr. Hayato Tsurugi and Professor Dr. Mamoru Tobisu for their insightful comments and encouragement, but also for the hard question which invented me to widen my research from various perspectives.

I would like to express my gratitude to Emeritus Professor Dr. Sensuke Ogoshi for their invaluable guidance, for watching over us with care, and for engaging in thoughtful discussions that have inspired and enriched my study. I would like to give my special thanks to Associate Professor Dr. Ryohei Doi (Tokyo Metropolitan University), Assistant Professor Dr. Hiroaki Iwamoto, postdoctoral fellow Dr. Amit Kumar Jaiswal for their continuous guidance, advice and assistance. I am also deeply grateful to Ms. Yukiko Mori, Ms. Chika Sugiki, Ms. Yuri Kishimoto, and Ms. Noriko Fujimoto for their kind help and heart-warming encouragement.

I thank my fellow labmates: Ms. Chiharu Akatsuka, Mr. Kenta Goto, Mr. Takuya Tsuruta, Mr. Shun Nagai, Mr. Masashi Yasuda, and Mr. Yasuhiro Yamamoto for the heartful encouragements to each other, improving together, and for all the fun we have had in our laboratory life and private time. I am deeply indebted to my respectful seniors in the Ogoshi Group: Dr. Takahiro Asada, Dr. Keita Ashida, Dr. Naoyoshi Ishida, Dr. Yasuhiro Yamauchi, Mr. Hiroto Imiya, Dr. Mahiro Sakuraba, Ms. Anna Shigaki, Ms. Chika Nishimura, Mr. Kodai Fukudome, Mr. Hideki Ito, Mr. Takahiro Kawakita, Ms. Denise Eimi Sunagawa, and Mr. Nozomi Yasui for their helpful advice and kind encouragements. I thank all of my juniors in the Ogoshi Group: Ms. Reina Okamoto, Mr. Koki Kajiwara, Mr. Daiki Kitazoe, Mr. Tomoya Terada, Mr. Yusei Hisata, Mr. Lueangratana Pacharapaul, Mr. Naoki Kajita, Mr. Yuyang Zhou, Mr. Taiki Negoro, Mr. Keisuke Nozaki, Mr. Yutaka Mondori, Mr. Kenta Koh, Ms. Setsuka Homma, Mr. Nobutaka Mito, Mr. Taichi Morishita, Mr. Genki Yamaguchi, Mr. Chihiro Yamaguchi, Mr. Naoya Iwamoto, Mr. Kimitaka Kambe, Mr. Yusuke Goto, Mr. Yusuke Tokura, Mr. Ryosuke Harada, Mr. Masakazu Tanigawa, Mr. Hayato Nishiguchi, Mr. Koki Baba, and Mr. Daina Morishita for their helpful assistance and heartful communications. I also thank the visiting research students: Mr. Andy, and Mr. Coco for sharing good times.

I have also received a lot of advice from other groups for my Ph.D. study. I explain my gratitude to Professor Dr. Satoshi Maeda (Hokkaido University), Associate Professor Dr. Yu Harabuchi (Hokkaido University), Dr. Takuma Ito (Hokkaido University), Mr. Wataru Kanna (Hokkaido University), Ms. Tsukika Miyazawa (Hokkaido University), Mr. Satoshi Matsutani (Hokkaido University), and Mr. Ren Yamada (Hokkaido University) for meaningful suggestions to theoretical studies in Chapter 2. I am grateful to Professor Dr. Takashi Hayashi, Associate Professor Dr. Koji Oohora, and Assistant Professor Dr. Shunsuke Kato for their helpful advice for the gas chromatography analyses. I would like to express my special thanks to the Analytical Instrumentation Facility, Graduate School of Engineering, Osaka University, for the measurement of spectral and analytical data. Especially, I am grateful to Associate Professor Dr. Yoshiya Fukumoto and Assistant Professor Dr. Kyoko Inoue for her advice for the nuclear magnetic resonance analyses, and technical specialist Mr. Hiroaki Tanaka for his advice for the mass spectrometry.

My sincere thanks also go to Professor Dr. Michael Ingleson (The University of Edinburgh), who provided me an opportunity to join his group as a visiting research student (from May 2024 to July 2024 in Edinburgh, Scotland, UK). I am also grateful to his labmates: Dr. Clement R. P. Millet, Dr. Dominic R. Willcox, Dr. Milan Kumar Bisai, Dr. Arnaud Osi, Dr. Shantaram S. Kothavale, Ms. Justyna Łosiewicz, Ms. Anna V. Schellbach for sharing wonderful time and their grateful help.

I acknowledge a grant from Chemistry Personnel Cultivation Program supported by Japan Chemical Industry Association (April 2022–March 2025).

Finally, I would like to express my utmost gratitude to my parents, brother, and sister: Mr. Takamitsu Hashimoto, Ms. Yoshiko Hashimoto, Mr. Masaki Hashimoto, and Ms. Kyoka Hashimoto for their attentive support and warm encouragement. I would also like to express my deepest gratitude to my wife: Ms. Sara Hashimoto for her unwavering support, understanding, and encouragement, which have been my greatest source of strength throughout my PhD student life.

January 2025.

Taiki Hashimoto

Taiki Hashimoto

Contents

Abbreviations

The following abbreviations are used in this thesis.

Å	angstrom
Ac	acetate
AFIR	artificial force induced reaction
AN	accepter number
aq.	aqueous
Ar	aryl
atm	atmospheric pressure
BAr_3	triarylborane
br	broad
Bu	butyl
ca.	circa
cal	calorie
calcd	calculated
cat.	catalyst
cf.	confer
CH_4	methane
CLA	classical Lewis adduct
CO	carbon monoxide
CO_2	carbon dioxide
conv.	conversion
COSY	correlation spectroscopy
°	degree(s)
°C	degrees Celsius
d	doublet
δ	chemical shift of NMR signal in ppm
DFT	density functional theory
e.g.	exempli gratia
EI	electron ionization
EQ	equilibrium structure
Eq.	equation
equiv.	equivalent
Et	ethyl
FLP	frustrated Lewis pair
GB	grove box
GB-AN	Gutmann-Beckett accepter number
GC	gas chromatography
GRRM	global reaction route mapping
h	hour(s)

H_2	molecular hydrogen
HMBC	hetero-nuclear multiple-bond connectivity
HMQC	hetero-nuclear multiple quantum coherence
HOMO	highest occupied molecular orbital
HPLC	high performance liquid chromatography
HRMS	high-resolution mass spectra
Hz	hertz
i	iso
i.e.	id est
IRC	intrinsic reaction coordinate
J	coupling constant in NMR
k	kilo
k_{obs}	observed rate constant
LA	Lewis acid
LB	Lewis base
LDA	lithium diisopropylamide
LOHC	liquid organic hydrogen carrier
LUMO	lowest unoccupied molecular orbital
M	mole per liter
m	multiplet
m	meta
Me	methyl
Mes	mesityl
MHz	mega hertz
min	minute(s)
mL	milliliter
μL	microliter
mol	mole
MS	mass spectrometry
n	normal
NMR	nuclear magnetic resonance
o	ortho
ref.	reference
p	para
Ph	phenyl
Pr	propyl
PSA	pressure swing adsorption
q	quartet
rt	room temperature
s	singlet
SC	single crystal
SC-AFIR	single-component artificial force induced reaction
sec	second

sept	septet
t	triplet
t	tertiary
TCI	Tokyo Chemical Industry
THF	tetrahydrofuran
TM	transition metal
TOF	turnover frequency
TON	turnover number
TS	transition state
V	volume
vs	versus
WGS	water-gas shift
w/o	without
wt%	weight percent
XRD	X-ray diffraction

General Introduction

Hydrogenation of *N*-heteroaromatics is a crucial method for rapidly producing saturated *N*-heterocycles, which are frequently found in bioactive molecules and pharmaceuticals.[1] In addition, recently, there has been growing interest in applying this hydrogenation, along with the dehydrogenation of the resulting saturated *N*-heterocycles, to molecular hydrogen storage and recovery technologies, as the dehydrogenation of saturated *N*-heterocycles has been reported to proceed under relatively mild conditions.[2] So far, the hydrogenations of *N*-heteroaromatics have been developed based on the use of precious metal catalysts; however, challenges remain regarding the toxicity, cost, and rarity of precious metal catalysts. (Figure 1).[1–3] Indeed, several research groups have focused on developing new catalysts based on earth-abundant metals.[4]

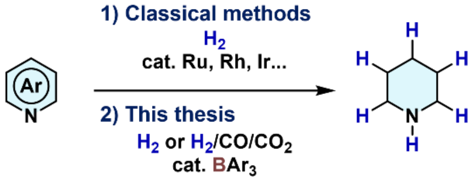

Figure 1. Catalytic hydrogenation of *N*-heteroaromatics.

Frustrated Lewis pairs (FLPs),[5,6] comprising less-toxic main-group compounds, have attracted much attention over the past two decades. FLPs are recognized as weakly bound noncovalent complexes comprising an electron acceptor (Lewis acid, LA) and an electron donor (Lewis base, LB), in which the formation of classical Lewis adducts (CLAs) is encumbered by steric repulsion between LA and LB (Figure 2, right). Whereas the typical chemical features of both the LA and the LB are usually quenched through the formation of CLAs (Figure 2, left), FLPs exhibit a much higher reactivity toward small molecules, e.g. molecular hydrogen (H_2),[7] carbon monoxide (CO),[8–10] carbon dioxide (CO_2),[11–17] and so on.

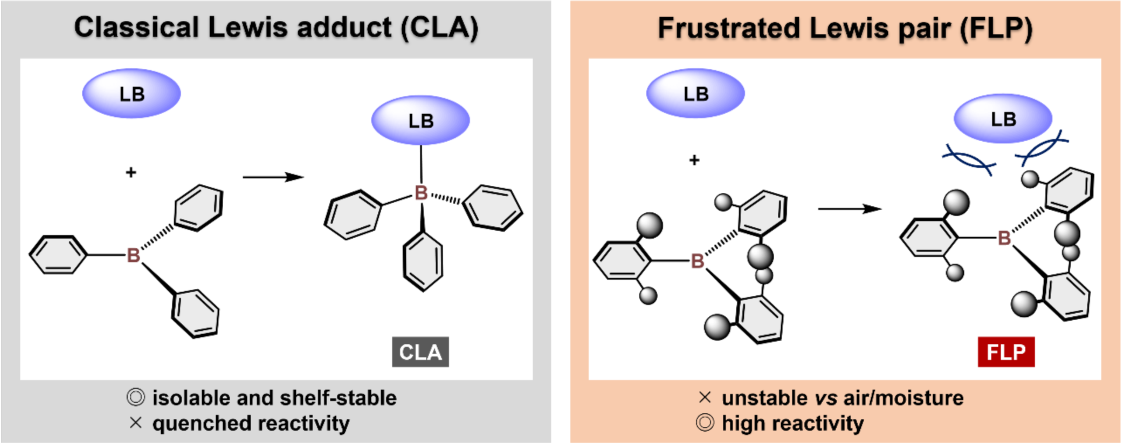

Figure 2. Generation of classical Lewis adducts (CLAs) and frustrated Lewis pairs (FLPs) through the reaction between Lewis acids (LAs) and Lewis bases (LBs).

In particular, FLPs have been widely applied to catalytic hydrogenation of unsaturated molecules.[7]

For example, Stephan and co-workers have been reported that $B(C_6F_5)_3$ (**B^1**) effectively catalyzed the hydrogenation of imines via the heterolytic cleavage of H_2 with an FLP comprising **B^1** and imines (Figure 3A).[18] The generation of FLPs using phosphines,[19–21] nitrogen-containing compounds such as quinoline derivatives,[22–26] cyclic ethers,[27,28] or carbenes[29] as LBs is well-known and has been applied to catalytic hydrogenation (Figure 3B). Nevertheless, the application of FLPs has largely been limited to serving as alternatives to transition metal catalysts.

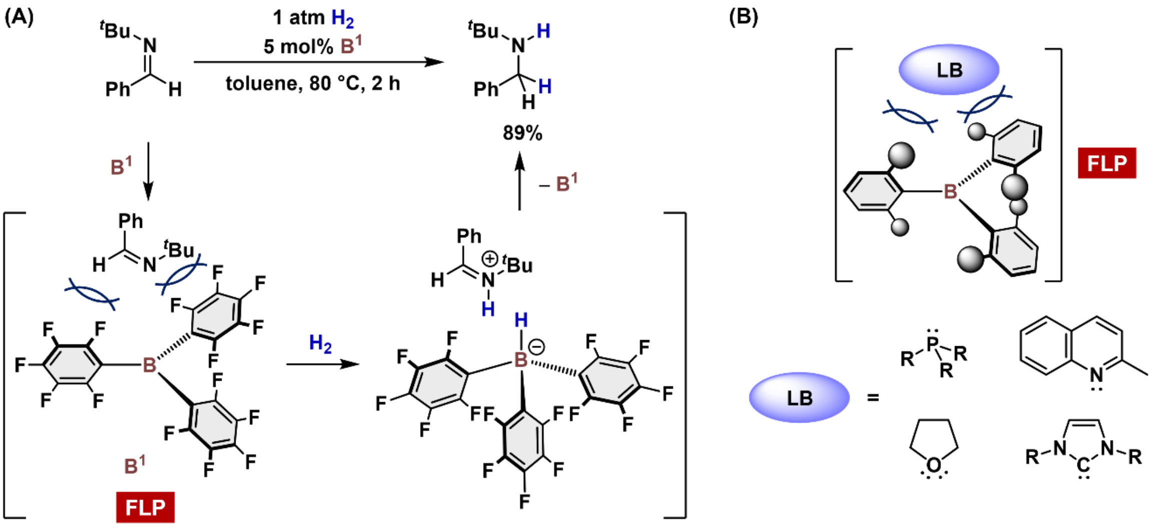

Figure 3. (A) **B^1**-catalyzed hydrogenation of imines. (B) Reported examples of Lewis bases (LBs) potentially generating FLPs.

In this context, our group has developed FLPs based on triarylborane (BAr_3) and demonstrated their applicability in the hydrogenation of unsaturated molecules, even under challenging conditions where potential borane quenchers are present.[30,31] For example, our group has reported BAr_3-catalyzed reductive alkylation of amine compounds (Figure 4),[32] wherein the BAr_3 promotes the dehydration condensation of aldehydes and amines and is also involved in generating an FLP to mediate hydrogenation of imine intermediates. This reductive alkylation produced a stoichiometric amount of H_2O that tends to trigger the irreversible decomposition of electrophilic boranes such as **B^1**.[33,34] To overcome this challenge, our group found that the use of a well-designed BAr_3 to generate a water-tolerant FLP enabled the efficient progress of the reductive alkylation.[6c,35,36]

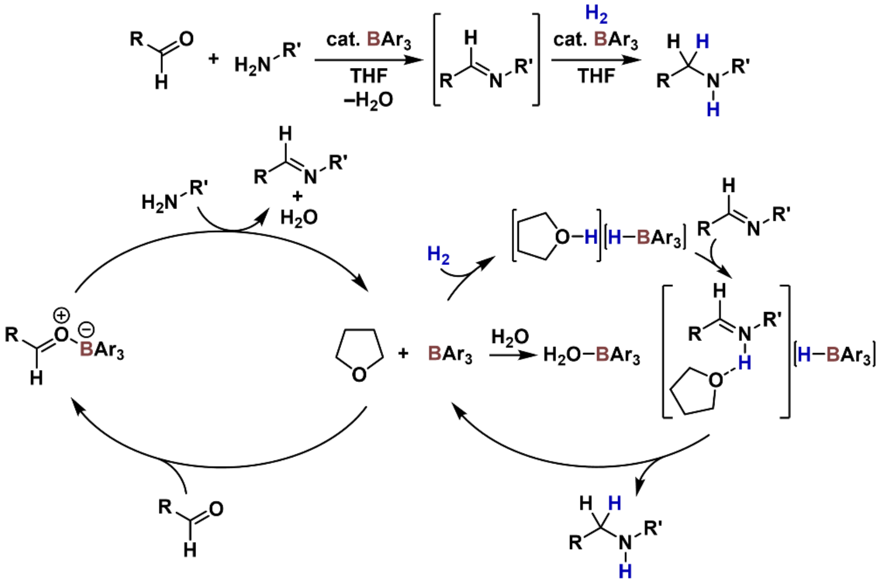

Figure 4. BAr_3-catalyzed reductive alkylation of amines with aldehydes, reported by our group (ref. 32).

Against this background, I envisioned that FLPs comprising precisely designed BAr_3 could enable transformations that are challenging to achieve with conventional transition metal catalysts. Particularly, I report the development of hydrogenation of *N*-heteroaromatics using either pure or crude H_2 in the presence of catalytic amounts of original BAr_3. As described later, crude H_2 is a mixed gas primarily composed of H_2, CO, and CO_2, which is industrially produced from various hydrocarbon resources including wastes and biomass.[37–40] Contaminants such as CO and CO_2 would thus induce deactivation of transition metal catalysts or trigger undesirable side reactions, making the use of transition metal catalysts under crude H_2 conditions challenging.

This thesis comprises five chapters: the General Introduction presented in this chapter, followed by three research chapters, and concluding with a final chapter summarizing the findings. In Chapter 1, I developed a molecules-based H_2 purification system that relies on the hydrogenation of *N*-heteroaromatics and the dehydrogenation of their hydrogenated derivatives as key processes. I found that crude H_2 containing excess amounts of CO, CO_2, and methane (CH_4) could also be applied to the hydrogenation system. In Chapter 2, the reaction mechanism of 2-methylquinoline hydrogenation under crude H_2 conditions was investigated using the artificial force induced reaction (AFIR) method. In Chapter 3, based on the results from Chapter 2, I developed a reaction system involving FLPs comprising olefins as Lewis bases and BAr_3 for the heterolytic cleavage of H_2. Specifically, this study focused on the hydrogenation of *N*-substituted indole derivatives with electron-rich olefinic moieties.

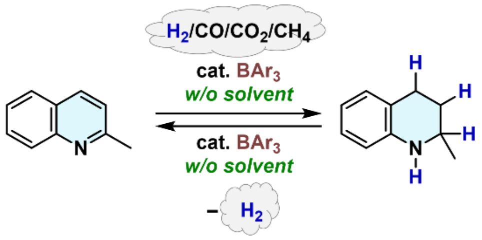

Figure 5. H_2 purification through sequential hydrogenation/dehydrogenation of *N*-heterocycles in the presence of a catalytic amount of BAr_3.

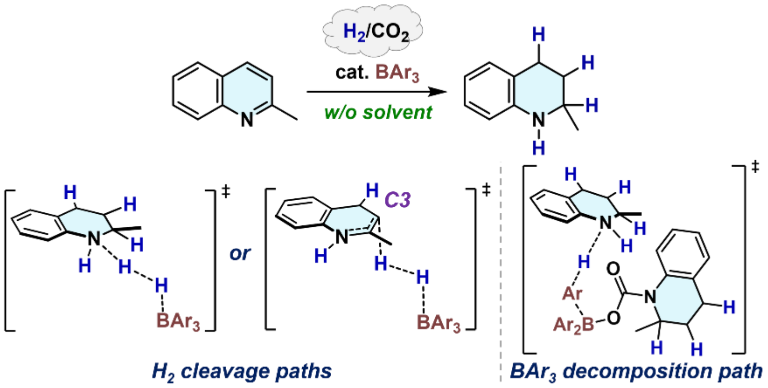

Figure 6. Key H_2-cleavage paths and BAr_3-decomposition path based on mechanistic studies.

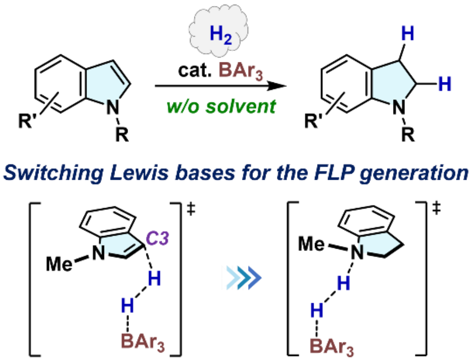

Figure 7. BAr_3-catalyzed hydrogenation of *N*-substituted indoles.

Figure 8 presents an overview of the BAr_3 catalysts investigated in this work.

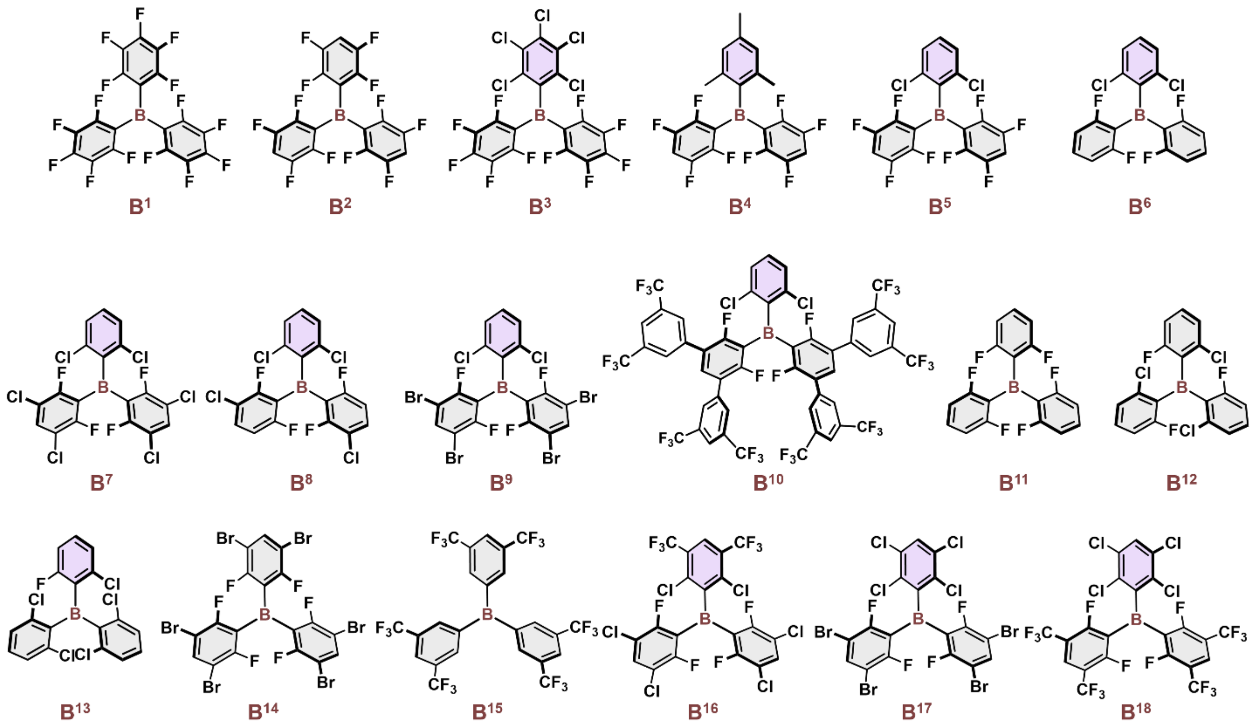

Figure 8. An overview of the BAr_3 catalysts investigated in this work.

References and notes

1. For selected reviews on hydrogenation of *N*-heteroaromatics, see: (a) Wang, D.-S.; Chen, Q.-A.; Lu, S.-M.; Zhou, Y.-G. *Chem. Rev.* **2012**, *112*, 2557. (b) Kim, A. N.; Stoltz, B. M. *ACS Catal.* **2020**, *10*, 13834. (c) Gunasekar, R.; Goodyear, R. L.; Silvestri, I. P.; Xiao, J. *Org. Biomol. Chem.* **2022**, *20*, 1794.
2. For selected reviews on application for hydrogen storage, see: (a) Modisha, P. M.; M. Ouma, C. N.; Garidzirai, R.; Wasserscheid, P.; Bessarabov, D. *Energy Fuels* **2019**, *33*, 2778. (b) Shimbayashi, T.; Fujita, K. *Tetrahedron* **2020**, *76*, 130946.
3. Blaser, H.-U. *Top. Catal.* **2010**, *53*, 997.
4. Bullock, R. M. ed. *Catalysis without Precious Metals*, (Wiley, 2010).
5. For pioneering work on FLP, see: Welch, G. C.; San Juan, R. R.; Masuda, J. D.; Stephan, D. W. *Science* **2006**, *314*, 1124.
6. For selected reviews on FLP, see: (a) Stephan, D. W.; Erker, G. *Angew. Chem., Int. Ed.* **2015**, *54*, 6400. (b) Jupp, A. R.; Stephan, D. W. *Trends Chem.* **2019**, *1*, 35. (c) Fasano, V.; Ingleson, M. J. *Synthesis* **2018**, *50*, 1783. (d) Carden, J. L.; Dasgupta, A.; Melen, R. L. *Chem. Soc. Rev.* **2020**, *49*, 1706.
7. For selected reviews on hydrogenation with FLP, see: (a) Lam, J.; Szkop, K. M.; Mosaferi, E.; Stephan, D. W. *Chem. Soc. Rev.* **2019**, *48*, 3592. (b) Scott, D. J.; Fuchter, M. J.; Ashley, A. E. *Chem. Soc. Rev.* **2017**, *46*, 5689. (c) Stephan, D. W. *J. Am. Chem. Soc.* **2021**, *143*, 20002.
8. Stephan, D. W. *Chem. Soc. Rev.* **2023**, *52*, 4632.
9. Stephan, D. W.; Erker, G. *Chem. Sci.* **2014**, *5*, 2625.
10. Stephan, D. W.; Erker, G. *Angew. Chem., Int. Ed.* **2010**, *49*, 46.

11. Ashley, A. E.; Thompson, A. L.; O’Hare, D. *Angew. Chem., Int. Ed.* **2009**, *48*, 9839.
12. Mömming, C. M.; Otten, E.; Kehr, G.; Fröhlich, R.; Grimme, S.; Stephan, D. W.; Erker, G. *Angew. Chem., Int. Ed.* **2009**, *48*, 6643.
13. Tran, S. D.; Tronic, T. A.; Kaminsky, W.; Heinekey, D. M.; Mayer, J. M. *Inorg. Chim. Acta* **2011**, *369*, 126.
14. Voss, T.; Mahdi, T.; Otten, E.; Fröhlich, R.; Kehr, G.; Stephan, D. W.; Erker, G. *Organometallics* **2012**, *31*, 2367.
15. Liu, Y.-L.; Kehr, G.; Daniliuc, C. G.; Erker, G. *Chem. Sci.* **2017**, *8*, 1097.
16. Jian, Z.; Kehr, G.; Daniliuc, C. G.; Wibbeling, B.; Erker, G. *Dalton Trans.* **2017**, *46*, 11715.
17. Jie, X.; Sun, Q.; Daniliuc, C. G.; Knitsch, R.; Hansen, M. R.; Eckert, H.; Kehr, G.; Erker, G. *Chem.-Eur. J.* **2020**, *26*, 1269.
18. Chase, P. A.; Jurca, T.; Stephan, D. W. *Chem. Commun.* **2008**, 1701.
19. Chase, P. A.; Welch, G. C.; Jurca, T.; Stephan, D. W. *Angew. Chem., Int. Ed.* **2007**, *46*, 8050.
20. Greb, L.; Oña-Burgos, P.; Schirmer, B.; Grimme, S.; Stephan, D. W.; Paradies, J. *Angew. Chem., Int. Ed.* **2012**, *51*, 10164.
21. Elmer, L.-M.; Kehr, G.; Daniliuc, C. G.; Siedow, M.; Eckert, H.; Tesch, M.; Studer, A.; Williams, K.; Warren, T. H.; Erker, G. *Chem.-Eur. J.* **2017**, *23*, 6056.
22. Eros, G.; Nagy, K.; Mehdi, H.; Pápai, I.; Nagy, P.; Kiraly, P.; Tarkanyi, G.; Soós, T. *Chem.-Eur. J.* **2012**, *18*, 574.
23. Mahdi, T.; del Castillo, J. N.; Stephan, D. W. *Organometallics* **2013**, *32*, 1971.
24. Wei, S.; Feng, X.; Du, H. *Org. Biomol. Chem.* **2016**, *14*, 8026.
25. Liu, Y.; Du, H. *J. Am. Chem. Soc.* **2013**, *135*, 12968.
26. Wang, W.; Feng, X. Du, H. *Org. Biomol. Chem.* **2016**, *14*, 6683.
27. Hounjet, L. J.; Bannwarth, C.; Garon, C. N.; Caputo, C. B.; Grimme, S.; Stephan, D. W. *Angew. Chem., Int. Ed.* **2013**, *52*, 7492.
28. Scott, D. J.; Fuchter, M. J.; Ashley, A. E. *Angew. Chem., Int. Ed.* **2014**, *53*, 10218.
29. Hoshimoto, Y.; Kinoshita, T.; Ohashi, M.; Ogoshi, S. *Angew. Chem., Int. Ed.* **2015**, *54*, 11666.
30. Sakuraba, M.; Hoshimoto, Y. *Synthesis* **2024**, *56*, 3421.
31. Morishita, T.; Hisata, Y.; Hashimoto, T.; Ogoshi, S.; Hoshimoto, Y. *J. Synth. Org. Chem., Jpn.* **2024**, *82*, 1097.
32. Hoshimoto, Y.; Kinoshita, T.; Hazra, S.; Ohashi, M.; Ogoshi, S. *J. Am. Chem. Soc.* **2018**, *140*, 7292.
33. Bergquist, C.; Bridgewater, B. M.; Harlan, C. J.; Norton, J. R.; Friesner, R. A.; Parkin, G. *J. Am. Chem. Soc.* **2000**, *122*, 10581.
34. Fasano, V.; Radcliffe, J. E.; Ingleson, M. J. *ACS Catal.* **2016**, *6*, 1793.
35. Gyömöre, Á.; Bakos, M.; Földes, T.; Pápai, I.; Domján, A.; Soós, T. *ACS Catal.* **2015**, *5*, 5366.
36. Dorkó, É.; Szabó, M.; Kótai, B.; Pápai, I.; Domján, A.; Soós, T. *Angew. Chem., Int. Ed.* **2017**, *56*, 9512.
37. Liu, K.; Song, C.; Subramani, V. Eds., *Hydrogen and Syngas Production and Purification Technologies*., Wiley (2010).

38. Dawood, F.; Anda, M.; Shafiullah, G. M. *Int. J. Hydrogen Energy* **2020**, *45*, 3847.
39. Voldsund, M.; Jordal, K.; Anantharaman, R. *Int. J. Hydrogen Energy* **2016**, *41*, 4969.
40. Holladay, J. D.; Hu, J.; King, D. L.; Wang, Y. *Catal. Today* **2009**, *139*, 244.

Chapter 1

Main group catalysis for H_2 purification based on liquid organic hydrogen carriers

Abstract: Molecular hydrogen (H_2) is one of the most important energy carriers. In the midterm future, a huge amount of H_2 will be produced from a variety of hydrocarbon sources through conversion and removal of contaminants such as CO and CO_2. However, bypassing these purification processes is desirable, given their energy consumption and environmental impact, which ultimately increases the cost of H_2. Here, I demonstrate a strategy to separate H_2 from a gaseous mixture of H_2/CO/CO_2/CH_4 that can include an excess of CO and CO_2 relative to H_2 and simultaneously store it in *N*-heterocyclic compounds that act as liquid organic hydrogen carriers (LOHCs), which can be applied to produce H_2 by subsequent dehydrogenation. My results demonstrate that LOHCs can potentially be used for H_2 purification from CO- and CO_2-rich crude H_2 in addition to their well-established use in H_2 storage.

1.1 Introduction

Molecular hydrogen (H_2) is an essential reductant that has been widely used in, e.g., petroleum refineries, the industrial production of ammonia and methanol, and the chemical industry. Moreover, H_2 is one of the most promising energy carriers of the future, given its high stability and thus transportability, its high gravimetric energy density, and the low environmental impact of its combustion product compared to those of hydrocarbon-based energy sources.[1–4] These features make H_2 an attractive candidate for the construction of a greener and sustainable economy, which is commonly referred to as the "hydrogen economy".[3] Thus, it can be expected that a huge amount of H_2, on a magnitude of more than 10^{12} standard cubic feet per year, will be produced from a wide range of hydrocarbon and renewable resources.[1,2] In this context, H_2 production combined with CO_2 capture and storage from hydrocarbon resources such as petroleum, coal, natural gas, and biomass represents a pragmatic choice for the midterm future due to the limited supply of renewable energy,[2] while the electrolysis of water using electricity obtained from renewable resources seems to be an alternative option in the long-term future.[5] The predominant contemporary route to H_2 production includes the intensive purification of crude H_2, which is a gaseous mixture of H_2, CO, CO_2, and other components that is produced by gasification, reforming, and/or water-gas shift (WGS) (process I in Figure 1.1A). Purification processes such as pressure swing adsorption (PSA), membrane separation, and cryogenic separation critically determine the purity of the H_2, which is sometimes required to exceed 99.99% for fuel cells, and influence the total energy consumption of the H_2 production process, making it cost inefficient. Notable advances have been made to improve the efficiency, H_2 recovery rate, and reproducibility of H_2 purification processes.[4] Nevertheless, an approach that could fundamentally solve all these challenging issues remains to be found.[1] Thus, although H_2 can currently be stored after or during the process I in Fig. 1.1A,[6] I envisaged a solution where H_2 could be stored in its carrier directly from crude H_2, which often includes more CO than H_2, without the requirement for any of the aforementioned shift and purification processes (process II in Figure 1.1A).[7]

Moreover, the recovery of H_2 after my proposed path ultimately leads to the production of highly pure H_2.

To this end, I focused on the use of liquid organic hydrogen carriers (LOHCs), which have been widely used for H_2 storage and transportation.[8–12] H_2 storage systems with LOHCs are based on a reaction sequence in which a H_2 lean state (H_0-LOHC) is hydrogenated to produce a H_2-rich state (H_x-LOHC), followed by a subsequent dehydrogenation of H_x-LOHC after storage/transport that regenerates H_2 and H_0-LOHC (Figure 1.1B). The use of LOHCs has been extensively researched, as the technical, environmental, and economic advantages of H_2 storage using LOHCs are widely accepted.[8] Furthermore, the pool of potential candidates for H_0-LOHCs has recently been expanded from the well-studied aromatic hydrocarbons to include heteroaromatics,[11–13] cyclic dipeptides,[14] amides,[15,16] cyclic ureas,[17] and oligoesters,[10] some of which provide hydrogenated products (H_x-LOHC) with H_2 storage capacity [H_2 weight % (wt %)] values that exceed the practical guidelines proposed by the European Union (5.0 wt %) and the U.S. government (5.5 wt %).[8] However, hitherto reported H_2 storage systems using LOHCs have predominantly been based on the use of transition metal catalysts. This presents a critical issue for H_2 separation in the presence of CO and CO_2, both of which can severely inhibit transition metal-catalyzed hydrogenation reactions.[6,9] Our group have successfully showed a strategy for H_2 separation from multicomponent gas mixtures such as $H_2/CO/CO_2$ via the main group-catalyzed hydrogenation of organic molecules in 2017.[7] Note here that Breakman-Danheux and co-workers[18] in 1996 and Jorschick and co-workers[19] in 2019 have independently reported transition metal-based heterogeneous compounds that have been applied to the hydrogenation of hydrocarbon-based LOHCs using contaminated H_2 including CO, CO_2, and/or gaseous hydrocarbons, which led to a marked suppression of the catalytic activity by CO despite the great excess of H_2 present.

Against this background, I have focused on main group catalysis[20,21] including the use of frustrated Lewis pairs (FLPs) that are composed of Lewis bases (LBs) and triarylboranes as the Lewis acids (LAs).[22–24] Triarylboranes of the type **B*n*** such as $B(C_6F_5)_3$ (**B¹**) have been reported to catalyze the hydrogenation of *N*-heteroaromatic compounds such as 2-methylquinoline (**MeQin**) under diluted conditions.[25–27] FLPs are well known to mediate the heterolytic cleavage of the H–H bond to generate [LB–H][H–LA] species (Figure 1.1C, I).[23] The subsequent proton/hydride transfer from [LB–H][H–LA] to *N*-heteroaromatic compounds facilitates the storage of H_2.[26] CO_2 fixation by FLPs has also been widely studied and found to proceed in either a reversible or irreversible manner (e.g., Figure 1.1C, II).[28,29] The hydrogenation of CO_2 has been reported in the presence of FLPs that are composed of **B¹** and nitrogen-based LBs (Figure 1.1C, III).[29–32] CO can reversibly bind to the boron center (Figure 1.1C, IV), which would kinetically affect the H_2 cleavage step.[29,33] Moreover, these gases contain a certain amount of H_2O, which often triggers the decomposition of triarylboranes to yield, e.g., [LB–H][HO–LA], although sophisticated strategies to minimize the influence of H_2O have been reported.[34,35] The reactions shown in Figure 1.1C (II to VI) can seriously affect the progress of the targeted catalytic hydrogenation in the presence of CO, CO_2, and H_2O when the undesired paths are irreversible (or nearly irreversible). Therefore, a suitable triarylborane that exhibits sufficient reactivity toward H_2 in cooperation with LBs, yet simultaneously avoids the aforementioned irreversible deactivation paths, would be highly desirable. Note that Voicu and co-workers[36] successfully applied an FLP comprising **B¹** and P^tBu_3 to the microfluidic separation of ethylene and ethane.

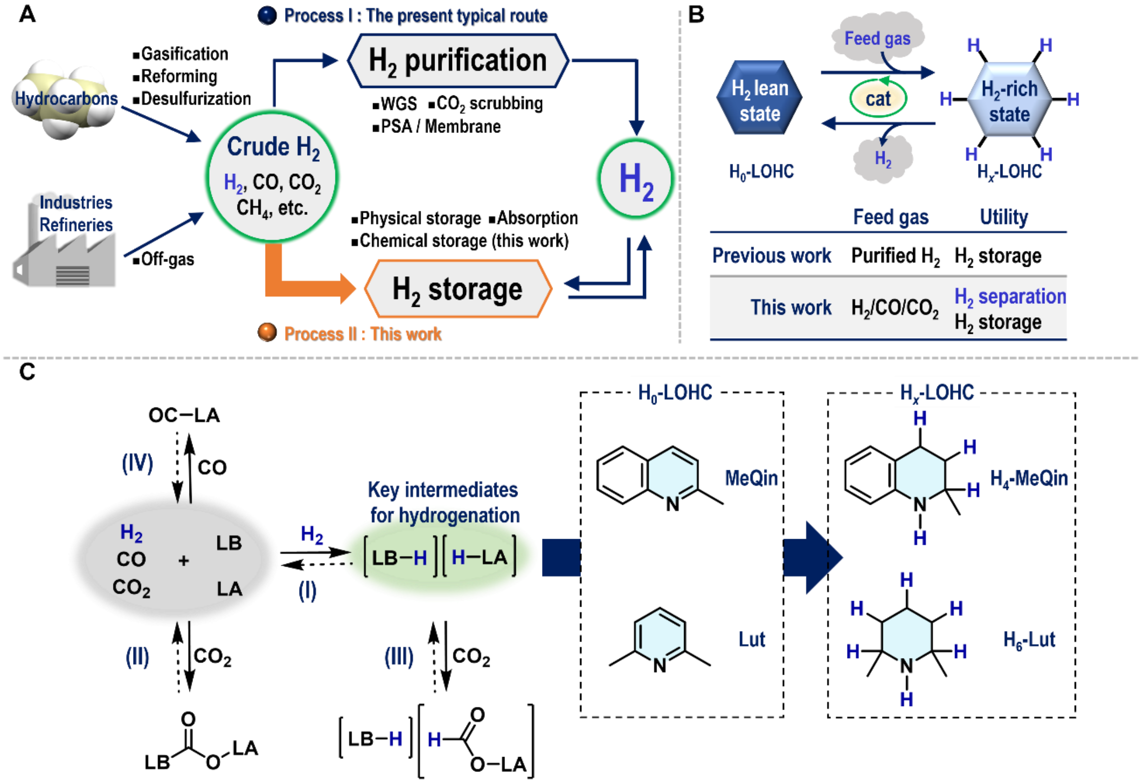

Figure 1.1. Research background and concept of this study. (A) Simplified schemes of representative contemporary routes of H_2 purification followed by H_2 storage (process I) and a conceptually novel route involving the simultaneous separation and storage of H_2 from crude H_2 (process II); WGS, water-gas shift; PSA, pressure swing adsorption. (B) Schematic illustration of the general concept behind LOHCs and the critical differences between well-established methods and this work. (C) Potential reactions among H_2, CO, CO_2, LA (Lewis acid/acidic part), and/or LB (Lewis base/basic part). Dashed arrows represent backward reactions that do not always occur under the same conditions as the corresponding forward reaction.

Here, I demonstrate the direct storage of H_2 in *N*-heterocyclic compounds such as **H_4-MeQin** and 2,6-dimethylpiperidine (**H_6-Lut**) under various mixed gas conditions including H_2, CO, CO_2, and CH_4 via a shelf-stable **B″**-catalyzed hydrogenation of **MeQin** and 2,6-lutidine (**Lut**), respectively. Furthermore, the same **B″** also catalyzes the dehydrogenation from **H_4-MeQin** to produce H_2 with concomitant generation of **MeQin**. The molar compositions of $H_2/CO/CO_2$ used in this work (1/1/1, 1/5/1, and 1/1/5) were based on the molar composition of the typical crude H_2 produced by hydrocarbon resources ($H_2/CO/CO_2$ = 1/1/0.2 to 1/2/0.5) and the typical PSA off-gas ($H_2/CO/CO_2$ = 1/0.1/2), albeit these compositions vary depending on the feedstock.[4] In addition, these gases include up to 0.9 mmol of H_2O (Table 1.S2), which should be considered under the applied conditions.

1.2 Results and discussion

The interconversion between **MeQin** and **H_4-MeQin** was used as a model LOHC system to separate H_2 under these mixed gas conditions (Figure 2). As expected, well-established transition metal complexes based on Rh (**TM**[1]), Ru (**TM**[2]), or Ir (**TM**[3])[37] did not catalyze the hydrogenation of **MeQin** (1.5 M in toluene) using a gaseous mixture of $H_2/CO/CO_2$ (4 atm each; runs 1 to 3), whereas **H_4-MeQin** was efficiently yielded when H_2 (99.95% purity, 4 atm) was used in the cases of **TM**[2] and **TM**[3].[38] A higher yield of **H_4-MeQin** (12%) was observed when 1 mol% **B**[1] was subjected to these mixed gas conditions (run 4A), although the deleterious influence of the contaminants (CO, CO_2, and/or H_2O) was again observed compared to the result obtained using pure H_2 (run 4B). Encouraged by this result, I explored the triarylboranes **B**[2] to **B**[6], which have been developed by Stephan and co-workers,[39] Ashley and coworkers,[40] and Soós and co-workers[26,41,42] (runs 5 to 9). The decreasing Lewis acidity exhibited by the boron centers when the C_6F_5 group in **B**[1] were replaced with three *para*-HC_6F_4 groups (**B**[2]) or with two *para*-HC_6F_4 groups and a 2,6-$Cl_2C_6H_3$ group (**B**[5]) was found to be critical, and **H_4-MeQin** was afforded in 63 and 81% yield when **B**[2] and **B**[5] were used, respectively (runs 5 and 8). I thus carried out additional structural modifications via the substitution of the *meta*-F atoms with respect to the boron atom in **B**[5] with Cl atoms (**B**[7]), H and Cl atoms (**B**[8]), Br atoms (**B**[9]), and $(CF_3)_2C_6H_3$ groups (**B**[10]) (runs 10 to 13). **B**[9] showed the best result, affording **H_4-MeQin** in 84% yield even in the presence of CO and CO_2 (run 12). Moreover, a significant enhancement in the hydrogenation of **MeQin** was observed when the reactions were conducted using **B**[5], **B**[7], **B**[9], and **B**[10] in the absence of solvent (Figure 1.S17); **B**[9] exhibited a catalyst turnover number (TON) of 1520 at 100 ºC in the presence of $H_2/CO/CO_2$ (30 atm each), which is far higher than the TONs obtained using **B**[5] (1000), **B**[7] (1400), or **B**[10] (1340) (runs 8, 10, 12, and 13; see also Figure 1.S18). Note that the TON eventually reached to 2960 when the **B**[9]-catalyzed hydrogenation of **MeQin** was carried out under the solvent-free conditions including H_2 (85 atm). The differences observed among **B**[5], **B**[7], **B**[9], and **B**[10] can be rationalized in terms of the electronic and steric properties of the *meta*-substituents, i.e., their electron-withdrawing ability, which influences the electron-accepting ability of the boron center, and their steric size, which should cause intramolecular steric repulsion among the introduced aryl groups (Table 1.S4 and Figure 1.S44).[43] In this context, the larger size of the Br atoms in **B**[9] compared to the F (**B**[5]) and Cl (**B**[7]) atoms can be expected to play a key role in maintaining high activity under the applied mixed gas conditions by destabilizing the four coordinated boron species that would be formed during the reactions involving CO, CO_2, and/or H_2O.

Both **B**[7] and **B**[9] exhibited high stability toward air and moisture. **B**[9] can be stored under ambient conditions (22 ºC, ca. 30% humidity) for at least 1 year without any apparent decomposition, while very minor levels (ca. 1%) of decomposition were observed for **B**[7] after 1 year of storage (Figures 1.S14 and 1.S15).

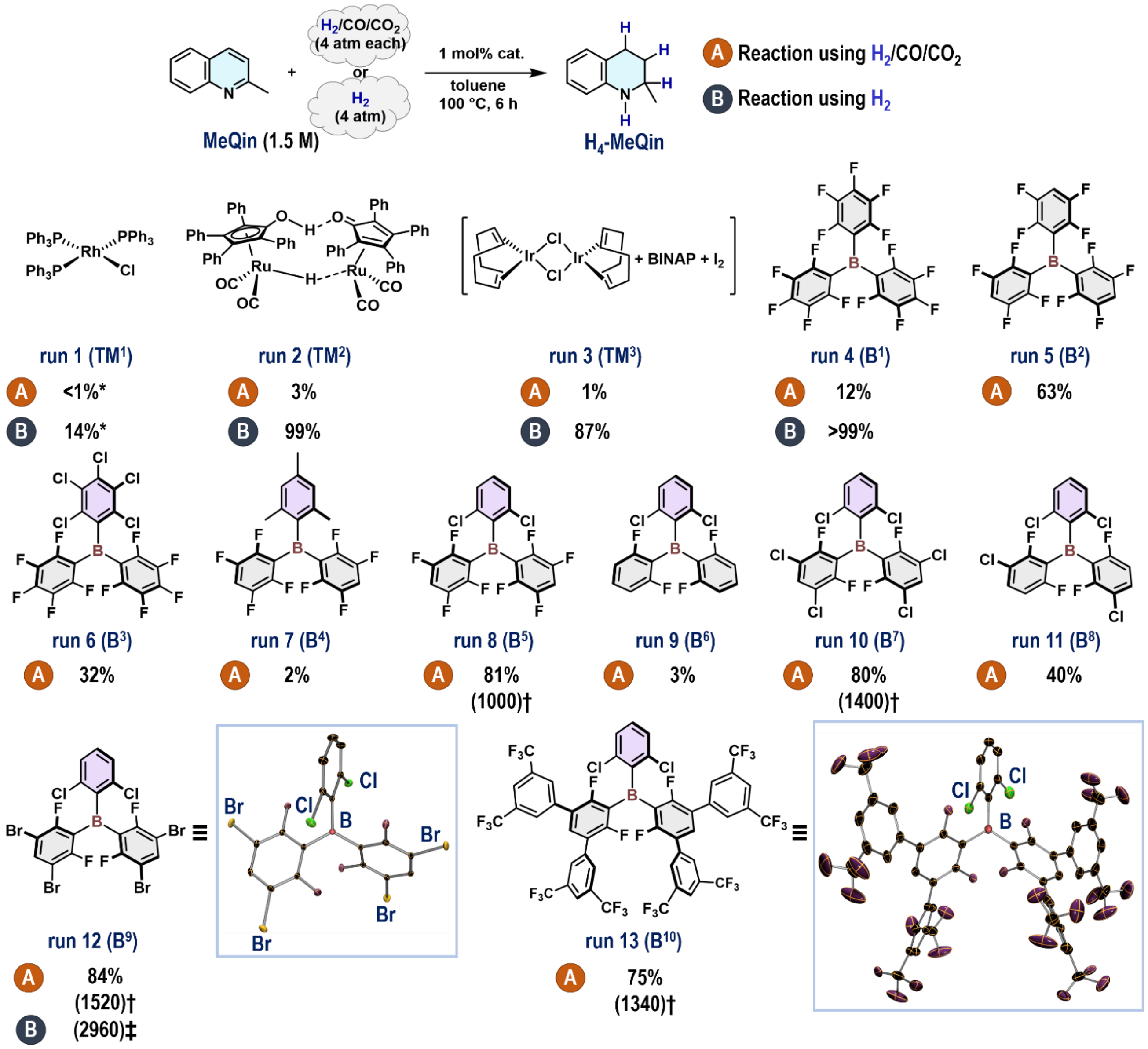

Figure 1.2. Optimization of the reaction conditions. General conditions for the catalytic hydrogenation of **MeQin**: A mixture of **MeQin** (2.5 mmol, 1.5 M in toluene) and **B*ⁿ*** (1 mol %) was treated with $H_2/CO/CO_2$ (4 atm each; conditions A) or H_2 (4 atm; conditions B) at 100 °C. Yields of **H_4-MeQin** were determined by GC analysis. The molecular structures of **B^9** and **B^{10}** were determined by single-crystal x-ray diffraction analysis and are shown with thermal ellipsoids at 30% probability (H atoms are omitted for clarity). BINAP, 2,2′-bis(diphenylphosphino)-1,1′-binaphthyl. *denotes 10 mol % catalyst. †denotes catalyst turnover number (TON) after a period of 48 h under solvent-free conditions using 0.1 mol % **B^n** and $H_2/CO/CO_2$ (30 atm each). ‡denotes catalyst TON after a period of 48 h under solvent-free conditions using 0.05 mol % **B^9** and H_2 (85 atm).

The **B^9**-catalyzed hydrogenation of **MeQin** (1 mol % catalyst, without solvent) also proceeded to furnish **H_4-MeQin** in >99 and 94% yield using CO-rich ($H_2/CO/CO_2$ = 4/20/4 atm; a model of syngas) and CO_2-rich ($H_2/CO/CO_2$ = 4/4/20 atm; a model of industrial off-gas) mixtures, respectively, although a longer reaction time was required in both cases (Figure 1.3A). These results imply that CO and CO_2 kinetically affect the catalytic activity of **B^9** toward hydrogenation, with obvious suppression when an excess of the contaminant CO_2 with respect to H_2 is present. The coexistence of CH_4 did not hamper the progress of the reaction.

I also explored the optimal conditions for the catalytic dehydrogenation of **H_4-MeQin** to afford **MeQin** (Figure 1.3B).[44,45] Without solvent, 2 mol % **B^5**, **B^7**, and **B^9** successfully catalyzed the production of **MeQin** in 84 to 88% yields at 200 °C for 6 h, whereas **B^1** and **B^{10}** exhibited inferior results (18 and 68%, respectively) under otherwise identical reaction conditions. The recovery of H_2 [193% yield; CO and CO_2 were not detected by gas chromatography (GC) analysis; Figure 1.S20] was confirmed during the **B^9**-catalyzed dehydrogenation of **H_4-MeQin** (2 h) to **MeQin** in 90% yield. Under the applied reaction conditions, the hydrogenation of **MeQin** and the dehydrogenation of **H_4-MeQin** could be catalyzed simultaneously by **B^9**.

To develop a strategy for the purification of the contaminated H_2, I designed a reaction system based on a **B^9**-catalyzed hydrogenation/dehydrogenation sequence starting from H_2/CO/CO2 [1/1/1 molar ratio; H_2 purity = (molar amount of H_2)/(sum of the molar amounts of H_2, CO, and CO_2) × 100 = 33.3%] as a feed gas (Figure 1.3C). In the presence of 2 mol % **B^9**, H_2 was directly stored in **H_4-MeQin** (0.95 mmol, 95%) from H_2/CO/CO_2 (5.4 equivalents each) via the hydrogenation of **MeQin** (1.0 mmol). After a simple evacuation, dehydrogenation of the obtained **H_4-MeQin** was carried out to generate H_2 (1.74 mmol, 174%) with a concomitant regeneration of **MeQin** (0.91 mmol, 91%). Thus, a significant increase in the H_2 purity from 33.3 to 99.9% was demonstrated by the efficient removal of CO (not detected by GC analysis) and CO_2 (detected in ca. 0.1%; Figure 1.S21) via a single cycle of the **B^9**-catalyzed hydrogenation/dehydrogenation sequence. The complete removal of CO in a single cycle would be especially noteworthy, as the removal of CO remains challenging in the well-developed multistep, multibed PSA and membrane technologies.[4]

I further explored the catalytic activity of **B^7** and **B^9** toward the hydrogenation of **Lut** to afford **H_6-Lut** under the mixed gas conditions (Figure 1.3D). This further investigation revealed that the H_2 storage capacity could be increased from 2.7 (**H_4-MeQin**) to 5.3 wt % (**H_6-Lut**). Note that **Lut** has been a challenging substrate in previously reported organoborane-catalyzed hydrogenations using H_2 even under diluted conditions.[46,47] In the presence of **B^7** (10 mol %) and the absence of solvent, **H_6-Lut** was formed in 81% yield using H_2 [20 atm; dried over 4 Å molecular sieves (MSs) before use], while a decrease in yield was observed for **B^9** (run 1). Without the dehydration of H_2, the hydrogenation of **Lut** also proceeded to afford **H_6-Lut** in 72% under identical conditions (Figure 1.S22). Moreover, **B^7** exhibited promising results for the simultaneous separation and storage of H_2 in **H_6-Lut** from CO- and CO_2-contaminated H_2 gas (runs 2 to 4), albeit an excess of H_2 with respect to the contaminants was present.

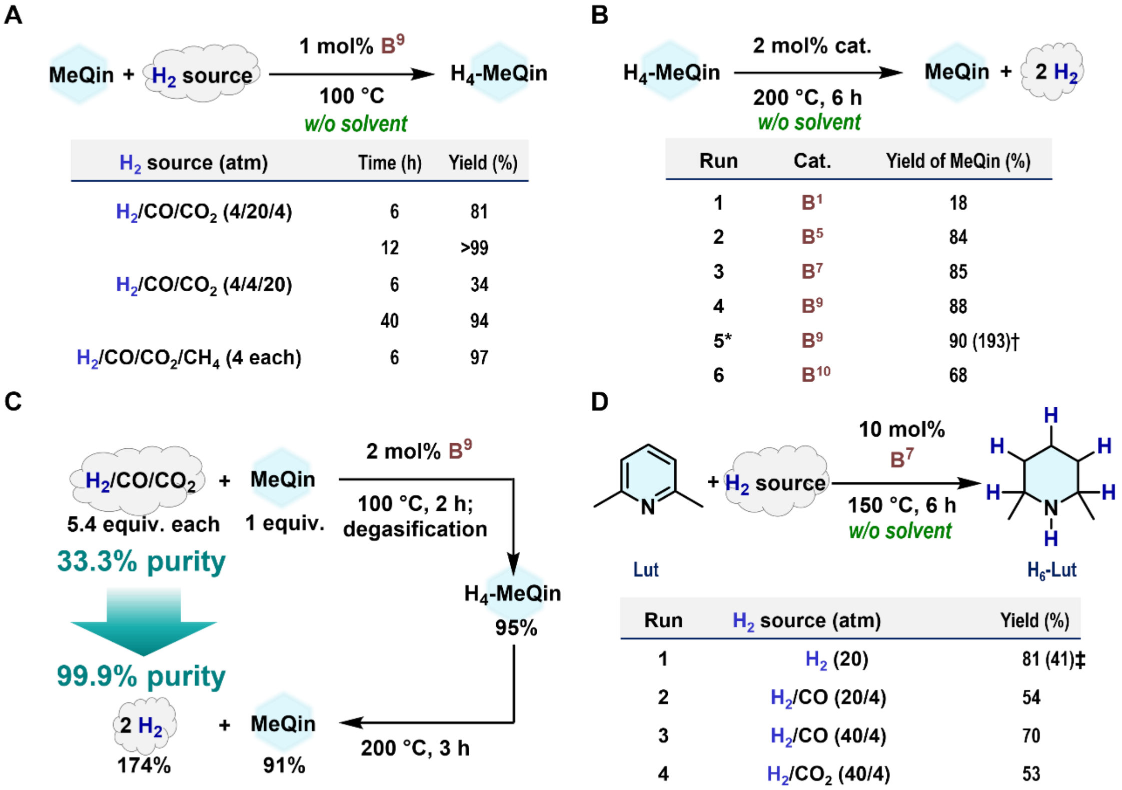

H_2 source (atm)	Time (h)	Yield (%)
$H_2/CO/CO_2$ (4/20/4)	6	81
	12	>99
$H_2/CO/CO_2$ (4/4/20)	6	34
	40	94
$H_2/CO/CO_2/CH_4$ (4 each)	6	97

Run	Cat.	Yield of MeQin (%)
1	B^1	18
2	B^5	84
3	B^7	85
4	B^9	88
5*	B^9	90 (193)†
6	B^{10}	68

Run	H_2 source (atm)	Yield (%)
1	H_2 (20)	81 (41)‡
2	H_2/CO (20/4)	54
3	H_2/CO (40/4)	70
4	H_2/CO_2 (40/4)	53

Figure 1.3. Direct H_2 purification/storage from contaminated H_2 gas based on the present catalytic process. (A) Exploration of the gas composition of the H_2 source. Yields of **H_4-MeQin** were determined using GC analysis. (B) Catalytic dehydrogenation of **H_4-MeQin** (3.8 mmol) to **MeQin** in the absence of solvent. Yields of **MeQin** were determined by GC analysis. *denotes 2 h. †denotes yield of recovered H_2 based on the collected volume (V = 164 ml, 7.32 mmol). (C) H_2 purification based on the **B^9**-catalyzed hydrogenation of **MeQin** (1.0 mmol) under mixed gas conditions and subsequent catalytic dehydrogenation. Yield of recovered H_2 based on the collected volume (V = 39.0 ml, 1.74 mmol); H_2 purity (%) = (molar amount of H_2)/(sum of the molar amounts of H_2, CO, and CO_2) × 100. (D) **B^7**-catalyzed hydrogenation of **Lut** using a variety of H_2 sources that were dried over 4 Å MS before use. ‡indicates that **B^9** was used.

To gain insight into the reaction mechanism for the present hydrogenation of *N*-heteroaromatic compounds in the presence of CO, CO_2, and H_2O, preliminary mechanistic studies were conducted using **MeQin** (Figure 1.4). First, I monitored the progress of the conversion of **MeQin** to **H_4-MeQin** using **B^1**, **B^7**, or **B^9** under each condition using solely H_2 or $H_2/CO/CO_2$ (Figure 1.4A). The production of **H_4-MeQin** exhibited a zeroth-order dependence on the concentration of **MeQin** with rate constants (k_{obs}) as follows: $3.08(29) \times 10^{-4}$ mol m^{-3} s^{-1} (H_2) and $3.56(60) \times 10^{-6}$ mol m^{-3} s^{-1} ($H_2/CO/CO_2$) (**B^1**); $1.71(6) \times 10^{-4}$ mol m^{-3} s^{-1} (H_2) and $1.66(5) \times 10^{-4}$ mol m^{-3} s^{-1} ($H_2/CO/CO_2$) (**B^7**); and $2.21(13) \times 10^{-4}$ mol m^{-3} s^{-1} (H_2) and $1.93(10) \times 10^{-4}$ mol m^{-3} s^{-1} ($H_2/CO/CO_2$) (**B^9**). Moreover, these results suggest that **H_4-MeQin** itself does not affect the rate of hydrogenation, as neither an increase nor decrease in the rate was observed increasing conversion to **H_4-MeQin**. Thus, the influence of CO and/or CO_2 is almost negligible for the **B^7**- and **B^9**-catalyzed hydrogenation processes, at least under conditions that do not involve excess amounts of CO/CO_2 with respect to H_2 (vide supra). In stark contrast, the **B^1**-catalyzed process was significantly inhibited in the presence of CO and/or CO_2. Control experiments using H_2/CO (10 atm each) and H_2/CO_2 (10 atm each) clarified that both CO and CO_2 affect the catalytic activity of **B^1** and that contamination with CO_2 is especially deleterious (Figure 1.4B). I also confirmed the kinetic orders in catalyst **B^7** [1.2(1)] and **B^9** [1.4(1)] under the H_2/CO/CO_2 atmosphere, demonstrating that these triarylboranes do catalyze the formation of **H$_4$-MeQin** (Figure 1.4C).

Next, the influence of CO_2, CO, and H_2O was investigated using **B^1** and **B^9**. The hydrogenation of **MeQin** was carried out in the presence of each borane (50 mol %) using H_2/CO_2 (2.5 atm each) at 100 ºC in toluene-d_8 and analyzed using multinuclear nuclear magnetic resonance (NMR) spectroscopy. In the case of **B^1**, the resultant mixture included C_6F_5H (20%), an equilibrium mixture of **[H$_4$-MeQin–CO$_2$–B^1]** and **[H$_3$-MeQin–CO$_2$–B^1][H$_5$-MeQin]** (12%),[28,29] and several unidentified compounds (Figure 1.4D and Figure 1.S38). Precipitation of the nitrogen-boron adduct **[H$_4$-MeQin–B^1]** was also confirmed. I separately confirmed that C_6F_5H was not formed in the absence of CO_2 (Figure 1.S41). These results clarify that CO_2 triggers the irreversible decomposition of **B^1** to yield C_6F_5H via protodeboronation from both **[H$_4$-MeQin–CO$_2$–B^1]** and **[H$_3$-MeQin–CO$_2$–B^1][H$_5$-MeQin]** under heating conditions. In stark contrast, when **B^9** was used, the generation of **H$_4$-MeQin** and recovery of **B^9** in >99% yields were observed under otherwise identical conditions. These results are consistent with the fact that the **B^9**-catalyzed hydrogenation of **MeQin** is not irreversibly inhibited by CO_2.

Density functional theory calculations were carried out at the *ω*B97X-D/6-311+G(d,p)//*ω*B97X-D/6-31G(d,p)//gas phase level of theory to shed light on the observed kinetic suppression of the hydrogenation of **MeQin** by CO.[48] The relative Gibbs energies (kcal mol^{-1}) for **OC–B^{n}** (Lewis pairs comprising CO and **B^{n}** and **TS–B^{n}** (saddle point species) with respect to [CO + **B^{n}**] (n = 1 and 9) are shown in Figure 1.4E. The coordination of CO to the boron atoms in both **B^1** and **B^9** is an endothermic process,[29,33] and coordination to the latter is far less favorable from a kinetic and thermodynamic perspective. The standard Gibbs free energies for the formation of **OC–B^{n}** are +3.2 (n = 1) and +8.1 (n = 9) kcal mol^{-1}, and the activation energies to overcome **TS–B^{n}** are +10.2 (n = 1) and +14.3 (n = 9) kcal mol^{-1}. These results rationalize the experimental results, i.e., the observations that contamination with excess CO kinetically affects both the **B^1**- and **B^9**-catalyzed hydrogenation of **MeQin** under the applied conditions, with this suppression being significant in the former case. The differences in the stability of **OC–B^{n}** should be related to the degree of geometric deviation from the ideal tetrahedral geometry around their boron centers, which can be evaluated on the basis of the value of τ_δ(B) [$\tau_\delta = \{360 - (\alpha + \beta)/141 \times \beta/\alpha\}$, where α and β are the largest and second largest C–B–C angles obtained from the gas phase-optimized structures of **OC–B^{n}**].[49] More efficient orbital overlap between the lone pair on the carbon atom in CO and the p orbital on the boron atom in **B^{n}** should result in higher stabilization of **OC–B^{n}** adducts, adopting a more ideal tetrahedral geometry [τ_δ(B) = 0.9 to 1.0] and a linear arrangement of the B–C–O atoms ($\measuredangle$B–C–O ≈ 180º). In the present study, the lower τ_δ(B) of 0.88 for **OC–B^9** indicates that its boron atom adopts a more distorted tetrahedral geometry compared to that of **OC–B1** [τ_δ(B) = 0.92], and the B–C–O atoms in **OC–B^9** are confirmed to exhibit a bent alignment (169.9º versus 179.6º in **OC–B^1**). These results thus demonstrate the effective destabilization of **OC–B^9** due to the increased steric repulsion between CO and the 2,6-$Cl_2C_6H_3$ group introduced on **B^9**, which eventually results in the reduced impact of CO on the **B^9** hydrogenation of **MeQin**.

I further evaluated the influence of H_2O on the hydrogenation (Figure 1.4F). GC analysis confirmed that no conversion of **MeQin** occurred in the presence of H_2 (4 atm) at 100 ºC when 10 mol% **[MeQin–H][HO–B^1]** was used. Although **H_4-MeQin** was furnished in 13% yield when 10 mol% **[MeQin–H][HO–B^9]** was used, the low yield again confirmed the deleterious influence of H_2O. On the basis of these results and the stability of **B^9** toward moisture at ambient conditions (vide supra), **[MeQin–H][HO–B^9]** was not generated under the applied conditions shown in Figures 1.2 and 1.3, although H_2O might be present as a contaminant.

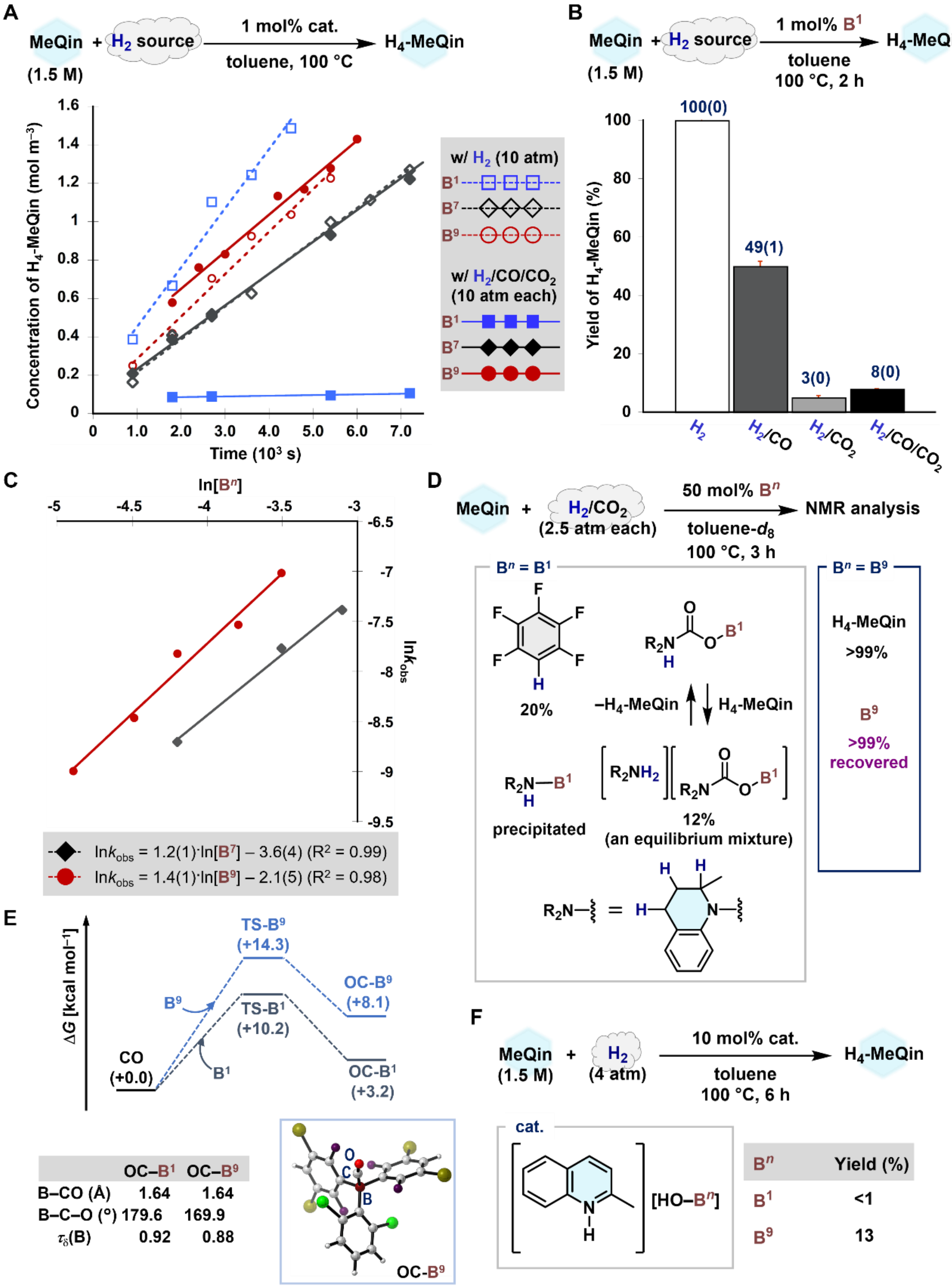

Figure 1.4. Mechanistic experiments. (A) Kinetic profiles of the concentration of **H_4-MeQin** (mol m^{-3}) with respect to reaction time (10^3 s) obtained from the hydrogenation of **MeQin** (1.5 M in toluene) in the presence of **B*ⁿ*** (n = 1, 7, and 9) and different H_2 sources (pure H_2 or $H_2/CO/CO_2$; 10 atm each). (B) Influence of the gas composition on the **B^1**-catalyzed hydrogenation of **MeQin**. Each experiment was pressurized with H_2 (10 atm) and/or CO_x (10 atm; x = 1 and/or 2). Average yields of independent three runs are shown with SEs. (C) Profile of $\ln k_{obs}$ with respect to ln[**B^n**] (n = 7 and 9). (D) Detailed analysis of the **B^n**-catalyzed hydrogenation of **MeQin** (n = 1 and 9) in the presence of H_2/CO_2 (2.5 atm each). Product yields were calculated using ^{19}F NMR analysis with $C_6H_5CF_3$ as the internal standard. In the case of **B^1**, several unidentified resonances were observed (for details, see Figure 1.S38). (E) Calculated free energy profiles for the formation of **OC–B^n** (n = 1 and 9) [kcal mol^{-1}; ωB97X-D/6-311+G(d,p)//ωB97X-D/6-31G(d,p) level]. The gas phase-optimized structure of **OC–B^9** and selected structural parameters for **OC–B^n** (n = 1 and 9) are also shown. (F) Hydrogenation of **MeQin** using **[MeQin–H][HO–B^n]** (n = 1 and 9). Yields of **H_4-MeQin** were determined via GC analysis.

1.3 Conclusion

The present results demonstrate a proof of concept for a H_2 purification technology based on LOHCs that goes beyond their well-established use in H_2 storage. This technology can be expected to change the industrial value of crude H_2 containing substantial amounts of CO, CO_2, and CH_4, which can be produced from a variety of carbon resources such as biomass and industrial off-gases. The operational simplicity of the present method should allow the construction of combined processes involving PSA and/or membranes. Moreover, this work demonstrates a new aspect of main group catalysis beyond its application as a simple alternative to well-established transition metal-catalyzed processes, i.e., the main group-catalyzed hydrogenation of unsaturated molecules under mixed gas conditions.

1.4 Supporting information

1.4.1. General considerations

Unless otherwise noted, all manipulations were conducted under a nitrogen atmosphere using standard Schlenk line or grove box (GB) techniques. Molecular sieves (4 Å) were activated by heating with a heat gun *in vacuo* (ca. 0.2 mmHg) for 5 min. ^{1}H, ^{11}B, ^{13}C, ^{19}F, and ^{31}P NMR spectra were recorded on Bruker AVANCE III 400 or JEOL JNM-400 spectrometers at 25 °C. The chemical shifts in the ^{1}H NMR spectra were recorded relative to Me_4Si or residual protonated solvent (C_6D_5H (δ 7.16), $CHCl_3$ (δ 7.26), C_7D_7H (δ 2.08), $CDHCl_2$ (δ 5.32)). The chemical shift in the ^{11}B NMR spectra was recorded relative to $BF_3{\cdot}(OCH_2CH_3)$ as an external standard. The chemical shifts in the ^{13}C NMR spectra were recorded relative to Me_4Si or deuterated solvent (C_6D_6 (δ 128.06), $CDCl_3$ (δ 77.16), CD_2Cl_2 (δ 53.84)). The chemical shifts in the ^{19}F NMR spectra were recorded relative to α,α,α-trifluorotoluene (δ −65.64). The chemical shifts in the ^{31}P NMR spectra were recorded relative to 85% H_3PO_4 as an external standard. Assignment of the resonances in ^{1}H and ^{13}C NMR spectra was based on ^{1}H−^{1}H COSY, HMQC, and/or HMBC experiments. High resolution mass spectrometry (HRMS) was performed at the Instrumental Analysis Center, Faculty of Engineering, Osaka University. A single-crystal X-ray diffraction analysis was carried out using the Rigaku XtaLAB Synergy equipping with the

HyPix-6000HE detector. Analytical gas chromatography (GC) was carried out on a Shimadzu GC-2025 gas chromatograph, equipped with a flame ionization detector, or a Shimadzu GC-2010 gas chromatograph, equipped with a barrier discharge ionization detector.

1.4.2. Materials

All commercially available reagents including super-dehydrated solvents (*n*-hexane, toluene, tetrahydrofuran, and diethyl ether) were purchased from Sigma Aldrich, Tokyo Chemical Industry (TCI) and FUJIFILM Wako Pure Chemical Corporation, and used as received. Benzene-*d*$_6$ and toluene-*d*$_8$ were distilled from sodium benzophenone ketyl prior to use. $CDCl_3$ and CD_2Cl_2 were stored inside the GB over molecular sieves (4 Å) after several freeze-pump-thaw cycles. 2-Methylquinoline (**MeQin**), 1,2,3,4-tetrahydro-2-methylquinoline (**H$_4$-MeQin**), and 2,6-lutidine (**Lut**) were purchased from TCI, and used after distillation over CaH_2. Triarylboranes (**B^2**, **B^3**, **B^4**, **B^5**, and **B^6**),[26,39-42] potassium (2,6-dichlorophenyl)trifluoroborate,[41] 1,5-dichloro-2,4-difluoro-3-iodobenzene,[50] 1-chloro-2,4-difluoro-3-iodobenzene,[50] and 1,5-dibromo-2,4-difluoro-3-iodobenzene[50] were prepared by following the reported procedures.

Gaseous chemicals including H_2, CO, CO_2, CH_4, H_2/CO (a 1:1 molar ratio), H_2/CO_2 (a 1:1 molar ratio), and $H_2/CO/CO_2$ (a 1:1:1 molar ratio) were purchased from Sumitomo Seika Chemicals Company, and used as received otherwise noted. Note that these gases include some impurities as shown in Table 1.S1.

	Impurity				
	N_2	**O_2**	**CO**	**CO_2**	**H_2**
H_2	**<200**	**<50**	**<1**	**<1**	**-**
CO	**<500**	**<100**	**-**	**<100**	**<100**
CH_4	**<5000**	**<500**	**-**	**<5000**	**-**

Table 1.S1. Impurities contaminated in H_2, CO, and CH_4 (shown in ppm).

Metrical data for the solid-state structures are available from Cambridge Crystallographic Data Centre: CCDC2162155 (**B^7**), 2162156 (**B^9**), 2162157 (**B^{10}**), 2162153 (**[MeQin–H][HO–B^1]**), 2162154 (**[MeQin–H][HO–B^9]**), 2164165 (**H$_4$-MeQin–B^1**).

1.4.3. Synthesis of B^7

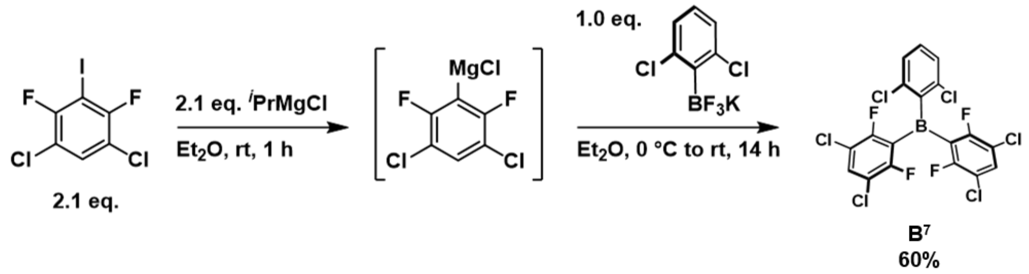

Figure 1.S1. Synthesis of **B^7**.

A solution of 1,5-dichloro-2,4-difluoro-3-iodobenzene (3.01 g, 9.75 mmol, 0.32 M in Et$_2$O) was slowly treated with ^{i}PrMgCl (4.9 mL, 9.8 mmol, 2.0 M in Et$_2$O). After stirring at room temperature for 1 h, the resultant solution was transferred into a suspension of potassium (2,6-dichlorophenyl)trifluoroborate (1.17 g, 4.63 mmol, 0.93 M in Et$_2$O) at 0 °C. The reaction mixture was then allowed to warm to room temperature, where it was stirred for another 14 h. After the removal of all volatiles *in vacuo*, the residue was extracted with hexane (50 mL × 5; warmed to 70 °C prior to use). The combined organic layer was concentrated *in vacuo* and washed with hexane (cooled to −20 °C prior to use) to afford **B^7** as a white solid (1.46 g, 2.80 mmol, 60%). A single crystal suitable for X-ray diffraction analysis was prepared by recrystallization from toluene/hexane at −35 °C. **^{1}H NMR** (400 MHz, C_6D_6): δ 6.80 (t, $^4J_{H,F}$ = 7.5 Hz, 2H); 6.76 (d, J = 8.0Hz, 2H), 6.46 (t, J = 8.0 Hz, 1H). **^{11}B NMR** (128 MHz, C_6D_6): δ 64.6 (br). **^{13}C{^{1}H} NMR** (101 MHz, C_6D_6): δ 159.1 (dd, J = 10.2 Hz, $^1J_{C,F}$ = 256.2 Hz), 141.1 (dm), 136.3, 134.8, 131.7, 127.2, 118.9 (dm), 117.9 (d, J = 22.2 Hz). **^{19}F NMR** (376 MHz, C_6D_6): δ −104.0 (d, $^4J_{H,F}$ = 7.5 Hz, 4F). X-ray data for **B^7** (Figure 1.S2): M = 520.73, colorless, orthorhombic, *Pbcn* (#60), a = 16.6550(3) Å, b = 10.3237(2) Å, c = 11.4217(2) Å, α = 90°, β = 90°, γ = 90°, V = 1963.86(6) Å^3, Z = 4, *Dcalcd* = 1.761 g/cm^3, T = −130 °C, R_1 (wR_2) = 0.0252 (0.0641).

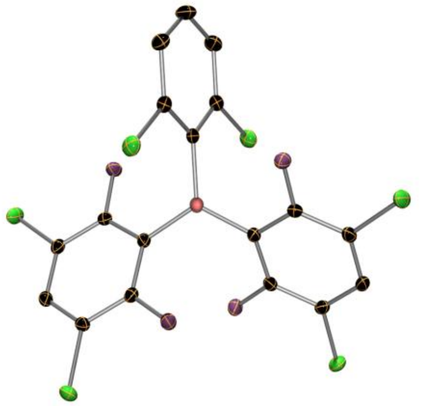

Figure 1.S2. Molecular structure of **B^7** with ellipsoids set at 30% probability. H atoms are omitted for clarity.

1.4.4. Synthesis of B^8

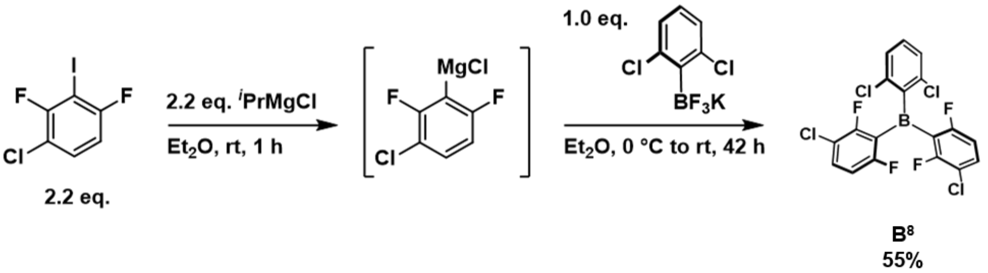

Figure 1.S3. Synthesis of **B^8**.

A solution of 1-chloro-2,4-difluoro-3-iodobenzene (3.02 g, 11.0 mmol, 0.33 M in Et$_2$O) was slowly treated with ^{i}PrMgCl (11.0 mL, 11.0 mmol, 1.0 M in Et$_2$O). After stirring at room temperature for 1 h, the resultant solution was transferred into a suspension of potassium (2,6-dichlorophenyl)trifluoroborate (1.24 g, 4.90 mmol, 0.49 M in Et$_2$O) at 0 °C. The reaction mixture was then allowed to warm to room temperature, where it was stirred for another 42 h. After the removal of all volatiles *in vacuo*, the residue was extracted with α,α,α-trifluorotoluene (50 mL × 3; warmed to 70 °C prior to use). The combined organic layer was concentrated *in vacuo* and washed with hexane (cooled to −20 °C prior to use) to afford **B⁸** as a white solid (1.21 g, 2.68 mmol, 55%). **^{1}H NMR** (400 MHz, C_6D_6): *δ* 6.86 (d, *J* = 8.4 Hz, 2H), 6.81 (dt, *J* = 6.0 Hz, *J* = 8.5 Hz, 2H), 6.57 (t, *J* = 8.4 Hz, 1H), 6.19 (t, *J* =9.0 Hz, 2H). **^{11}B NMR** (128 MHz, C_6D_6): *δ* 62.8 (br). **^{13}C{^{1}H} NMR** (101 MHz, C_6D_6): *δ* 164.3 (dd, *J* = 9.6 Hz, $^{1}J_{C,F}$ = 256.1 Hz), 160.8 (dd, *J* = 11.1 Hz, $^{1}J_{C,F}$ = 257.1 Hz), 142.3 (dm), 136.4 (d, *J* = 11.6 Hz), 134.9, 131.2, 127.1, 118.6 (dm), 117.2 (dd, *J* = 3.8 Hz, *J* = 21.2 Hz), 112.6 (dd, *J* = 3.8 Hz, *J* = 27.0 Hz). **^{19}F NMR** (376 MHz, C_6D_6): *δ* −102.0 (d, *J* = 11.3 Hz, 2F), −102.2 (br, 2F).

1.4.5. Synthesis of B^{9}

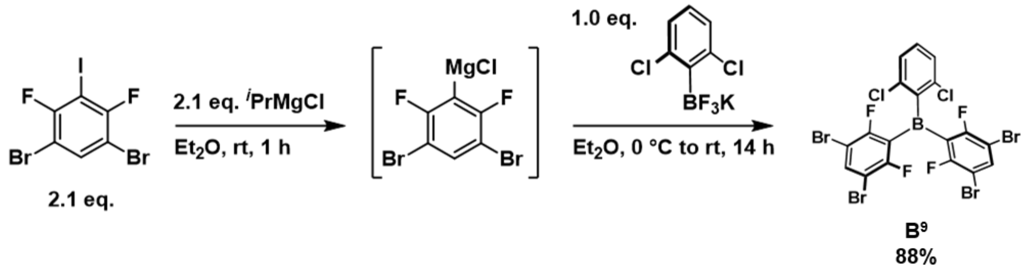

Figure 1.S4. Synthesis of **B⁹**.

A solution of 1,5-dibromo-2,4-difluoro-3-iodobenzene (3.45 g, 8.67 mmol, 0.29 M in Et_2O) was slowly treated with ^{i}PrMgCl (8.7 mL, 8.7 mmol, 1.0 M in Et_2O). After stirring at room temperature for 1 h, the resultant solution was trnsferred into a suspension of potassium (2,6-dichlorophenyl)trifluoroborate (1.05 g, 4.15 mmol, 0.42 M in Et_2O) at 0 °C. The reaction mixture was then allowed to warm to room temperature, where it was stirred for another 14 h. After the removal of all volatiles *in vacuo*, the residue was extracted with α,α,α-trifluorotoluene (50 mL × 3; warmed to 70 °C prior to use). The combined organic layer was concentrated *in vacuo* and washed with hexane (cooled to −20 °C prior to use) to afford **B⁹** as a white solid (2.56 g, 3.66 mmol, 88%). A single crystal suitable for X-ray diffraction analysis was prepared by recrystallization from toluene/hexane at −35 °C. **^{1}H NMR** (400 MHz, C_6D_6): *δ* 7.20 (t, $^{4}J_{H,F}$ = 7.2 Hz, 2H), 6.74 (d, *J* = 8.0 Hz, 2H), 6.45 (t, *J* = 8.0 Hz, 1H). **^{11}B NMR** (128 MHz, C_6D_6): *δ* 60.5 (br). **^{13}C{^{1}H} NMR** (101 MHz, C_6D_6): *δ* 160.7 (dd, *J* =9.6 Hz, $^{1}J_{C,F}$ = 255.2 Hz), 141.6, 141.2 (dm), 134.8, 131.6, 127.2, 118.8 (dm), 105.5 (m). **^{19}F NMR** (376 MHz, C_6D_6): *δ* −95.1 (d, $^{4}J_{H,F}$ = 7.5 Hz, 4F). X-ray data for **B⁹** (Figure 1.S5): *M* = 698.53, colorless, monoclinic, *C2/c* (#15), *a* = 30.3351(3) Å, *b* = 8.1009(1) Å, *c* = 17.1872(2) Å, *α* = 90°, *β* = 101.162(1)°, *γ* = 90°, *V* = 4143.72(8) Å^{3}, Z = 8, *Dcalcd* = 2.239 g/cm^{3}, T = −150 °C, R_1 (wR_2) = 0.0309 (0.0782).

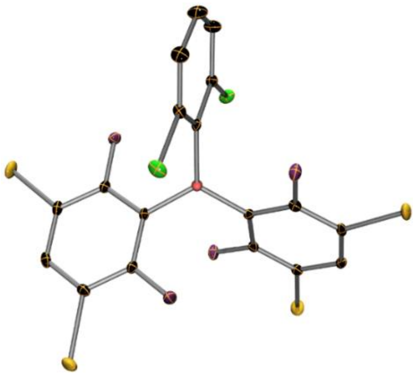

Figure 1.S5. Molecular structure of **B^9** with ellipsoids set at 30% probability. H atoms are omitted for clarity.

1.4.6. Synthesis of B^{10}

1.4.6.1. Synthesis of 1,5-difluoro-2,4-di(3,5-bis(trifluoromethyl)phenyl)benzene

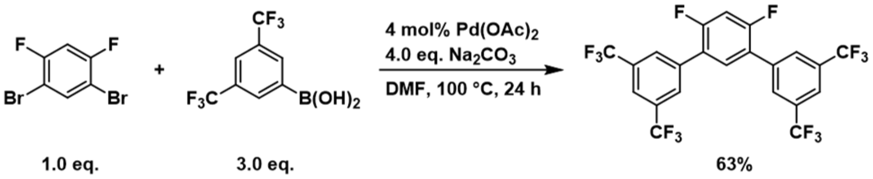

Figure 1.S6. Synthesis of 1,5-difluoro-2,4-di(3,5-bis(trifluoromethyl)phenyl)benzene.

To a solution of 1,5-dibromo-2,4-difluorobenzene (1.51 g, 5.55 mmol, 0.11 M in *N,N*-dimethylformamide) was added 3,5-bis(trifluoromethyl)phenylboronic acid (4.31 g, 16.7 mmol), Pd(OAc)$_2$ (50.0 mg, 0.223 mmol) and Na$_2$CO$_3$ (2.36 g, 22.3 mmol). The reaction mixture was stirred at 100 °C for 24 h. Then, deionized water (30 mL) was added to the resultant mixture at room temperature, followed by the extraction of the organic layer with Et$_2$O (20 mL × 3). The combined organic layer was concentrated *in vacuo*. The residue was distilled at 170 °C under reduced pressure (ca. 0.2 mmHg) to afford 1,5-difluoro-2,4-di(3,5-bis(trifluoromethyl)phenyl)benzene as colorless liquid, which eventually solidified into a white solid at room temperature (1.87 g, 3.47 mmol, 63%). **^{1}H NMR** (400 MHz, CDCl$_3$): δ 7.99 (s, 4H), 7.94 (s, 2H), 7.54 (t, J = 8.2 Hz, 1H), 7.18 (t, J = 10.0 Hz, 1H). **^{13}C{^{1}H} NMR** (101 MHz, CDCl$_3$): δ 159.9 (dd, J = 12.1 Hz, $^1J_{C,F}$ = 256.5 Hz), 136.4, 132.4 (q, J = 33.7 Hz), 132.1, 129.3, 123.9 (dd, J = 6.6 Hz, J = 12.1 Hz), 123.3 (q, $^1J_{C,F}$ = 273.7 Hz), 122.3, 106.1 (t, J = 26.8 Hz). **^{19}F NMR** (376 MHz, CDCl$_3$): δ −62.9 (s, 12F), −112.0 (t, J = 7.5 Hz, 2F). HRMS (EI$^+$): m/z Calcd for $C_{22}H_8F_{14}$ 538.0402, found 538.0398.

1.4.6.2. Synthesis of 1-iode-2,6-difluoro-3,5-di(3,5-bis(trifluoromethyl)phenyl)benzene

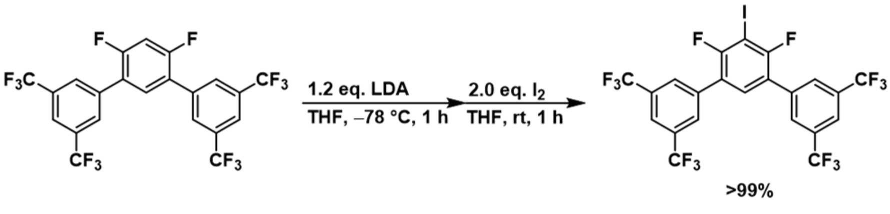

Figure 1.S7. Synthesis of 1-iode-2,6-difluoro-3,5-di(3,5-bis(trifluoromethyl)phenyl)benzene.

A solution of diisopropylamine (1.19 mL, 8.47 mmol, 0.17 M in THF) was slowly treated with *n*-BuLi (5.3 mL, 8.5 mmol, 1.6 M in hexane) at −78 °C. After stirring at −78 °C for 1 h, the resultant solution was slowly transferred into a solution of 1,5-difluoro-2,4-di(3,5-bis(trifluoromethyl)phenyl)benzene (3.81 g, 7.08 mmol, 0.14 M in THF) at −78 °C. After stirring for 1 h at −78 °C, a solution of I_2 (3.6 g, 14 mmol, 0.28 M in THF) was added, and the resultant mixture was then allowed to warm to room temperature, where it was stirred for another 1 h. After diluted with 30 mL saturated aqueous $Na_2S_2O_3$ solution, the mixture was poured into water (100 mL) and the organic layer was extracted with hexane (50 mL × 3). The combined organic layer was concentrated *in vacuo* and purified by the chromatography on a silica gel eluted with hexane. Removal of all volatiles *in vacuo* afforded 1-iode-2,6-difluoro-3,5-di(3,5-bis(trifluoromethyl)phenyl)benzene as a white solid (4.70 g, 7.08 mmol, >99%). **^{1}H NMR** (400 MHz, $CDCl_3$): δ 7.97 (s, 6H); 7.52 (t, J = 8.0 Hz, 1H). **^{13}C{^{1}H} NMR** (101 MHz, $CDCl_3$): δ 159.6 (dd, J = 6.1 Hz, $^{1}J_{\mathrm{C,F}}$ = 252.5 Hz), 135.9, 132.5 (q, J = 34.0 Hz), 132.0, 129.3, 123.9 (dd, J = 6.6 Hz, J = 15.2 Hz), 123.2 (q, $^{1}J_{\mathrm{C,F}}$ = 273.7 Hz), 122.6, 74.1 (t, J = 31.3 Hz). **^{19}F NMR** (376 MHz, $CDCl_3$): δ −62.8 (s, 12F), −92.3 (d, $^{4}J_{\mathrm{H,F}}$ = 7.5 Hz, 2F). HRMS (EI$^+$): m/z Calcd for $C_{22}H_7F_{14}I$ 663.9369, found 663.9379.

1.4.6.3. Synthesis of **B^{10}**

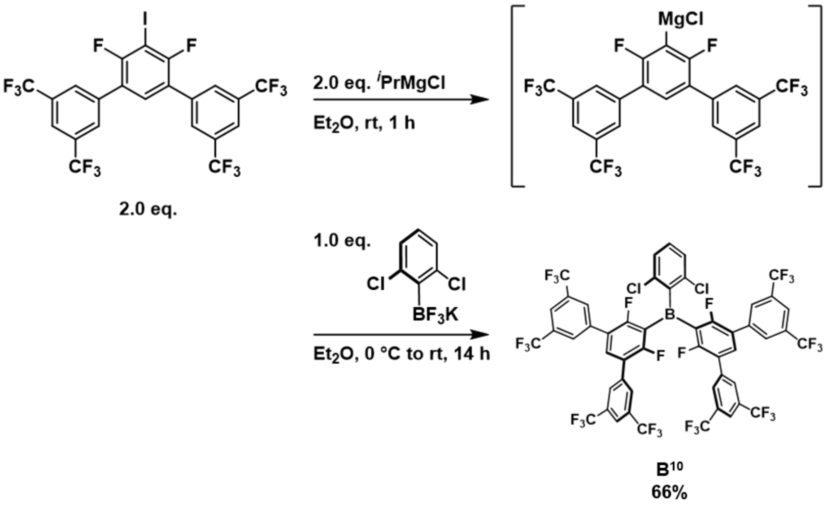

Figure 1.S8. Synthesis of **B^{10}**.

A solution of 1-iode-2,6-difluoro-3,5-di(3,5-bis(trifluoromethyl)phenyl)benzene (2.15 g, 3.24 mmol, 0.11 M in Et_2O) was slowly treated with ^{i}PrMgCl (3.3 mL, 3.3 mmol, 1.0 M in Et_2O). After stirring at room temperature for 1 h, the resultant solution was transferred into a suspension of potassium (2,6-dichlorophenyl)trifluoroborate (410 mg, 1.62 mmol, 0.16 M in Et_2O) at 0 °C. The reaction mixture was then allowed to warm to room temperature, where it was stirred for another 14 h. After the removal of all volatiles *in vacuo*, the residue was extracted with α,α,α-trifluorotoluene (50 mL × 3; warmed to 70 °C prior to use). The combined organic layers were concentrated *in vacuo* and washed with hexane (cooled to −20 °C prior to use) to afford **B^{10}** as a white solid (1.32 g, 1.07 mmol, 66%). A single crystal suitable for X-ray diffraction analysis was prepared by recrystallization from α,α,α-trifluorotoluene at −35 °C. **^{1}H NMR** (400 MHz, $CDCl_3$): δ 7.94 (br, 12H), 7.71 (t, J = 8.2 Hz, 2H), 7.33 (br, 3H). **^{11}B NMR** (128 MHz, $CDCl_3$): Not observed. **^{13}C{^{1}H} NMR** (101 MHz, C_6D_6): δ 162.0 (d, $^1J_{C,F}$ = 173.7 Hz), 137.2, 136.2, 134.8, 132.4 (q, J = 22.6 Hz), 131.7, 129.4, 127.4, 123.9, 123.2 (q, $^1J_{C,F}$ = 182.8 Hz), 122.4. Resonances of the C_{ipso} with respect to the boron atom were not observed. **^{19}F NMR** (376 MHz, $CDCl_3$) δ −66.1 (s, 24F), −103.7 (d, $^4J_{H,F}$ = 7.5 Hz, 4F). X-ray data for **B^{10}** (Figure 1.S9): M = 1234.51, colorless, monoclinic, $P2/n$ (#13), a = 12.3665(3) Å, b = 9.6717(2) Å, c = 23.4111(5) Å, α = 90°, β = 100.471(2)°, γ = 90°, V = 2753.46(11) Å^3, Z = 2, $Dcalcd$ = 1.489 g/cm^3, T = −150 °C, R_1 (wR_2) = 0.0831 (0.2620). In order to improve accuracy of the refinement, solvated C_7H_8 molecules were masked by the program Olex2 v1.3.

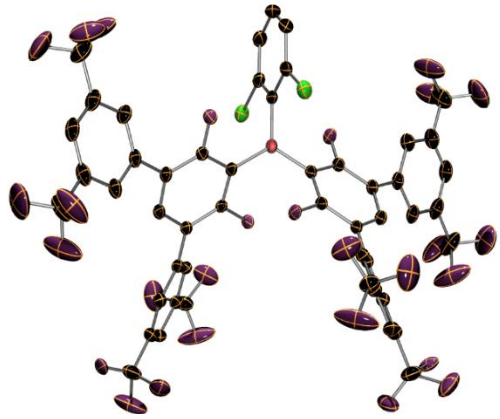

Figure 1.S9. Molecular structure of **B^{10}** with ellipsoids set at 30% probability. H atoms are omitted for clarity.

1.4.7. Synthesis of [MeQin–H][HO–B^1]

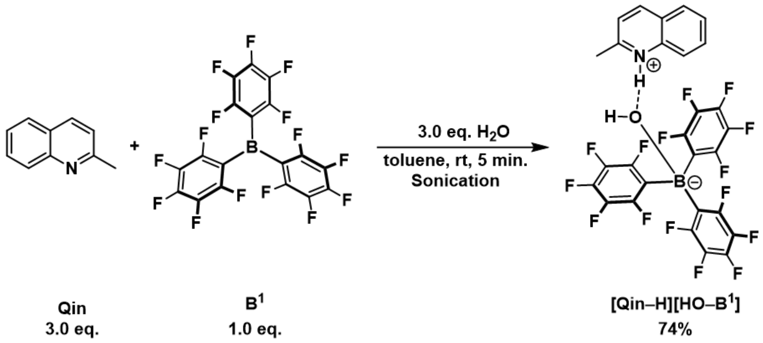

Figure 1.S10. Synthesis of **[MeQin–H][HO–B^1]**.

To a solution of **B^1** (102 mg, 0.199 mmol, 0.040 M in toluene) was subsequently added **MeQin** (86 mg, 0.60 mmol) and deionized H_2O (10.8 μL, 0.600 mmol). The reaction mixture was then sonicated (frequency: 37 kHz) for 5 min. After the removal of all volatiles *in vacuo*, the residue was washed with hexane to afford **[MeQin–H][HO–B^1]** as a white solid (99.4 mg, 0.148 mmol, 74%). A single crystal suitable for X-ray diffraction analysis was prepared by recrystallization from toluene at room temperature. **^{1}H NMR** (400 MHz, CD_2Cl_2): δ 8.66 (d, J = 8.8 Hz, 1H), 8.05 (m, 2H), 7.89 (dt, J = 1.2 Hz, J = 7.9 Hz, 1H), 7.80 (t, J = 7.6 Hz, 1H), 7.60 (d, J = 8.8 Hz, 1H), 2.80 (s, 3H). Resonances of N–*H*/*H*O–B derived from H_2O were not confirmed. **^{11}B NMR** (128 MHz, CD_2Cl_2): δ −3.7 (s). **^{13}C{^{1}H} NMR** (101 MHz, CD_2Cl_2): δ 157.7, 148.3 (dm, $^{1}J_{C,F}$ = 241.4 Hz), 145.6, 139.3 (dd, J = 13.1 Hz, $^{1}J_{C,F}$ = 247.4 Hz), 138.7, 137.2 (dd, J = 14.1 Hz, $^{1}J_{C,F}$ = 228.3 Hz), 134.7, 129.9, 128.9, 127.2, 124.0, 123.3, 120.7, 20.6 (d, J = 7.1 Hz). **^{19}F NMR** (376 MHz, CD_2Cl_2): δ −135.8 (d, J = 18.8 Hz, 6F), −161.2 (t, J = 20.7 Hz, 3F), −165.7 (m, 6F). X-ray data for **[MeQin–H][HO–B^{1}]** (Figure 1.S11): M = 673.19, colorless, triclinic, *P-1* (#2), a = 8.2453(2) Å, b = 10.0093(2) Å, c = 16.2936(3) Å, α = 98.863(2)°, β = 98.367(2)°, γ = 96.052(2)°, V = 1303.22(5) Å^3, Z = 2, *Dcalcd* = 1.715 g/cm^3, T = −100 °C, R_1 (wR_2) = 0.0322 (0.0928).

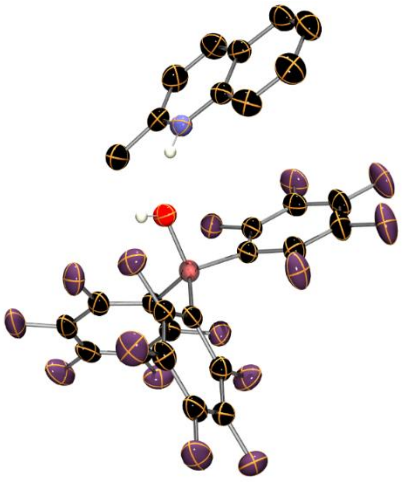

Figure 1.S11. Molecular structure of **[MeQin–H][HO–B^{1}]** with ellipsoids set at 30% probability. H atoms except those derived from H_2O are omitted for clarity.

1.4.8. Synthesis of [MeQin–H][HO–B^{9}]

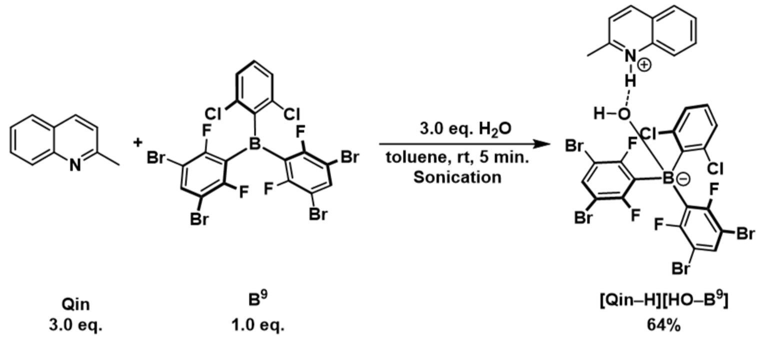

Figure 1.S12. Synthesis of **[MeQin–H][HO–B^{9}]**.

To a solution of **B^{9}** (70 mg, 0.10 mmol, 0.020 M in toluene) was subsequently added **MeQin** (43 mg, 0.30 mmol) and deionized H_2O (5.4 µL, 0.30 mmol). The reaction mixture was then sonicated (frequency: 37 kHz) for 5 min. After the removal of all volatiles *in vacuo*, the residue was washed with hexane to afford **[MeQin–H][HO–B^{9}]** as a white solid (54.7 mg, 0.0636 mmol, 64%). A single crystal suitable for X-ray diffraction analysis was prepared by recrystallization from toluene at room temperature. **^{1}H NMR** (400 MHz, CD_2Cl_2): δ 8.53 (d, J = 8.4 Hz, 1H), 7.98 (t, J = 7.4 Hz, 2H), 7.78 (dt, J = 7.2 Hz, J = 11.3 Hz, 1H), 7.70 (d, J

= 7.6 Hz, 1H), 7.51 (d, *J* = 8.4 Hz, 1H), 7.38 (m, 2H), 7.18 (d, *J* = 7.6 Hz, 2H), 7.01 (t, *J* = 7.6 Hz, 1H), 2.74 (s, 3H). Resonances of N–*H*/*H*O–B derived from H_2O were not confirmed. **^{11}B NMR** (128 MHz, CD_2Cl_2): δ −1.6 (s). **^{13}C{^{1}H} NMR** (101 MHz, CD_2Cl_2): δ 161.1 (d, *J* =17.2 Hz, $^1J_{C,F}$ = 243.4 Hz), 157.9, 144.0, 140.3, 139.8, 133.8, 132.7, 129.1, 128.4, 127.3, 127.1, 123.1, 122.1, 104.0, 104.0 (d, *J* = 32.3 Hz), 21.2 (d, *J* = 6.1 Hz). Resonances of the C_{ipso} with respect to the boron atom were not observed. **^{19}F NMR** (376 MHz, CD_2Cl_2): δ −99.1 (d, *J* = 3.8 Hz, 4F). X-ray data for **[MeQin–H][HO–B^9]** (Figure 1.S13): *M* = 859.73, colorless, monoclinic, *P2₁/n* (#14), *a* = 13.6615(2) Å, *b* = 13.2687(2) Å, *c* = 18.1974(3) Å, α = 90°, β = 95.418(2)°, γ = 90°, *V* = 3283.91(9) Å^3, Z = 4, *Dcalcd* = 1.739 g/cm^3, T = −100 °C, R_1 (wR_2) = 0.0401 (0.1094). In order to improve accuracy of the refinement, solvated H_2O molecules were masked by the program Olex2 v1.3.

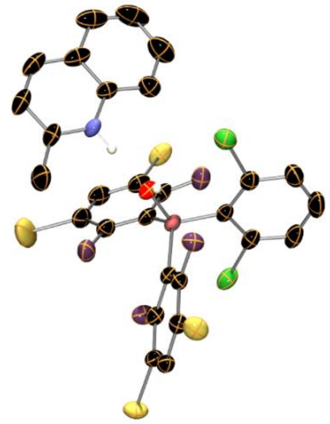

Figure 1.S13. Molecular structure of **[MeQin–H][HO–B^9]** with ellipsoids set at 30% probability. H atoms except those derived from H_2O are omitted for clarity.

1.4.9. Evaluation of stability of B^7 and B^9 toward air and moisture

Crystalline powders of **B^7** and **B^9** were kept in a shelf under the ambient conditions (30% humidity, 22 °C), and the decomposition of these boranes were monitored by NMR analyses for the period of 1 year (Figures 1.S14 and 1.S15). These results revealed no observable decomposition on **B^9**, while a trace amount of decomposition was also confirmed for **B^7**.

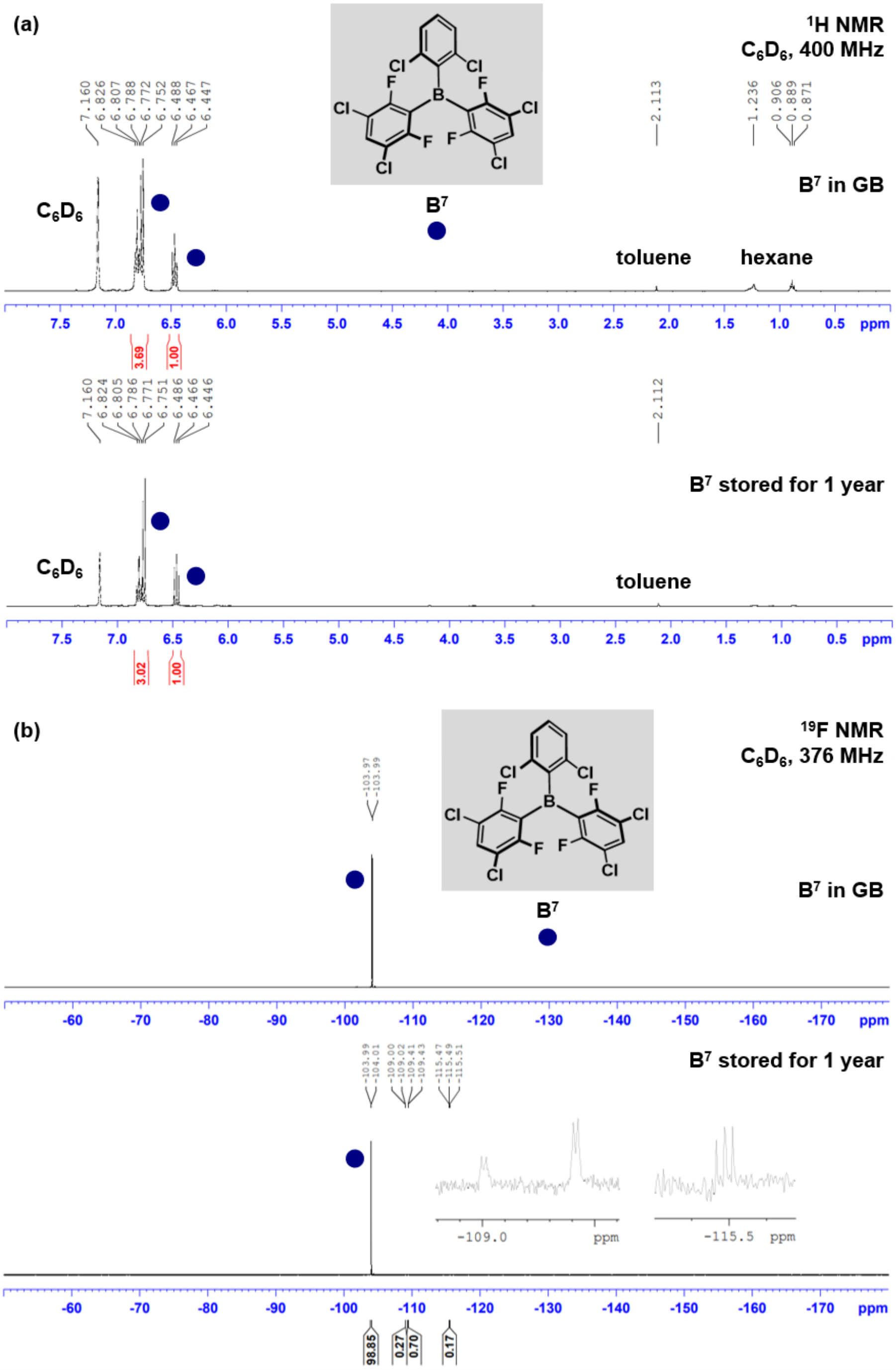

Figure 1.S14. Stability of **B**^{7} toward air and moisture. (a) ^{1}H NMR spectra. (b) ^{19}F NMR spectra.

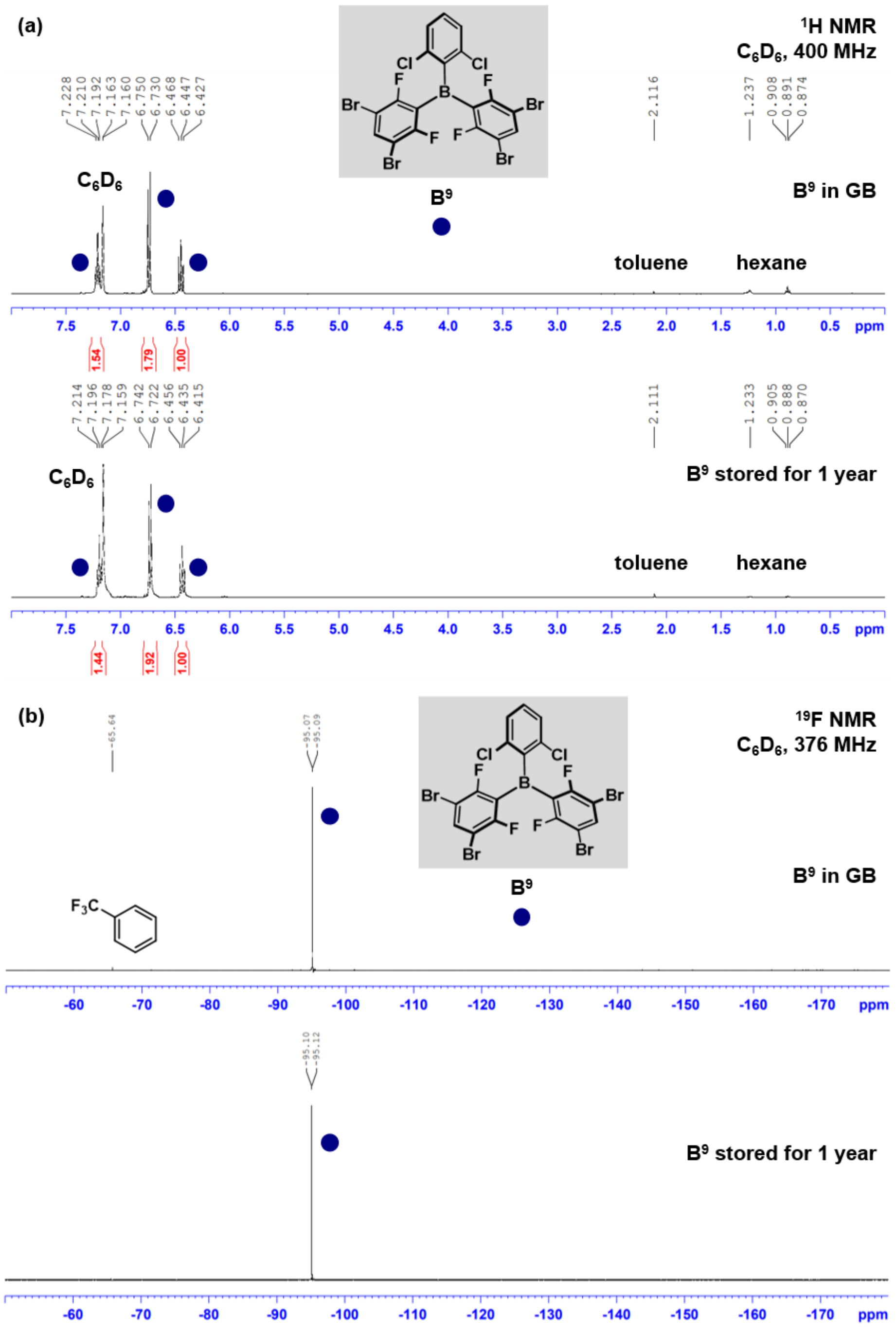

Figure 1.S15. Stability of **B**^{9} toward air and moisture. (a) ^{1}H NMR spectra. (b) ^{19}F NMR spectra.

1.4.10. Titration of H_2O contaminated in the used gases

A pressure-tight NMR tube (Wilmad-LabGrass 542-PV-7; V = 1.8 mL) was charged with 1,3-dimethoxybenzene (65 mg, 0.47 mmol; an internal standard) and C_6D_6 (500 µL). Once sealed, the NMR tube was pressurized with H_2 (5 atm), CO_2 (5 atm), or H_2/CO/CO_2 (1.6 atm each) and analyzed by ^{1}H NMR. All experiments were repeated three times, and the averaged values (ppm) are used for the amount of H_2O contaminated in each gas reagent (Table 1.S2).

Run	H_2	CO_2	$H_2/CO/CO_2$
1	34400	1420	3660
2	41500	1880	3380
3	34700	2090	3380
average	36867	1797	3473

Table 1.S2. Amount of H_2O (ppm) contaminated in used gases.

1.4.11. Screening of catalysts in hydrogenation of MeQin

1.4.11.1. Reaction with transition-metal (TM) catalysts (runs 1–3 in Figure 2)

General: A 10 mL autoclave was charged with **MeQin**, TM complexes, tetradecane (an internal standard) and toluene. Once sealed, the autoclave was pressurized with $H_2/CO/CO_2$ (4 atm each; Condition A) or H_2 (4 atm; Condition B) and heated at 100 °C for 6 h. After degassed at room temperature, the yield of **H_4-MeQin** was determined by GC analysis.

Run 1-A: Followed by the general procedures using $H_2/CO/CO_2$ (4 atm each), **MeQin** (107.4 mg, 0.750 mmol), Rh-based complex **TM^1** (69.6 mg, 0.0752 mmol), tetradecane (55.8 mg), and toluene (0.5 mL) were employed, giving **H_4-MeQin** in <1% GC yield.

Run 1-B: Followed by the general procedures using H_2 (4 atm), **MeQin** (107.4 mg, 0.750 mmol), Rh-based complex **TM^1** (69.4 mg, 0.0750 mmol), tetradecane (57.7 mg), and toluene (0.5 mL) were employed, giving **H_4-MeQin** in 14% GC yield.

Run 2-A: Followed by the general procedures using $H_2/CO/CO_2$ (4 atm each), **MeQin** (107.4 mg, 0.750 mmol), Ru-based complex **TM^2** (8.10 mg, 0.00707 mmol), tetradecane (57.6 mg), and toluene (0.5 mL) were employed, giving **H_4-MeQin** in 3% GC yield.

Run 2-B: Followed by the general procedures using H_2 (4 atm), **MeQin** (107.4 mg, 0.750 mmol), Ru-based complex **TM^2** (8.12 mg, 0.00709 mmol), tetradecane (58.2 mg), and toluene (0.5 mL) were employed, giving **H_4-MeQin** in 99% GC yield.

Run 3-A: Followed by the general procedures using $H_2/CO/CO_2$ (4 atm each), **MeQin** (107.4 mg, 0.750 mmol), $[Ir(cod)_2Cl]_2$ (5.08 mg, 0.00694 mmol), *rac*-BINAP (10.4 mg, 0.0167 mmol), I_2 (19.2 mg, 0.0756 mmol), tetradecane (60.2 mg), and toluene (0.5 mL) were employed, giving **H_4-MeQin** in 1% GC yield.

Run 3-B: Followed by the general procedures using H_2 (4 atm), **MeQin** (107.4 mg, 0.750 mmol), $[Ir(cod)_2Cl]_2$ (5.04 mg, 0.00689 mmol), *rac*-BINAP (10.2 mg, 0.0164 mmol), I_2 (19.1 mg, 0.0753 mmol), tetradecane (60.7 mg), and toluene (0.5 mL) were employed, giving **H_4-MeQin** in 87% GC yield.

Experiments using Ru-MACHO (purchased from TCI and used as received): Followed by the general procedures using $H_2/CO/CO_2$ (4 atm each), **MeQin** (358.3 mg, 2.50 mmol), Ru-MACHO (15.1 mg, 0.249 mmol), tetradecane (61.7 mg), and toluene (1.7 mL) were employed; however, production of **H_4-MeQin** was detected in <1% GC yield.

I have also carried out the following experiment based on the literature conditions that were applied for the hydrogenation of Ru complexes supported by pincer ligands;[51] I employed $H_2/CO/CO_2$ (4 atm each), **MeQin** (358.7 mg, 2.50 mmol), Ru-MACHO (15.2 mg, 0.0250 mmol), KO*ᵗ*Bu (28.1 mg, 0.250 mmol), tetradecane (59.7 mg), and THF (1.7 mL), and heated at 100 °C for 6 h. However, **H_4-MeQin** was detected in <1% GC yield.

Experiment using Pd/C: Followed by the general procedures using $H_2/CO/CO_2$ (4 atm each), **MeQin** (356.5 mg, 2.49 mmol), Pd/C (Pd 10% on carbon, 26.7 mg, 0.0251 mmol), tetradecane (60.5 mg), and toluene (1.7 mL) were employed, giving **H_4-MeQin** in 1% GC yield.

1.4.11.2. Reaction with B$''$ catalyst (runs 4–13 in Figure 1.2 and Figure 1.S16)

General using $H_2/CO/CO_2$ (Condition A): A 30 mL autoclave was charged with **MeQin** (2.5 mmol), **B$''$** (0.025 mmol; 1 mol%), and tetradecane (an internal standard), and toluene (1.67 mL). Once sealed, the autoclave was pressurized with $H_2/CO/CO_2$ (4 atm each) and heated at 100 °C for 6 h. After degassed at room temperature, the yield of **H_4-MeQin** was determined by GC analysis (Figure 1.2).

General using H_2 (Condition B): A autoclave was charged with **MeQin** (0.75 mmol, otherwise noted), **B$''$** (0.075 mmol; 10 mol% otherwise noted), and toluene (0.5 mL). Tetradecane or pentadecane was added as an internal standard. Once sealed, the autoclave was pressurized with H_2 (4 atm) and heated at 100 °C for 6 h. After degassed at room temperature, the yield of **H_4-MeQin** was determined by GC analysis (for run 4-B using 1 mol% **B^1**, see Figure 1.2; for others, see Figure 1.S16).

Run 4-A: Followed by the general procedures using $H_2/CO/CO_2$ (4 atm each), **MeQin** (359.5 mg), **B^1** (12.8 mg), and tetradecane (57.2 mg) were employed, giving **H_4-MeQin** in 12% GC yield.

Run 4-B: Followed by the general procedures using H_2 (4 atm), **MeQin** (356.9 mg), **B^1** (12.9 mg; 1 mol%), and tetradecane (57.2 mg) were employed, giving **H_4-MeQin** in >99% GC yield.

Run 5-A: Followed by the general procedures using $H_2/CO/CO_2$ (4 atm each), I independently conducted two experiments using **B^2** to accurately evaluate the catalyst activity of **B^2**. In the first experiment, **MeQin** (356.1 mg), **B^2** (11.5 mg), and tetradecane (68.7 mg) were employed to afford **H_4-MeQin** in 62% GC yield. In the second, **MeQin** (357.9 mg), **B^2** (11.4 mg), and tetradecane (65.5 mg) were employed to afford **H_4-MeQin** in 63% GC yield. The average of these two experiments (63%) is shown in Figure 1.2.

Run 5-B: Followed by the general procedures with a 10 mL autoclave using H_2 (4 atm), **MeQin** (107.4 mg), **B^2** (34.4 mg), and tetradecane (71.2 mg) were employed, giving **H_4-MeQin** in 99% GC yield.

Run 6-A: Followed by the general procedures using $H_2/CO/CO_2$ (4 atm each), I independently conducted two experiments using **B^3** to accurately evaluate the catalyst activity of **B^3**. In the first experiment, **MeQin** (357.4 mg), **B^3** (15.0 mg), and tetradecane (60.7 mg) were employed to afford **H_4-MeQin** in 27% GC yield. In the

second, **MeQin** (362.0 mg), **B**^{3} (14.9 mg), and tetradecane (63.4 mg) were employed to afford **H$_4$-MeQin** in 36% GC yield. The average of these two experiments (32%) is shown in Figure 1.2.
Run 6-B: Followed by the general procedures with a 10 mL autoclave using H_2 (4 atm), **MeQin** (107.4 mg), **B**^{3} (44.5 mg), and tetradecane (71.2 mg) were employed, giving **H$_4$-MeQin** in >99% GC yield.

Run 7-A: Followed by the general procedures using $H_2/CO/CO_2$ (4 atm each), **MeQin** (360.8 mg), **B**^{4} (10.7 mg), and tetradecane (59.9 mg) were employed, giving **H$_4$-MeQin** in 2% GC yield.
Run 7-B: Followed by the general procedures with a 10 mL autoclave using H_2 (4 atm), **MeQin** (107.4 mg), **B**^{4} (32.0 mg), and pentadecane (75.3 mg) were employed, giving **H$_4$-MeQin** in 84% GC yield.

Run 8-A: Followed by the general procedures using $H_2/CO/CO_2$ (4 atm each), I independently conducted three experiments using **B**^{5} to accurately evaluate the catalyst activity of **B**^{5}. In the first experiment, **MeQin** (360.8 mg), **B**^{5} (11.5 mg), and tetradecane (59.6 mg) were employed to afford **H$_4$-MeQin** in 72% GC yield. In the second, **MeQin** (358.9 mg), **B**^{5} (11.4 mg), and tetradecane (63.2 mg) were employed to afford **H$_4$-MeQin** in 86% GC yield. In the third, **MeQin** (358.3 mg), **B**^{5} (11.4 mg), and tetradecane (61.3 mg) were employed to afford **H$_4$-MeQin** in 85% GC yield. The average of these three experiments (81%) is shown in Figure 1.2.
Run 8-B: Followed by the general procedures with a 10 mL autoclave using H_2 (4 atm), **MeQin** (107.4 mg), **B**^{5} (34.1 mg), and pentadecane (71.3 mg) were employed, giving **H$_4$-MeQin** in >99% GC yield.

Run 9-A: Followed by the general procedures using $H_2/CO/CO_2$ (4 atm each), **MeQin** (354.6 mg), **B**^{6} (9.6 mg), and tetradecane (64.2 mg) were employed, giving **H$_4$-MeQin** in 3% GC yield.
Run 9-B: Followed by the general procedures with a 10 mL autoclave using H_2 (4 atm), **MeQin** (107.4 mg), **B**^{6} (28.7 mg), and tetradecane (75.4 mg) were employed, giving **H$_4$-MeQin** in 71% GC yield.

Run 10-A: Followed by the general procedures using $H_2/CO/CO_2$ (4 atm each), I independently conducted three experiments using **B**^{7} to accurately evaluate the catalyst activity of **B**^{7}. In the first experiment, **MeQin** (355.8 mg), **B**^{7} (13.1 mg), and tetradecane (60.2 mg) were employed to afford **H$_4$-MeQin** in 67% GC yield. In the second, **MeQin** (358.8 mg), **B**^{7} (13.1 mg), and tetradecane (58.8 mg) were employed to afford **H$_4$-MeQin** in 87% GC yield. In the third, **MeQin** (355.5 mg), **B**^{7} (13.1 mg), and tetradecane (63.6 mg) were employed to afford **H$_4$-MeQin** in 87% GC yield. The average of these three experiments (80%) is shown in Figure 1.2.
Run 10-B: Followed by the general procedures with a 10 mL autoclave using H_2 (4 atm), **MeQin** (122.6 mg), **B**^{7} (39.0 mg), and pentadecane (66.1 mg) were employed, giving **H$_4$-MeQin** in >99% GC yield.

Run 11-A: Followed by the general procedures using $H_2/CO/CO_2$ (4 atm each), **MeQin** (356.1 mg), **B**^{8} (11.3 mg), and tetradecane (60.5 mg) were employed, giving **H$_4$-MeQin** in 40% GC yield.
Run 11-B: Followed by the general procedures with a 10 mL autoclave using H_2 (4 atm), **MeQin** (107.4 mg), **B**^{8} (33.9 mg), and tetradecane (59.1 mg) were employed, giving **H$_4$-MeQin** in >99% GC yield.

Run 12-A: Followed by the general procedures using $H_2/CO/CO_2$ (4 atm each), I independently conducted three experiments using **B^9** to accurately evaluate the catalyst activity of **B^9**. In the first experiment, **MeQin** (360.1 mg), **B^9** (17.5 mg), and tetradecane (60.5 mg) were employed to afford **H$_4$-MeQin** in 83% GC yield. In the second, **MeQin** (356.0 mg), **B^9** (17.4 mg), and tetradecane (60.7 mg) were employed to afford **H$_4$-MeQin** in 86% GC yield. In the third, **MeQin** (358.8 mg), **B^9** (17.6 mg), and tetradecane (60.8 mg) were employed to afford **H$_4$-MeQin** in 82% GC yield. The average of these three experiments (84%) is shown in Figure 1.2.

Run 12-B: Followed by the general procedures with a 30 mL autoclave using H_2 (4 atm), **MeQin** (108.6 mg), **B^9** (52.4 mg), and tetradecane (58.6 mg) were employed, giving **H$_4$-MeQin** in >99% GC yield.

Run 13-A: Followed by the general procedures using $H_2/CO/CO_2$ (4 atm each), I independently conducted three experiments using **B^{10}** to accurately evaluate the catalyst activity of **B^{10}**. In the first experiment, **MeQin** (359.1 mg), **B^{10}** (30.7 mg), and tetradecane (60.1 mg) were employed to afford **H$_4$-MeQin** in 63% GC yield. In the second, **MeQin** (360.6 mg), **B^{10}** (30.7 mg), and tetradecane (62.8 mg) were employed to afford **H$_4$-MeQin** in 86% GC yield. In the third, **MeQin** (359.8 mg), **B^{10}** (30.9 mg), and tetradecane (60.3 mg) were employed to afford **H$_4$-MeQin** in 77% GC yield. The average of these three experiments (75%) is shown in Figure 1.2.

Run 13-B: Followed by the general procedures with a 30 mL autoclave using H_2 (4 atm), **MeQin** (114.0 mg), **B^{10}** (92.2 mg), and tetradecane (62.0 mg) were employed, giving **H$_4$-MeQin** in >99% GC yield.

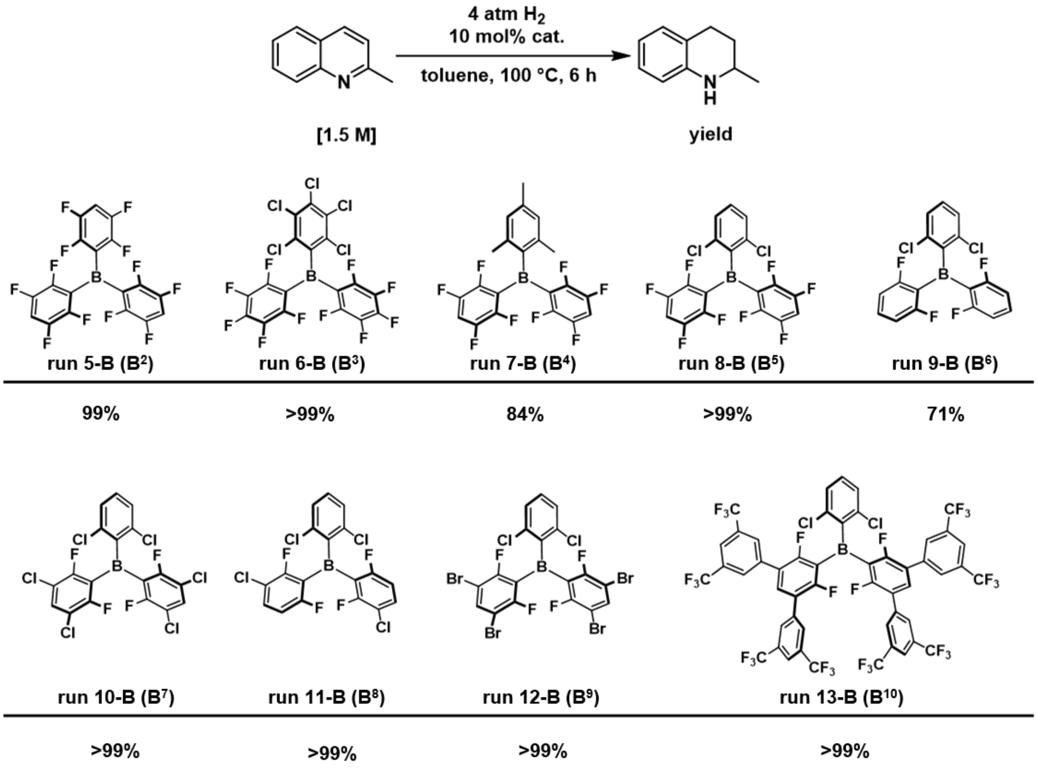

Figure 1.S16. Hydrogenation of **MeQin** using H_2.

1.4.12. Hydrogenation of MeQin using H_2/CO/CO_2 without solvent

1.4.12.1. Screening of catalysts (Figure 1.S17)

General: A 30 mL autoclave was charged with **MeQin** (3.0 mmol), **B^n** (0.030 mmol), and tetradecane (an internal standard). Once sealed, the autoclave was pressurized with H_2/CO/CO_2 (4 atm each; Condition A) or H_2 (4 atm; Condition B) and heated at 100 °C for 6 h. After degassed at room temperature, the yield of **H_4-MeQin** was determined by GC analysis.

Run 1-A: Followed by the general procedures using H_2/CO/CO_2 (4 atm each), **MeQin** (429.5 mg), **B^1** (15.5 mg), and tetradecane (233.9 mg) were employed, giving **H_4-MeQin** in 3% GC yield.
Run 1-B: Followed by the general procedures using H_2 (4 atm), **MeQin** (431.6 mg), **B^1** (15.3 mg), and tetradecane (235.6 mg) were employed, giving **H_4-MeQin** in 7% GC yield.

Run 2-A: Followed by the general procedures, **MeQin** (431.3 mg), **B^5** (13.7 mg), and tetradecane (231.2 mg) were employed, giving **H_4-MeQin** in 97% GC yield.

Run 3-A: Followed by the general procedures, **MeQin** (438.1 mg), **B^7** (15.6 mg), and tetradecane (237.8 mg) were employed, giving **H_4-MeQin** in 99% GC yield.

Run 4-A: Followed by the general procedures, **MeQin** (439.9 mg), **B^9** (21.0 mg), and tetradecane (236.4 mg) were employed, giving **H_4-MeQin** in >99% GC yield. I also carried out this reaction with **MeQin** (423.8 mg), **B^9** (20.9 mg), and tetradecane (242.8 mg) for 3 h, giving **H_4-MeQin** in 81% GC yield

Run 5-A: Followed by the general procedures, **MeQin** (436.1 mg), **B^{10}** (36.8 mg), and tetradecane (227.6 mg) were employed, giving **H_4-MeQin** in 84% GC yield.

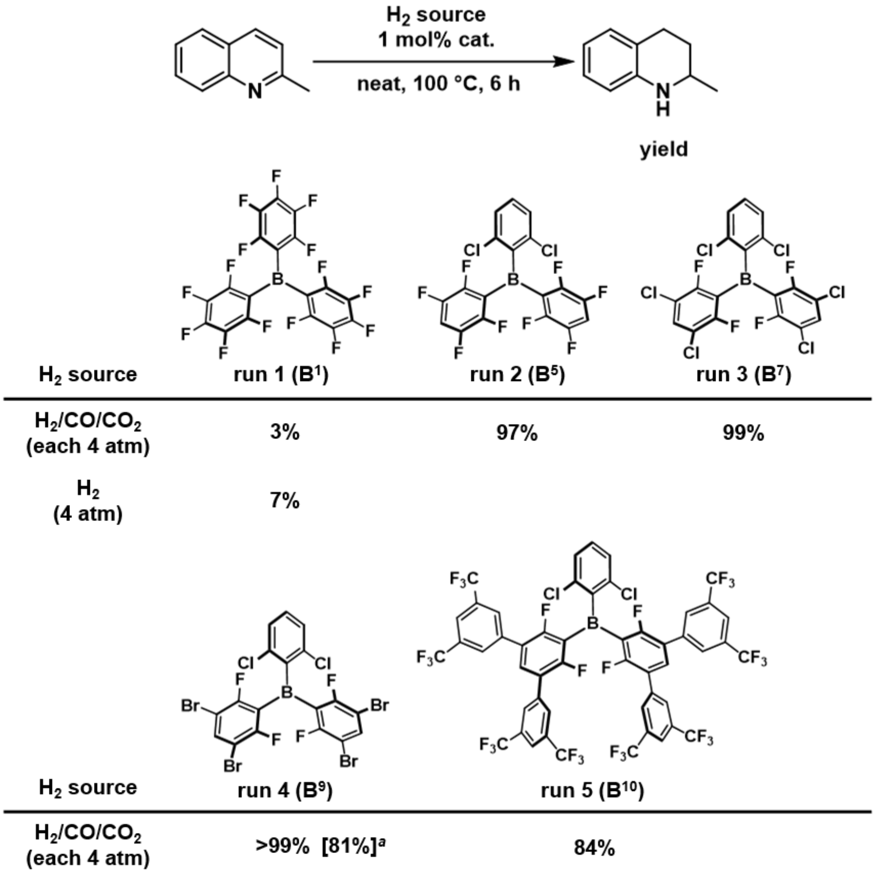

H_2 source	run 1 (B^1)	run 2 (B^5)	run 3 (B^7)
$H_2/CO/CO_2$ (each 4 atm)	3%	97%	99%
H_2 (4 atm)	7%		

H_2 source	run 4 (B^9)	run 5 (B^{10})
$H_2/CO/CO_2$ (each 4 atm)	>99% [81%][a]	84%

Figure 1.S17. Screening of catalysts. [a]3 h.

1.4.12.2. Catalyst turnover number exhibited by B^n ($n = 1, 5, 7, 9, 10$) under solvent-free and mixed gas conditions (Figure 1.S18)

General: A 30 mL autoclave was charged with **MeQin** (25.0 mmol), $\mathbf{B^n}$ (0.025 mmol), and tetradecane (an internal standard). Once sealed, the autoclave was pressurized with $H_2/CO/CO_2$ (30 atm each; Condition A) or H_2 (85 atm; Condition B) and heated at 100 °C for 48 h. After degassed at room temperature, the yield of **H_4-MeQin** was determined by GC analysis.

Run 1-A: Followed by the general procedures using $H_2/CO/CO_2$ (30 atm each), **MeQin** (3.578 g), $\mathbf{B^1}$ (12.9 mg), and tetradecane (240.0 mg) were employed, giving **H_4-MeQin** in <1% GC yield.

Run 2-A: Followed by the general procedures using $H_2/CO/CO_2$ (30 atm each), **MeQin** (3.580 g), $\mathbf{B^5}$ (11.3 mg), and tetradecane (233.5 mg) were employed, giving **H_4-MeQin** in 50% GC yield.

Run 3-A: Followed by the general procedures using $H_2/CO/CO_2$ (30 atm each), **MeQin** (3.575 g), $\mathbf{B^7}$ (13.1 mg), and tetradecane (242.2 mg) were employed, giving **H_4-MeQin** in 70% GC yield.

Run 4-A: Followed by the general procedures using $H_2/CO/CO_2$ (30 atm each), **MeQin** (3.593 g), $\mathbf{B^9}$ (17.5

mg), and tetradecane (239.5 mg) were employed, giving **H_4-MeQin** in 76% GC yield.

Run 4-B: Followed by the general procedures using H_2 (85 atm), **MeQin** (7.16 g, 50.0 mmol), **B^9** (17.6 mg), and tetradecane (240.0 mg) were employed, giving **H_4-MeQin** in 74% GC yield.

Run 5-A: Followed by the general procedures using $H_2/CO/CO_2$ (30 atm each), **MeQin** (3.582 g), **B^{10}** (30.8 mg), and tetradecane (244.2 mg) were employed, giving **H_4-MeQin** in 67% GC yield.

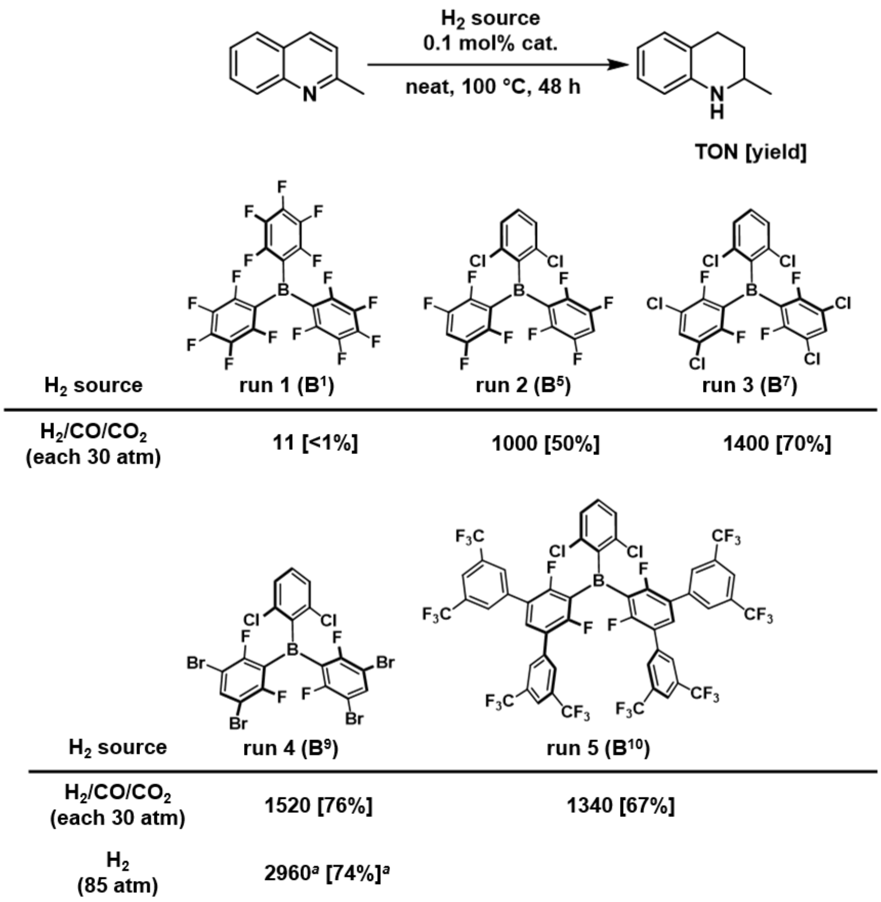

Figure 1.S18. Catalyst turnover number exhibited by **B^n** ($n = 1, 5, 7, 9, 10$) under the solvent-free and mixed gas conditions. [a]0.05 mol% **B^9** was used.

1.4.12.3. Exploration of the gas compositions included in H_2-source

General: A 30 mL autoclave was charged with **MeQin** (3.0 mmol), **B^9** (0.030 mmol), and tetradecane (an internal standard). Once sealed, the autoclave was pressurized with each H_2-source and heated at 100 °C. After degassed at room temperature, the yield of **H_4-MeQin** was determined by GC analysis. The results are shown in Figure 1.3A.

Use of $H_2/CO/CO_2$ (4 atm/20 atm/4 atm): Followed by the general procedures, **MeQin** (426.8 mg), **B^9** (21.0 mg), and tetradecane (238.1 mg) were employed and the autoclave was pressurized with CO (16 atm) and $H_2/CO/CO_2$ (4 atm each). After period of 6 h, **H_4-MeQin** was afforded in 81% GC yield. I also carried out this reaction with **MeQin** (424.6 mg), **B**^{9} (21.0 mg), and tetradecane (241.6 mg) for 12 h, giving **H$_4$-MeQin** in >99% GC yield

Use of H$_2$/CO/CO$_2$ (4 atm/4 atm/20 atm): Followed by the general procedures, **MeQin** (425.2 mg), **B**^{9} (20.8 mg), and tetradecane (238.9 mg) were employed and the autoclave was pressurized with CO$_2$ (16 atm) and H$_2$/CO/CO$_2$ (4 atm each). After period of 6 h, **H$_4$-MeQin** was afforded in 34% GC yield. I also carried out this reaction with **MeQin** (425.8 mg), **B**^{9} (21.0 mg), and tetradecane (244.1 mg) for 40 h, giving **H$_4$-MeQin** in 94% GC yield

Use of H$_2$/CO/CO$_2$/CH$_4$ (4 atm/4 atm/4 atm/4 atm): Followed by the general procedures, **MeQin** (429.4 mg), **B**^{9} (20.9 mg), and tetradecane (239.7 mg) were employed and the autoclave was pressurized with CH$_4$ (4 atm) and H$_2$/CO/CO$_2$ (4 atm each). After period of 6 h, **H$_4$-MeQin** was afforded in 97% GC yield.

1.4.13. Screening of catalysts in dehydrogenation of H$_4$-MeQin

General: A 10 mL two-necked flask was charged with **H$_4$-MeQin** (3.8 mmol), **B**^{n} (0.075 mmol), and tetradecane (an internal standard). The reaction mixture was heated at 200 °C for 6 h, and then allowed to cool to room temperature. The yield of **MeQin** was determined by GC analysis. The results are shown in Figure 1.3B.

Run 1: Followed by the general procedures, **H$_4$-MeQin** (552.5 mg), **B**^{1} (38.1 mg), and tetradecane (102.6 mg) were employed, giving **MeQin** in 18% GC yield.

Run 2: Followed by the general procedures, **H$_4$-MeQin** (534.8 mg), **B**^{5} (34.1 mg), and tetradecane (100.1 mg) were employed, giving **MeQin** in 84% GC yield.

Run 3: Followed by the general procedures, **H$_4$-MeQin** (539.3 mg), **B**^{7} (39.1 mg), and tetradecane (96.6 mg) were employed, giving **MeQin** in 85% GC yield.

Run 4: Followed by the general procedures, **H$_4$-MeQin** (535.4 mg), **B**^{9} (52.4 mg), and tetradecane (100.0 mg) were employed, giving **MeQin** in 88% GC yield.

Run 5: Followed by the general procedures, **H$_4$-MeQin** (538.1 mg), **B**^{10} (92.4 mg), and tetradecane (100.9 mg) were employed, giving **MeQin** in 68% GC yield.

1.4.14. H$_2$ recovery via B^9-catalyzed dehydrogenation of H$_4$-MeQin

The schematic representation of a reaction setup is shown in Figure 1.S19. A 10 mL two-neck flask was charged with **H$_4$-MeQin** (542 mg, 3.79 mmol), **B**^{9} (52.4 mg, 0.0750 mmol) and tetradecane (103.9 mg; an internal standard). The reaction mixture was stirred at 200 °C for 2 h, and then allowed to cool to room temperature. H_2 was collected in a graduated cylinder to calculate the yield of H_2 based on its collected volume (164 mL, 7.32 mmol). The yield of **MeQin** and the purity of the collected H_2 were determined by GC analysis.

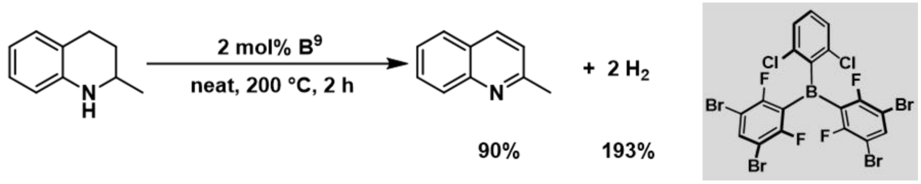

B^9

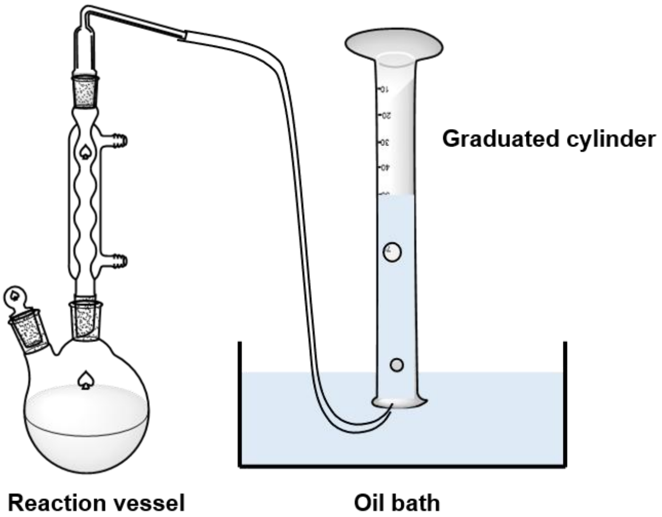

Figure 1.S19. The reaction setup for H_2 collection.

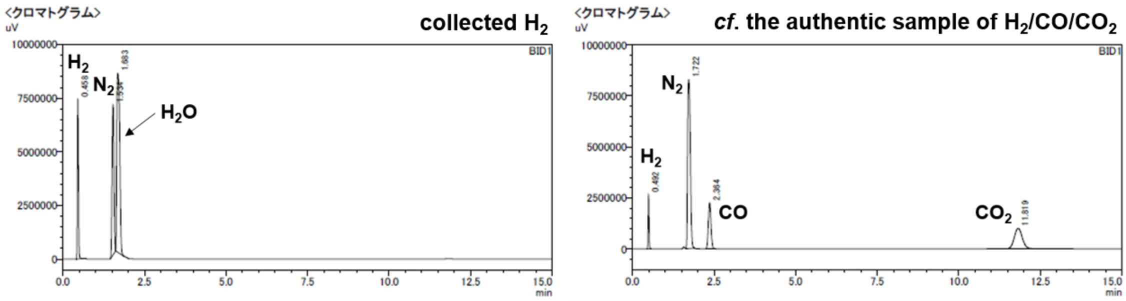

Figure 1.S20. GC chromatograms for the collected H_2 gas (shown in left) and an authentic sample of $H_2/CO/CO_2$ (1:1:1 molar ratio; shown in right) used in this work.

1.4.15. B^9-catalyzed hydrogenation/dehydrogenation sequences from $H_2/CO/CO_2$

A 30 mL autoclave was charged with **MeQin** (145 mg, 1.01 mmol), **B**^{9} (13.9 mg, 0.199 mmol), and tetradecane (59.5 mg; an internal standard). Once sealed, the autoclave was pressurized with $H_2/CO/CO_2$ (4 atm each; 5.4 mmol each based on $n = PV/RT$, where $T = 273.15$ K, $P = 4$ atm, $V = 30$ mL) and heated to 100 °C for 2 h. After cooling to room temperature, all volatiles were removed *in vacuo*, and GC analysis showed the production of **H$_4$-MeQin** in 95%. Then, the reaction mixture was transferred into a 10 mL two-neck flask (Figure 1.S19). During this manipulation, the residue inside the autoclave reactor was extracted with toluene in order to minimize the loss of reagents. The toluene was then removed *in vacuo*; however, this is not essential for the following dehydrogenation. The reaction mixture was then stirred at 200 °C for 3 h. The volume of collected gas was measured using a graduated cylinder to calculate the yield of H_2 (39.0 mL, 1.74 mmol). The conversion of **H_4-MeQin** (94%), the yield of **MeQin** (91%), and the purity of the collected H_2 gas were determined using GC analysis. As shown in Figure 1.S21, CO was not detected (or its concentration is less than a detection limit of the GC), while 0.1% molar of CO_2 with respect to that of H_2 was detected after the background calibration (vide infra). However, I cannot rule out a possibility that a trace amount of CO_2 (0.1%) was contaminated during the collection of H_2 (i.e. from silicon oil) and/or the injection of the recovered H_2 into the GC (i.e. from air).

H_2 purity = (molar amount of H_2)/(sum of the molar amounts of H_2, CO, and CO_2)×100
= (1.74)/(1.74 + 0 + 0.00178) ×100
= 99.9%

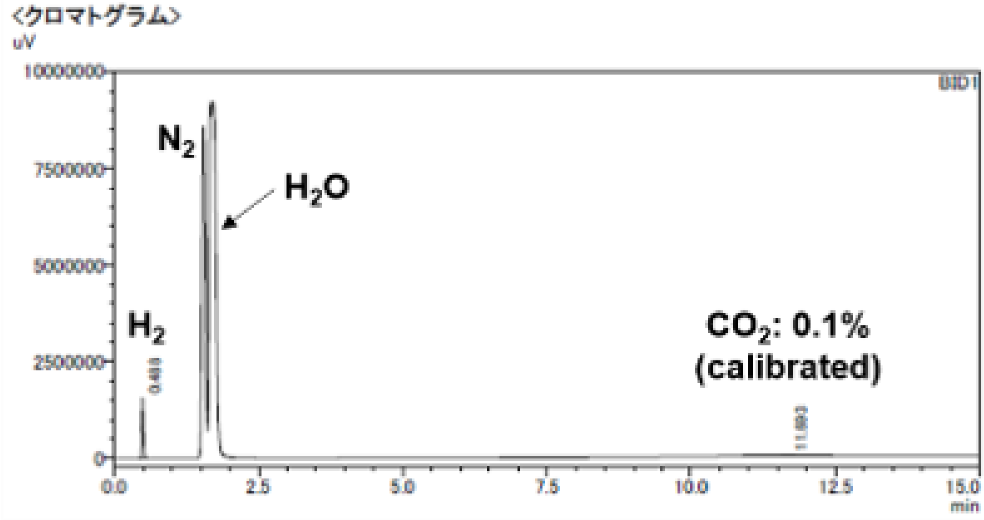

Figure 1.S21. The GC chromatogram for the collected H_2.

I experimentally confirmed that a certain amount of CO_2 and H_2O were inevitably contaminated from air and/or silicon oil that was used for H_2 collection. In order to accurately evaluate the H_2 purity, I performed a background calibration of CO_2 through several control experiments using N_2 gas. In fact, as shown in Table 1.S3, the contamination of CO_2 was always confirmed when N_2 gas, collected through the same experimental procedures as mentioned above (Figure 1.S19), was analyzed by GC. Based on these experiments, an average amount of CO_2 contaminated from air and/or silicon oil was estimated as shown in Table 1.S3, which was used for the correction of H_2 purity.

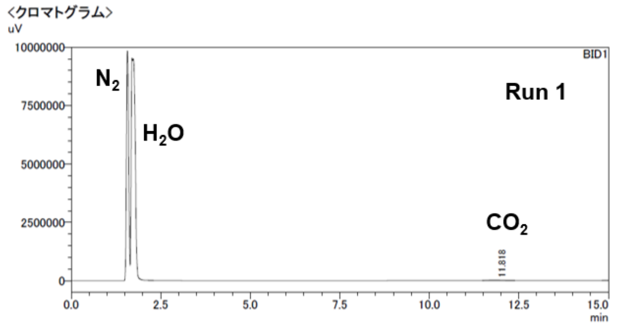

Run	Area values of CO_2
1	272898
2	273634
3	278042
average	274858
standard error	1600

Table 1.S3. Background correction of CO_2 contaminated from air/silicon oil.

1.4.16. Optimization of reaction conditions for hydrogenation of Lut

General: The gases used in this reaction was dehydrated over molecular sieves (4 Å) prior to use for at least 12 h. A 30 mL autoclave was charged with **Lut** (1.0 mmol), **B*ⁿ*** (0.10 mmol), and tetradecane (an internal standard). Once sealed, the autoclave was pressurized with H_2-source and heated at 150 °C for 6 h. After degassed at room temperature, the yield of **H_6-Lut** was determined by GC analysis. The results of runs 1–4 are shown in Figure 1.3D and those of run 5–6 are shown in Figure 1.S22.

Run 1: Followed by the general procedures using dehydrated H_2 (20 atm), **Lut** (108.9 mg), **B^7** (52.0 mg), and tetradecane (79.4 mg) were employed and the autoclave was pressurized with dehydrated H_2 (20 atm), giving **H_6-Lut** in 81% GC yield. I also carried out this reaction with **Lut** (102.7 mg), **B^9** (69.6 mg), and tetradecane (79.9 mg), giving **H_6-Lut** in 41% GC yield

Run 2: Followed by the general procedures using dehydrated H_2/CO (20 atm/4 atm), **Lut** (108.8 mg), **B^7** (51.9 mg), and tetradecane (81.9 mg) were employed and the autoclave was pressurized with dehydrated H_2/CO (4 atm each) and H_2 (16 atm), giving **H_6-Lut** in 54% GC yield.

Run 3: Followed by the general procedures using dehydrated H_2/CO (40 atm/4 atm), **Lut** (112.1 mg), **B^7** (52.1 mg), and tetradecane (81.8 mg) were employed and the autoclave was pressurized with dehydrated H_2/CO (4 atm each) and H_2 (36 atm), giving **H_6-Lut** in 70% GC yield.

Run 4: Followed by the general procedures using dehydrated H_2/CO_2 (40 atm/4 atm), **Lut** (110.3 mg), **B^7** (52.0 mg), and tetradecane (83.2 mg) were employed and the autoclave was pressurized with dehydrated H_2/CO_2 (4 atm each) and H_2 (36 atm), giving **H_6-Lut** in 53% GC yield.

Run 5: Followed by the general procedures using H_2 (20 atm), **Lut** (114.1 mg), **B^7** (52.1 mg), and tetradecane (87.4 mg) were employed and the autoclave was pressurized with H_2 (20 atm; not treated with molecular sieves (4 Å)), giving **H_6-Lut** in 72% GC yield.

Run 6: Followed by the general procedures using dehydrated H_2/CO (4 atm each), **Lut** (109.0 mg), **B^7** (52.1

mg), and tetradecane (81.9 mg) were employed and the autoclave was pressurized with dehydrated H_2/CO (4 atm each), giving **H_6-Lut** in 38% GC yield.

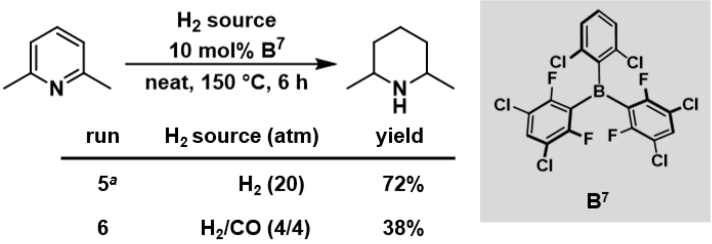

run	H_2 source (atm)	yield
5[a]	H_2 (20)	72%
6	H_2/CO (4/4)	38%

Figure 1.S22. Hydrogenation of Lut. [a]H_2 without dehydration.

1.4.17. Mechanistic studies

1.4.17.1. Determination of the reaction rate constants in the hydrogenation of MeQin

General using H_2/CO/CO_2 (Condition A): A mixture of **MeQin** (1.5 M), **B''** ([**B''** = 0.015 M]), and tetradecane (an internal standard) in toluene was prepared and equally divided into 10 autoclave reactors (V = 10 mL). Once sealed, each reactor was pressurized with H_2/CO/CO_2 (10 atm each) and heated at 100 °C. The conversion of **MeQin** and the yield of **H_4-MeQin** were monitored by GC analysis. In several cases, these experiments were repeated twice to confirm the reproducibility.

General using H_2 (Condition B): A mixture of **MeQin** (1.5 M), **B''** ([**B''** = 0.015 M]), and tetradecane (an internal standard) in toluene was prepared and equally divided into 10 autoclave reactors (V = 10 mL). Once sealed, each reactor was pressurized with H_2 (10 atm) and heated at 100 °C. The conversion of **MeQin** and the yield of **H_4-MeQin** were monitored by GC analysis. In several cases, these experiments were repeated twice to confirm the reproducibility.

Run 1-A using B^9: Followed by the general procedures using H_2/CO/CO_2 (10 atm each), I independently conducted two experiments to confirm the reproducibility. In the first experiment, **MeQin** (1.07 g, 7.47 mmol), **B^9** (52.4 mg, 0.0750 mmol), tetradecane (597 mg), and toluene (5.0 mL) were employed, which demonstrated that the rate constant for the formation of **H_4-MeQin** is 1.93(10) × 10^{-4} (mol m^{-3} s^{-1}) as shown in Figure 1.S23. In the second, **MeQin** (1.29 g, 9.01 mmol), **B^9** (63.1 mg, 0.0903 mmol), tetradecane (718 mg), and toluene (6.0 mL) were employed, which demonstrated that the and rate constant for the formation of **H_4-MeQin** is 1.69(3) × 10^{-4} (mol m^{-3} s^{-1}).

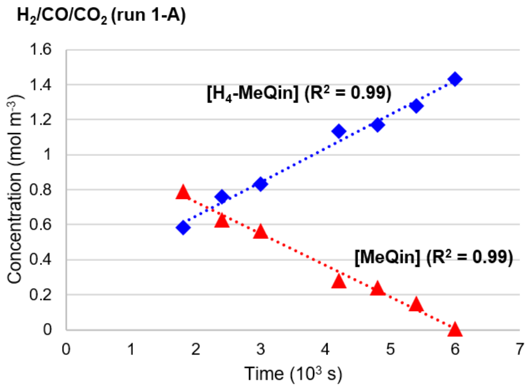

$$-\frac{d[\boldsymbol{MeQin}]}{dt} = k_{\boldsymbol{MeQin}} = 1.80(9) \times 10^{-4}\ [mol\ m^{-3}\ s^{-1}]$$

$$\frac{d[\boldsymbol{H_4 - MeQin}]}{dt} = k_{\boldsymbol{H4-MeQin}} = 1.93(10) \times 10^{-4}\ [mol\ m^{-3}\ s^{-1}]$$

Each gas was pressurized at 10 atm.

Figure 1.S23. Time-concentration profiles for run 1-A.

Run 1-B using $\mathbf{B^9}$: Followed by the general procedures using H_2 (10 atm), I independently conducted two experiments to confirm the reproducibility. In the first experiment, **MeQin** (1.29 g, 9.01 mmol), $\mathbf{B^9}$ (62.8 mg, 0.0899 mmol), tetradecane (694 mg), and toluene (6.0 mL) were employed, which demonstrated that the rate constant for the formation of **$\mathbf{H_4}$-MeQin** is 2.21(13) × 10^{-4} (mol m^{-3} s^{-1}) as shown in Figure 1.S24. In the second, **MeQin** (1.29 g, 9.01 mmol), $\mathbf{B^9}$ (62.9 mg, 0.0900 mmol), tetradecane (716 mg), and toluene (6.0 mL) were employed, which demonstrated that the rate constant for the formation of **$\mathbf{H_4}$-MeQin** is 1.82(8) × 10^{-4} (mol m^{-3} s^{-1}).

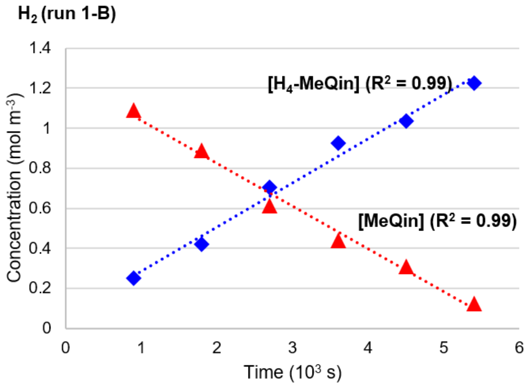

$$-\frac{d[\boldsymbol{MeQin}]}{dt} = k_{\boldsymbol{MeQin}} = 2.14(12) \times 10^{-4}\ [mol\ m^{-3}\ s^{-1}]$$

$$\frac{d[\boldsymbol{H_4 - MeQin}]}{dt} = k_{\boldsymbol{H4-MeQin}} = 2.21(13) \times 10^{-4}\ [mol\ m^{-3}\ s^{-1}]$$

$\mathbf{H_2}$ was pressurized at 10 atm.

Figure 1.S24. Time-concentration profiles for run 1-B.

Run 2-A using $\mathbf{B^1}$: Followed by the general procedures using $H_2/CO/CO_2$ (10 atm each), **MeQin** (1.07 g, 7.47 mmol), $\mathbf{B^1}$ (38.4 mg, 0.0750 mmol), tetradecane (605 mg), and toluene (5.0 mL) were employed, which demonstrated that the rate constant for the formation of **$\mathbf{H_4}$-MeQin** is 3.56(60) × 10^{-6} (mol m^{-3} s^{-1}) as shown in Figure 1.S25.

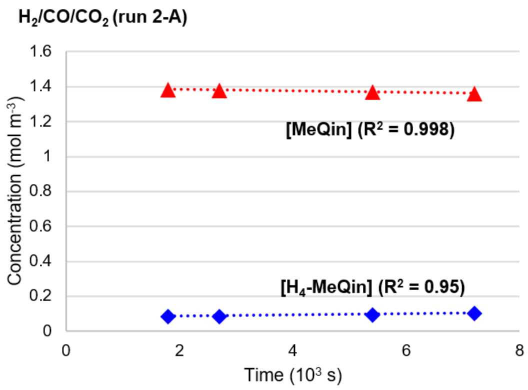

$$-\frac{d[\boldsymbol{MeQin}]}{dt} = k_{\boldsymbol{MeQin}} = 4.51(15) \times 10^{-6}\ [mol\ m^{-3}\ s^{-1}]$$

$$\frac{d[\boldsymbol{H_4-MeQin}]}{dt} = k_{H4-\boldsymbol{MeQin}} = 3.56(60) \times 10^{-6}\ [mol\ m^{-3}\ s^{-1}]$$

Each gas was pressurized at 10 atm.

Figure 1.S25. Time-concentration profiles for run 2-B.

Run 2-B using B^1: Followed by the general procedures using H_2 (10 atm), **MeQin** (1.07 g, 7.47 mmol), **B**^{1} (38.4 mg, 0.0750 mmol), tetradecane (608 mg), and toluene (5.0 mL) were employed, which demonstrated that the rate constant for the formation of **H$_4$-MeQin** is 3.08(29) × 10^{-4} (mol m^{-3} s^{-1}) as shown in Figure 1.S26.

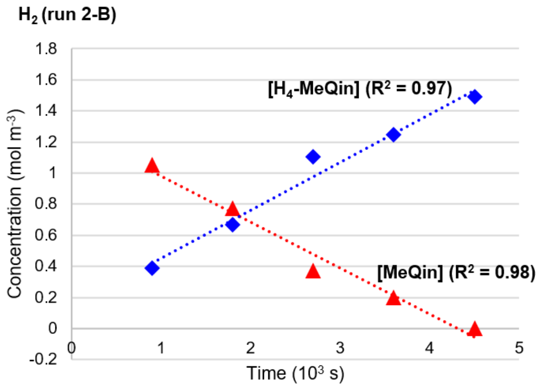

$$-\frac{d[\boldsymbol{MeQin}]}{dt} = k_{\boldsymbol{MeQin}} = 2.97(26) \times 10^{-4}\ [mol\ m^{-3}\ s^{-1}]$$

$$\frac{d[\boldsymbol{H_4-MeQin}]}{dt} = k_{H4-\boldsymbol{MeQin}} = 3.08(29) \times 10^{-4}\ [mol\ m^{-3}\ s^{-1}]$$

H_2 was pressurized at 10 atm.

Figure 1.S26. Time-concentration profiles for run 2-B.

Run 3-A using B^7: Followed by the general procedures using H_2/CO/CO_2 (10 atm each), **MeQin** (1.07 g, 7.47 mmol), **B**^{7} (39.1 mg, 0.0751 mmol), tetradecane (606 mg), and toluene (5.0 mL) were employed, which demonstrated that the rate constant for the formation of **H$_4$-MeQin** is 1.66(5) × 10^{-4} (mol m^{-3} s^{-1}) as shown in Figure 1.S27.

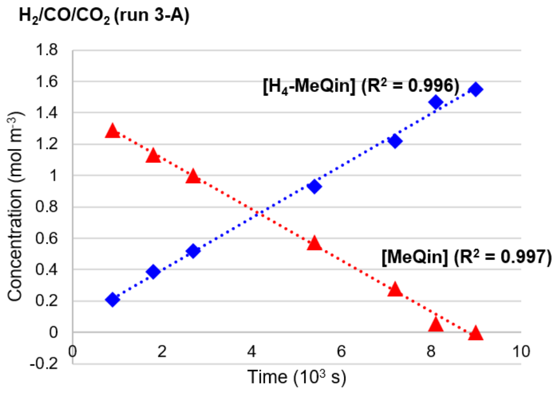

$$-\frac{d[\boldsymbol{MeQin}]}{dt} = k_{\boldsymbol{MeQin}} = 1.63(4) \times 10^{-4}\ [mol\ m^{-3}\ s^{-1}]$$

$$\frac{d[\boldsymbol{H_4 - MeQin}]}{dt} = k_{\boldsymbol{H4-MeQin}} = 1.66(5) \times 10^{-4}\ [mol\ m^{-3}\ s^{-1}]$$

Each gas was pressurized at 10 atm.

Figure 1.S27. Time-concentration profiles for run 3-A.

Run 3-B using B^7: Followed by the general procedures using H_2 (10 atm), **MeQin** (1.07 g, 7.47 mmol), **B**^{7} (39.1 mg, 0.0751 mmol), tetradecane (604 mg), and toluene (5.0 mL) were employed, which demonstrated that the rate constant for the formation of **H_4-MeQin** is 1.71(6) × 10^{-4} (mol m^{-3} s^{-1}) as shown in Figure 1.S28.

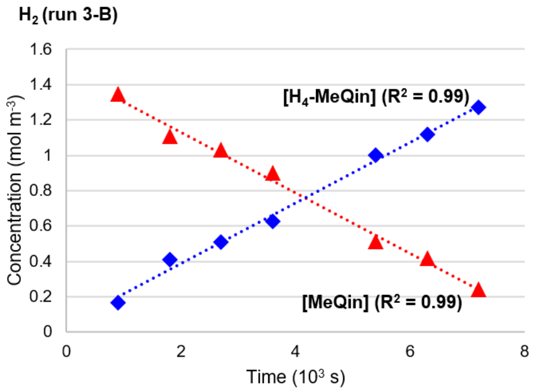

$$-\frac{d[\boldsymbol{MeQin}]}{dt} = k_{\boldsymbol{MeQin}} = 1.71(7) \times 10^{-4}\ [mol\ m^{-3}\ s^{-1}]$$

$$\frac{d[\boldsymbol{H_4 - MeQin}]}{dt} = k_{\boldsymbol{H4-MeQin}} = 1.71(6) \times 10^{-4}\ [mol\ m^{-3}\ s^{-1}]$$

H_2 was pressurized at 10 atm.

Figure 1.S28. Time-concentration profiles for run 3-B.

1.4.17.2. Influences of gas composition in B^1-catalyzed hydrogenation of MeQin

A mixture of **MeQin** (429.6 mg, 3.0 mmol, 1.5 M), **B**^{1} (15.4 mg, 0.030 mmol, [**B**^{1} = 0.015 M]), and tetradecane (an internal standard) in toluene was prepared and equally divided into 4 autoclave reactors (*V* = 10 mL). Once sealed, each reactor was pressurized with H_2 (10 atm), H_2/CO (10 atm each), H_2/CO_2 (10 atm each), and $H_2/CO/CO_2$ (10 atm each) and heated at 100 °C for 2 h. After degassed at room temperature, the yield of **H_4-MeQin** was determined by GC analysis. I repeated these experiments at least twice for each gas composition in order to confirm their reproducibility.

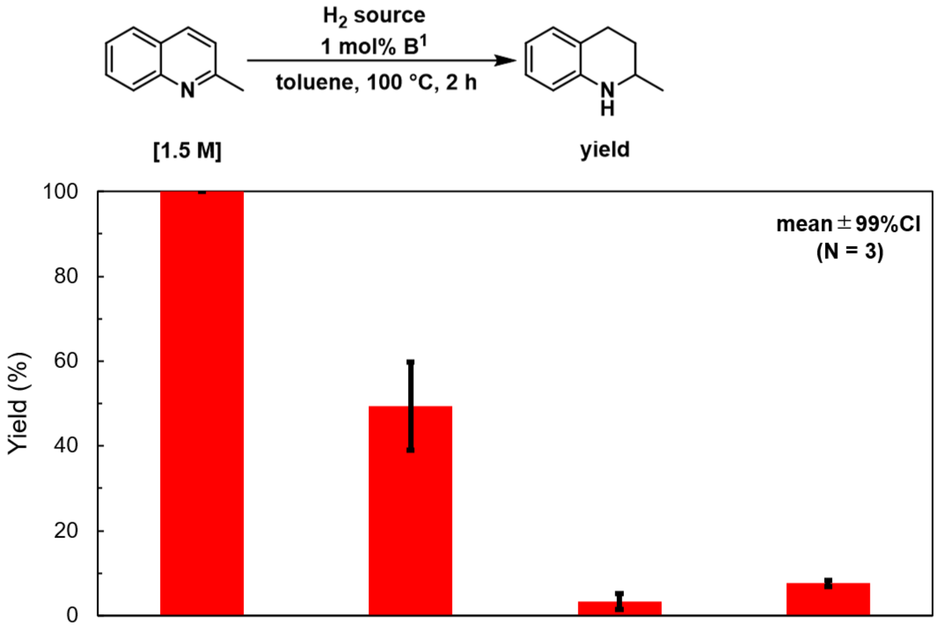

Gas (atm)	H_2 (10)	H_2/CO (10/10)	H_2/CO_2 (10/10)	H_2/CO/CO_2 (10/10/10)
run 1	100	48	4	8
run2	100	52	3	7
run 3	-	48	3	8
average	100	49	3	8
standard error	0	1	0.2	0.09
standard deviation	0	1.8	0.3	0.1
99% confidencial interval	-	10	2	1

Figure 1.S29. Influences of gas composition in **B**^{1}-catalyzed hydrogenation of **MeQin**.

1.4.17.3. Determination of kinetic order in B^9

General: A mixture of **MeQin** (1.5 M), **B**^{9} ([**B**^{9} = 0.0075 M, 0.010 M, 0.0015 M, 0.0225 M, 0.030 M]), and tetradecane (an internal standard) in toluene was prepared and equally divided into 10 autoclave reactors (V = 10 mL). Once sealed, each reactor was pressurized with H_2/CO/CO_2 (10 atm each) and heated at 100 °C. The conversion of **MeQin** and the yield of **H_4-MeQin** were monitored by GC analysis. These experiments were repeated twice to confirm the reproducibility.

Run 1: Followed by the general procedures, I independently conducted two experiments to confirm the reproducibility. In the first experiment, **MeQin** (2.15 g, 15.0 mmol), **B**^{9} (52.4 mg, 0.0750 mmol), tetradecane (1.20 g), and toluene (10 mL) were employed, which demonstrated that the rate constant for the formation of **H_4-MeQin** is 1.29(5) × 10^{-4} (mol m^{-3} s^{-1}) as shown in Figure 1.S30. In the second, **MeQin** (2.16 g, 15.1 mmol), **B**^{9} (52.4 mg, 0.0750 mmol), tetradecane (1.20 g), and toluene (10 mL) were employed, which demonstrated that the and rate constant for the formation of **H_4-MeQin** is 1.19(5) × 10^{-4} (mol m^{-3} s^{-1}).

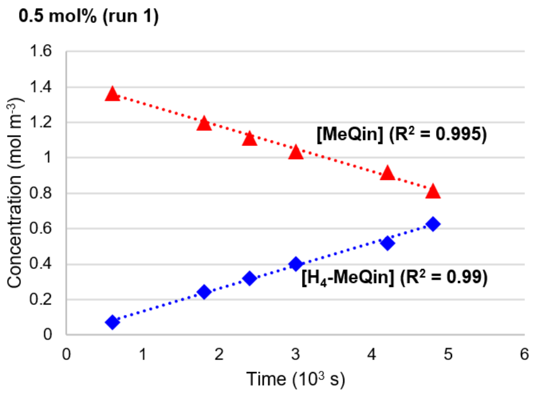

$$-\frac{d[\boldsymbol{MeQin}]}{dt} = k_{\boldsymbol{MeQin}} = 1.27(4) \times 10^{-4}\ [mol\ m^{-3}\ s^{-1}]$$

$$\frac{d[\boldsymbol{H_4 - MeQin}]}{dt} = k_{H4-\boldsymbol{MeQin}} = 1.29(5) \times 10^{-4}\ [mol\ m^{-3}\ s^{-1}]$$

Figure 1.S30. Time-concentration profiles for run 1.

Run 2: Followed by the general procedures, I independently conducted two experiments to confirm the reproducibility. In the first experiment, **MeQin** (1.43 g, 9.99 mmol), **B**^{9} (52.4 mg, 0.0750 mmol), tetradecane (806 mg), and toluene (6.7 mL) were employed and, which demonstrated that the rate constant for the formation of **H$_4$-MeQin** is 2.13(8) × 10^{-4} (mol m^{-3} s^{-1}) as shown in Figure 1.S31. In the second, **MeQin** (1.43 g, 9.99 mmol), **B**^{9} (52.3 mg, 0.0749 mmol), tetradecane (798 mg), and toluene (6.7 mL) were employed and, which demonstrated that the rate constant for the formation of **H$_4$-MeQin** is 2.09(11) × 10^{-4} (mol m^{-3} s^{-1}).

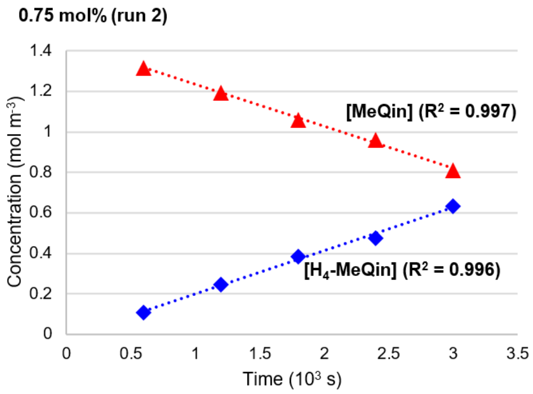

$$-\frac{d[\boldsymbol{MeQin}]}{dt} = k_{\boldsymbol{MeQin}} = 2.08(7) \times 10^{-4}\ [mol\ m^{-3}\ s^{-1}]$$

$$\frac{d[\boldsymbol{H_4 - MeQin}]}{dt} = k_{H4-\boldsymbol{MeQin}} = 2.13(8) \times 10^{-4}\ [mol\ m^{-3}\ s^{-1}]$$

Figure 1.S31. Time-concentration profiles for run 2.

Run 3: Followed by the general procedures, I independently conducted two experiments to confirm the reproducibility. In the first experiment, **MeQin** (862 mg, 6.02 mmol), **B**^{9} (63.0 mg, 0.0902 mmol), tetradecane (481 mg), and toluene (4.0 mL) were employed and, which demonstrated that the rate constant for the formation of **H$_4$-MeQin** is 5.76(51) × 10^{-4} (mol m^{-3} s^{-1}) as shown in Figure 1.S32. In the second, **MeQin** (859 mg, 6.00 mmol), **B**^{9} (62.9 mg, 0.0900 mmol), tetradecane (485 mg), and toluene (4.0 mL) were employed and, which demonstrated that the rate constant for the formation of **H$_4$-MeQin** is 4.93(47) × 10^{-4} (mol m^{-3} s^{-1}).

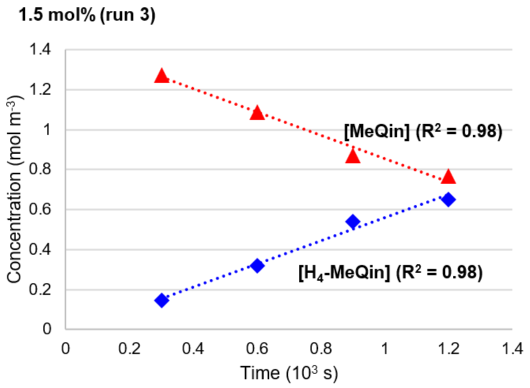

$$-\frac{d[\boldsymbol{MeQin}]}{dt} = k_{\boldsymbol{MeQin}} = 5.80(56) \times 10^{-4}\ [mol\ m^{-3}\ s^{-1}]$$

$$\frac{d[\boldsymbol{H_4-MeQin}]}{dt} = k_{\boldsymbol{H4-MeQin}} = 5.76(51) \times 10^{-4}\ [mol\ m^{-3}\ s^{-1}]$$

Figure 1.S32. Time-concentration profiles for run 3.

Run 4: Followed by the general procedures, I independently conducted two experiments to confirm the reproducibility. In the first experiment, **MeQin** (644 mg, 4.50 mmol), $\mathbf{B^9}$ (62.8 mg, 0.0899 mmol), tetradecane (370 mg), and toluene (3.0 mL) were employed and, which demonstrated that the rate constant for the formation of $\mathbf{H_4}$**-MeQin** is 8.57(66) × 10^{-4} (mol m^{-3} s^{-1}) as shown in Figure 1.S33. In the second, **MeQin** (647 mg, 4.52 mmol), $\mathbf{B^9}$ (62.8 mg, 0.0899 mmol), tetradecane (360 mg), and toluene (3.0 mL) were employed and, which demonstrated that the rate constant for the formation of $\mathbf{H_4}$**-MeQin** is 9.36(117) × 10^{-4} (mol m^{-3} s^{-1}).

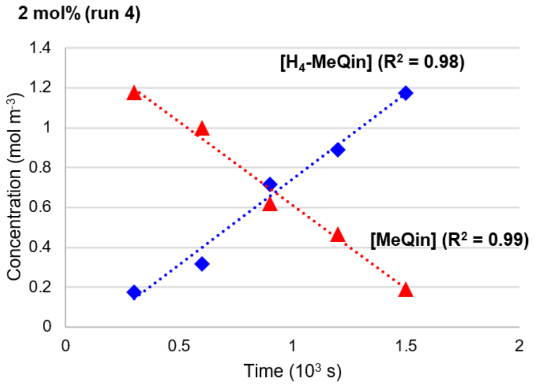

$$-\frac{d[\boldsymbol{MeQin}]}{dt} = k_{\boldsymbol{MeQin}} = 8.35(58) \times 10^{-4}\ [mol\ m^{-3}\ s^{-1}]$$

$$\frac{d[\boldsymbol{H_4-MeQin}]}{dt} = k_{\boldsymbol{H4-MeQin}} = 8.57(66) \times 10^{-4}\ [mol\ m^{-3}\ s^{-1}]$$

Figure 1.S33. Time-concentration profiles for run 4.

Order in $\mathbf{B^9}$: From these results, a plot of k_{int} vs. [$\mathbf{B^9}$] and the corresponding log-log profile are given (Figure 1.S34), suggesting the first order dependence on $\mathbf{B^9}$.

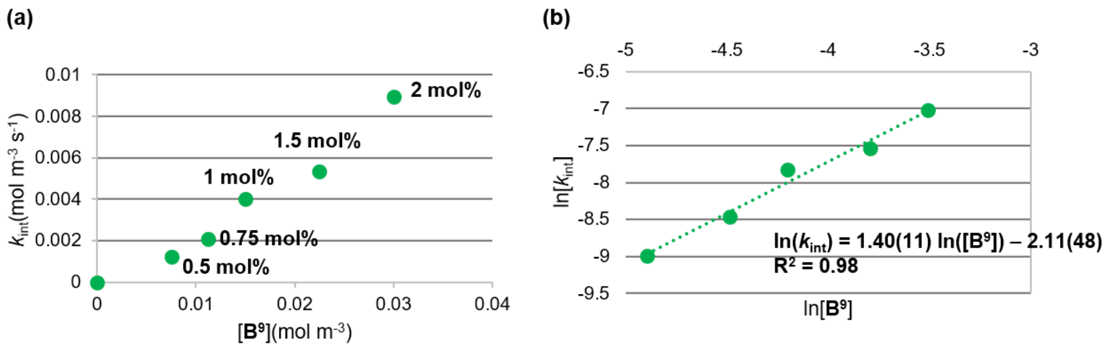

Figure 1.S34. Order in $\mathbf{B}^9$. (a) Kinetic order in [$\mathbf{B}^9$]. (b) A profile of lnk_{int} with respect to ln[$\mathbf{B}^9$].

1.4.17.4. Determination of kinetic order in $\mathbf{B}^7$

General: A mixture of **MeQin** (1.5 M), $\mathbf{B}^7$ ([$\mathbf{B}^7$ = 0.030 M, 0.045 M]), and tetradecane (an internal standard) in toluene was prepared and equally divided into 8 (run 1) or 4 (run 2) autoclave reactors (V = 10 mL). Once sealed, each reactor was pressurized with $H_2/CO/CO_2$ (10 atm each) heated at 100 °C. The conversion of **MeQin** and the yield of **H_4-MeQin** were monitored by GC analysis, resulting into the determination of the initial rate constant k_{obs}.

Run 1: Followed by the general procedures, **MeQin** (860 mg, 6.01 mmol), $\mathbf{B}^7$ (62.5 mg, 0.120 mmol), tetradecane (494 mg), and toluene (4 mL) were employed, which demonstrated that the rate constant for the formation of **H_4-MeQin** generation is 4.23(50) × 10^{-4} (mol m^{-3} s^{-1}) as shown in Figure 1.S35.

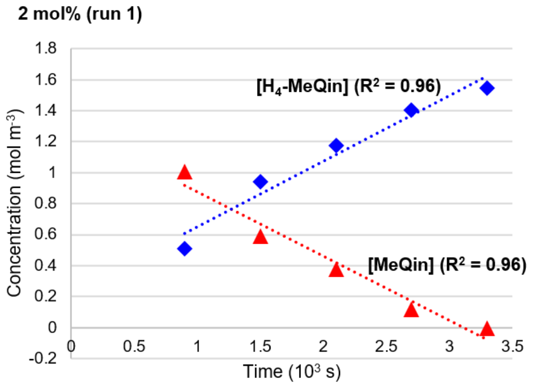

$$-\frac{d[\boldsymbol{MeQin}]}{dt} = k_{\boldsymbol{MeQin}} = 4.14(47) \times 10^{-4}\ [mol\ m^{-3}\ s^{-1}]$$

$$\frac{d[\boldsymbol{H_4 - MeQin}]}{dt} = k_{\boldsymbol{H4-MeQin}} = 4.23(50) \times 10^{-4}\ [mol\ m^{-3}\ s^{-1}]$$

Figure 1.S35. Time-concentration profiles for run 1.

Run 2: Followed by the general procedures, **MeQin** (430 mg, 3.00 mmol), $\mathbf{B}^7$ (46.9 mg, 0.0901 mmol), tetradecane (248.7 mg), and toluene (2 mL) were employed, which demonstrated that the rate constant for the formation of **H_4-MeQin** generation is 6.19(32) × 10^{-4} (mol m^{-3} s^{-1}) as shown in Figure 1.S36.

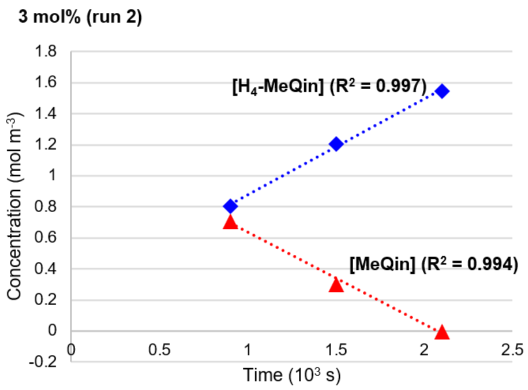

$$-\frac{d[\boldsymbol{MeQin}]}{dt} = k_{\boldsymbol{MeQin}} = 5.93(47)\times10^{-4}\ [mol\ m^{-3}\ s^{-1}]$$

$$\frac{d[\boldsymbol{H_4-MeQin}]}{dt} = k_{H4-MeQin} = 6.19(32)\times10^{-4}\ [mol\ m^{-3}\ s^{-1}]$$

Figure 1.S36. Time-concentration profiles for run 2.

Order in B^7: From these results, a plot of k_{obs} vs. [**B**^{7}] and the corresponding log-log profile are given (Figure 1.S37), suggesting the first order dependence on **B**^{7}.

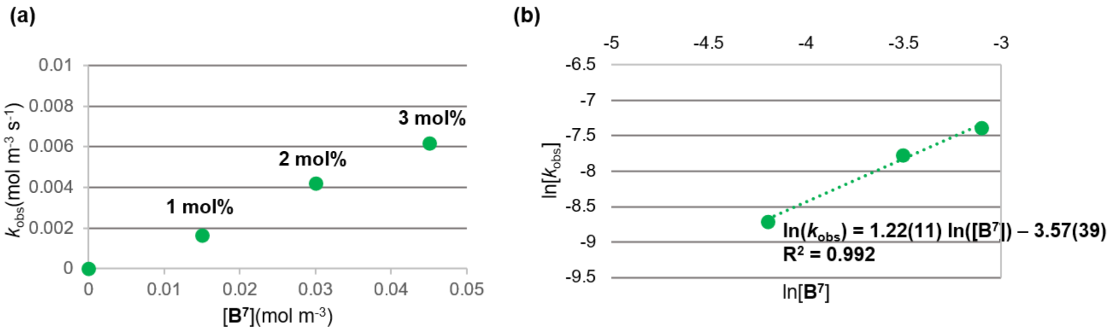

Figure 1.S37. Order in **B**^{7}. (a) Kinetic order in [**B**^{7}]. (b) A profile of lnk_{obs} with respect to ln[**B**^{7}].

1.4.17.5. Reaction of MeQin with B^1 in the presence of H_2/CO_2

A pressure-tight NMR tube (Wilmad-LabGrass 542-PV-7; V = 1.8 mL) was charged with **MeQin** (15.0 mg, 0.105 mmol), **B^1** (25.6 mg, 0.0500 mmol) and α,α,α-trifluorotoluene (23.9 mg, 0.164 mmol; an internal standard). Once sealed, the NMR tube was pressurized with H_2/CO_2 (2.5 atm each), followed by heating at 100 °C for 3 h. Then, the ^{1}H, ^{11}B, and ^{19}F NMR analyses were conducted. X-ray data for **H$_4$-MeQin–B^1** (Fig S38d): M = 659.20, colorless, monoclinic, $P2_1/n$ (#14), a = 8.5215(2) Å, b = 14.9248(3) Å, c = 20.1080(3) Å, α = 90°, β = 100.571(2)°, γ = 90°, V = 2513.97(9) Å^3, Z = 4, $Dcalcd$ = 1.742 g/cm^3, T = −150 °C, R_1 (wR_2) = 0.0280 (0.0765).

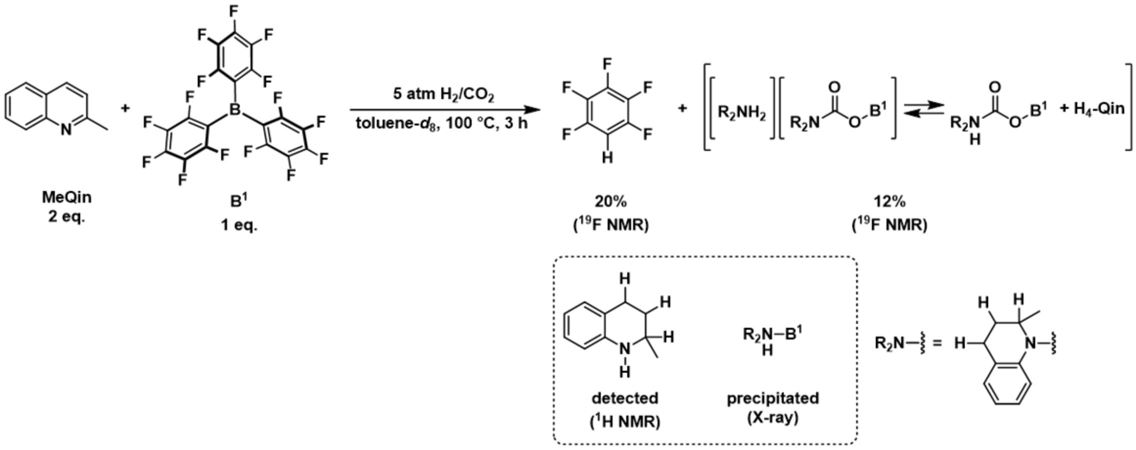
MeQin
2 eq.
B^1
1 eq.
5 atm H$_2$/CO$_2$
toluene-d_8, 100 °C, 3 h
20%
(^{19}F NMR)
12%
(^{19}F NMR)
+ H$_4$-Qin
detected
(^{1}H NMR)
precipitated
(X-ray)

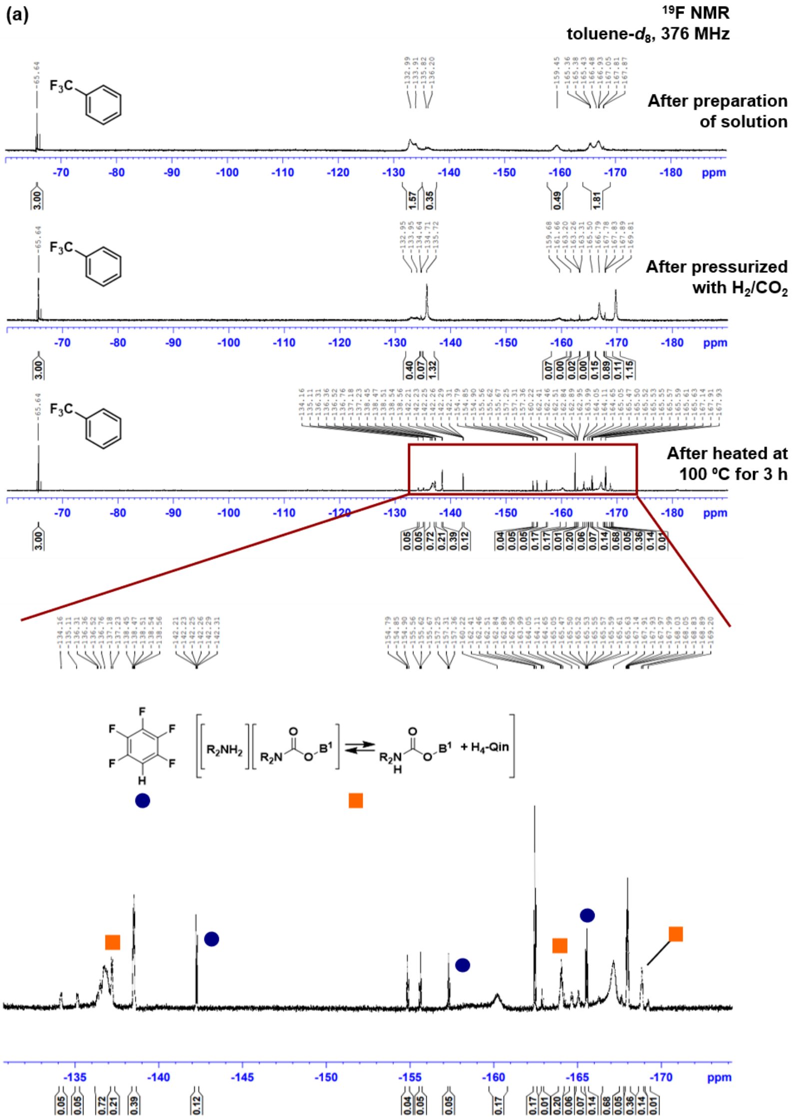
(a)
^{19}F NMR
toluene-d_8, 376 MHz
After preparation of solution
After pressurized with H$_2$/CO$_2$
After heated at 100 °C for 3 h
ppm

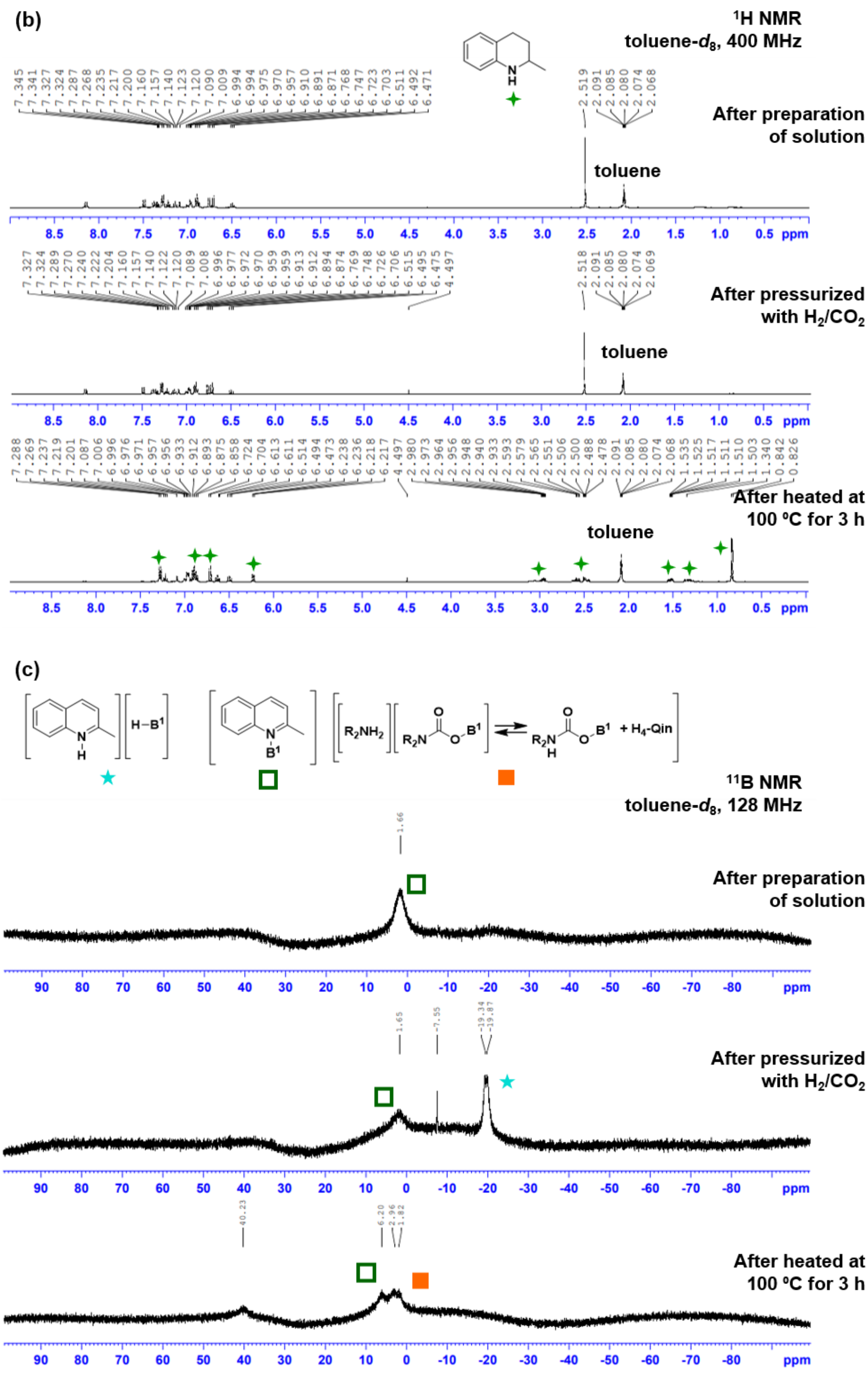
(b)
^{1}H NMR
toluene-d_8, 400 MHz
N
H
After preparation of solution
7.345 7.341 7.327 7.324 7.287 7.268 7.235 7.217 7.200 7.160 7.157 7.140 7.123 7.120 7.090 7.009 6.994 6.994 6.975 6.970 6.957 6.910 6.891 6.871 6.768 6.747 6.723 6.703 6.511 6.492 6.471
2.519 2.091 2.085 2.080 2.074 2.068
toluene
8.5 8.0 7.5 7.0 6.5 6.0 5.5 5.0 4.5 4.0 3.5 3.0 2.5 2.0 1.5 1.0 0.5 ppm
After pressurized with H_2/CO_2
7.327 7.324 7.289 7.270 7.240 7.222 7.204 7.160 7.157 7.140 7.122 7.120 7.089 7.008 6.996 6.977 6.972 6.970 6.959 6.959 6.913 6.912 6.894 6.874 6.769 6.748 6.726 6.706 6.515 6.495 6.475 4.497
2.518 2.091 2.085 2.080 2.074 2.069
toluene
8.5 8.0 7.5 7.0 6.5 6.0 5.5 5.0 4.5 4.0 3.5 3.0 2.5 2.0 1.5 1.0 0.5 ppm
After heated at 100 ºC for 3 h
7.288 7.269 7.237 7.219 7.201 7.087 7.006 6.996 6.976 6.971 6.957 6.956 6.933 6.912 6.893 6.875 6.858 6.724 6.704 6.613 6.611 6.514 6.494 6.473 6.238 6.236 6.218 6.217 4.497 2.980 2.973 2.964 2.956 2.948 2.940 2.933 2.593 2.579 2.565 2.551 2.506 2.500 2.488 2.478 2.091 2.085 2.080 2.074 2.068 1.535 1.525 1.517 1.511 1.510 1.503 1.340 0.842 0.826
toluene
8.5 8.0 7.5 7.0 6.5 6.0 5.5 5.0 4.5 4.0 3.5 3.0 2.5 2.0 1.5 1.0 0.5 ppm
(c)
N
H
H–B^1
★
N
B^1
□
R_2NH_2
R_2N
O
O
B^1
R_2N
H
O
O
B^1
+ H_4-Qin
■
^{11}B NMR
toluene-d_8, 128 MHz
After preparation of solution
1.66
□
90 80 70 60 50 40 30 20 10 0 -10 -20 -30 -40 -50 -60 -70 -80 ppm
After pressurized with H_2/CO_2
1.65
-7.55
-19.34
-19.87
□
★
90 80 70 60 50 40 30 20 10 0 -10 -20 -30 -40 -50 -60 -70 -80 ppm
After heated at 100 ºC for 3 h
40.23
6.20
2.96
1.82
□
■
90 80 70 60 50 40 30 20 10 0 -10 -20 -30 -40 -50 -60 -70 -80 ppm

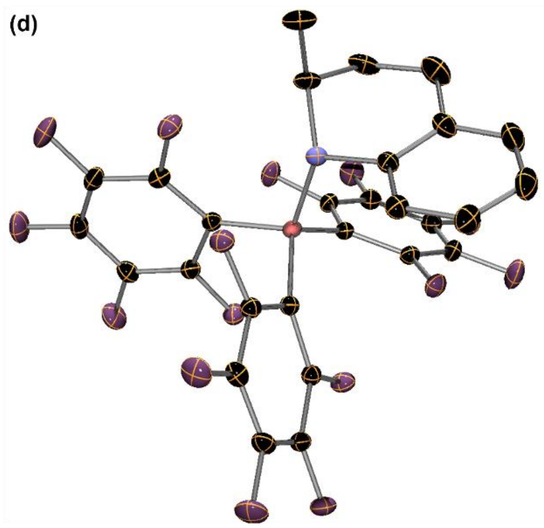

Figure 1.S38. Reaction of **MeQin** with **B^1** in the presence of H_2/CO_2. (a) ^{19}F NMR spectra. (b) ^{1}H NMR spectra. (c) ^{11}B NMR spectra. (d) Molecular structure of **H$_4$-MeQin–B^1** with ellipsoids set at 30% probability; H atoms are omitted for clarity.

1.4.17.6. Reaction of MeQin with B^9 in the presence of H_2/CO_2

A pressure-tight NMR tube (Wilmad-LabGrass 542-PV-7; V = 1.8 mL) was charged with **MeQin** (13.9 mg, 0.0971 mmol), **B^9** (34.8 mg, 0.0498 mmol) and α,α,α-trifluorotoluene (24.0 mg, 0.164 mmol; an internal standard). Once sealed, the NMR tube was pressurized with H_2/CO_2 (2.5 atm each), followed by heating at 100 °C for 3 h. Then the ^{1}H, ^{11}B, and ^{19}F NMR analyses were conducted.

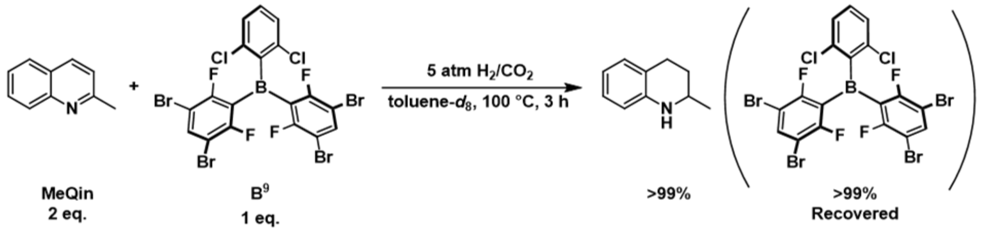

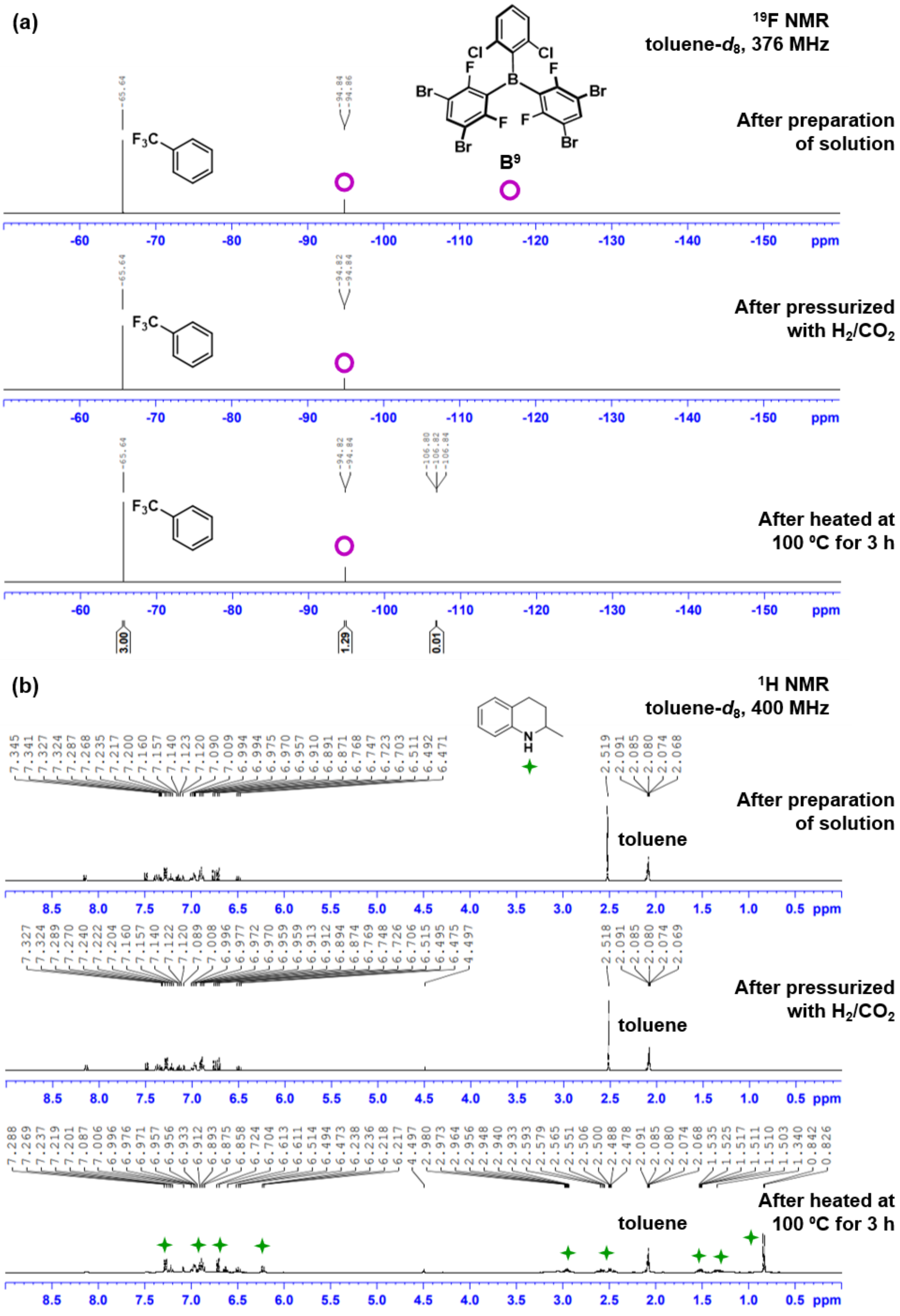
(a)
19F NMR
toluene-d8, 376 MHz
B9
After preparation of solution
After pressurized with H2/CO2
After heated at 100 ºC for 3 h
F3C
-65.64
-94.84
-94.86
-94.82
-106.80
-106.82
-106.84
3.00
1.29
0.01
-60 -70 -80 -90 -100 -110 -120 -130 -140 -150 ppm
(b)
1H NMR
toluene-d8, 400 MHz
toluene
N H
After preparation of solution
After pressurized with H2/CO2
After heated at 100 ºC for 3 h
2.519
2.091
2.085
2.080
2.074
2.068
2.518
2.069
4.497
8.5 8.0 7.5 7.0 6.5 6.0 5.5 5.0 4.5 4.0 3.5 3.0 2.5 2.0 1.5 1.0 0.5 ppm

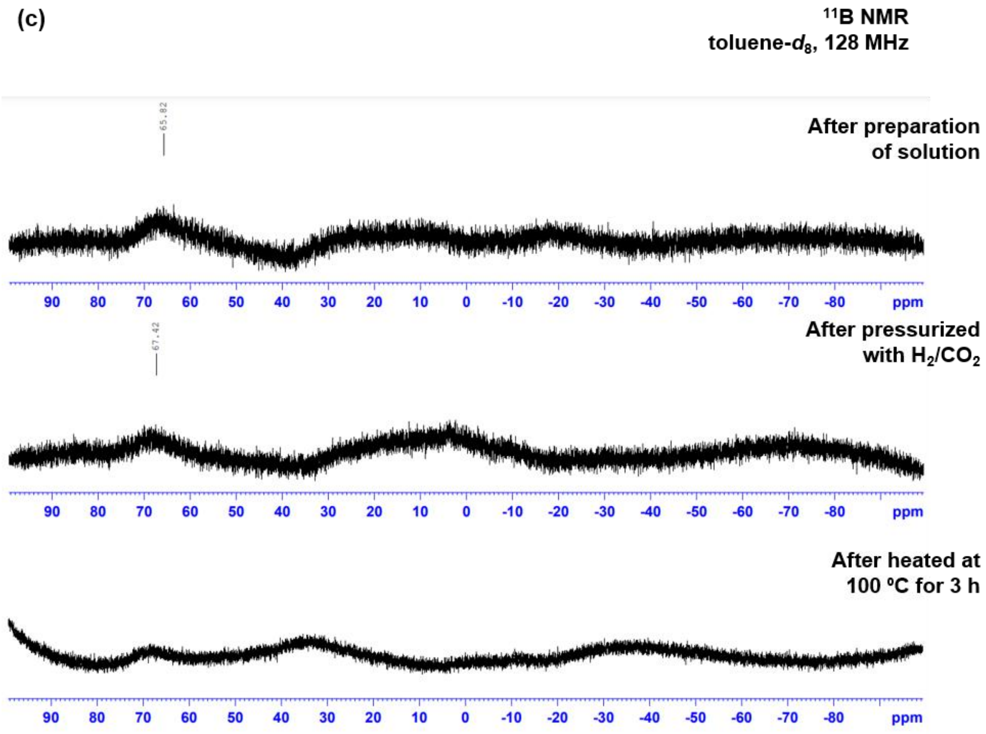

Figure 1.S39. Reaction of **MeQin** with **B^9** in the presence of H_2/CO_2. (a) ^{19}F NMR spectra. (b) ^{1}H NMR spectra. (C) ^{11}B NMR spectra.

1.4.17.7. Reaction of H$_4$-MeQin with B^1 in the presence of CO$_2$

A pressure-tight NMR tube (Wilmad-LabGrass 542-PV-7; $V = 1.8$ mL) was charged with **H$_4$-MeQin** (14.3 mg, 0.0971 mmol), and **B^1** (25.6 mg, 0.0500 mmol). Once sealed, the NMR tube was pressurized with CO_2 (5 atm), followed by heating at 100 °C for 1 h. Then, the ^{1}H, ^{11}B, and ^{19}F NMR analyses were conducted.

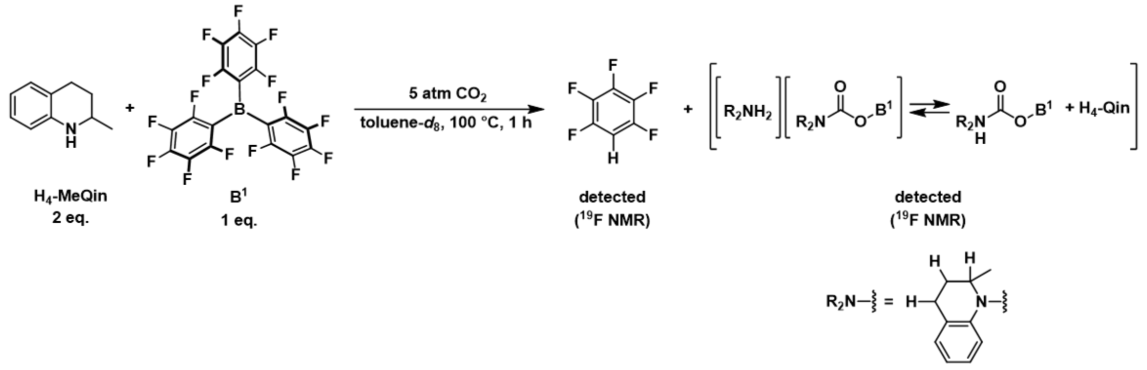

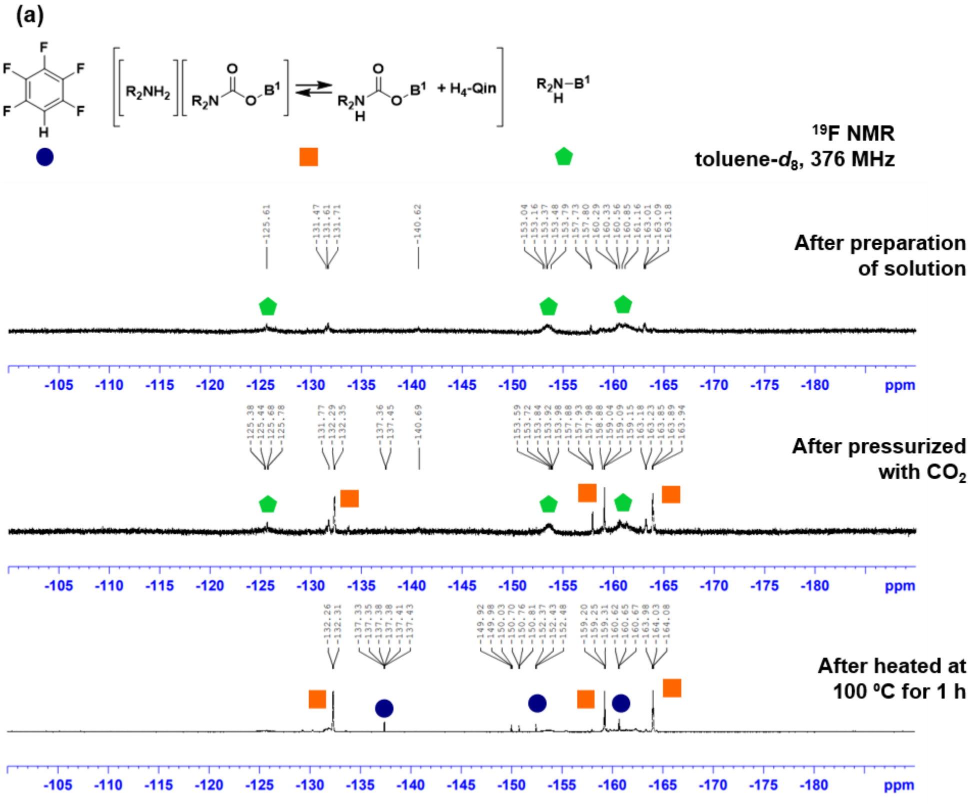
(a)
R_2NH_2
R_2N
B^1
+ H_4-Qin
R_2N-B^1
^{19}F NMR
toluene-d_8, 376 MHz
After preparation of solution
-125.61
-131.47
-131.61
-131.71
-140.62
-153.04
-153.16
-153.37
-153.48
-153.79
-157.73
-157.80
-160.29
-160.33
-160.56
-160.85
-161.16
-163.01
-163.09
-163.18
After pressurized with CO_2
-125.38
-125.44
-125.68
-125.78
-131.77
-132.29
-132.35
-137.36
-137.45
-140.69
-153.59
-153.72
-153.84
-153.92
-153.98
-157.88
-157.93
-157.98
-158.88
-159.04
-159.09
-159.15
-163.18
-163.23
-163.85
-163.89
-163.94
After heated at 100 °C for 1 h
-132.26
-132.31
-137.33
-137.35
-137.38
-137.38
-137.41
-137.43
-149.92
-149.98
-150.03
-150.70
-150.76
-150.81
-152.37
-152.43
-152.48
-159.20
-159.25
-159.31
-160.62
-160.65
-160.67
-163.98
-164.03
-164.08
-105
-110
-115
-120
-125
-130
-135
-140
-145
-150
-155
-160
-165
-170
-175
-180
ppm

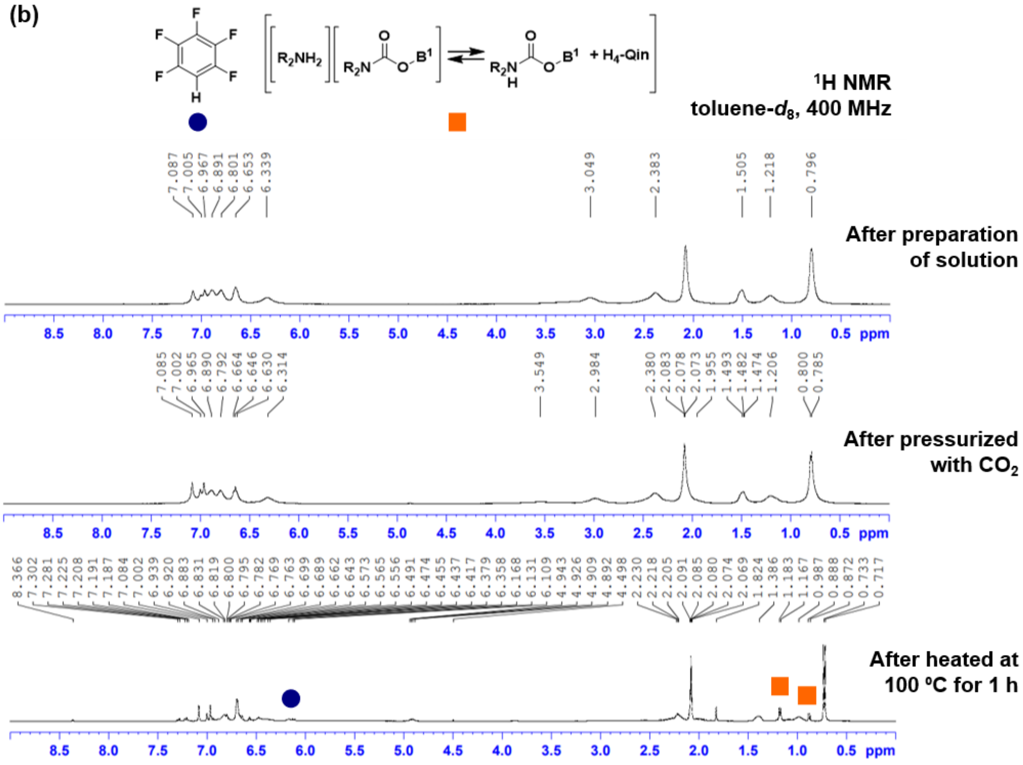
(b)
R_2NH_2
R_2N
B^1
+ H_4-Qin
^{1}H NMR
toluene-d_8, 400 MHz
After preparation of solution
7.087
7.005
6.967
6.891
6.801
6.653
6.339
3.049
2.383
1.505
1.218
0.796
After pressurized with CO_2
7.085
7.002
6.965
6.890
6.792
6.664
6.646
6.630
6.314
3.549
2.984
2.380
2.083
2.078
2.073
1.955
1.493
1.482
1.474
1.206
0.800
0.785
After heated at 100 °C for 1 h
8.366
7.302
7.281
7.225
7.208
7.191
7.187
7.084
7.002
6.939
6.920
6.883
6.831
6.819
6.800
6.795
6.782
6.769
6.763
6.699
6.689
6.662
6.643
6.573
6.565
6.556
6.491
6.474
6.455
6.437
6.417
6.379
6.358
6.168
6.131
6.109
4.943
4.926
4.909
4.892
4.498
2.230
2.218
2.205
2.091
2.085
2.080
2.074
2.069
1.824
1.386
1.183
1.167
0.987
0.888
0.872
0.733
0.717
8.5
8.0
7.5
7.0
6.5
6.0
5.5
5.0
4.5
4.0
3.5
3.0
2.5
2.0
1.5
1.0
0.5
ppm

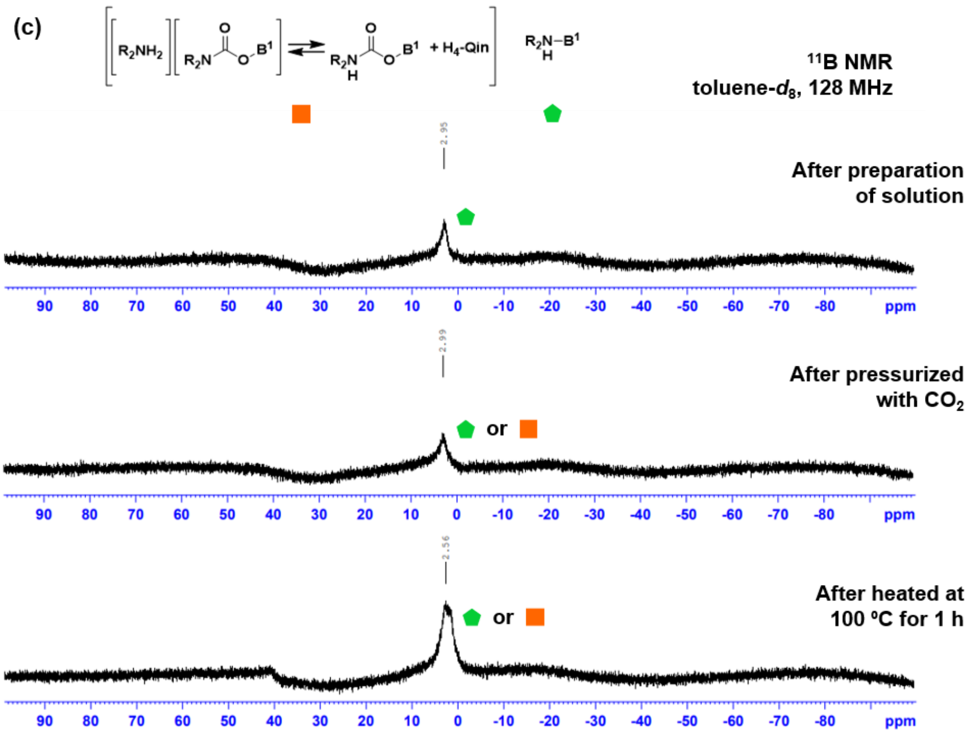

Figure 1.S40. Reaction of **H_4-MeQin** with **B^1** in the presence of CO_2. (a) ^{19}F NMR spectra. (b) ^1H NMR spectra. (C) ^{11}B NMR spectra.

1.4.17.8. Reaction of [H_4-MeQin–B^1] with H_2 followed by CO_2

A pressure-tight NMR tube (Wilmad-LabGrass 542-PV-7; V = 1.8 mL) was charged with **H_4-MeQin** (14.8 mg, 0.101 mmol), and **B^1** (25.6 mg, 0.0500 mmol). Once sealed, the NMR tube was pressurized with H_2 (2.5 atm), followed by heating at 100 °C for 1 h. Then, the ^1H, ^{11}B, and ^{19}F NMR analyses were conducted. Next, this NMR tube was pressurized with CO_2 (2.5 atm), followed by heating at 100 °C for 1 h. Then, the ^1H, ^{11}B, and ^{19}F NMR analyses were again conducted.

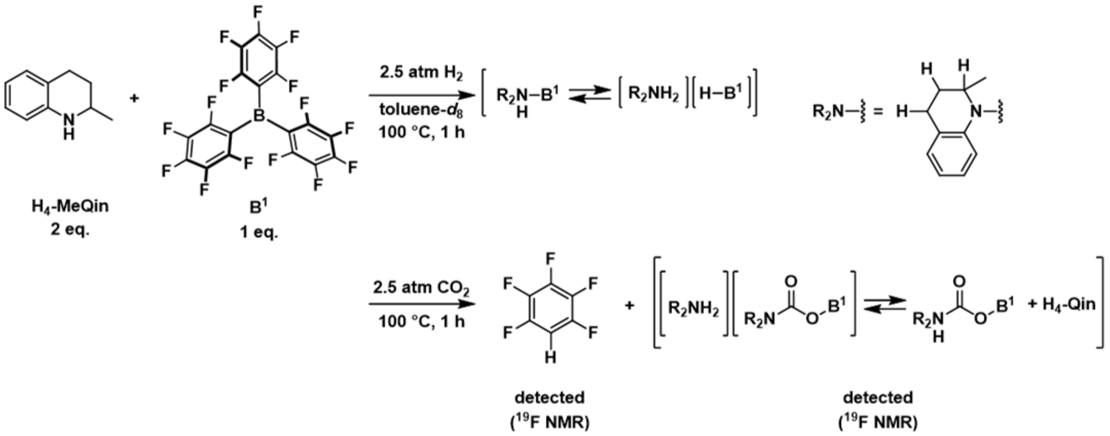

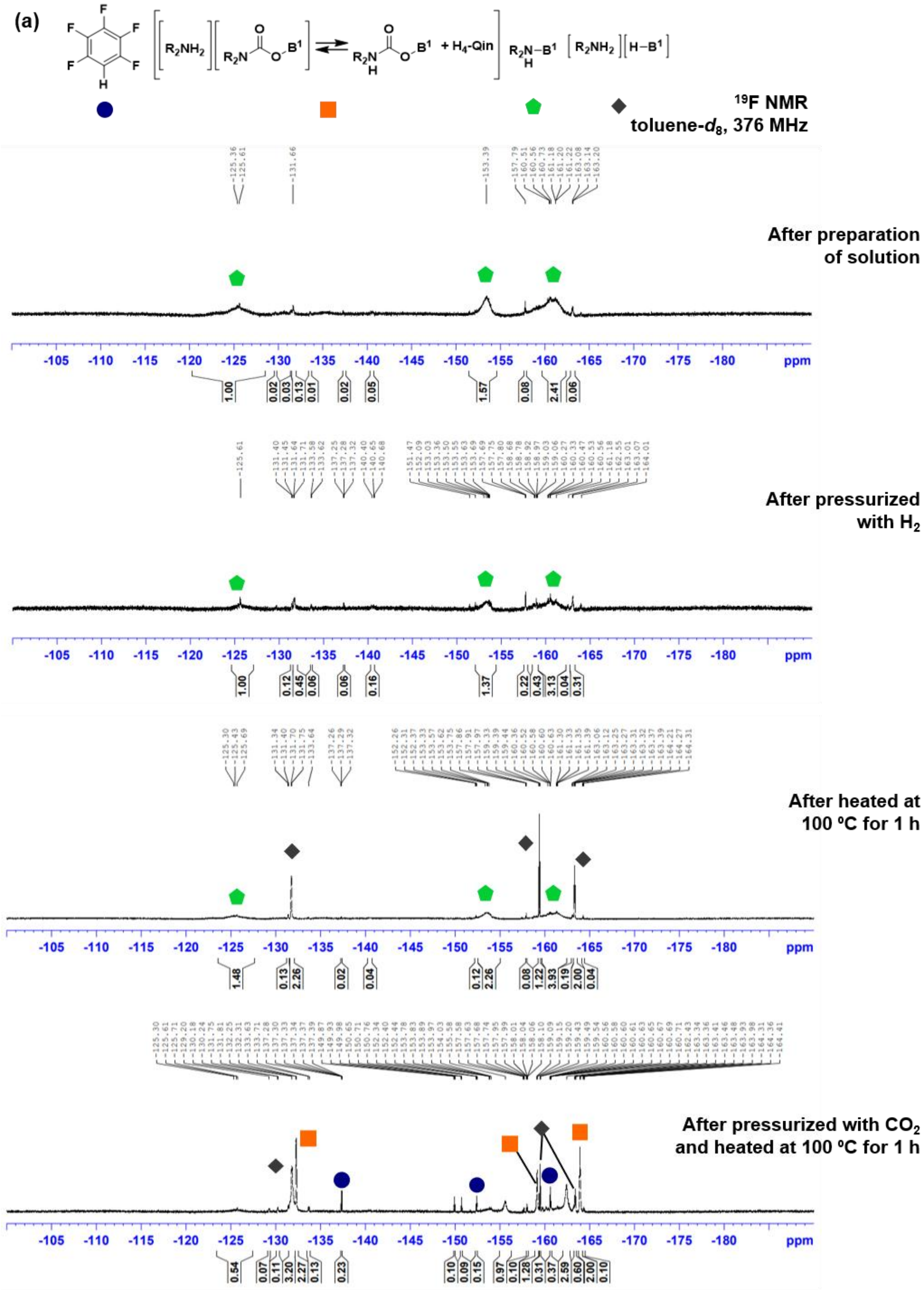
(a)
[R2NH2][R2NC(O)O–B1] ⇌ R2NHC(O)O–B1 + H4-Qin
R2NH–B1
[R2NH2][H–B1]
19F NMR
toluene-d8, 376 MHz
After preparation of solution
After pressurized with H2
After heated at 100 ºC for 1 h
After pressurized with CO2 and heated at 100 ºC for 1 h
-105 -110 -115 -120 -125 -130 -135 -140 -145 -150 -155 -160 -165 -170 -175 -180 ppm

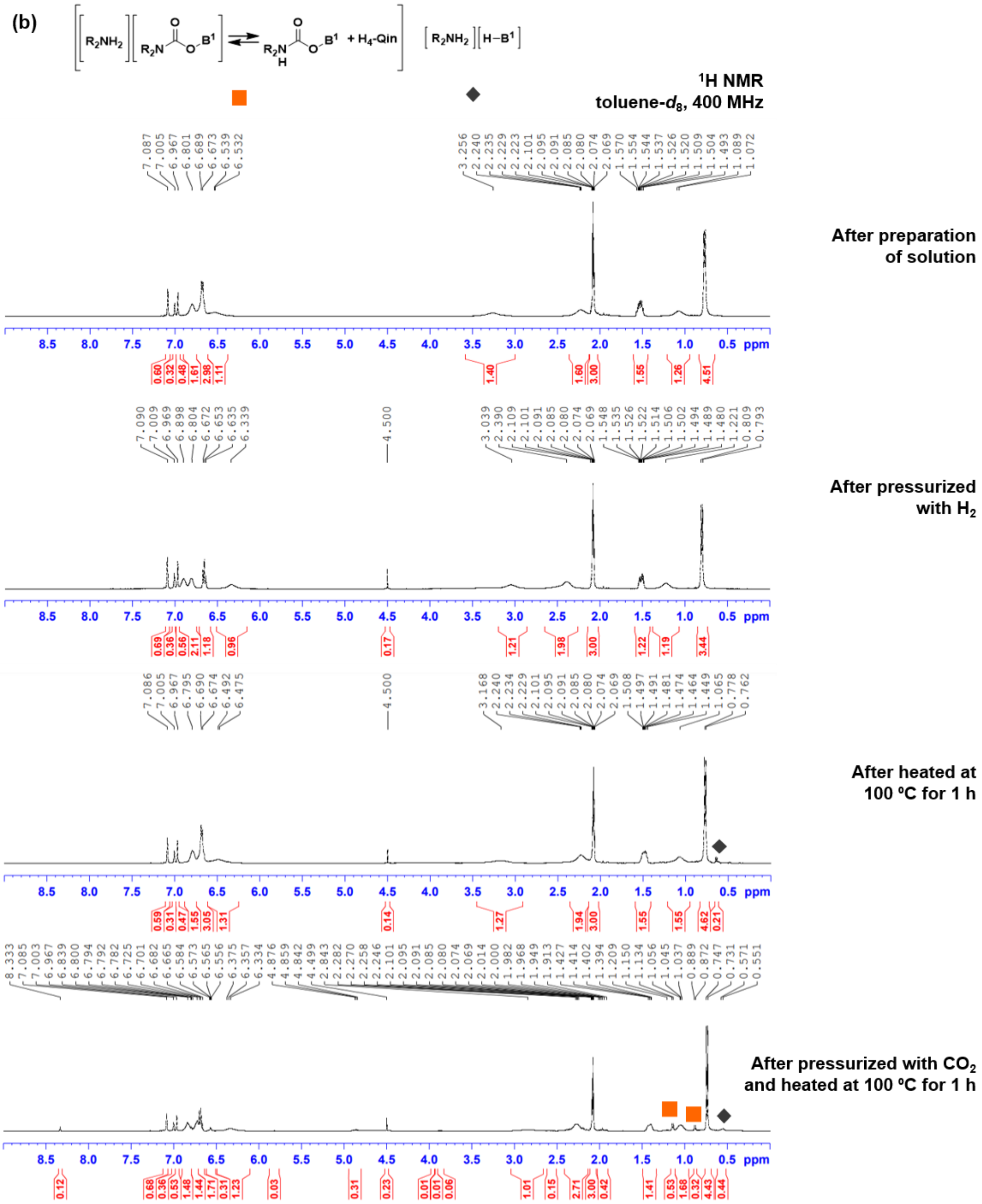
(b)
R2NH2
R2N
O
B1
R2N
H
+ H4-Qin
[R2NH2][H−B1]
1H NMR
toluene-d8, 400 MHz
After preparation of solution
7.087 7.005 6.967 6.801 6.689 6.673 6.539 6.532
3.256 2.240 2.235 2.229 2.223 2.101 2.095 2.091 2.085 2.080 2.074 2.069 1.570 1.554 1.544 1.537 1.526 1.520 1.509 1.504 1.493 1.089 1.072
0.60 0.32 0.48 1.61 2.98 1.11 1.40 1.60 3.00 1.55 1.26 4.51
After pressurized with H2
7.090 7.009 6.969 6.898 6.804 6.672 6.653 6.635 6.339
4.500
3.039 2.390 2.109 2.101 2.091 2.085 2.080 2.074 2.069 1.548 1.535 1.526 1.522 1.514 1.506 1.502 1.494 1.489 1.480 1.221 0.809 0.793
0.69 0.36 0.56 2.11 1.18 0.96 0.17 1.21 1.98 3.00 1.22 1.19 3.44
After heated at 100 ºC for 1 h
7.086 7.005 6.967 6.795 6.690 6.674 6.492 6.475
4.500
3.168 2.240 2.234 2.229 2.101 2.095 2.091 2.085 2.080 2.074 2.069 1.508 1.497 1.491 1.481 1.474 1.464 1.449 1.065 0.778 0.762
0.59 0.31 0.47 1.55 3.05 1.31 0.14 1.27 1.94 3.00 1.55 1.55 4.62 0.21
After pressurized with CO2 and heated at 100 ºC for 1 h
8.333 7.085 7.003 6.967 6.839 6.800 6.794 6.792 6.782 6.725 6.701 6.682 6.665 6.584 6.573 6.565 6.556 6.375 6.357 6.334 4.876 4.859 4.842 4.499 2.843 2.282 2.270 2.258 2.246 2.101 2.095 2.091 2.085 2.080 2.074 2.069 2.014 2.000 1.982 1.968 1.949 1.913 1.427 1.414 1.402 1.394 1.209 1.150 1.134 1.056 1.045 1.037 0.889 0.872 0.747 0.731 0.571 0.551
0.12 0.68 0.36 0.53 1.48 1.44 1.71 0.31 1.23 0.03 0.31 0.23 0.01 0.01 0.06 1.01 0.15 2.71 3.00 0.42 1.41 0.53 1.68 0.32 4.43 0.44
8.5 8.0 7.5 7.0 6.5 6.0 5.5 5.0 4.5 4.0 3.5 3.0 2.5 2.0 1.5 1.0 0.5 ppm

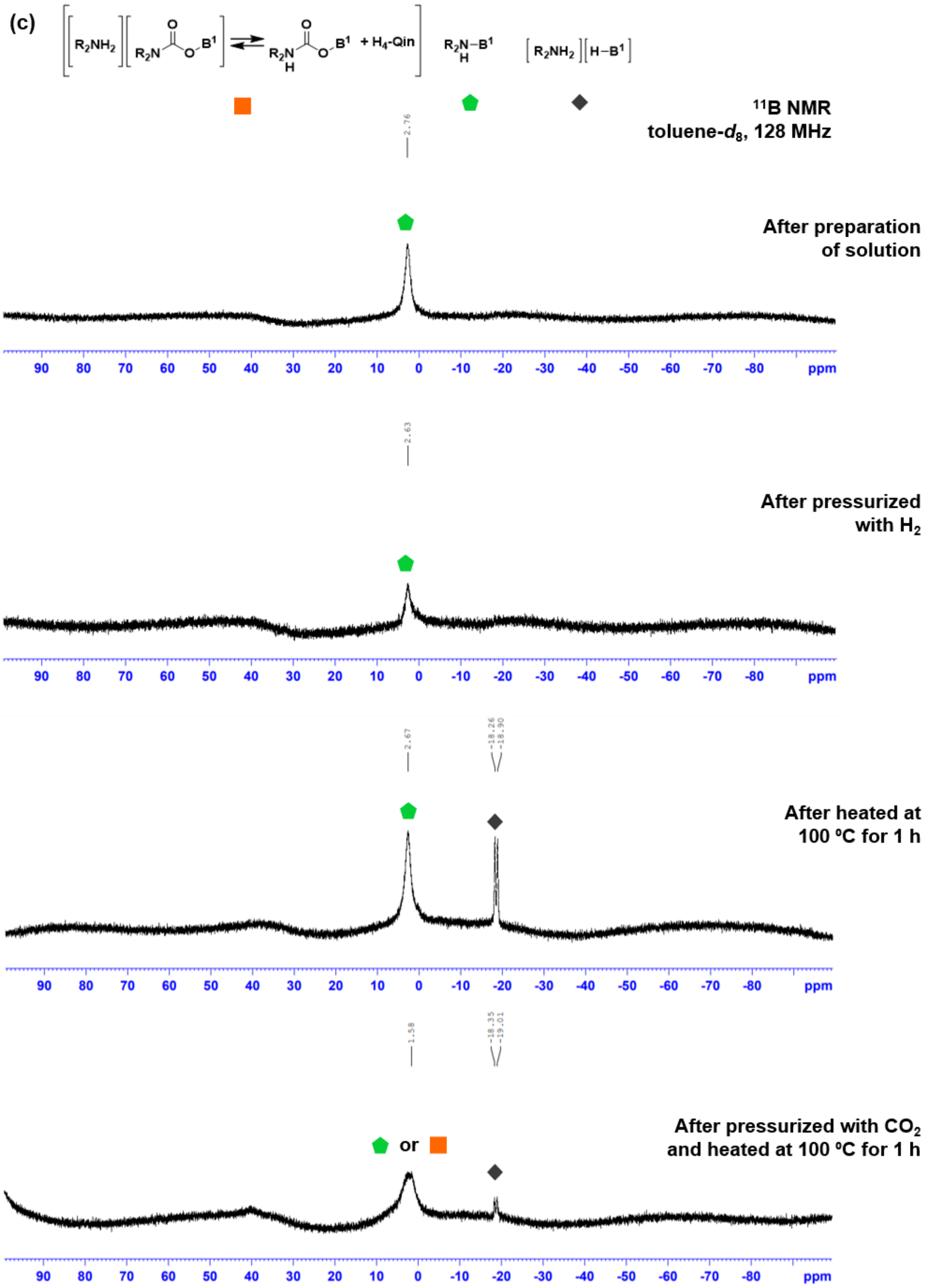

Figure 1.S41. Reaction of **[H_4-MeQin–B^1]** with H_2 followed by CO_2. (a) ^{19}F NMR spectra. (b) ^{1}H NMR spectra. (C) ^{11}B NMR spectra.

1.4.17.9. Hydrogenation of MeQin using [MeQin–H][HO–B^1] or [MeQin–H][HO–B^9]

General: A 30 mL autoclave was charged with **MeQin** (0.225 mmol), **[MeQin–H][HO–B″]** (0.025 mmol), and tetradecane (an internal standard), and toluene (0.17 mL). Once sealed, the autoclave was pressurized with H_2 (4 atm) and heated at 100 °C for 6 h. After degassed at room temperature, the yield of **H_4-MeQin** was determined by GC analysis. The results were shown in Figure 1.4F.

Use of [MeQin–H][HO–B^1]: Followed by the general procedures, **MeQin** (31.2 mg), **[MeQin–H][HO–B^1]** (16.9 mg), and tetradecane (13.9 mg) were employed, giving **H$_4$-MeQin** in <1% GC yield.

Use of [MeQin–H][HO–B^9]: Followed by the general procedures, **MeQin** (32.3 mg), **[MeQin–H][HO–B^9]** (21.3 mg), and tetradecane (19.6 mg) were employed, giving **H$_4$-MeQin** in 13% GC yield.

1.4.18. Comparison of Lewis acidity among B^n by Gutmann-Beckett method

General: A J. Young tube was charged with **B^n** (0.060 mmol), triethylphosphine oxide (8.1 mg, 0.057 mmol), and C_6D_6 (n = 1-9) or CD_2Cl_2 (n = 10). Then, the ^{31}P NMR analyses were conducted. The acceptor number (AN) was calculated according to the literature and summarized in Table 1.S4.[52]

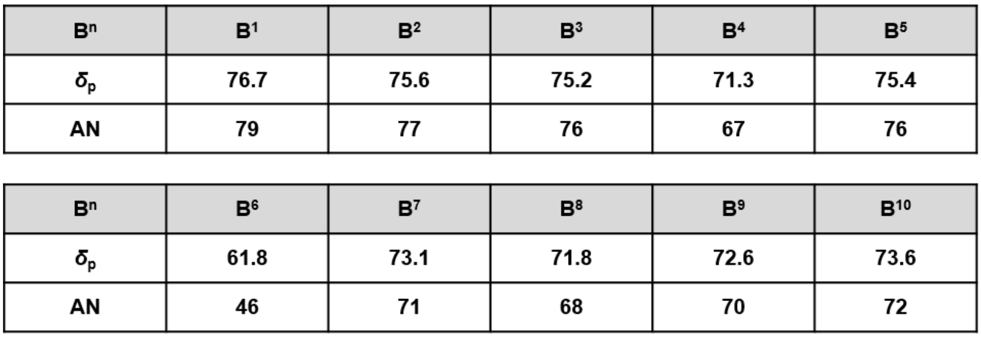

B^n	B^1	B^2	B^3	B^4	B^5	B^6	B^7	B^8	B^9	B^{10}
δ_p	76.7	75.6	75.2	71.3	75.4	61.8	73.1	71.8	72.6	73.6
AN	79	77	76	67	76	46	71	68	70	72

Table 1.S4. Comparison of Lewis acidity based on the Gutmann-Beckett method.

1.4.19. Computational details

The density functional theory (DFT) calculations were performed with Gaussian 16 (Revision C.01) software.[53] All the structures were optimized at the *ω*B97X-D[54] level of theory with the 6-31G(d,p) basis sets. Frequency calculations were performed to verify that intermediates have no imaginary frequency, whereas the transition structures have only one imaginary frequency. The appropriateness of the connections between each reactant and product via a transition state was confirmed using intrinsic reaction coordinate (IRC). Single-point energy calculations were carried out at *ω*B97X-D/6-311+G(d,p)/gas-phase level of theory otherwise noted. A polarizable continuum model (PCM)[55] was adopted, and the parameters for quinoline were used. The reported Gibbs free energies were calculated at 298.15 K. These calculations involve a certain margin of error.

1.4.19.1. Structural optimization of B^{n} and their LUMO energy levels

In general, optimization of **B**^{n} was carried out based on the geometrical parameters obtained by SC-XRD analysis. The energy levels of LUMO were then calculated by the single point calculation (Figure 1.S42).

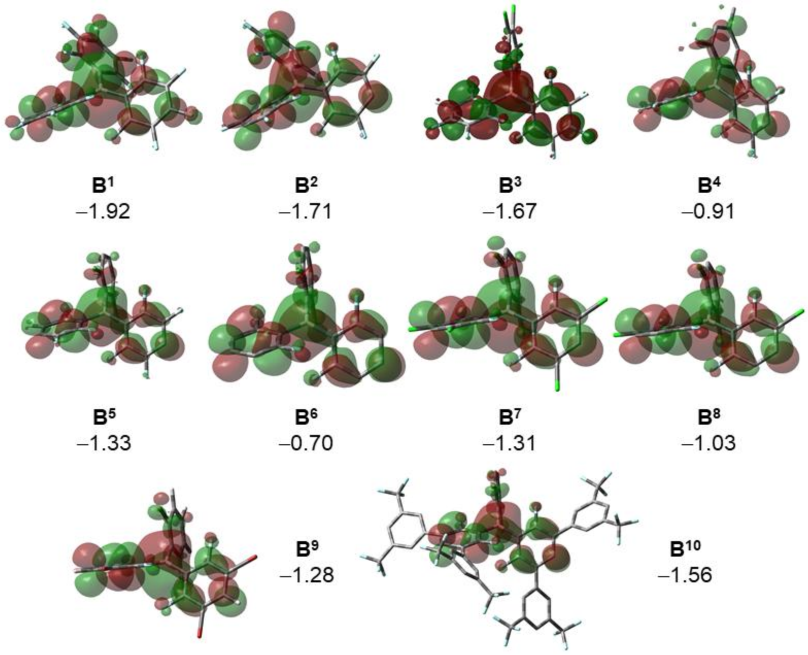

Figure 1.S42. LUMO of **B**^{n} and their energy levels (eV).

1.4.19.2. Theoretical investigation of reaction between B^{n} and CO

The optimized molecular structure of **OC–B**^{n} and saddle point species **TS-B**^{n} (*n*= 1, 5, 7, 9-10) with their relative Gibbs free energy (ΔG° kcal·mol^{-1}) with respect to [CO + **B**^{n}] (+ 0.0 kcal·mol^{-1}) are summarized in Figure 1.S43.

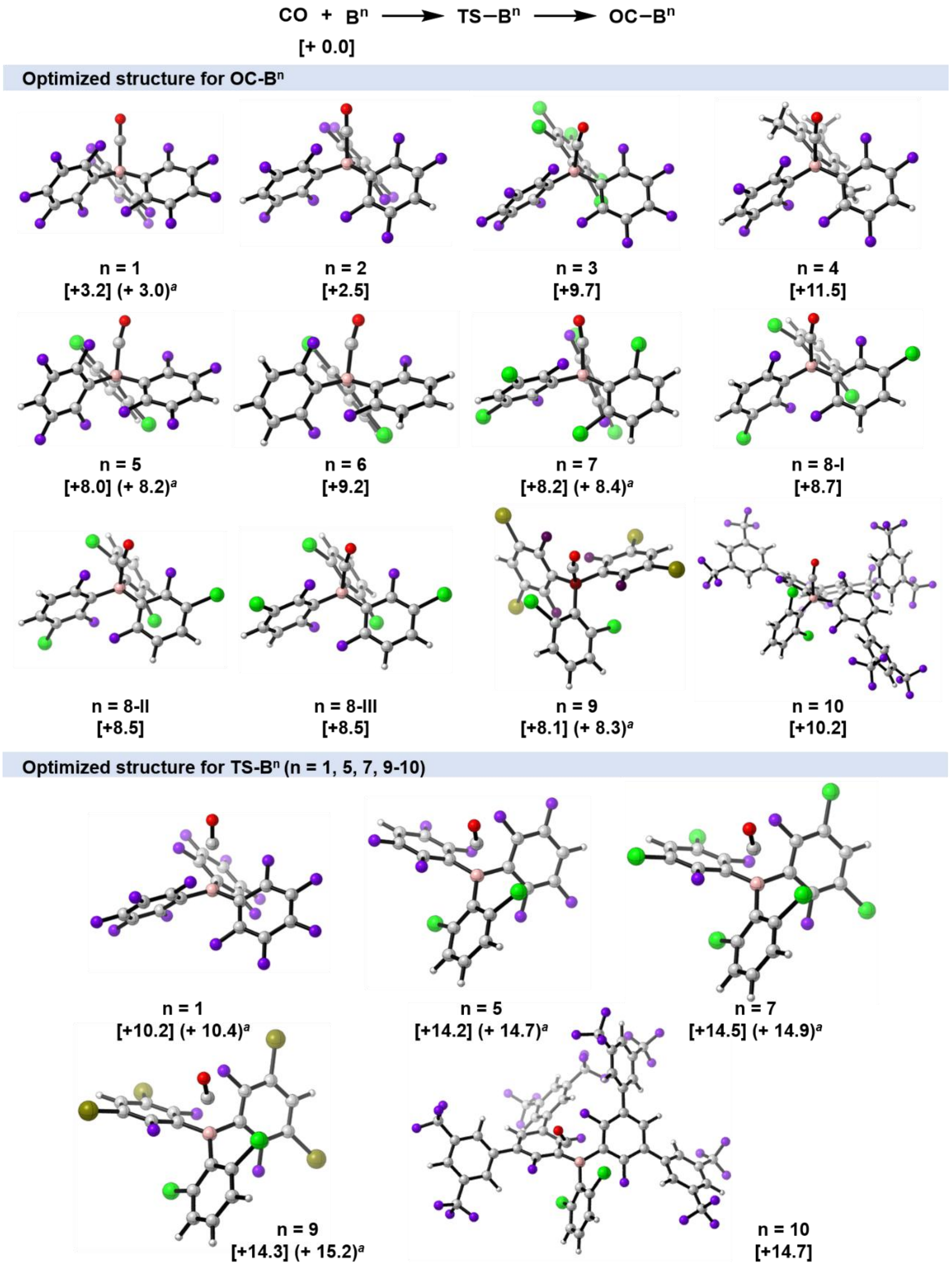

Figure 1.S43. Optimized structure of **OC–B*ⁿ*** and saddle point species **TS-B*ⁿ*** (*n*= 1, 5, 7, 9-10). The relative Gibbs free energy (kcal·mol^{-1}) with respect to [CO + B^{n}] (+ 0.0 kcal·mol^{-1}) is shown. ^{a}SPC results calculated at the *ω*B97X-D/6-311+G(d,p)/PCM (quinoline) level of theory.

1.4.19.3. Discussion on the effects of *meta*-substituents on B^{n} (n = 5, 7, 9-10)

In the **B**^{n}-catalyzed hydrogenation of **MeQin** in the co-presence of CO and CO$_2$ under the applied neat conditions (n= 1, 5, 7, 9-10; Fig S18), the higher catalyst turnover number (TON) was confirmed in the following order; **B**^{9} (1480) > **B**^{7} (1400) > **B**^{10} (1340) > **B**^{5} (1000) >> **B**^{1} (11). These results demonstrated the importance of the introduction of four F and two Cl atoms at the *ortho*-positions with respect to the boron center. Then, to clarify an impact of *meta*-substituents, I analyzed these results based on the parameters obtained by the Gutmann-Beckett method and the energy levels of their LUMO (Figure 1.S44a). It should be noted that the Gutmann-Beckett acceptor numbers (GB-ANs) should be influenced by both an electron-accepting ability on the boron atom, i.e. the energy level of LUMO, and steric repulsions that occurred between Et$_3$P=O (i.e. a front strain) and/or between other Ar groups (i.e. a back strain) (Figure 1.S44b).[43] For **B**^{5}, **B**^{7}, and **B**^{9}–**B**^{10}, TON shows a good correlation with GB-ANs. In contrast, a profile of TON with respect to the energy levels of LUMO shows a rather large variation. Based on these results and the size of substituents such as F, Cl, Br,[56] and (CF$_3$)$_2$C$_6$H$_3$, the *meta*-substituents play a key role to establish the suitable Lewis acidity not only by regulating of the electron-accepting ability on the boron atom but also by inducing the proper front/back strains. In this context, the (CF$_3$)$_2$C$_6$H$_3$ groups in **B**^{10} can reduce their steric demanding via the rotation of C$_{Ar}$–C$_{Ar}$ bond, which was indeed observed in **OC–B**^{10}.

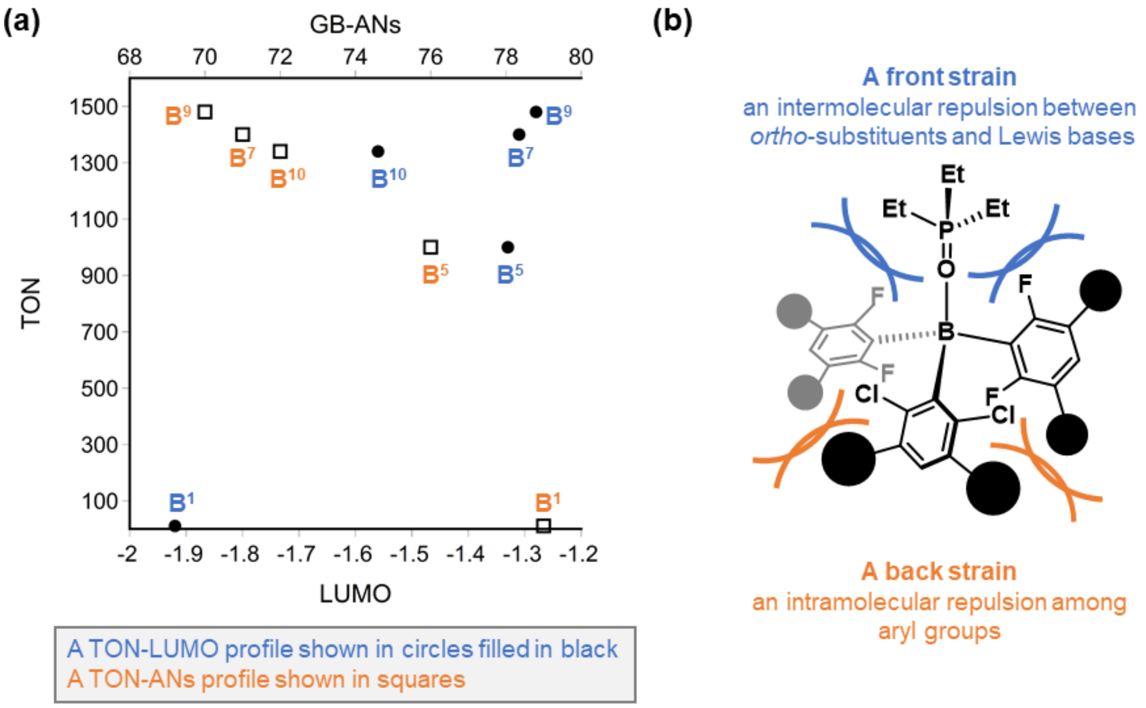

Figure 1.S44. Discussion on the effects of *meta*-substituents on **B**^{n} (n = 5, 7, 9-10). (a) Profiles of TON vs the LUMO energies in eV (shown in black-filled circles) and vs Gutmann-Beckett acceptor numbers (GB-ANs; shown in squares). (b) A schematic representation for a concept of front and back strains generated via the complexation of Et$_3$P=O–**B**^{n} (n = 5, 7, 9-10).

1.5 References and notes

1. Liu, K.; Song, C.; Subramani, V. Eds., *Hydrogen and Syngas Production and Purification Technologies* (Wiley, 2010).
2. Dawood, F.; Anda, M.; Shafiullah, G. M. *Int. J. Hydrogen Energy* **2020**, *45*, 3847.
3. Voldsund, M.; Jordal, K.; Anantharaman, R. *Int. J. Hydrogen Energy* **2016**, *41*, 4969.
4. Holladay, J. D.; Hu, J.; King, D. L.; Wang, Y. *Catal. Today* **2009**, *139*, 244.
5. Nishiyama, H.; Yamada, T.; Nakabayashi, M.; Maehara, Y.; Yamaguchi, M.; Kuromiya, Y.; Nagatsuma, Y.; Tokudome, H.; Akiyama, S.; Watanabe, T.; Narushima, R.; Okunaka, S.; Shibata, N.; Takata, T.; Hisatomi, T.; Domen, K. *Nature* **2021**, *598*, 304.
6. Okada, Y.; Saito, M.; Wakayama, S.; Shimura, M. Patent US8758722, **2014**; https://patents.google.com/patent/JP5737853B2/en.
7. Hoshimoto, Y.; Ogoshi, S.; Tanaka, T.; Kawamoto, N. Patent JP2017206474A, **2017**; https://patents.google.com/patent/JP2017206474A/en.
8. Gianotti, E.; Taillades-Jacquin, M.; Rozière, J.; Jones, D. J. *ACS Catal.* **2018**, *8*, 4660.
9. Jorschick, H.; Preuster, P.; Bösmann, A.; Wasserscheid, P. *Sustain. Energy Fuels* **2021**, *5*, 1311.
10. Zou, Y.-Q.; von Wolff, N.; Anaby, A.; Xie, Y.; Milstein, D. *Nat. Catal.* **2019**, *2*, 415.
11. Shimbayashi, T.; Fujita, K. *Tetrahedron* **2020**, *76*, 130946.
12. He, T.; Pei, Q.; Chen, P. *J. Energy Chem.* **2015**, *24*, 587.
13. Fujita, K.; Wada, T.; Shiraishi, T. *Angew. Chem., Int. Ed.* **2017**, *56*, 10886.
14. Hu, P.; Fogler, E.; Diskin-Posner, Y.; Iron, M. A.; Milstein, D. *Nat. Commun.* **2015**, *6*, 6859.
15. Hu, P.; Ben-David, Y.; Milstein, D. *Angew. Chem. Int. Ed.* **2016**, *55*, 1061.
16. Kothandaraman, J.; Kar, S.; Sen, R.; Goeppert, A.; Olah, G. A.; Surya Prakash, G. K. *J. Am. Chem. Soc.* **2017**, *139*, 2549.
17. Xie, Y.; Hu, P.; Ben-David, Y.; Milstein, D. *Angew. Chem. Int. Ed.* **2019**, *58*, 5105.
18. Breakman-Danheux, C.; Fontana, A.; Laurent, P.; Lolivier, P. *Fuel* **1996**, *75*, 579.
19. Jorschick, H.; Vogl, M.; Preuster, P.; Bosmann, A.; Wasserscheid, P. *Int. J. Hydrogen Energy* **2019**, *44*, 31172.
20. Revunova, K.; Nikonov, G. I. *Dalton Trans.* **2015**, *44*, 840.
21. Oestreich, M.; Hermeke, J.; Mohr, J.; *Chem. Soc. Rev.* **2015**, *44*, 2202.
22. Welch, G. C.; San Juan, R. R.; Masuda, J. D.; Stephan, D. W. *Science* **2006**, *314*, 1124.
23. Jupp, A. R.; Stephan, D. W. *Trends Chem.* **2019**, *1*, 35.
24. Stephan, D. W. *J. Am. Chem. Soc.* **2021**, *143*, 20002.
25. Geier, S. J.; Chase, P. A.; Stephan, D. W. *Chem. Commun.* **2010**, *46*, 4884.
26. Erös, G.; Nagy, K.; Mehdi, H.; Pápai, I.; Nagy, P.; Király, P.; Tárkányi, G.; Soós, T. *Chem.-Eur. J.* **2012**, *18*, 574.
27. Scott, D. J.; Fuchter, M. J.; Ashley, A. E. *Angew. Chem. Int. Ed.* **2014**, *53*, 10218.
28. Momming, C. M.; Otten, E.; Kehr, G.; Frohlich, R.; Grimme, S.; Stephan, D. W.; Erker, G. *Angew. Chem. Int. Ed.* **2009**, *48*, 6643.

29. Stephan, D. W.; Erker, G. *Chem. Sci.* **2014**, *5*, 2625.
30. Voss, T.; Mahdi, T.; Otten, E.; Frohlich, R.; Kehr, G.; Stephan, D. W.; Erker, G. *Organometallics* **2012**, *31*, 2367.
31. Ashley, A. E.; Thompson, A. L.; O'Hare, D. *Angew. Chem., Int. Ed.* **2009**, *48*, 9839.
32. Tran, S. D.; Tronic, T. A.; Kaminsky, W.; Heinekey, D. M.; Mayer, J. M. *Inorg. Chim. Acta* **2011**, *369*, 126.
33. Finze, M.; Bernhardt, E.; Terheiden, A.; Berkei, M.; Willner, H.; Christen, D.; Oberhammer, H.; Aubke, F. *J. Am. Chem. Soc.* **2002**, *124*, 15385.
34. Fasano, V.; Ingleson, M. J. *Synthesis* **2018**, *50*, 1783.
35. Hoshimoto, Y.; Ogoshi, S. *ACS Catal.* **2019**, *9*, 5439.
36. Voicu, D.; Stephan, D. W.; Kumacheva, E. *ChemSusChem* **2015**, *8*, 4202.
37. Wang, W.-B.; Lu, S.-M.; Yang, P.-Y.; Han, X.-W.; Zhou, Y.-G. *J. Am. Chem. Soc.* **2003**, *125*, 10536.
38. I also confirmed that the hydrogenation of **MeQin** under otherwise identical mixed gas conditions did not proceed effectively and that **H_4-MeQin** was obtained only in ~1% when Ru-MACHO and Pd/C were used as catalysts.
39. Ullrich, M.; Lough, A. J.; Stephan, D. W. *J. Am. Chem. Soc.* **2009**, *131*, 52.
40. Ashley, A. E.; Herrington, T. J.; Wildgoose, G. G.; Zaher, H.; Thompson, A. L.; Rees, N. H.; Kramer, T.; O'Hare, D. *J. Am. Chem. Soc.* **2011**, *133*, 14727.
41. Gyömöre, Á.; Bakos, M.; Földes, T.; Pápai, I.; Domján, A.; Soós, T. *ACS Catal.* **2015**, *5*, 5366.
42. Dorkó, É.; Kótai, B.; Földes, T.; Gyömöre, A.; Pápai, I.; Soós, T. *J. Organomet. Chem.* **2017**, *847*, 258.
43. Chase, P. A.; Henderson, L. D.; Piers, W. E.; Parvez, M.; Clegg, W.; Elsegood, M. R. J. *Organometallics* **2006**, *25*, 349.
44. Kojima, M.; Kanai, M. *Angew. Chem. Int. Ed.* **2016**, *55*, 12224.
45. Maier, A. F. G.; Tussing, S.; Schneider, T.; Florke, U.; Qu, Z.-W.; Grimme, S.; Paradies, J. *Angew. Chem., Int. Ed.* **2016**, *55*, 12219.
46. Liu, Y.; Du, H. *J. Am. Chem. Soc.* **2013**, *135*, 12968.
47. Eisenberger, P.; Bestvater, B. P.; Keske, E. C.; Crudden, C. M. *Angew. Chem., Int. Ed.* **2015**, *54*, 2467.
48. The effect of using quinoline as the reaction medium was also simulated using the polarizable continuum model (PCM), which provided virtually identical results.
49. Reineke, M. H.; Sampson, M. D.; Rheingold, A. L.; Kubiak, C. P. *Inorg. Chem.* **2015**, *54*, 3211.
50. Manka, J. T.; Kaszynski, P. *J. Fluor. Chem.* **2003**, *124*, 39.
51. Sanchez, P.; Hernandez-Juarez, M.; Rendon, N.; Lopez-Serrano, J.; Santos, L. L.; Alvarez, E.; Paneque, M.; Suarez, A. *Dalton Trans.* **2020**, *49*, 9583.
52. Beckett, M. A.; Strickland, G. C.; Holland, J. R.; Varma, K. S. *Polymer* **1996**, *37*, 4629.
53. Gaussian 16, Revision C.01, Frisch, M. J.; Trucks, G. W.; Schlegel, H. B.; Scuseria, G. E.; Robb, M. A.; Cheeseman, J. R.; Scalmani, G.; Barone, V.; Petersson, G. A.; Nakatsuji, H.; Li, X.; Caricato, M.; Marenich, A. V.; Bloino, J.; Janesko, B. G.; Gomperts, R.; Mennucci, B.; Hratchian, H. P.; Ortiz, J. V.; Izmaylov, A. F.; Sonnenberg, J. L.; Williams-Young, D.; Ding, F.; Lipparini, F.; Egidi, F.; Goings, J.; Peng,

B.; Petrone, A.; Henderson, T.; Ranasinghe, D.: Zakrzewski, V. G.; Gao, J.; Rega, N.; Zheng, G.; Liang, W.; Hada, M.; Ehara, M.; Toyota, K.; Fukuda, R.; Hasegawa, J.; Ishida, M.; Nakajima, T.; Honda, Y.; Kitao, O.; Nakai, H.; Vreven, T.; Throssell, K.; Montgomery Jr., J. A.; Peralta, J. E.; Ogliaro, F.; Bearpark, M. J.; Heyd, J. J.; Brothers, E. N.; Kudin, K. N.; Staroverov, V. N.; Keith, T. A.; Kobayashi, R.; Normand, J.; Raghavachari, K.; Rendell, A. P.; Burant, J. C.; Iyengar, S. S.; Tomasi, J.; Cossi, M.; Millam, J. M.; Klene, M.; Adamo, C.; Cammi, R.; Ochterski, J. W.; Martin, R. L.; Morokuma, K.; Farkas, O.; Foresman, J. B.; Fox, D. J. Gaussian, Inc., Wallingford CT, 2019.

54. Chai, J. D.; Gordon, M. H. *Phys. Chem. Chem. Phys.* **2008**, *10*, 6615.
55. Tomasi, J.; Mennucci, B.; Cammi, R. *Chem. Rev.* **2005**, *105*, 2999.
56. Cordero, B.; Gomes, V.; Platero-Prats, A. E.; Reves, M.; Echeverria, J.; Cremades, E.; Barragan, F.; Alvarez, S. *Dalton Trans.* **2008**, 2832.

Chapter 2

Elucidating multicomponent mechanisms in the catalytic hydrogenation of 2-methylquinoline under crude-H_2 conditions: a key H_2-cleavage process by a boron−olefin Lewis pair

Abstract: The mechanisms of the triarylborane-catalyzed hydrogenation of 2-methylquinoline (**MeQin**) in the presence of CO_2 were investigated using the artificial force induced reaction (AFIR) method. When $B(C_6F_5)_3$ (**B^1**) is used as the catalyst, the hydrogenation proceeds via intermolecular proton and hydride transfer from **[MeQin–H][H–B^1]** to a 1,4-dihydroquinoline intermediate (***p*-H$_2$-MeQin**). However, I confirmed that **B^1** quickly decomposes via a CO_2-capture reaction with 2-methyl-1,2,3,4-tetrahydroquinoline (**H$_4$-MeQin**) followed by thermally induced proto-deboronation. When $B(2,6\text{-}Cl_2C_6H_3)(3,5\text{-}Br_2\text{-}2,6\text{-}F_2C_6H)_2$ (**B^9**) is employed, the dissociation of CO_2 from the corresponding CO_2-capture product can occur prior to the irreversible proto-deboronation step, and the hydrogenation of **MeQin** thus continues efficiently. Moreover, the AFIR analysis suggested that a frustrated Lewis pair (FLP) comprising the boron atom of **B^9** and the olefinic carbon in ***p*-H$_2$-MeQin** mediates the heterolytic cleavage of H_2. Based on these mechanistic details, I identified the modified catalyst $B(2\text{-}Cl\text{-}6\text{-}FC_6H_3)_3$ (**B^{12}**) that demonstrates a remarkable catalyst turnover number (TON = 4,000) in the hydrogenation of **MeQin**.

2.1 Introduction

In Chapter 1, I demonstrated the triarylborane (**B^n**)-catalyzed hydrogenation of *N*-heteroaromatics using a gaseous mixture of H_2, CO, CO_2, and CH_4 as a model of crude H_2,[1–4] proceeding via the generation of frustrated Lewis pairs (FLPs).[5–8] I have also demonstrated proof-of-concept for a molecule-based H_2 purification system in Chapter 1,[9–14] i.e., a reaction sequence involving the $B(2,6\text{-}Cl_2C_6H_3)(3,5\text{-}Br_2\text{-}2,6\text{-}F_2C_6H)_2$ (**B^9**)-catalyzed hydrogenation of 2-methylquinoline (**MeQin**) under crude-H_2 conditions and subsequent **B^9**-catalyzed dehydrogenation of 2-methyl-1,2,3,4-tetrahydroquinoline (**H$_4$-MeQin**), which afforded pure H_2 with concomitant regeneration of **MeQin**.[9,10] $B(C_6F_5)_3$ (**B^1**) did not show sufficient activity in the hydrogenation of **MeQin** using crude H_2. Given that crude H_2 will be continuously produced on a huge scale from a variety of hydrocarbon resources, including biomass and wastes, in the mid- to long-term future,[4,15] I am interested in further optimizing borane-catalyzed H_2-purification systems based on the hydrogenation and dehydrogenation of *N*-heteroaromatics. Toward this end, I decided to clarify the mechanisms of the hydrogenation of the model substrate **MeQin**, as well as the undesired quenching paths of boranes caused by contaminants. Although a mechanism for the $B(2,4,6\text{-}Me_3C_6H_2)(2,3,5,6\text{-}F_4C_6H)_2$ (**B^4**)-catalyzed hydrogenation of **MeQin** has previously been proposed by Soós and co-workers,[16] the presence of CO and CO_2 may change the mechanistic scenario. Therefore, to explore the reaction pathways under crude-H_2 conditions, I decided to employ the artificial force induced reaction (AFIR) method, as this approach enables an automated search of complex reaction networks in multicomponent systems without requiring specific initial structures.[17–19]

Herein, I report the reaction mechanisms involved in the **B^1**- and **B^9**-catalyzed hydrogenation of **MeQin** in the presence of CO_2 based on an AFIR analysis (Figure 2.1). I discovered that the primary mechanism changes depending on whether the homoleptic **B^1** or heteroleptic **B^9** catalyst is used. For the **B^9**-catalyzed system, I found that the H_2-cleavage path is mediated by a combination of the Lewis-acidic boron center and the Lewis basic olefinic carbon atom in the 1,4-dihydroquinoline intermediate (***p*-H$_2$-MeQin**); this mode of H_2 cleavage has so far remained underexplored.[20,21] The details of the CO_2-induced proto-deboronation paths and further modifications to increase catalyst robustness are also discussed.

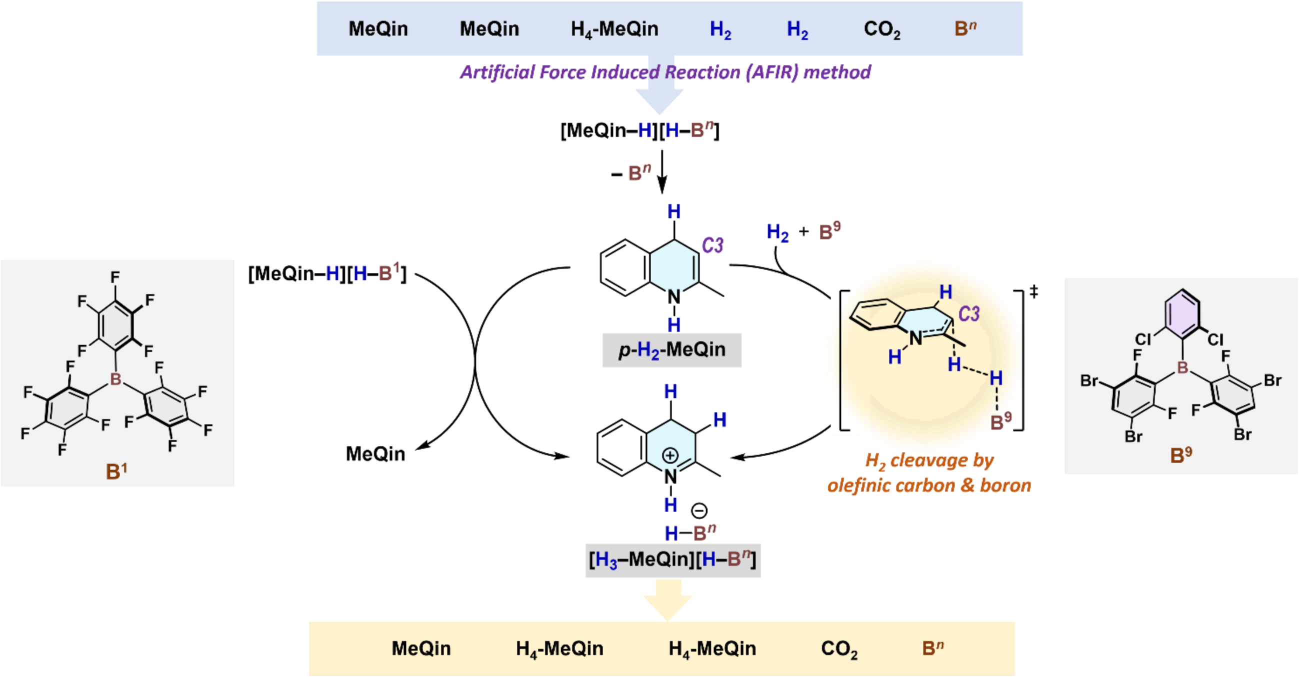

Figure 2.1. Simplified primary mechanisms for the **B^n**-catalyzed hydrogenation of **MeQin**, as explored using the AFIR method with an input of seven molecules (*this work*).

2.2 Computational details

The GRRM23 program package was used in this study.[22] For the DFT energy and gradient calculations, I used the Gaussian 16 program suite.[23] To obtain the initial geometries along the reaction paths, I performed a single component-AFIR (SC-AFIR) search at the GFN2-xTB level. In particular, for the geometries listed in Tables 2.S2, 2.S4, 2.S6, and 2.S8, the NoBondRearrange option was applied to explore the subsequent reaction paths. This option limits the SC-AFIR search to geometries that have the same bonding pattern as the input geometry. A weak force of $\gamma = 23.9/[N \times (N-1)/2]$ kcal mol^{-1} was applied to all atomic pairs within the system in order to prevent the molecules from moving too far from the reaction center during the SC-AFIR search, where N is the number of atoms. In the SC-AFIR search, the key reaction paths were relaxed using the locally updated planes (LUP) method (denoted by LUP paths).[24,25] The transition states (TSs) and equilibrium geometries (EQs) were optimized at the DFT level by referring to the LUP paths obtained from the SC-AFIR search. I used the UωB97X-D functional and Def2-SVP basis set under the assumption of vacuum conditions (denoted by the UωB97X-D/Def2-SVP level) for the optimization of the molecular structures, followed by single-point energy calculations at the UωB97X-D/Def2-TZVP level. Intrinsic-reaction-coordinate (IRC) calculations were carried out from all the optimized TSs at the same level of theory for connecting EQs. The Gibbs free energy values at 300 K were calculated using ideal-gas, rigid-rotor, and harmonic-vibrational models, whereby all harmonic frequencies below 50 cm^{-1} were adjusted to 50 cm^{-1}.

2.3 Results and discussion

I explored potential surfaces with GFN2-xTB including seven components, i.e., **B*ⁿ*** (n = 1 or 9), two molecules of **MeQin**, **H_4-MeQin**, two molecules of H_2, and CO_2. Based on these results, DFT calculations were carried out, and results for the hydrogenation and CO_2-triggered catalyst-decomposition paths are shown in Figures 2–4. Preliminary mechanistic studies revealed that CO reversibly coordinates to the boron centers to form CO−**B^n**, which predominantly causes kinetic suppression of the progress of hydrogenation. In addition, the presence of CH_4 does not affect the catalytic activity of **B^n** under the previously applied reaction conditions. Thus, I excluded the influences of CO and CH_4 from the present considerations. Figures 2 and 3 show the reaction mechanisms for the **B^1**- and **B^9**-mediated hydrogenation of **MeQin** to produce **H_4-MeQin**. The relative Gibbs free energies (ΔG in kcal mol^{-1}) are given with respect to [**B^n** + 2 **MeQin** + **H_4-MeQin** + 2 H_2 + CO_2] (0.0 kcal mol^{-1}).

First, in the system using **B^1** as the catalyst (Figure 2.2), an FLP species comprising **B^1** and **MeQin** mediates the heterolytic cleavage of H_2 to form **[MeQin−H][H−B^1]** (*Step-1*: $\Delta G = -15.9$ kcal mol^{-1}) via **TS1** (+12.1 kcal mol^{-1}). Subsequently, the hydride in the [**H−B^1**]$^-$ unit migrates to the [**H−MeQin**]$^+$ counterpart, yielding ***p*-H_2-MeQin** with concomitant regeneration of **B^1** (*Step-2a*: $\Delta G = -5.7$ kcal mol^{-1}) via **TS2a** (+0.5 kcal mol^{-1}). Although the formation of 1,2-dihydroquinoline (***o*-H_2-MeQin**) via *Step-2b* has previously been proposed to be likely by Soós,[20] I found that *Step-2b* is kinetically less favorable by +7.1 kcal mol^{-1} than *Step-2a* under the present multicomponent conditions. An FLP species comprising **B^1** and **H_4-MeQin** then mediates the heterolysis of H_2 to form **[H_5-MeQin][H−B^1]** (*Step-3a*: $\Delta G = -11.8$ kcal mol^{-1}) via **TS3a** (+5.5 kcal mol^{-1}). As shown in Figure 2, the optimized structure of **TS3a** represents an association complex involving **B^1**, H_2, **H_4-MeQin**, and **MeQin**, and the cleavage of the H1–H2 bond cooperatively proceeds at the B and N1 atoms. In addition, the N1−H3 bond is oriented toward the N2 atom in **MeQin**, which enables facile proton transfer in the subsequent *Step-4* via **TS4** (−4.1 kcal mol^{-1}). The transfer hydrogenation of ***p*-H_2-MeQin** then occurs from **[MeQin−H][H−B^1]** via the subsequent H^+- (*Step-5*) and H^-- (*Step-6*) transfer processes via **TS5** (−11.7 kcal mol^{-1}) and **TS6** (−7.2 kcal mol^{-1}), respectively, wherein **[MeQin−H][H−B^1]** is formed through *Step-3a* and *Step-4*. I also found a possible path for the heterolysis of H_2 via the generation of an FLP species comprising the boron atom in **B^1** and the C=C bond in ***p*-H_2-MeQin** (*Step-3b*) via **TS3b** (+9.1 kcal mol^{-1}); however, in the **B^1** system, this path is unfavorable compared to *Step-3a*. Based on these results, both *Step-2a* and *Step-3a* are involved in the rate-determining events, and the total activation energy isthus $\Delta G^{\ddagger}$ = +21.4 kcal mol^{-1}.

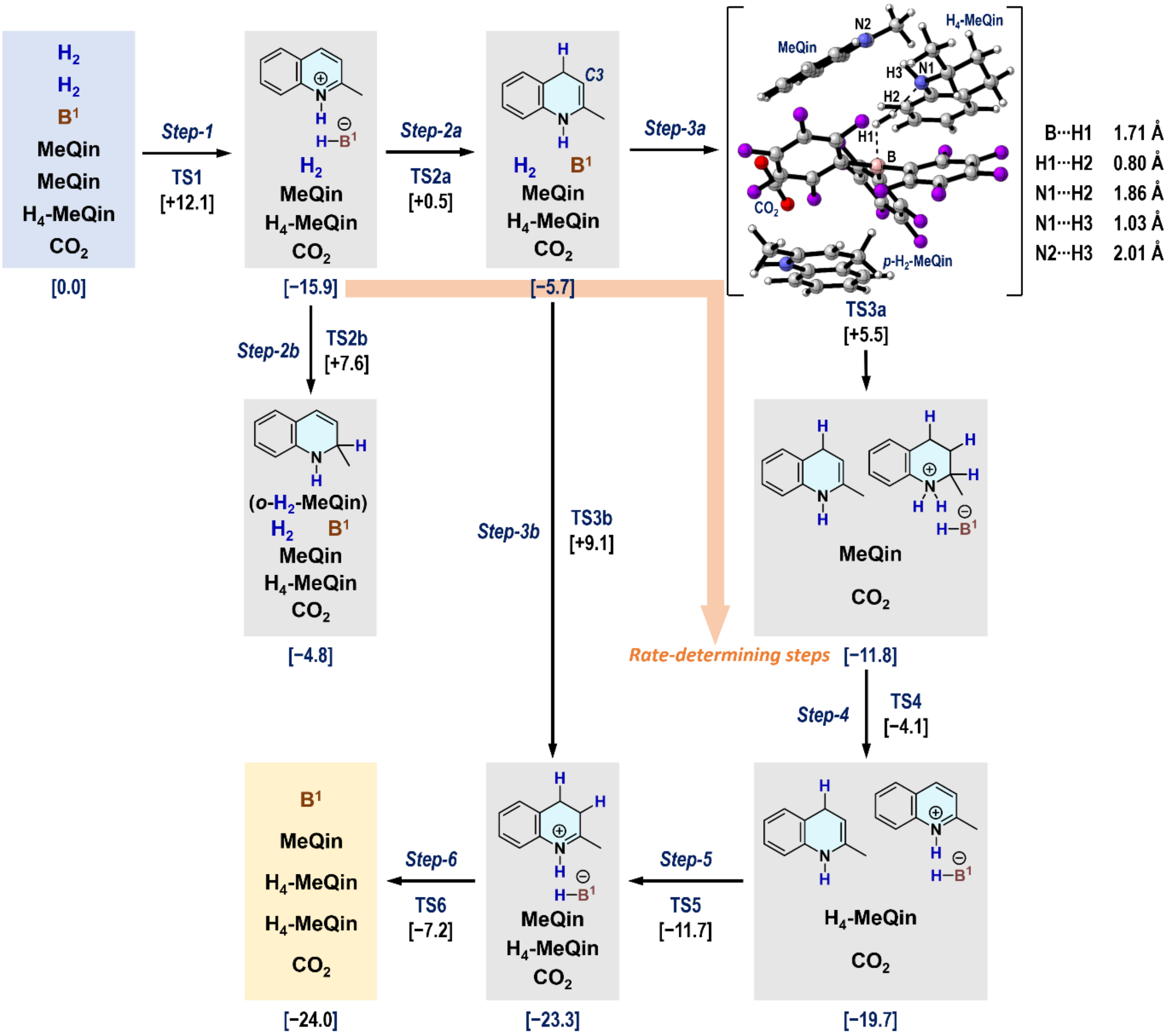

Figure 2.2. Calculated free-energy profiles for the hydrogenation of **MeQin** with $\mathbf{B^1}$ [kcal mol^{-1}: UωB97X-D/Def2-TZVP//UωB97X-D/Def2-SVP]. The endpoints of the IRC calculations were used in the plot, assuming that conformational changes within the same molecular structure are connected without an energy barrier. The input included $\mathbf{B^1}$, two molecules of **MeQin**, $\mathbf{H_4}$**-MeQin**, two molecules of H_2, and CO_2. An optimized gas-phase structure of **TS3a** and selected interatomic parameters are also given.

As in the case of $\mathbf{B^1}$, in the $\mathbf{B^9}$ system (Figure 2.3), **[MeQin−H][H−**$\mathbf{B^9}$**]** is initially formed through *Step-1′* ($\Delta G = -23.2$ kcal mol^{-1}) via **TS1′** (+1.5 kcal mol^{-1}), followed by subsequent hydride migration to provide ***p*-**$\mathbf{H_2}$**-MeQin** (*Step-2′*) via **TS2′** (0.0 kcal mol^{-1}). However, in contrast to the $\mathbf{B^1}$ system, the heterolysis of H_2 via an FLP species comprising $\mathbf{B^9}$ and the olefinic C3 atom in ***p*-**$\mathbf{H_2}$**-MeQin** (*Step-3b′*) via **TS3b′** (+1.4 kcal mol^{-1}) would be competitive with but slightly more favorable than the path including transfer hydrogenation from another molecule of **[MeQin−H][H−**$\mathbf{B^9}$**]** (*Step-3a′*) via **TS3a′** (+1.5 kcal mol^{-1}). The produced **[**$\mathbf{H_3}$**-MeQin][H−**$\mathbf{B^9}$**]** is converted into $\mathbf{H_4}$**-MeQin** via hydride migration with concomitant regeneration of $\mathbf{B^9}$ via *Step-6′*. Thus, the rate-determining events in the $\mathbf{B^9}$-catalyzed hydrogenation involve *Step-2′* and *Step-3b′* ($\Delta G^{\ddagger} = +24.6$ kcal mol^{-1}). These results are consistent with the results of previously reported kinetic experiments, i.e., **B**^{1} exhibited a higher rate than **B**^{9} when pure H_2 was used in the hydrogenation of **MeQin**.[9]

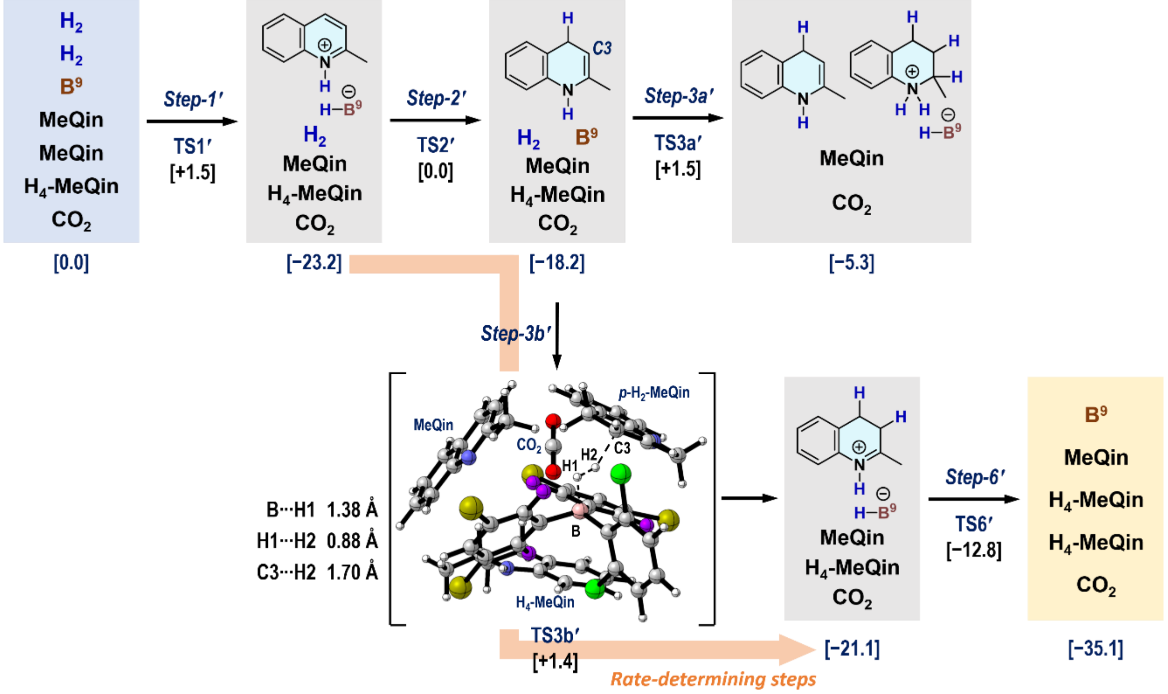

Figure 2.3. Free-energy profiles for the hydrogenation of **MeQin** with **B**^{9} [kcal mol^{-1}] calculated at the UωB97X-D/Def2-TZVP//UωB97X-D/Def2-SVP levels. The endpoints of the IRC calculations were used in the plot, assuming that conformational changes within the same molecular structure are connected without an energy barrier. The input included **B**^{9}, two molecules of **MeQin**, **H$_4$-MeQin**, two molecules of H_2, and CO_2. An optimized gas-phase structure of **TS3b′** and selected interatomic parameters are also given.

I then turned my attention to exploring the mechanisms of the CO_2-induced decomposition of **B**^{1} and **B**^{9}.[26] My previous preliminary studies demonstrated that the reaction between **MeQin** and **B**^{1} in the presence of H_2/CO_2 at 100 °C resulted in significant decomposition of **B**^{1} via an irreversible proto-deboronation yielding HC_6F_5; however, the corresponding proto-deboronation was not observed when **B**^{9} was used under otherwise identical conditions.[9] I also confirmed that the CO_2-triggered proto-deboronation can be expected to occur after the generation of **H$_4$-MeQin**. To clarify these details, AFIR calculations were carried out (Figure 2.4). It should be noted that two molecules of H_2 were included in the AFIR calculations of the **B**^{9} system (i.e. $n = 9$, $m = 2$); however, these H_2 molecules did not influence the results discussed below. The reactions start with the capture of CO_2 by the borane and **H$_4$-MeQin** to provide **[H$_4$-MeQin−CO$_2$−B$''$]** ($n = 1$ or 9; *Step-7* or *Step-7′*). Subsequent deprotonation by another molecule of **H$_4$-MeQin** gives **[H$_3$-MeQin−CO$_2$−B$''$][H$_5$-MeQin]** ($n = 1$ or 9; *Step-8* or *Step-8′*), which connects to the proto-deboronation path. This proto-deboronation takes place between the *N*−H$^+$ moiety in the ammonium cation unit and one of the *B*-aryl groups in **B$''$**, i.e., the C_6F_5 group in **B**^{1} (*Step-9*) or the 3,5-Br_2-2,6-F_2C_6H group in **B**^{9} (*Step-9′*). The CO_2-capture processes occur smoothly in a reversible manner for both **B**^{1} and **B**^{9} via **TS7** (+13.2 kcal mol^{-1}) and **TS7′** (+19.5 kcal mol^{-1}), respectively. These results also suggest that the CO_2-capture reactions occur with lower energy barriers compared to the **B^1**- and **B^9**-mediated hydrogenation processes ($\Delta G^{\ddagger}$ = +21.4 and +24.6 kcal mol^{-1}, respectively; Figures 2.2 and 2.3). However, the subsequent proton-transfer to form **[H$_3$-MeQin−CO$_2$−B^{n}][H$_5$-MeQin]** is substantially exothermic in the case of **B^1** (*Step-8*: ΔG = −9.1 kcal mol^{-1}) via **TS8** (+12.0 kcal mol^{-1}), and thus the backward CO$_2$-dissociation process can be expected to be limited due to the high energy barrier of $\Delta G_{\mathrm{rev}}^{\ddagger}$ = +22.3 kcal mol^{-1}. Although the energy barrier in the proto-deboronation step ($\Delta G_{\mathrm{decomp}}^{\ddagger}$ = +23.3 kcal mol^{-1} via **TS9**; Figure 2.4B) is slightly higher than $\Delta G_{\mathrm{rev}}^{\ddagger}$, both reactions would compete under the reaction conditions involving pressurized CO$_2$. In contrast, the corresponding CO$_2$-dissociation can proceed reversibly in the case of **B^9** even after the formation of **[H$_3$-MeQin−CO$_2$−B^9][H$_5$-MeQin]** ($\Delta G_{\mathrm{rev}}^{\ddagger}$ = +9.6 kcal mol^{-1}), enabling catalytically active **B^9** to be provided to the hydrogenation path, as the proto-deboronation from **[H$_3$-MeQin−CO$_2$−B^9][H$_5$-MeQin]** is kinetically unfavorable ($\Delta G_{\mathrm{decomp}}^{\ddagger}$ = +24.7 kcal mol^{-1}). These results can be rationalized by the combined electronic and steric effects of the *B*-aryl groups in **B^9**, i.e., the substitution of a C$_6$F$_5$ group in **B^1** with a less electrophilic but sterically more demanding 2,6-Cl$_2$C$_6$H$_3$ group effectively destabilizes **[H$_3$-MeQin−CO$_2$−B^9][H$_5$-MeQin]** and **TS9′** (Figure 2.4C).

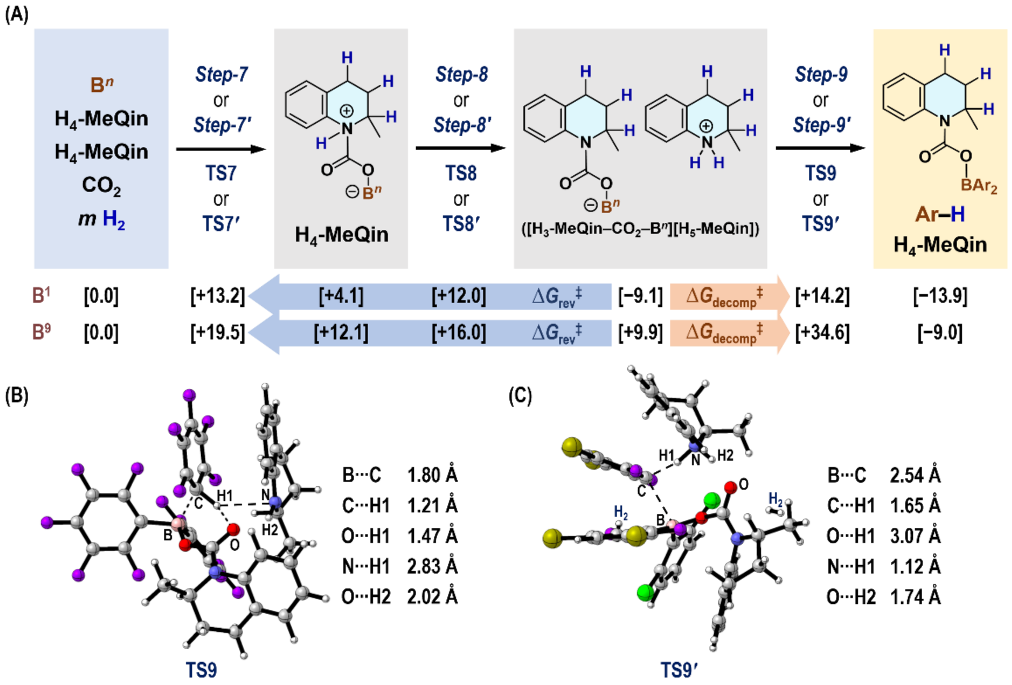

Figure 2.4. (A) Free-energy profiles for the decomposition of **B^{n}** [kcal mol^{-1}] calculated at the UωB97X-D/Def2-TZVP//UωB97X-D/Def2-SVP level. The endpoints of the IRC calculations were used in the plot, assuming that conformational changes within the same molecular structure are connected without an energy barrier. The input included **B^{n}**, two molecules of **H$_4$-MeQin**, *m* molecules of H$_2$ ($n = 1$, $m = 0$; $n = 9$, $m = 2$), and CO$_2$. Optimized gas-phase structures of (B) **TS9** and (C) **TS9′** and selected interatomic parameters are also given.

Once the critical paths of borane decomposition were clarified, I then explored more robust boranes exhibiting higher TONs in the co-presence of CO$_2$ with the support of AFIR. I calculated the total energy barriers ($\Delta G_{\mathrm{TS9}}^{\ddagger}$; defined in Figure 2.5) for the proto-deboronation with respect to [**B**^{n} + 2 **H$_4$-MeQin** + CO_2] for boranes **B**^{1}, **B**^{2}, **B**^{5}, **B**^{6}, **B**^{9},and **B**^{11}–**B**^{13} (Figure 2.5). Boranes exhibiting higher $\Delta G_{\mathrm{TS9}}^{\ddagger}$ values should show higher TONs. The results indicated that **B**^{12}, which has three *o*-Cl atoms, and **B**^{13}, which has five *o*-Cl atoms, would be expected to be robust catalysts, as their $\Delta G_{\mathrm{TS9}}^{\ddagger}$ values were calculated to be +42.1 and +48.9 kcal mol^{-1}, respectively. Next, I carried out the hydrogenation of **MeQin** with 0.05 mol% **B**^{n} at 100 °C under an H_2/CO_2 (25 atm each) atmosphere. To fully explore the robustness of the boranes, I repeatedly pressurized the system with H_2 to reach a total pressure of 50 atm once a day when a significant decrease in the total pressure was confirmed after the last 24 h. As shown in Figure 2.5, the TON values generally increased with increasing $\Delta G_{\mathrm{TS9}}^{\ddagger}$ values, and **B**^{12} exhibited a TON of 4,000 after a period of 11 days. However, despite **B**^{13} having the highest $\Delta G_{\mathrm{TS9}}^{\ddagger}$ value, its use resulted in a TON of only 69. This result can be rationalized in terms of the increased difficulty of the hydrogenation step via the cleavage of H_2 due to the significantly decreased Lewis acidity of **B**^{13}. In terms of turnover frequency (TOF), shelf-stable **B**^{9} was again confirmed to be a suitable catalyst, as it exhibited a higher TOF of 480 day^{-1} under solvent-free hydrogenation conditions using H_2/CO_2 compared to **B**^{12} (TOF = 364 day^{-1}). Nevertheless, the present results indicate that unprecedentedly active and robust triarylboranes can be designed based on the modification of **B**^{12} and **B**^{13}.

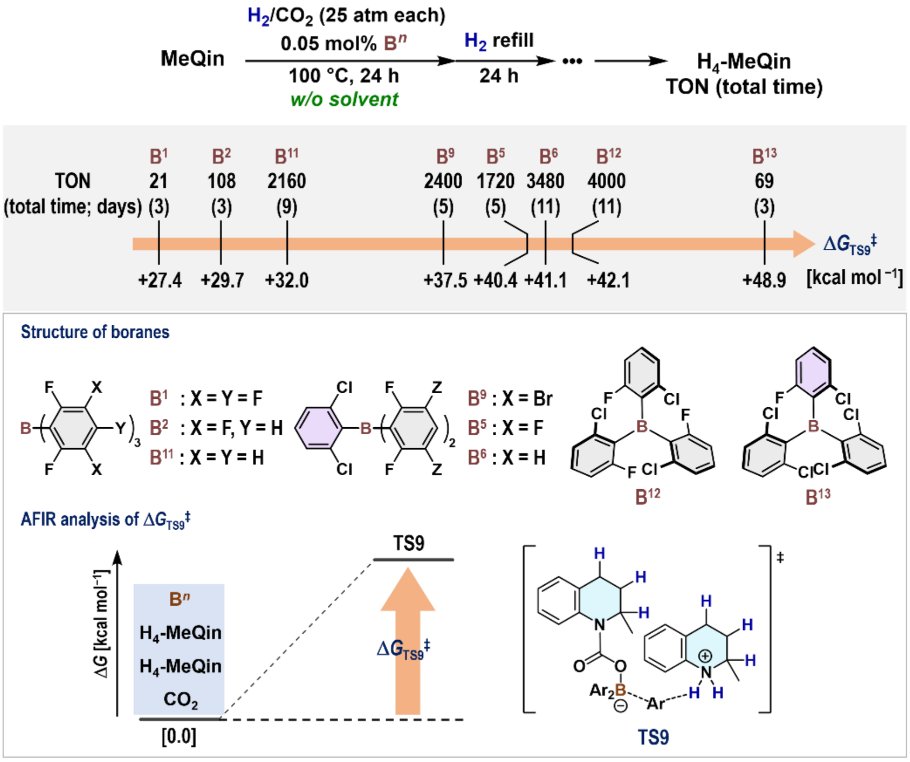

Figure 2.5. Evaluation of catalyst robustness based on turnover numbers (TONs). General conditions: all reactions were conducted in an autoclave (30 mL), wherein **MeQin** (50 mmol), the specified **B**^{n} catalyst (0.025 mmol, 0.05 mol%), and tetradecane as an internal standard were added, followed by pressurization with a gaseous mixture of H_2/CO_2 (25 atm each). Then, the reaction mixture was heated (100 ºC) for 24 h. If the total pressure significantly decreased within a period of 24 h, more H_2 was added to reach a total pressure of 50 atm. The product yield was determined by GC analysis. $\Delta G_{\mathrm{TS9}}^{\ddagger}$ values were calculated at the UωB97X-D/Def2-TZVP//UωB97X-D/Def2-SVP level.

2.4 Conclusions

In summary, I have elucidated the detailed mechanisms of the triarylborane-catalyzed hydrogenation of 2-methylquinoline (**MeQin**) in the presence of CO_2. To understand these multicomponent mechanisms, I employed the artificial force induced reaction (AFIR) method to analyze both the hydrogenation processes (involving seven molecules) and the CO_2-induced borane decomposition processes (involving four molecules). In the case of $B(C_6F_5)_3$ (**B^1**), the hydrogenation of **MeQin** predominantly proceeds via intermolecular transfer hydrogenation from **[MeQin−H][H−B^1]** to a 1,4-dihydroquinoline intermediate (***p*-H$_2$-MeQin**; shown in the left cycle in Figure 2.1B). However, **B^1** tends to decompose via a CO_2-capture reaction involving 2-methyl-1,2,3,4-tetrahydroquinoline (**H$_4$-MeQin**) followed by irreversible proto-deboronation. In contrast, in the case of $B(2,6\text{-}Cl_2C_6H_3)(3,5\text{-}Br_2\text{-}2,6\text{-}F_2C_6H)_2$ (**B^9**), the dissociation of CO_2 from the corresponding CO_2-capture species proceeds with a significantly lower energy barrier compared to the proto-deboronation step. Thus, **B^9** effectively catalyzes the hydrogenation of **MeQin** even in the presence of CO_2 without significant decomposition. Notably, the AFIR analysis suggested that the **B^9**-mediated hydrogenation primarily involves heterolytic H_2 cleavage by a frustrated Lewis pair (FLP) comprising **B^9** and the olefinic C3-carbon in ***p*-H$_2$-MeQin** (right cycle in Figure 2.1B). Given that these boron−olefin FLP species remain largely unexplored, the present mechanistic insights should facilitate the design of unprecedented hydrogenation reactions based on the use of triarylboranes and C=C bonds, expanding the potential of molecule-based H_2-purification technologies. Based on these AFIR results, I successfully achieved a catalyst turnover number of 4,000 in the main-group-catalyzed hydrogenation of **MeQin** using $B(2\text{-}Cl\text{-}6\text{-}F\text{-}C_6H_3)_3$ (**B^{12}**).

2.5 Supporting information

2.5.1. General considerations

Unless otherwise noted, all manipulations were conducted under a nitrogen atmosphere using standard Schlenk line or glovebox techniques. Analytical gas chromatography (GC) was carried out on a Shimadzu GC-2025 gas chromatograph, equipped with a flame ionization detector.

2.5.2. Materials

Commercially available reagents were purchased from Sigma Aldrich, Tokyo Chemical Industry (TCI) and FUJIFILM Wako Pure Chemical Corporation, and used as received. 2-Methylquinoline (**MeQin**), and tetradecane were purchased from TCI, and used after distillation over CaH_2. H_2 and H_2/CO_2 gas was purchased from Sumitomo Seika Chemicals Company, and used as received. Note that H_2 gas includes some impurities, as shown in Table 2.S1.

	Impurity				
	N_2	O_2	CO	CO_2	H_2
H_2	<200	<50	<1	<1	-

Table 2.S1. Impurities contaminated in H_2 (shown in ppm).

2.5.3. Evaluation of catalyst turnover numbers

General: A 30 mL autoclave was charged with **MeQin** (ca. 50 mmol) and **B^{n}** (ca. 0.025 mmol; 0.05 mol%). Tetradecane was added as an internal standard. Once sealed, the autoclave was pressurized with H_2/CO_2 (25 atm each) and heated at 100 °C. Through this experiment, I repeatedly pressurized H_2 to reach the total pressure of 50 atm at room temperature once a day, if the total pressure significantly decreased within the last 24 h. After I confirmed that the total pressure decrease became insignificant, I further heated the system for an additional 24 h. Then, the reaction was degassed at room temperature and the yield of **H$_4$-MeQin** was determined by GC analysis (Figure 5).

Using B^{1}: Followed by the general procedure, **MeQin** (7.18 g; 50.1 mmol), **B^{1}** (13.0 mg; 0.0254 mmol), and tetradecane (239 mg; 1.20 mmol) were employed, and the autoclave was heated for 3 days, giving **H$_4$-MeQin** in 1% GC yield and TON 21.

Using B^{2}: Followed by the general procedure, **MeQin** (7.20 g; 50.3 mmol), **B^{2}** (11.2 mg; 0.0245 mmol), and tetradecane (244 mg; 1.23 mmol) were employed, and the autoclave was heated for 3 days, giving **H$_4$-MeQin** in 3% GC yield and TON 108.

Using B^{5}: Followed by the general procedure, **MeQin** (7.15 g; 49.9 mmol), **B^{5}** (11.3 mg; 0.0248 mmol), and tetradecane (241 mg; 1.21 mmol) were employed, and the autoclave was heated for 5 days, giving **H$_4$-MeQin** in 43% GC yield and TON 1720.

Using B^{6}: Followed by the general procedure, **MeQin** (7.12 g; 49.7 mmol), **B^{6}** (9.4 mg; 0.025 mmol), and tetradecane (242 mg; 1.22 mmol) were employed, and the autoclave was heated for 11 days, giving **H$_4$-MeQin** in 87% GC yield and TON 3480.

Using B^{9}: Followed by the general procedure, **MeQin** (7.18 g; 50.1 mmol), **B^{9}** (17.4 mg; 0.0249 mmol), and tetradecane (243 mg; 1.22 mmol) were employed, and the autoclave was heated for 5 days, giving **H$_4$-MeQin** in 60% GC yield and TON 2400.

Using B^{11}: Followed by the general procedure, **MeQin** (7.16 g; 50.0 mmol), **B^{11}** (8.7 mg; 0.025 mmol), and tetradecane (240 mg; 1.21 mmol) were employed, and the autoclave was heated for 9 days, giving **H$_4$-MeQin** in 54% GC yield and TON 2160.

Using B^{12}: Followed by the general procedure, **MeQin** (7.16 g; 50.0 mmol), **B^{12}** (10.1 mg; 0.0253 mmol), and tetradecane (244 mg; 1.23 mmol) were employed, and the autoclave was heated for 11 days, giving **H$_4$-MeQin** in >99% GC yield and TON 4000.

Using B^{13}: Followed by the general procedure, **MeQin** (7.16 g; 50.0 mmol), **B^{13}** (10.7 mg; 0.0247 mmol), and tetradecane (243 mg; 1.22 mmol) were employed, and the autoclave was heated for 3 days, giving **H_4-MeQin** in 2% GC yield and TON 69.

2.5.4. Theoretical studies

2.5.4.1. The hydrogenation of MeQin with B^1

The reaction path network for the hydrogenation of **MeQin** with **B^1**, which includes the estimated products and each reaction mechanism with the energy barrier, is shown in Figure 2.S1. Circles show each group of molecular structures based on their bonding patterns.

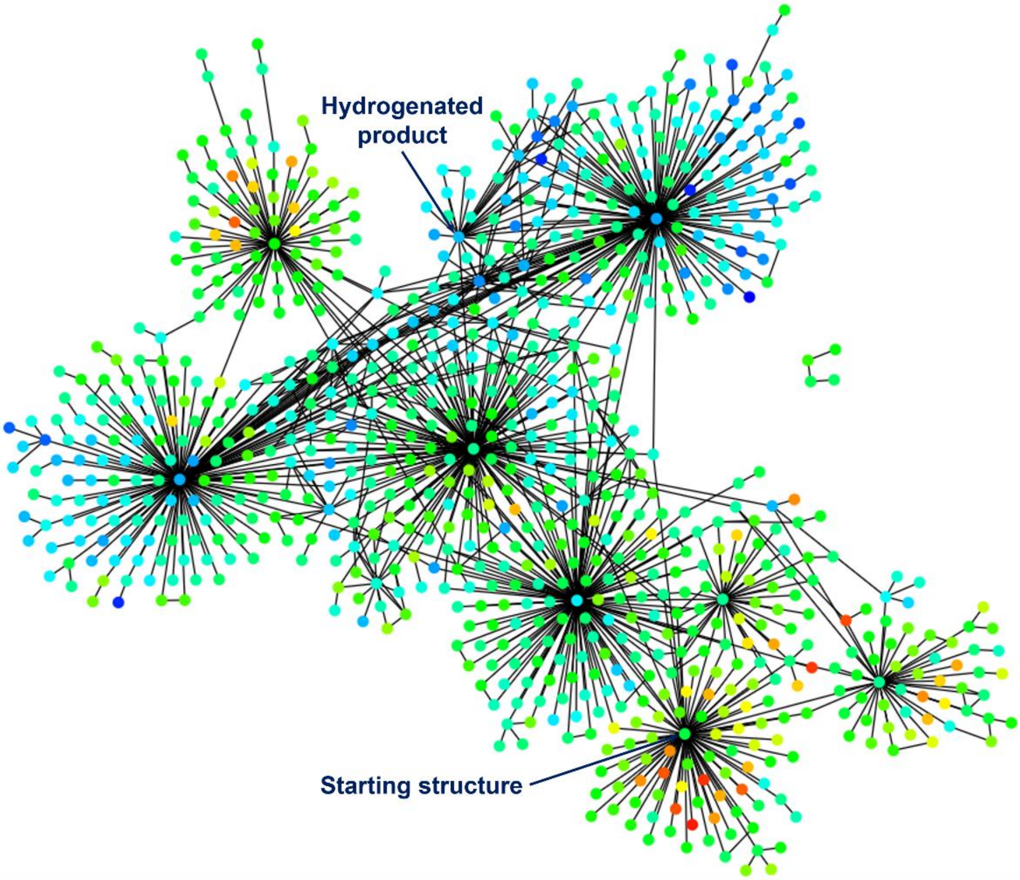

Figure 2.S1. The reaction path network for the hydrogenation of **MeQin** with **B^1**.

In particular, for the geometries listed in Table 2.S2, the NoBondRearrange option was applied to explore the subsequent reaction paths.

Table 2.S2. Selected geometries applied to explore the subsequent reaction paths.

H_2 H_2 B^1 MeQin MeQin H_4-MeQin CO_2	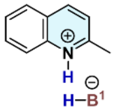 H_2 MeQin H_4-MeQin CO_2	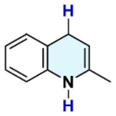 H_2 B^1 MeQin H_4-MeQin CO_2	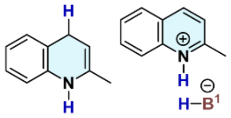 H_4-MeQin CO_2
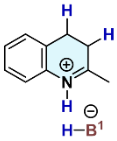 MeQin H_4-MeQin CO_2	B^1 MeQin H_4-MeQin H_4-MeQin CO_2	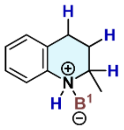 H_2 H_2 MeQin MeQin CO_2	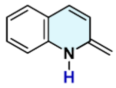 H_2 B^1 *o*-H_2-MeQin H_4-MeQin CO_2

Plausible mechanisms for the hydrogenation of **MeQin** with $\mathbf{B^1}$ are shown in Figure 2.2. The molecular structures of related compounds are summarized in Table 2.S3.

Table 2.S3. DFT-optimized structures in Figure 2.2.

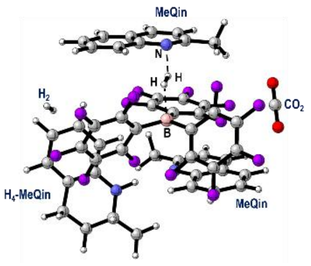 **TS1**	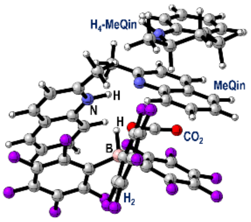 **Products of *Step-1***	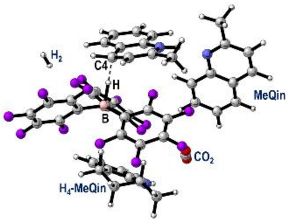 **TS2a**
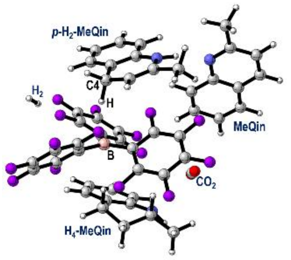 **Products of *Step-2a***	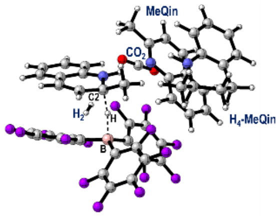 **TS2b**	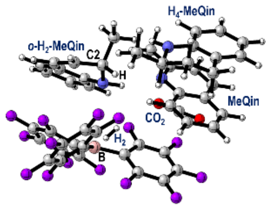 **Products of *Step-2b***

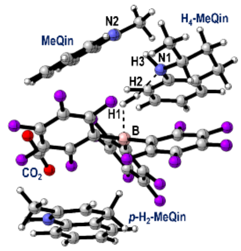

TS3a

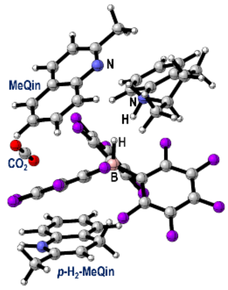

Products of *Step-3a*

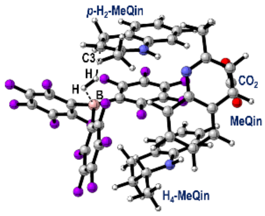

TS3b

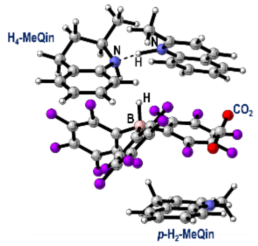

TS4

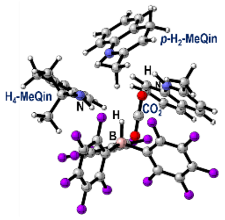

Products of *Step-4*

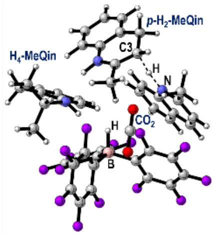

TS5

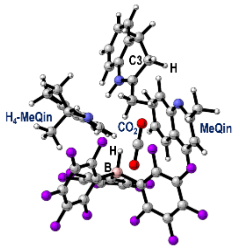

Products of *Step-5*

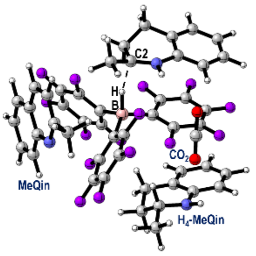

TS6

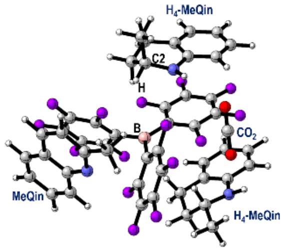

Products of *Step-6*

2.5.4.2. The hydrogenation of MeQin with B^9

The reaction path network for the hydrogenation of **MeQin** with **B^9**, which includes the estimated products and each reaction mechanism with the energy barrier, is shown in Figure 2.S2. Circles show each group of molecular structures based on their bonding patterns.

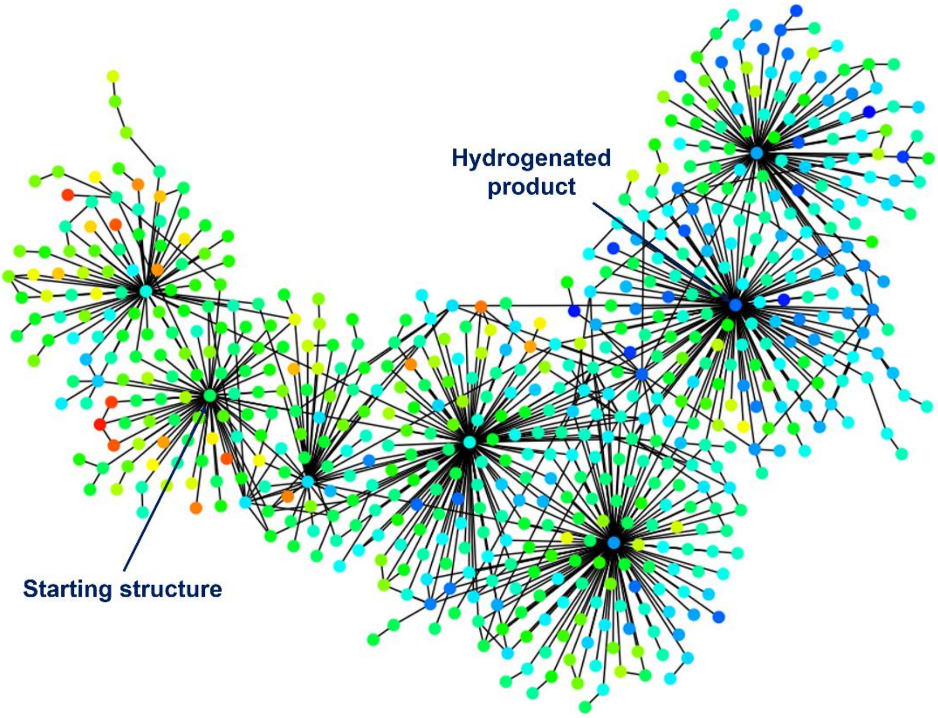

Figure 2.S2. The reaction path network for the hydrogenation of **MeQin** with **B^9**.

In particular, for the geometries listed in Table 2.S4, the NoBondRearrange option was applied to explore the subsequent reaction paths.

Table 2.S4. Selected geometries applied to explore the subsequent reaction paths.

H_2 H_2 B^9 **MeQin** **MeQin** **H_4-MeQin** CO_2	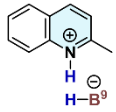 H_2 **MeQin** **H_4-MeQin** CO_2	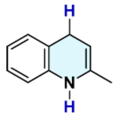 H_2 B^9 **MeQin** **H_4-MeQin** CO_2	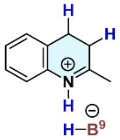 **MeQin** **H_4-MeQin** CO_2
B^9 **MeQin** **H_4-MeQin** **H_4-MeQin** CO_2	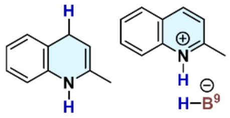 **H_4-MeQin** CO_2		

Plausible mechanisms for the hydrogenation of **MeQin** with **B^9** are shown in Figure 2.3. The molecular structures of related compounds are summarized in Table 2.S5.

Table 2.S5. DFT-optimized structures in Figure 2.3.

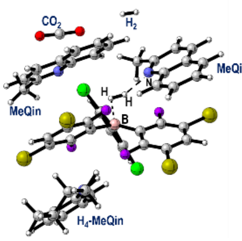 **TS1′**	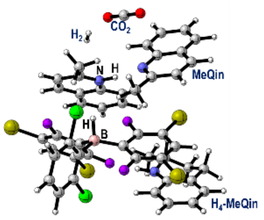 **Products of *Step-1′***	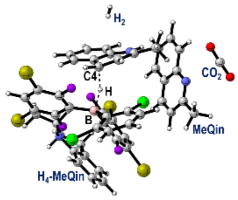 **TS2′**
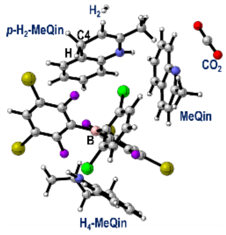 **Products of *Step-2′***	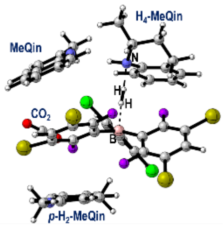 **TS3a′**	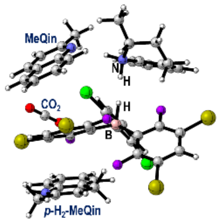 **Products of *Step-3a′***
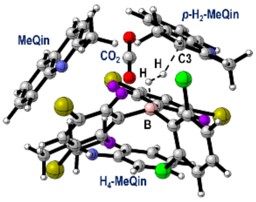 **TS3b′**	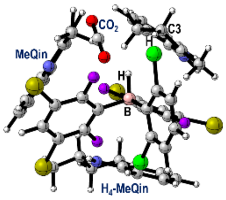 **Products of *Step-3b′***	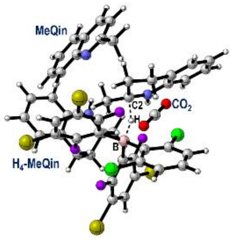 **TS6′**
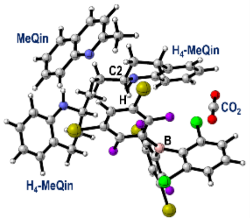 **Products of *Step-6′***		

2.5.4.3. The CO$_2$-induced decomposition of B^1

The reaction path network for the CO$_2$-induced decomposition of **B^1**, which includes the estimated products and each reaction mechanism with the energy barrier, is shown in Figure 2.S3. Circles show each group of molecular structures based on their bonding patterns.

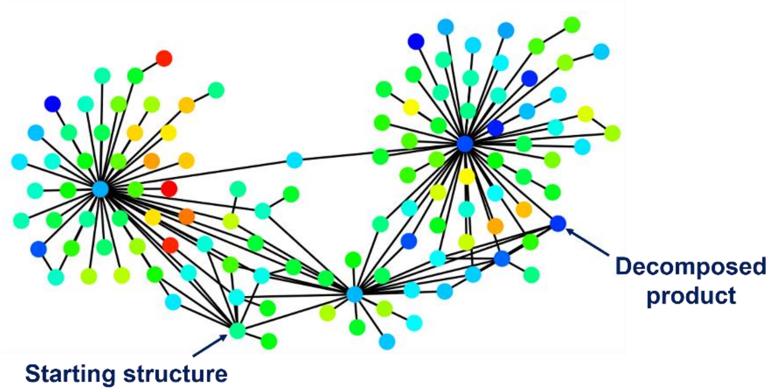

Figure 2.S3. The reaction path network for the CO_2-induced decomposition of $\mathbf{B^1}$.

In particular, for the geometries listed in Table 2.S6, the NoBondRearrange option was applied to explore the subsequent reaction paths.

Table 2.S6. Selected geometries applied to explore the subsequent reaction paths.

B^1 H_4-MeQin H_4-MeQin CO_2	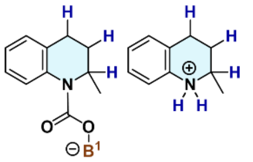	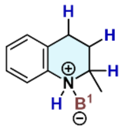 H_4-MeQin CO_2

Plausible mechanisms for the CO_2-induced decomposition of $\mathbf{B^1}$ are shown in Figure 2.4. The molecular structures of related compounds are summarized in Table 2.S7.

Table 2.S7. DFT-optimized structures in Figure 2.4 ($\mathbf{B^1}$).

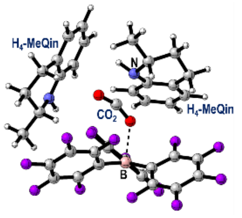 **TS7**	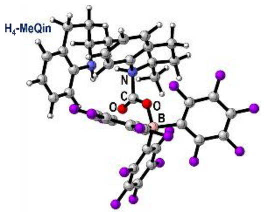 **Products of *Step-7***	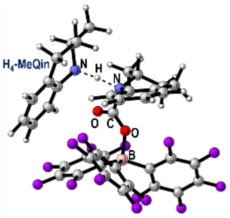 **TS8**
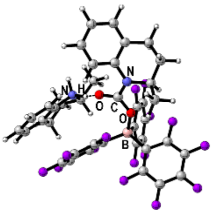 **Products of *Step-8***	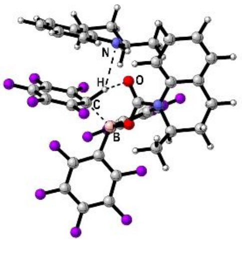 **TS9**	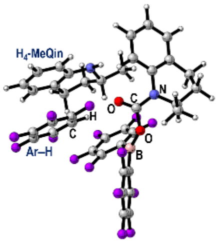 **Products of *Step-9***

2.5.4.4. The CO_2-induced decomposition of **B^9**

The reaction path network for the CO_2-induced decomposition of **B^9**, which includes the estimated products and each reaction mechanism with the energy barrier, is shown in Figure 2.S4. Circles show each group of molecular structures based on their bonding patterns.

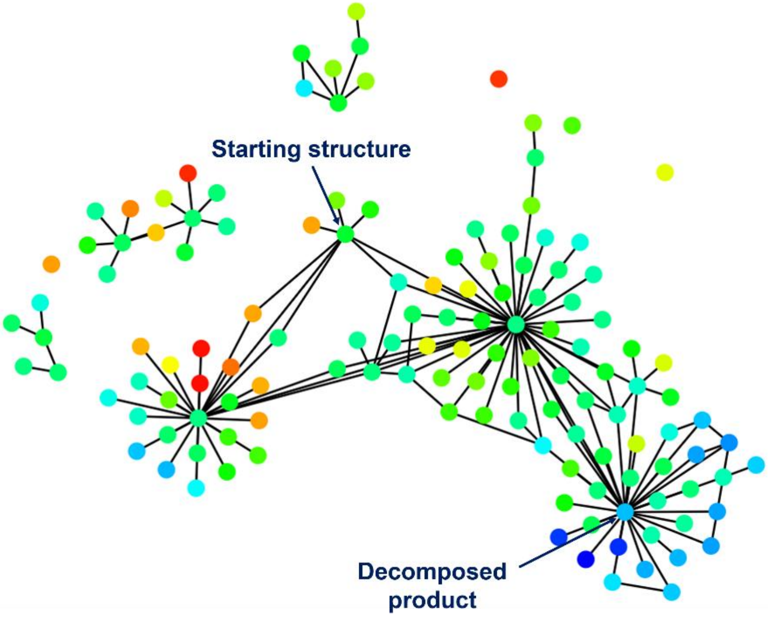

Figure 2.S4. The reaction path network for the CO_2-induced decomposition of **B^9**.

In particular, for the geometries listed in Table 2.S8, the NoBondRearrange option was applied to explore the subsequent reaction paths.

Table 2.S8. Selected geometries applied to explore the subsequent reaction paths.

B^9 H_4-MeQin H_4-MeQin CO_2 H_2 H_2	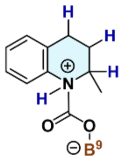 H_4-MeQin H_2 H_2	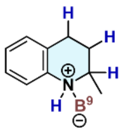 H_4-MeQin CO_2 H_2 H_2	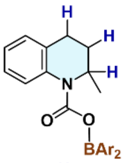 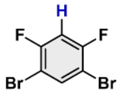 H_4-MeQin H_2 H_2

Plausible mechanisms for the CO_2-induced decomposition of **B^9** are shown in Figure 2.4. The molecular structures of related compounds are summarized in Table 2.S9.

Table 2.S9. DFT-optimized structures in Figure 2.4 (**B^9**).

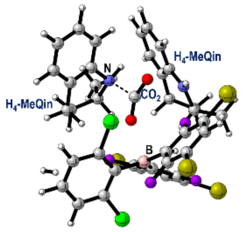 **TS7′**	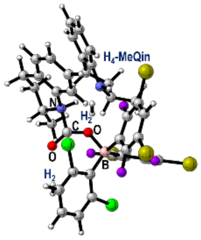 **Products of *Step-7′***	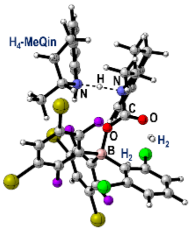 **TS8′**
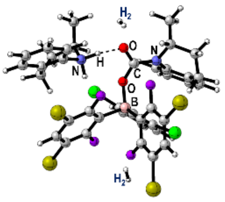 **Products of *Step-8′***	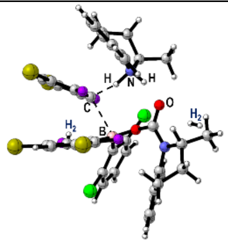 **TS9′**	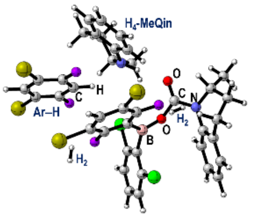 **Products of *Step-9′***

2.5.4.5. Evaluation of B″ catalyst robustness (n = 1, 2, 5, 6, 9, and 11–13)

The total energy barriers ($\Delta G_{\mathrm{TS9}}{}^{\ddagger}$, defined in Figure 2.5) for the proto-deboronation with respect to [**B″** + 2 **H$_4$-MeQin** + CO_2] for boranes **B^1**, **B^2**, **B^5**, **B^6**, **B^9**, and **B^{11}**–**B^{13}** are shown in Figure 2.5. The molecular structures of **TS9** for each borane are summarized in Table 2.S10.

Table 2.S10. DFT-optimized structures in Figure 2.5.

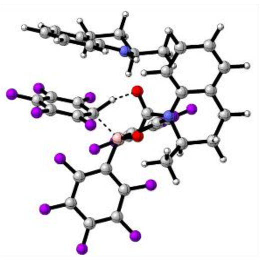 **TS9(B^1)**	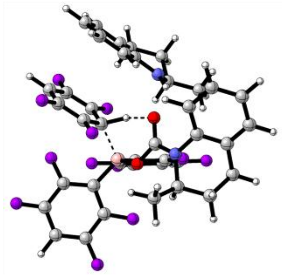 **TS9(B^2)**	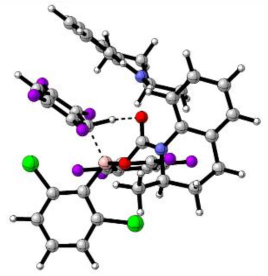 **TS9(B^5)**
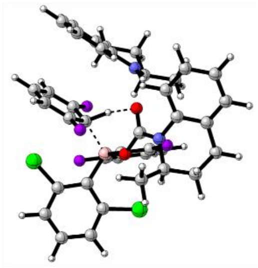 **TS9(B^6)**	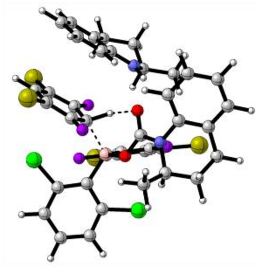 **TS9(B^9)**	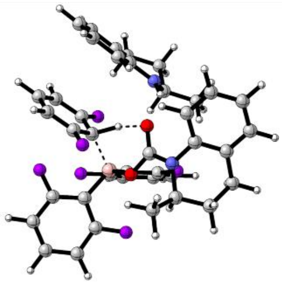 **TS9(B^{11})**

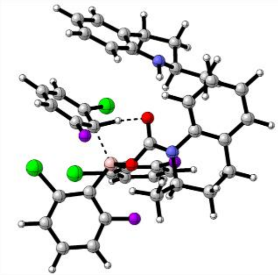 **TS9(B^{12})**	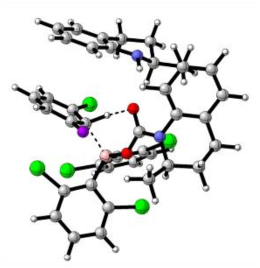 **TS9(B^{13})**	

2.6 References and notes

1. Dawood, F.; Anda, M.; Shafiullah, G. M. *Int. J. Hydrogen Energy* **2020**, *45*, 3847.
2. Voldsund, M.; Jordal, K.; Anantharaman, R. *Int. J. Hydrogen Energy* **2016**, *1*, 1.
3. Holladay, J. D.; Hu, J.; King, D. L.; Wang, Y. *Catal. Today* **2009**, *139*, 244.
4. Gunathilake, C.; Soliman, I.; Panthi, D.; Tandler, P.; Fatani, O.; Ghulamullah, N. A.; Marasinghe, D.; Farhath, M.; Madhujith, T.; Conrad, K.; Du, Y.; Jaroniec, M. *Chem. Soc. Rev.* **2024**, DOI: 10.1039/d3cs00731f.
5. Welch, G. C.; San Juan, R. R.; Masuda, J. D.; Stephan, D. W. *Science* **2006**, *314*, 1124.
6. Stephan, D. W.; Erker, G. *Angew. Chem., Int. Ed.* **2015**, *54*, 6400.
7. Jupp, A. R.; Stephan, D. W. *Trends Chem.* **2019**, *1*, 35.
8. Stephan, D. W. *J. Am. Chem. Soc.* **2021**, *143*, 20002.
9. Hashimoto, T.; Asada, T.; Ogoshi, S.; Hoshimoto, Y. *Sci. Adv.* **2022**, *8*, eade0189.
10. Morishita, T., Hisata, Y., Hashimoto, T., Ogoshi, S., Hoshimoto, Y. *J. Synth. Org. Chem., Jpn.* **2024**, *82*, 1097.
11. Jorschick, H.; Preuster, P.; Bösmann, A.; Wasserscheid, P. *Sustain. Energy Fuels* **2021**, *5*, 1311.
12. Li, S.; Lin, L.; Wang, Z.; Ma, D. *Innovation* **2023**, *4*, 100353.
13. Król, A.; Gajec, M.; Holewa-Rataj, J.; Kukulska-Zając, E.; Rataj, M. *Energies* **2024**, *17*, 3794.
14. Munyentwali, A.; Tan, K. C.; He, T. *Prog. Nat. Sci. Mater. Int.* **2024**, DOI: 10.1016/j.pnsc.2024.07.021.
15. International Energy Agency, *Global Hydrogen Review 2023*, **2023**. https://www.iea.org/reports/global-hydrogen-review-2023.
16. Erös, G.; Nagy, K.; Mehdi, H.; Pápai, I.; Nagy, P.; Király, P.; Tárkányi, G.; Soós, T. *Chem.-Eur. J.* **2012**, *18*, 574.
17. Maeda, S.; Harabuchi, Y.; Takagi, M.; Taketsugu, T.; Morokuma, K. *Chem. Rec.* **2016**, *16*, 2232.
18. Maeda, S.; Harabuchi, Y.; Takagi, M.; Saita, K.; Suzuki, K.; Ichino, T.; Sumiya, Y.; Sugiyama, K.; Ono, Y. *J. Comput. Chem.* **2018**, *39*, 233.
19. Maeda, S.; Harabuchi, Y. *Wiley Interdiscip. Rev. Comput. Mol. Sci.* **2021**, *11*, 1.
20. Mahdi, T.; Heiden, Z. M.; Grimme, S.; Stephan, D. W. *J. Am. Chem. Soc.* **2012**, *134*, 4088.
21. Xu, Y.; Yang, Y.; Liu, Y.; Li, Z. H.; Wang, H. *Nat. Catal.* **2023**, *6*, 16.
22. Maeda, S.; Harabuchi, Y.; Sumiya, Y.; Takagi, M.; Suzuki, K.; Sugiyama, K.; Ono, Y.; Hatanaka, M.; Osada, Y.; Taketsugu, T.; Morokuma, K.; Ohno, K. GRRM23.

23. Gaussian 16, Revision C.01, Frisch, M. J.; Trucks, G. W.; Schlegel, H. B.; Scuseria, G. E.; Robb, M. A.; Cheeseman, J. R.; Scalmani, G.; Barone, V.; Petersson, G. A.; Nakatsuji, H.; Li, X.; Caricato, M.; Marenich, A. V.; Bloino, J.; Janesko, B. G.; Gomperts, R.; Mennucci, B.; Hratchian, H. P.; Ortiz, J. V.; Izmaylov, A. F.; Sonnenberg, J. L.; Williams-Young, D.; Ding, F.; Lipparini, F.; Egidi, F.; Goings, J.; Peng, B.; Petrone, A.; Henderson, T.; Ranasinghe, D.: Zakrzewski, V. G.; Gao, J.; Rega, N.; Zheng, G.; Liang, W.; Hada, M.; Ehara, M.; Toyota, K.; Fukuda, R.; Hasegawa, J.; Ishida, M.; Nakajima, T.; Honda, Y.; Kitao, O.; Nakai, H.; Vreven, T.; Throssell, K.; Montgomery Jr., J. A.; Peralta, J. E.; Ogliaro, F.; Bearpark, M. J.; Heyd, J. J.; Brothers, E. N.; Kudin, K. N.; Staroverov, V. N.; Keith, T. A.; Kobayashi, R.; Normand, J.; Raghavachari, K.; Rendell, A. P.; Burant, J. C.; Iyengar, S. S.; Tomasi, J.; Cossi, M.; Millam, J. M.; Klene, M.; Adamo, C.; Cammi, R.; Ochterski, J. W.; Martin, R. L.; Morokuma, K.; Farkas, O.; Foresman, J. B.; Fox, D. J. Gaussian, Inc., Wallingford CT, 2019.
24. Choi, C.; Elber, R. *J. Chem. Phys.* **1991**, *94*, 751.
25. Ayala, P. Y.; Schlegel, H. B. *J. Chem. Phys.* **1997**, *107*, 375.
26. Mömming, C. M.; Otten, E.; Kehr, G.; Fröhlich, R.; Grimme, S.; Stephan, D. W.; Erker, G. *Angew. Chem. Int. Ed.* **2009**, *48*, 6643.

Chapter 3

Boosting Turnover in the Triarylborane-Catalyzed Hydrogenation of *N*-Substituted Indoles via Olefin-to-Nitrogen Lewis-Base Switching in H_2-Cleavage Steps

Abstract: The shelf-stable heteroleptic borane $B(2,6\text{-}Cl_2C_6H_3)(3,5\text{-}Br_2\text{-}2,6\text{-}F_2C_6H)_2$ (**B**$^{\mathbf{9}}$) efficiently catalyzes the solvent-free hydrogenation of various substituted indoles to indolines with an unprecedented turnover number of 8,500, which is more than 400-fold higher than that reported for $B(C_6F_5)_3$ (**B**$^{\mathbf{1}}$) under diluted conditions. Mechanistic studies revealed that this hydrogenation proceeds via an olefin-to-nitrogen switching of Lewis bases involved in the H_2-cleavage steps: initially, H_2 cleavage is mediated by a frustrated Lewis pair (FLP) comprising the indole C3-carbon and boron atoms, which then switches to an FLP system comprising the indoline nitrogen and boron atoms after formation of the indoline. This study demonstrates the potential of relatively benign main-group elements for the catalytic synthesis of valuable *N*-containing molecules using H_2.

3.1 Introduction

The construction of 2,3-dihydroindole moieties, also called indolines, has attracted much attention in the pharmaceutical field owing to their unique structural features and biological properties. The indoline scaffold, which comprises a benzene ring fused with a pyrrolidine ring, offers key advantages in drug design; in particular, its noncoplanar structure enhances water solubility, and its benzene ring engages in hydrophobic interactions with protein residues. By virtue of these characteristics, indoline derivatives have found therapeutic applications, e.g., as anticancer, antitumor, and antihypertension agents (Figure 3.1).[1,2] For the synthesis of indolines, the catalytic hydrogenation of indole derivatives stands out as an atom-economical approach that avoids the generation of stoichiometric waste associated with conventional reducing agents such as $NaBH_3CN$.[3,4] Various transition-metal catalysts have been developed for the hydrogenation of indoles, which achieve turnover numbers (TONs) in the hundreds.[1,5–8] The use of triarylborane catalysts represents an attractive alternative to conventional methods using stoichiometric reductants or transition-metal catalysts because the time- and cost-intensive removal of byproducts such as excess salts or potentially toxic metal residues is avoided. Therefore, considering the extensive progress in the triarylborane-catalyzed hydrogenation of unsaturated compounds,[9–11] the triarylborane-catalyzed hydrogenation of indoles via heterolytic cleavage of H_2 mediated by frustrated Lewis pairs (FLPs) can be considered as a promising strategy for the synthesis of indolines. However, the triarylborane-catalyzed hydrogenation of indole derivatives remains largely unexplored, mainly because the indoline products may cause catalyst deactivation under conventional conditions.

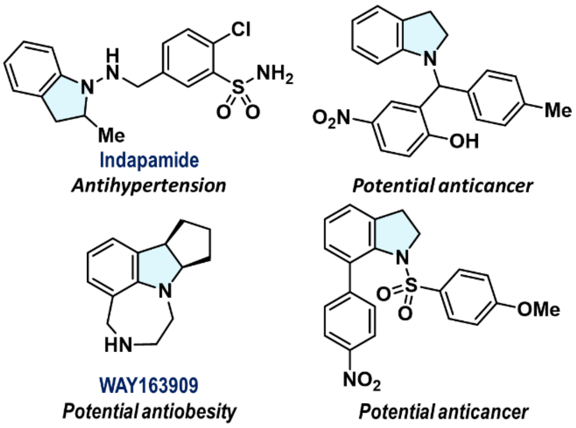

Figure 3.1. Selected examples of *N*-substituted indoline derivatives.

In 2011, Stephan and co-workers reported the $B(C_6F_5)_3$ (**B**^{1})-catalyzed hydrogenation of 1-methylindole (**1a**) and its derivatives in toluene using H_2 (103 atm) at 80 °C;[12] however, in 2016, Paradies and co-workers pointed out difficulties in reproducing the reported result. Instead, they demonstrated that the microwave-assisted hydrogenation of **1a** catalyzed by **B**^{1} in toluene under H_2 (4 atm) at 140 °C yielded a TON of 11 (left in Figure 3.2A).[13] Recently, Niu, Lang, Ma and co-workers reported the catalytic hydrogenation of *N*-methyl indole derivatives in toluene using a Zr-based metal-organic framework (MOF; NU-1000-FLP-H_2) containing an $[(\text{aryl})_3P\text{–}H][H\text{–}$**B**$^1]$ unit, achieving a TON of 18 (right in Figure 3.2A).[14] However, the catalytic performance of such **B**^{1}-based systems is substantially lower than that of transition-metal catalysts. Moreover, the air- and moisture-sensitivity of **B**^{1} presents considerable practical challenges. Given these limitations, I aimed to develop an efficient, robust, and practical triarylborane catalyst for the hydrogenation of indoles to valuable indolines (notably, the price of 1-methylindoline (**2a**) is 85 times higher than that of **1a**).[15]

Herein, I report the solvent-free hydrogenation of various substituted indoles catalyzed by shelf-stable $B(2,6\text{-}Cl_2C_6H_3)(3,5\text{-}Br_2\text{-}2,6\text{-}F_2C_6H)_2$ (**B**^{9}) under a H_2 atmosphere (Figure 3.2B). Remarkably, **B**^{9} achieves a TON of 8,500 in the hydrogenation of **1a**. The key to effectively enhancing the TON is the use of triarylboranes that resist irreversible proto-deboronation in the presence of both indolines and H_2. Mechanistic studies revealed that the present hydrogenation involves an olefin-to-nitrogen switching of the Lewis bases during the formation of FLP species with boranes (Figure 3.2C).

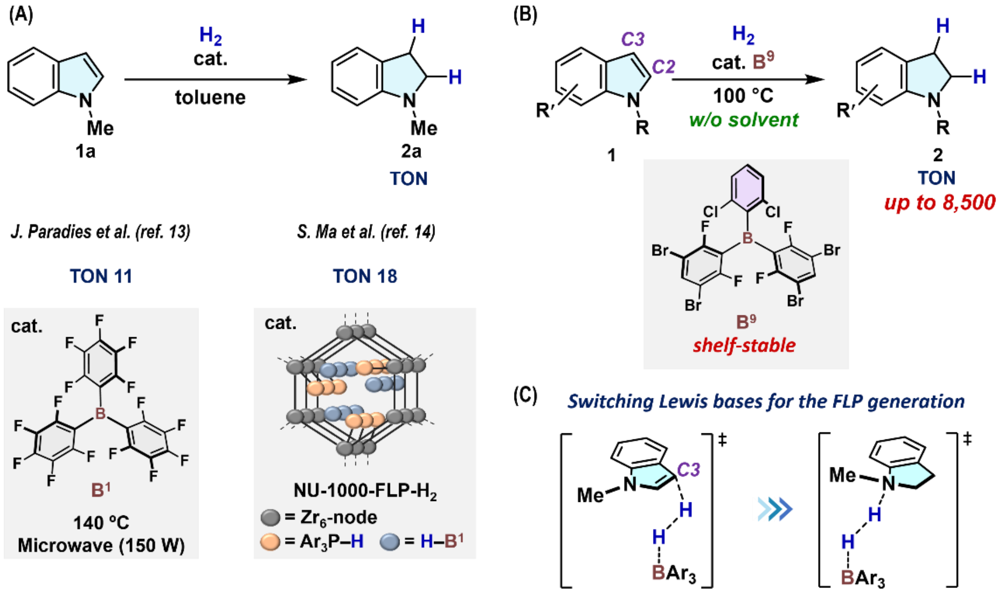

Figure 3.2. (A) Catalytic hydrogenation of 1-methylindole (**1a**) to give 1-methylindoline (**2a**); **B**^{1} catalyst under microwave condition (ref. 13); NU-1000-FLP-H_2 catalyst (ref 14). (B) **B**^{9}-catalyzed hydrogenation of *N*-substituted indoles under solvent-free conditions (*this work*). (C) Key olefin-to-nitrogen Lewis-base switching in FLP-mediated H_2-cleavage steps.

3.2 Results and discussion

I began my investigation by examining the reasons behind the lack of examples of the **B**^{1}-catalyzed hydrogenation of indoles, which contrasts with the successful application of **B**^{1} in the hydrogenation of various *N*-containing unsaturated molecules such as imines, quinolines, and pyridines via FLPs containing N and B atoms.[9,10] Indeed, **2a** was formed in only 2% yield (TON = 2) when conducting the hydrogenation of **1a** using 1 mol% **B**^{1} under solvent-free conditions at 100 °C (Eq. 1 in Figure 3.3A). Resconi and co-workers reported that the reaction between **1a** and **B**^{1} in CH_2Cl_2 at room temperature for more than 4 days led to the isolation of a **(*C2*-1a)·B**^{1} adduct.[16] It was proposed that this adduct stems from the C3-to-C2 migration of the **B**^{1} unit from the initially formed **(*C3*-1a)·B**^{1}, albeit that experimental evidence that would support the generation of the latter C3-adduct was not presented. To investigate whether these adducts are related to the deactivation of **B**^{1}, I attempted the isolation of **(*C3*-1a)·B**^{1}. Eventually, a single crystal of **(*C3*-1a)·B**^{1} was obtained by slow diffusion of *n*-hexane into a toluene solution of **1a** and **B**^{1} at −35 °C, enabling its structural characterization by single-crystal X-ray diffraction analysis, although the isolated yield could not be determined. As shown in Figure 3.3B, the formation of the C3–B bond was unambiguously confirmed. I subsequently optimized the gas-phase structure of **(*C3*-1a)·B**^{1} (+6.0 kcal mol^{-1}) theoretically at the M06-2X/Def2-TZVP//M06-2X/Def2-SVP level. The relative Gibbs energies (ΔG) in Figure 3.3C are given with respect to [**1a** + **B**^{1}] (0.0 kcal mol^{-1}). Moreover, I optimized the structure of **(*C2*-1a)·B**^{1} (+2.7 kcal mol^{-1}). These results indicate that the formation of **(*C2*-1a)·B**^{1} and **(*C3*-1a)·B**^{1} is endothermic, suggesting that these adducts are unlikely to affect the catalytic activity of **B**^{1}. Importantly, I found that the association complex **[(*C3*-1a)···B**^{1}**]** (+2.7 kcal mol^{-1}), which involves a pair of separated but preorganized boron 2p and olefinic π orbitals, was generated (Figure 3.S7). Thus, **[(*C3*-1a)···B¹]** can act as an olefin–borane FLP species for the mediation of the heterolytic cleavage of H_2, although such species have so far remained elusive.[17,18] In fact, a path leading to **[(*C3*-1a)–H][H–B¹]** (+20.5 kcal mol^{-1}) from H_2 and **[(*C3*-1a)···B¹]** via **TS10$_{(C3\text{-}B1)}$** (+27.7 kcal mol^{-1}) was more favorable than a path for the cleavage of H_2 with a nitrogen–borane FLP via **TS10$_{(N\text{-}B1)}$** (+31.3 kcal mol^{-1}). Then, I turned my attention to exploring the potential role of **2a** in the decomposition of **B¹** (Eq. 2 in Figure 3.3A). Heating a mixture of **2a** and **B¹** in the presence of H_2 (14 atm) at 100 °C in C_6D_6 resulted in the generation of HC_6F_5 in 83% yield via the irreversible proto-deboronation from a four-coordinated boron species including the **B¹** unit, with concomitant formation of **[2a–H][H–B¹]**. Given that the generation of HC_6F_5 was negligible in the absence of H_2 under identical conditions, the thermolysis of **[2a–H][H–B¹]** is most likely responsible for the proto-deboronation yielding HC_6F_5. These results indicate that an effective borane catalyst must facilitate the proton/hydride transfer from **[2a–H][H–B¹]** to another indole molecule before the irreversible proto-deboronation occurs.

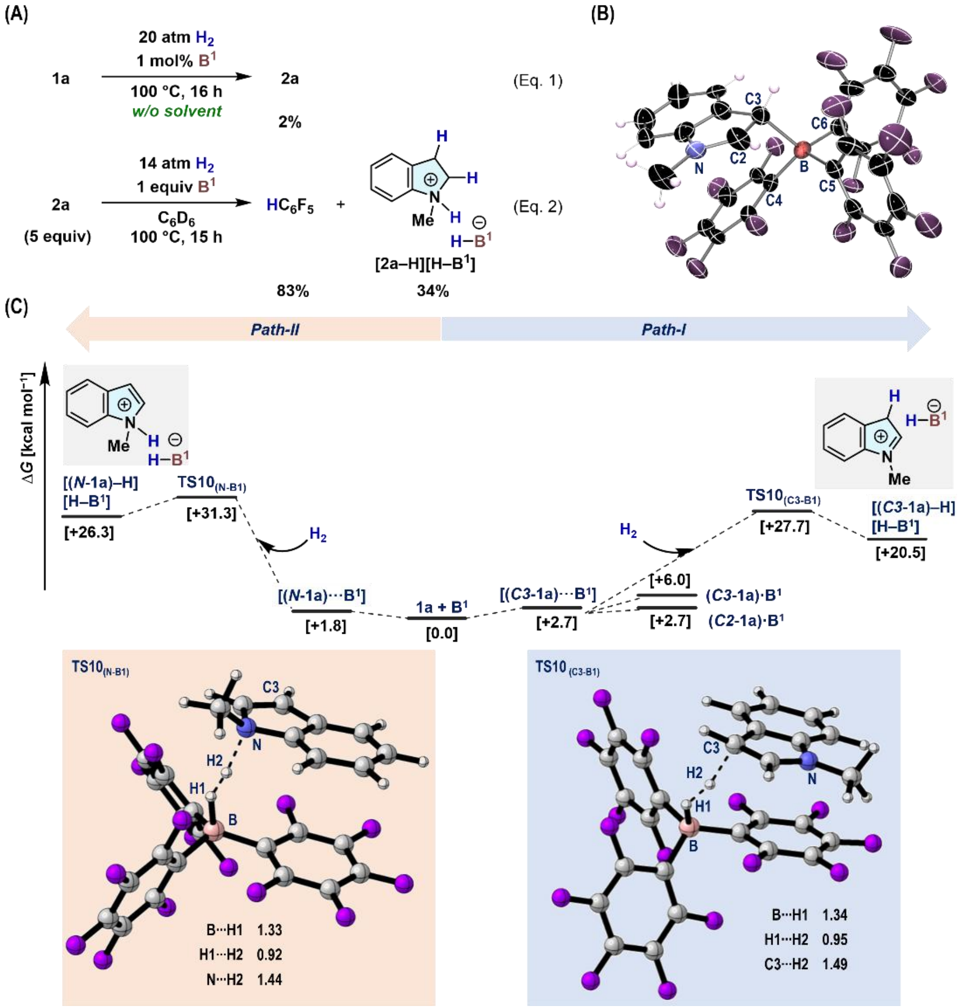

Figure 3.3. (a) **B¹**-catalyzed hydrogenation of **1a** using H_2 (20 atm) at 100 °C under solvent-free conditions (Eq. 1); results for the reaction between **2a** (5 equiv) and **B¹** at 100 °C in C_6D_6 are also shown (Eq. 2). (b) Molecular structure of **(*C3*-1a)·B¹** (thermal ellipsoids: 30% probability), determined by single-crystal X-ray diffraction analysis. Selected bond lengths (Å) and angles (°): B–C3 1.80 (1), N–C2 1.28 (1), C2–C3 1.46 (2),

C3–B–C4 101.7 (8), C3–B–C5 107.6 (8), C3–B–C6 112.9 (8). (c) Theoretical analysis of the reaction between **1a**, **B^1**, and H_2, calculated at the M06-2X/Def2-TZVP//M06-2X/Def2-SVP level. Relative Gibbs energies (kcal mol^{-1}) are given with respect to **[1a + B^1]** (0.0 kcal mol^{-1}). Structures of the selected transition states **TS10$_{(C3-B1)}$** and **TS10$_{(N-B1)}$** are shown with selected atom distances (Å).

To optimize the triarylboranes for the solvent-free hydrogenation of **1a**, I carried out the reaction using 1 mol% boranes, including homoleptic (**B^2**, **B^{11}**, **B^{12}**, **B^{14}**, and **B^{15}**)[19-23] and heteroleptic (**B^3**–**B^7**, **B^9**, and **B^{16}**–**B^{18}**)[24-29] species (Figure 3.4). Decreasing the intrinsic Lewis acidity of the boron atom by substituting the C_6F_5 groups in **B^1** (TON = 2; Figure 3.3A) with 2,3,5,6-F_4C_6H groups (**B^2**), 2,6-$F_2C_6H_3$ groups (**B^{11}**), and 3,5-Br_2-2,6-F_2C_6H (**B^{14}**) increased the TON to 68, 71, and 44, respectively (Figure 3.4, runs 1−3). Introduction of sterically demanding 2-Cl-6-FC_6H_3 groups (**B^{12}**) substantially decreased the TON to 6 (Figure 3.4, run 4). In contrast, **B^{15}**, which bears sterically less hindered but strongly electron-withdrawing 3,5-$(CF_3)_2C_6H_3$ groups showed excellent catalytic activity (TON = 93; Figure 3.4, run 5), although its high sensitivity to air and moisture limits the scope of practical applications.

Recently, our group have demonstrated that heteroleptic triarylboranes that bear 2,6-Cl_2-aryl groups efficiently catalyze the hydrogenation of quinolines and *in-situ*-generated imines, even in the presence of Lewis bases such as CO_2 and H_2O.[24,26] The shelf-stable boranes **B^9** and **B^7** exhibited high activity (TON = 94; Figure 3.4, runs 6 and 7), comparable to that of the more moisture-sensitive **B^5** (Figure 3.4, run 8). Upon slightly modifying the 2,6-$Cl_2C_6H_3$ group in **B^7** and **B^9** by introducing *meta*-CF_3 (**B^{16}**) or *meta*-Cl (**B^{17}**) groups, high catalytic activity was maintained (TON = 92), providing **2a** in excellent yield (Figure 3.4, runs 9 and 10). However, replacing the *meta*-Br atoms in **B^{17}** with *meta*-CF_3 groups remarkably decreased the catalytic activity, whereby **B^{18}** furnished **2a** in only 17% yield (Figure 3.4, run 11). Boranes **B^3** and **B^6** did not catalyze the hydrogenation of **1a** (Figure 3.4, runs 12 and 13), even though the local environment surrounding the B atoms is nearly identical to that of **B^5**, **B^7**, **B^7**, **B^{16}**, and **B^{17}**. Replacing the 2,6-Cl_2-aryl groups with a 2,4,6-$Me_3C_6H_2$ substituent (**B^4**) was also unsuccessful (TON = 2; Figure 3.4, run 14).

Given their synthetic accessibility and practical utility, I compared the catalytic activity of **B^5**, **B^7**, and **B^9** by measuring their turnover frequencies (TOFs) using 0.02 mol% catalyst loading under H_2 (60 atm). The TOF values increased from 2,300 d^{-1} for **B^5** (*meta*-F) to 2,650 d^{-1} for **B^7** (*meta*-Cl), and 2,850 d^{-1} for **B^9** (*meta*-Br), demonstrating that remote back strain given by the *meta*-substituents exerts a considerable influence on the catalyst performance and robustness.[30] Notably, when the solvent-free hydrogenation of **1a** was conducted with 0.01 mol% **B^9** over 8 d with daily recharging of H_2 (60 atm), the TON reached 8,500, demonstrating the practical potential of main-group catalysis for such hydrogenation reactions.

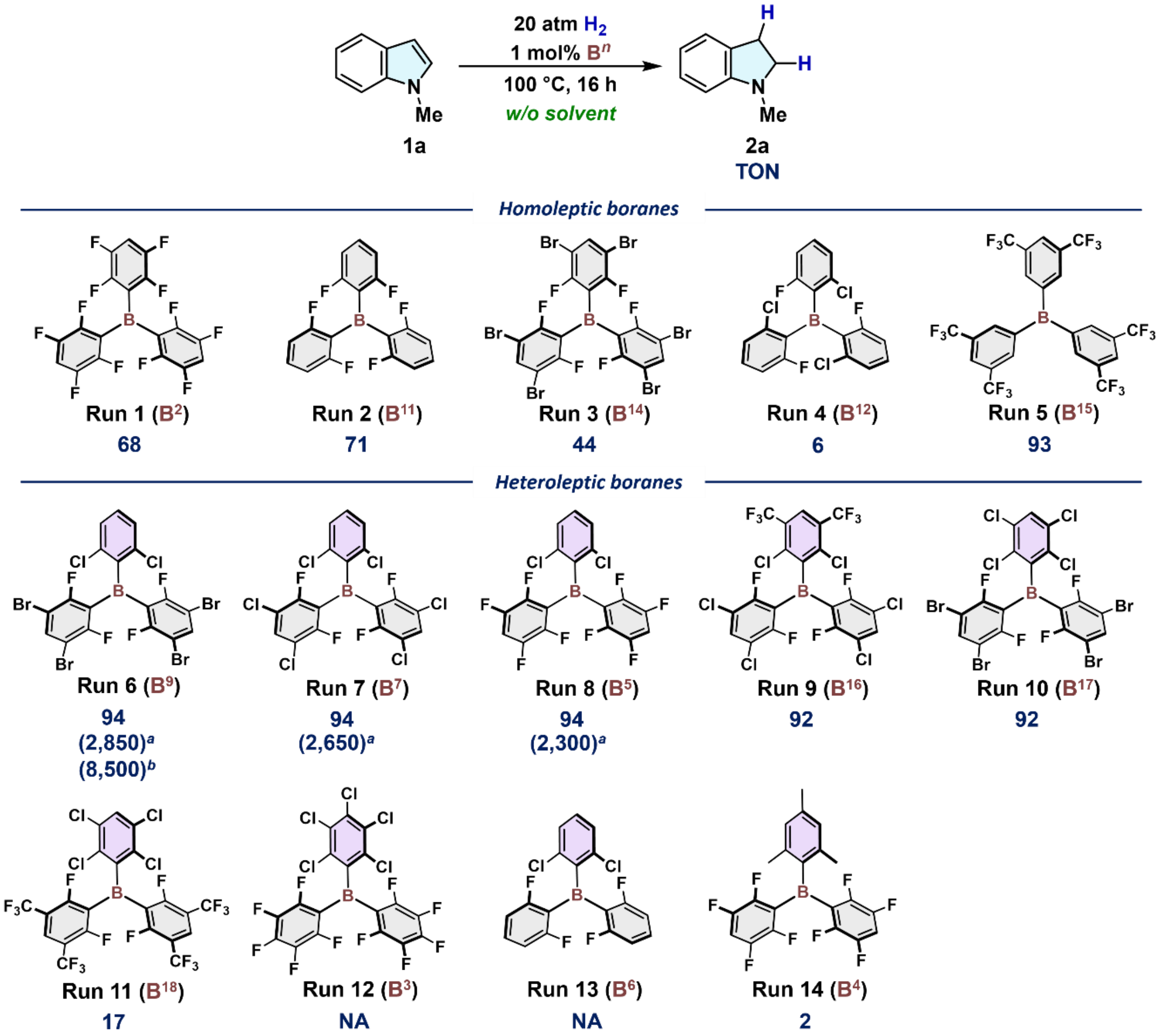

Figure 3.4. Catalyst screening under solvent-free conditions. General conditions: An autoclave (30 mL) was filled with **1a** (2.5 mmol), $\mathbf{B}^{n}$ (n = 2–7, 9, 11, 12, and 14–18; 0.025 mmol), and tetradecane as an internal standard. After pressurization with H_2 (20 atm), the mixture was stirred at 100 °C for 16 h. Conversion of **1a** and the catalyst turnover number (TON) were determined by GC analysis. [*a*] Catalyst turnover frequency (TOF in day^{-1}) using 0.02 mol% $\mathbf{B}^{n}$ and H_2 (60 atm). [*b*] TON after a period of 8 days using 0.01 mol% $\mathbf{B}^{9}$. H_2 was pressurized to reach a total pressure of 60 atm once per day. NA: not available.

Figure 3.5 illustrates plausible reaction mechanisms for the $\mathbf{B}^{9}$-catalyzed hydrogenation of **1a** to **2a**, where the ΔG values are referenced to $[\mathbf{B}^{9} + \mathbf{1a} + \mathbf{2a} + \mathbf{H_2}]$ (0.0 kcal mol^{-1}). According to my findings with $\mathbf{B}^{1}$ (Figure 3.3C), I considered two possible paths for the heterolytic cleavage of H_2 mediated by $\mathbf{B}^{9}$-based FLP species, i.e., one involving the olefinic C3 atom (path-I) and another involving the indole nitrogen atom (path-II) (Figure 3.5A). I confirmed that path-I, which affords **[(*C3*-1a)–H][H–B**^{9}**]** (+21.1 kcal mol^{-1}) via $\mathbf{TS10}_{(\mathbf{C3\text{-}B9})}$ (+33.8 kcal mol^{-1}), would be favored over path-II, which furnishes **[(*N*-1a)–H][H–B**^{9}**]** (+30.3 kcal mol^{-1}) via $\mathbf{TS10}_{(\mathbf{N\text{-}B9})}$ (+36.7 kcal mol^{-1}). Subsequently, in path-I, hydride migration smoothly takes place via **TS11** (+22.9 kcal mol^{-1}) to yield **2a**. Once **2a** is generated, path-III, which involves H_2 activation with indoline nitrogen and $\mathbf{B}^{9}$, becomes plausible, as evident from the decomposition of $\mathbf{B}^{1}$ from **[2a–H][H–B**^{1}**]**

(Eq. 2 in Figure 3.3B). DFT calculations suggested that path-III takes place predominantly to afford **[2a–H][H–B^9]** (+10.8 kcal mol^{-1}) via **TS12** (+24.1 kcal mol^{-1}), followed by an intermolecular proton transfer via **TS13** (+29.3 kcal mol^{-1}) to another molecule of **1a** to generate **[(*C3*-1a)–H][H–B^9]** with concomitant regeneration of **2a**. The total energy barrier for overcoming these steps ($\Delta G^{\ddagger}$ = +29.3 kcal mol^{-1}) is lower than that of path-I ($\Delta G^{\ddagger}$ = +33.8 kcal mol^{-1}), which indicates that the catalytic cycle shifts from path-I to path-III with increasing concentration of **2a**. The increase in the concentration of **2a** under the present conditions (H_2: 60 atm) may also induce the proto-deboronation of triarylboranes by promoting the generation of **[2a–H][H–B$''$]**. Nevertheless, **[2a–H][H–B^9]** would be effectively destabilized through back strain between the 2,6-$Cl_2C_6H_3$ and 3,5-Br_2-2,6-F_2C_6H groups, thus preventing the proto-deboronation and facilitating the subsequent hydride transfer.

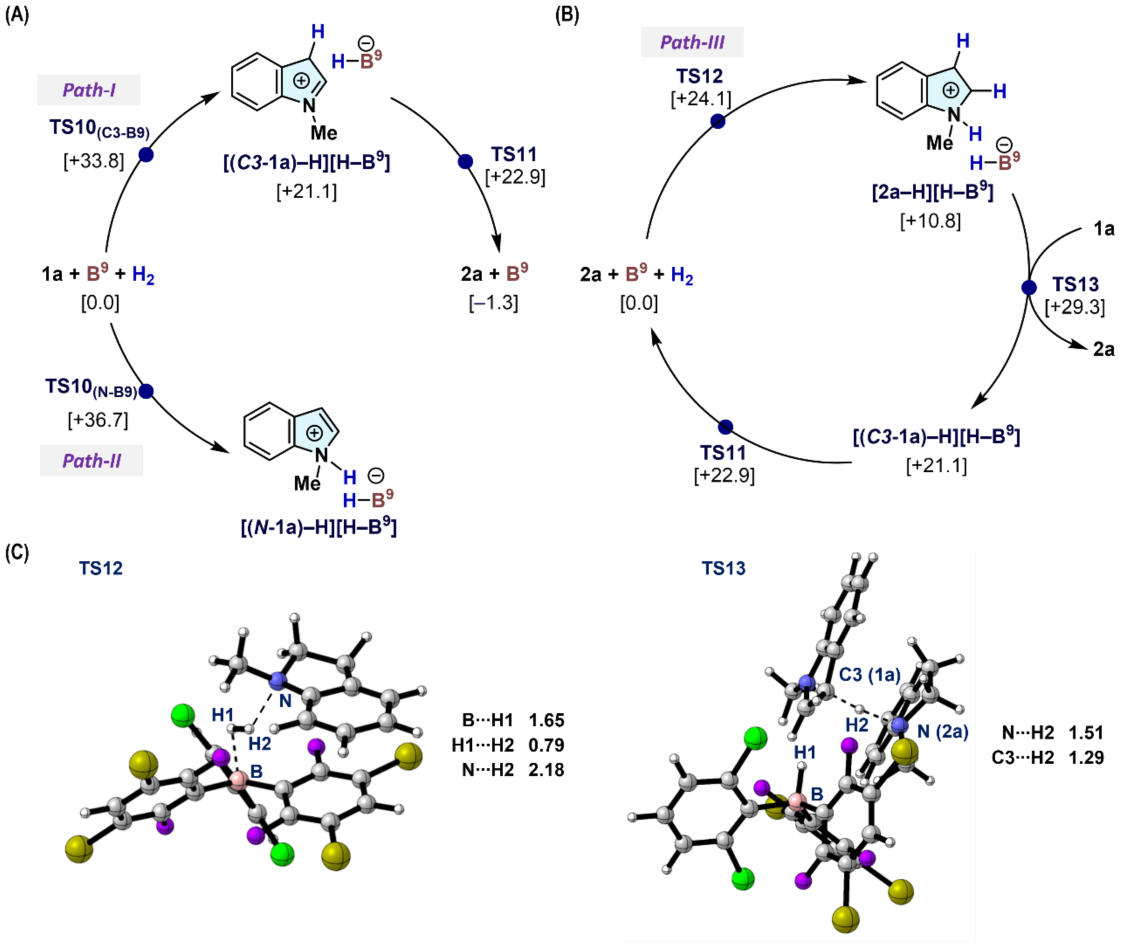

Figure 3.5. Plausible reaction mechanisms for the hydrogenation of **1a** with **B^9** via (A) **TS10$_{(C3\text{-}B9)}$**/**TS10$_{(N\text{-}B9)}$** and (B) **TS12**. The relative Gibbs energies (kcal mol^{-1}), calculated at the M06-2X/Def2-TZVP//M06-2X/Def2-SVP//gas-phase level, are given with respect to **[1a + 2a + B^9 + H$_2$]**, while the initial state is shown as (A) **[1a + B^9+ H$_2$]** or (B) [**2a** + **B^9** + **H$_2$**] for clarity. (C) Optimized molecular structures of **TS12** and **TS13** with selected geometrical parameters (in Å).

Finally, I explored the applicability of shelf-stable **B^9** to the solvent-free hydrogenation of substituted indoles **1** to yield indolines **2** (Figure 3.6). Various 1-methylindole derivatives (**1b**–**1f**) were converted to the corresponding indolines (**2b**–**2f**) in excellent yield, albeit that **2g** was obtained from C2-methylated **1g** (m.p. ~55 °C) in merely 74% yield owing to the increased steric hindrance at the C2 position. Although **B**^{9} did not work well, the use of **B**^{1} gave 1-methyl-2phenylindoline (**2h**) in 29% yield. It should be emphasized here that the present **B**^{9}-catalyzed system can also be applied to *N*-substituted indoles (**1i**–**1m**), which have remained unexplored as substrates for main-group-based catalytic systems. In the presence of 1 mol% **B**^{9}, indolines bearing *N*-Et (**2i**) and *N*-^{i}Pr (**2j**) groups were synthesized in 90% and 78% yield, respectively. Tricyclic lilolidine (m.p. ~85 °C) **1k** was also suitable for the present solvent-free system and afforded **2k** in 94% yield. Conversely, **B**^{9} showed low catalytic activity for the hydrogenation of 1-phenyl-1*H*-indole (**1l**), giving **2l** in only 15% yield, even when using 2 mol% catalyst. This low reactivity can most likely be attributed to the decreased Lewis basicity at the C3 position, which would impede the H_2 activation with **B**^{9} in the initial catalytic cycle (*cf.* path-I in Figure 3.5). In this context, a mixed catalyst system of **B**^{1} and **B**^{9} (1 mol% each) substantially increased the yield of **2l** to 94%, improving the result with 2 mol% **B**^{1} alone (87%), which can be ascribed to **B**^{1} predominantly mediating the H_2 cleavage with the indole C3 atom and the **2a**/**B**^{9} pair promoting the following process. Moreover, **2l** was afforded 98% yield when the mixture of **B**^{9} and **2a** (2 mol% each) was applied, demonstrating the critical effect of shifting the H_2 cleavage mechanism. Indole **1m** (m.p. ~78 °C), which contains a strongly electron-withdrawing SO_2Ph moiety, was also suitable and afforded **2m** in 47% yield in the presence of 1 mol% **B**^{1}. Therefore, **B**^{9} is more suitable for the hydrogenation of indoles that bear *N*-electron-donating alkyl groups and/or sterically less hindered nitrogen centers, whereas **B**^{1} is preferable for substrates with *N*-electron-withdrawing or bulky substituents, as these groups reduce the risk of proto-deboronation.

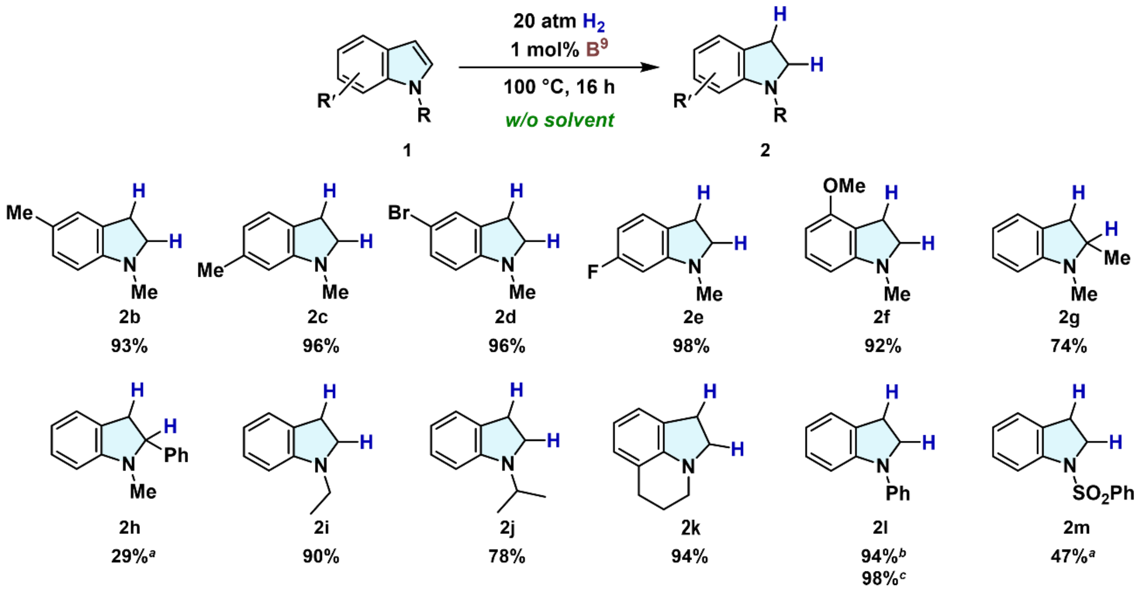

Figure 3.6. Triarylborane-catalyzed synthesis of substituted indolines **2** via hydrogenation of indoles **1** under solvent-free conditions. General conditions: An autoclave (30 mL) was filled with **1** (2.5 mmol), **B**^{9} (0.025 mmol), and tetradecane as an internal standard. After pressurization with H_2 (20 atm), the mixture was stirred at 100 °C for 16 h. The product yield was determined by GC analysis. ^{a}1 mol% **B**^{1} was used. ^{b}A mixture of **B**^{1} and **B**^{9} (1 mol% each) was used. ^{c} A mixture of **B**^{9} and **2a** (2 mol% each) was used.

3.3 Conclusions

In summary, I have demonstrated that shelf-stable $B(2,6\text{-}Cl_2C_6H_3)(3,5\text{-}Br_2\text{-}2,6\text{-}F_2C_6H)_2$ (**B**^{9}) efficiently catalyzes the solvent-free hydrogenation of various substituted indoles to indolines. Remarkably, I achieved an unprecedented turnover number (TON) of 8,500 in the main-group-catalyzed hydrogenation of 1-methylindole (**1a**), representing a more than 400-fold improvement over hitherto reported systems based on $B(C_6F_5)_3$. Mechanistic studies revealed that the hydrogenation of **1a** involves an olefin-to-nitrogen switching of Lewis bases in the critical H_2-cleavage steps. Specifically, the initial H_2 activation is mediated by a frustrated Lewis pair (FLP) comprising the indole C3-carbon and boron atoms, while an FLP species comprising the indoline nitrogen and boron atoms promotes the subsequent H_2 activation leading to indoline **2a**. Thus, the design of an effective triarylborane should prevent borane decomposition, which occurs via thermally induced proto-deboronation from [indoline–H][H–borane] species. In this context, judiciously designed **B**^{9} showed notable applicability for the synthesis of *N*-substituted indolines, which have rarely been synthesized using main-group-based catalysts. Therefore, this work demonstrates the high potential of triarylboranes as catalysts for the hydrogenation of unsaturated molecules to produce valuable nitrogen-containing compounds.

3.4 Supporting information

3.4.1. General considerations

Unless otherwise noted, all manipulations were conducted under a nitrogen atmosphere using standard Schlenk line or glovebox techniques. ^{1}H, ^{11}B, and ^{19}F NMR spectra were recorded on a Bruker AVANCE III 400. The chemical shifts (ppm) in the ^{1}H NMR spectra were recorded relative to tetramethylsilane or residual protonated solvent (C_6D_5H (δ 7.16), $CHCl_3$ (δ 7.26)). The chemical shift in the ^{11}B NMR spectra was recorded relative to $BF_3\cdot(OCH_2CH_3)$ as an external standard. The chemical shifts in the ^{19}F NMR spectra were recorded relative to α,α,α-trifluorotoluene (δ −65.64). Single crystal X-ray diffraction data were collected with a Rigaku XtaLAB Synergy diffractometer equipped with a HyPix-6000HE detector. Analytical gas chromatography (GC) was carried out on a Shimadzu GC-2025 gas chromatograph, equipped with a flame ionization detector.

3.4.2. Materials

All commercially available reagents including super-dehydrated solvents (*n*-hexane, toluene) were purchased from Sigma Aldrich, Angene Chemical, Tokyo Chemical Industry (TCI) and FUJIFILM Wako Pure Chemical Corporation, and used as received. Benzene-d_6 was distilled from sodium benzophenone ketyl prior to use. $CDCl_3$ was stored over molecular sieves (4 Å). 1-methylindole (**1a**), tetradecane, and dodecane were purchased from TCI or Angene Chemical, and used after distillation over CaH_2. Some of the indole derivatives (**1b**, **1c**, **1e**, **1f**, **1i**, and **1j**) were prepared by following the reported procedures.[31] H_2 gas was purchased from Sumitomo Seika Chemicals Company, and used as received. Note that this gas includes some impurities, as shown in Table 3.S1.

	Impurity				
	N_2	O_2	CO	CO_2	H_2
H_2	<200	<50	<1	<1	-

Table 3.S1. Impurities contaminated in H_2 (shown in ppm).

Metrical data for the solid-state structures is available from Cambridge Crystallographic Data Centre: CCDC2401790 (**(*C3*-1a)·B^1**).

3.4.3. Crystallization of (*C3*-1a)·B^1

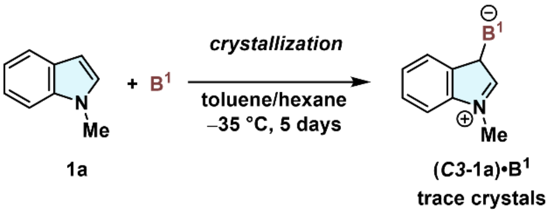

Figure 3.S1. Crystallization of **(*C3*-1a)·B^1**.

To a solution of **B^1** (155 mg, 0.303 mmol, 0.3 M in toluene) was added **1a** (38.7 mg, 0.295 mmol). The reaction mixture was stirred for 5 min, and hexane was added over the resultant solution (ca. 2 mL). A single-crystal suitable for X-ray diffraction analysis was obtained by crystallization from toluene/hexane at −35 °C after the period of 5 days. X-ray data for **(*C3*-1a)·B^1** (Figure 3.S2): $M = 643.16$, colorless, monoclinic, $P2_1$ (#4), $a = 7.5418(10)$ Å, $b = 16.6471(13)$ Å, $c = 9.6601(10)$ Å, $\alpha = 90°$, $\beta = 106.581(12)°$, $\gamma = 90°$, $V = 1162.4(2)$ Å^3, Z = 2, $Dcalcd = 1.838$ g/cm^3, T = −150 °C, R_1 (wR_2) = 0.1004 (0.2621).

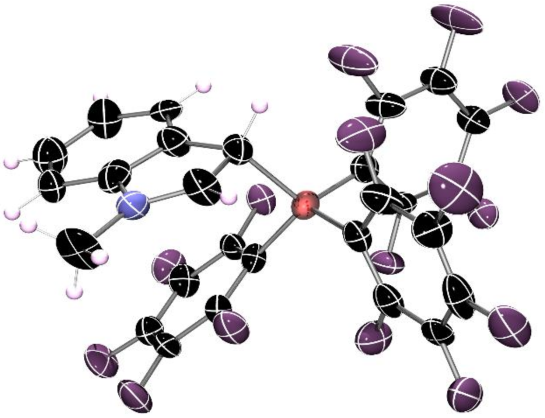

Figure 3.S2. Molecular structure of **(*C3*-1a)·B^1** with ellipsoids set at 30% probability

3.4.4. Screening of catalysts in hydrogenation of 1a

3.4.4.1. Reactions with 1 mol% triarylborane catalysts (Eq.1 in Figure 3.3a and runs 1–14 in Figure 3.4)

General: A 10 mL autoclave was charged with **1a** (ca. 2.5 mmol) and borane (ca. 0.025 mmol; 1 mol%).

Tetradecane was added as an internal standard. Once sealed, the autoclave was pressurized with H_2 (20 atm) and heated at 100 °C for 16 h. After degassing at room temperature, the yield of **2a** was determined by the GC analysis.

Eq. 1 in Figure 3a: Followed by the general procedure, **1a** (324 mg; 2.47 mmol), $\mathbf{B}^{\mathbf{1}}$ (13.0 mg; 0.0254 mmol), and tetradecane (229 mg; 1.15 mmol) were employed, giving **2a** in 2% GC yield.

Run 1 in Figure 4: Followed by the general procedure, **1a** (331 mg; 2.52 mmol), $\mathbf{B}^{\mathbf{2}}$ (11.4 mg; 0.0249 mmol), and tetradecane (233 mg; 1.17 mmol) were employed, giving **2a** in 68% GC yield.

Run 2 in Figure 4: Followed by the general procedure, **1a** (326 mg; 2.49 mmol), $\mathbf{B}^{\mathbf{11}}$ (8.3 mg; 0.024 mmol), and tetradecane (230 mg; 1.16 mmol) were employed, giving **2a** in 71% GC yield.

Run 3 in Figure 4: Followed by the general procedure, **1a** (331 mg; 2.52 mmol), $\mathbf{B}^{\mathbf{14}}$ (21.5 mg; 0.0261 mmol), and tetradecane (232 mg; 1.17 mmol) were employed, giving **2a** in 44% GC yield.

Run 4 in Figure 4: Followed by the general procedure, **1a** (326 mg; 2.49 mmol), $\mathbf{B}^{\mathbf{12}}$ (9.9 mg; 0.025 mmol), and tetradecane (236 mg; 1.19 mmol) were employed, giving **2a** in 6% GC yield.

Run 5 in Figure 4: Followed by the general procedure, **1a** (337 mg; 2.57 mmol), $\mathbf{B}^{\mathbf{15}}$ (16.6 mg; 0.0255 mmol), and tetradecane (227 mg; 1.14 mmol) were employed, giving **2a** in 93% GC yield.

Run 6 in Figure 4: Followed by the general procedure, **1a** (335 mg; 2.55 mmol), $\mathbf{B}^{\mathbf{9}}$ (17.7 mg; 0.0253 mmol), and tetradecane (229 mg; 1.15 mmol) were employed, giving **2a** in 94% GC yield.

Run 7 in Figure 4: Followed by the general procedure, **1a** (336 mg; 2.56 mmol), $\mathbf{B}^{\mathbf{7}}$ (13.3 mg; 0.0255 mmol), and tetradecane (231 mg; 1.16 mmol) were employed, giving **2a** in 94% GC yield.

Run 8 in Figure 4: Followed by the general procedure, **1a** (339 mg; 2.58 mmol), $\mathbf{B}^{\mathbf{5}}$ (12.1 mg; 0.0266 mmol), and tetradecane (234 mg; 1.18 mmol) were employed, giving **2a** in 94% GC yield.

Run 9 in Figure 4: Followed by the general procedure, **1a** (334 mg; 2.55 mmol), $\mathbf{B}^{\mathbf{16}}$ (17.3 mg; 0.0277 mmol), and tetradecane (236 mg; 1.19 mmol) were employed, giving **2a** in 92% GC yield.

Run 10 in Figure 4: Followed by the general procedure, **1a** (335 mg; 2.55 mmol), $\mathbf{B}^{\mathbf{17}}$ (19.6 mg; 0.0255 mmol), and tetradecane (233 mg; 1.17 mmol) were employed, giving **2a** in 92% GC yield.

Run 11 in Figure 4: Followed by the general procedure, **1a** (329 mg; 2.51 mmol), $\mathbf{B}^{\mathbf{18}}$ (18.2 mg; 0.0251 mmol), and tetradecane (234 mg; 1.18 mmol) were employed, giving **2a** in 17% GC yield.

Run 12 in Figure 4: Followed by the general procedure, **1a** (328 mg; 2.50 mmol), **B^3** (15.1 mg; 0.0254 mmol), and tetradecane (232 mg; 1.17 mmol) were employed, not giving **2a**.

Run 13 in Figure 4: Followed by the general procedure, **1a** (327 mg; 2.49 mmol), **B^6** (9.6 mg; 0.025 mmol), and tetradecane (232 mg; 1.17 mmol) were employed, not giving **2a**.

Run 14 in Figure 4: Followed by the general procedure, **1a** (324 mg; 2.47 mmol), **B^4** (10.4 mg; 0.0243 mmol), and tetradecane (228 mg; 1.15 mmol) were employed, giving **2a** in 2% GC yield.

3.4.4.2. Catalyst turnover frequencies exhibited by triarylboranes (B^5, B^7, and B^9; runs 1–3 in Figure 3.S3)

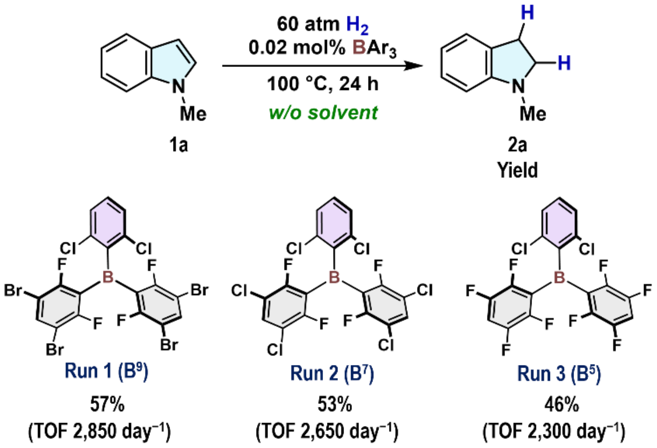

Figure 3.S3. Catalytic solvent-free hydrogenation of **1a** using **B^5**, **B^7**, and **B^9**.

General: A 30 mL autoclave was charged with **1a** (ca. 100 mmol), and borane (ca. 0.020 mmol; 0.02 mol%). Tetradecane was added as an internal standard. Once sealed, the autoclave was pressurized with H_2 (60 atm) and heated at 100 °C for 24 h. After degassing at room temperature, the yield of **2a** was determined by GC analysis.

Run 1: Followed by the general procedure, **1a** (13.0 g; 99.1 mmol), **B^9** (14.0 mg; 0.0200 mmol), and tetradecane (945 mg; 4.76 mmol) were employed, giving **2a** in 57% GC yield.

Run 2: Followed by the general procedure, **1a** (13.1 g; 99.9 mmol), **B^7** (10.6 mg; 0.0204 mmol), and tetradecane (1.00 g; 5.04 mmol) were employed, giving **2a** in 53% GC yield.

Run 3: Followed by the general procedure, **1a** (13.0 g; 99.1 mmol), **B^5** (9.0 mg; 0.020 mmol), and tetradecane (948 mg; 4.78 mmol) were employed, giving **2a** in 46% GC yield.

3.4.4.3. Catalyst turnover number exhibited by B^9 (Figure 3.S4)

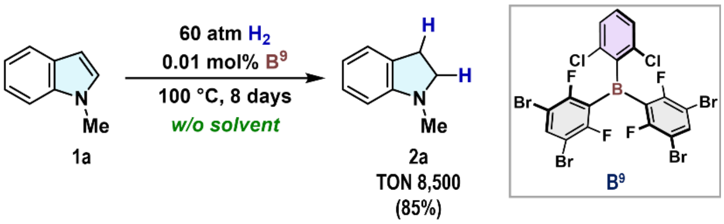

Figure 3.S4. **B^9**-catalyzed solvent-free hydrogenation of **1a**.

A 30 mL autoclave was charged with **1a** (26.1 g, 199 mmol) and **B^9** (14.1 mg, 0.0202 mmol; 0.01 mol%). Tetradecane (2.03 g; 10.2 mmol) was added as an internal standard. Once sealed, the autoclave was pressurized with H_2 (60 atm) and heated at 100 °C. Through this experiment, I repeatedly pressurized H_2 to reach the total pressure of 60 atm at room temperature once a day. After heating for 8 days, **2a** was afforded in 85% GC yield (Figure 3.S4).

3.4.5. Stoichiometric reaction between B^1 and 2a in the presence of H_2

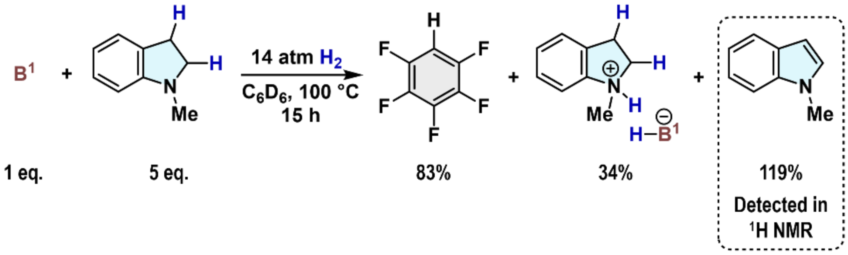

Figure 3.S5. Stoichiometric reaction between **B^1** and **2a** in the presence of H_2.

A high-pressure valved NMR tube (TCI S-5-500-HW-EX1-HPV-7; V = 1.8 mL) was charged with **2a** (33.8 mg, 0.254 mmol), **B^1** (25.7 mg, 0.0502 mmol), and 1,3-dibromo-4,6-difluorobenzene (13.3 mg, 0.0489 mmol; an internal standard). Once sealed, the NMR tube was pressurized with H_2 (14 atm) and heated at 100 °C for 15 h. Then the ^{1}H, ^{11}B, and ^{19}F NMR analyses were conducted (Figure 3.S6). The yield of the products was determined by ^{19}F NMR spectra.[32]

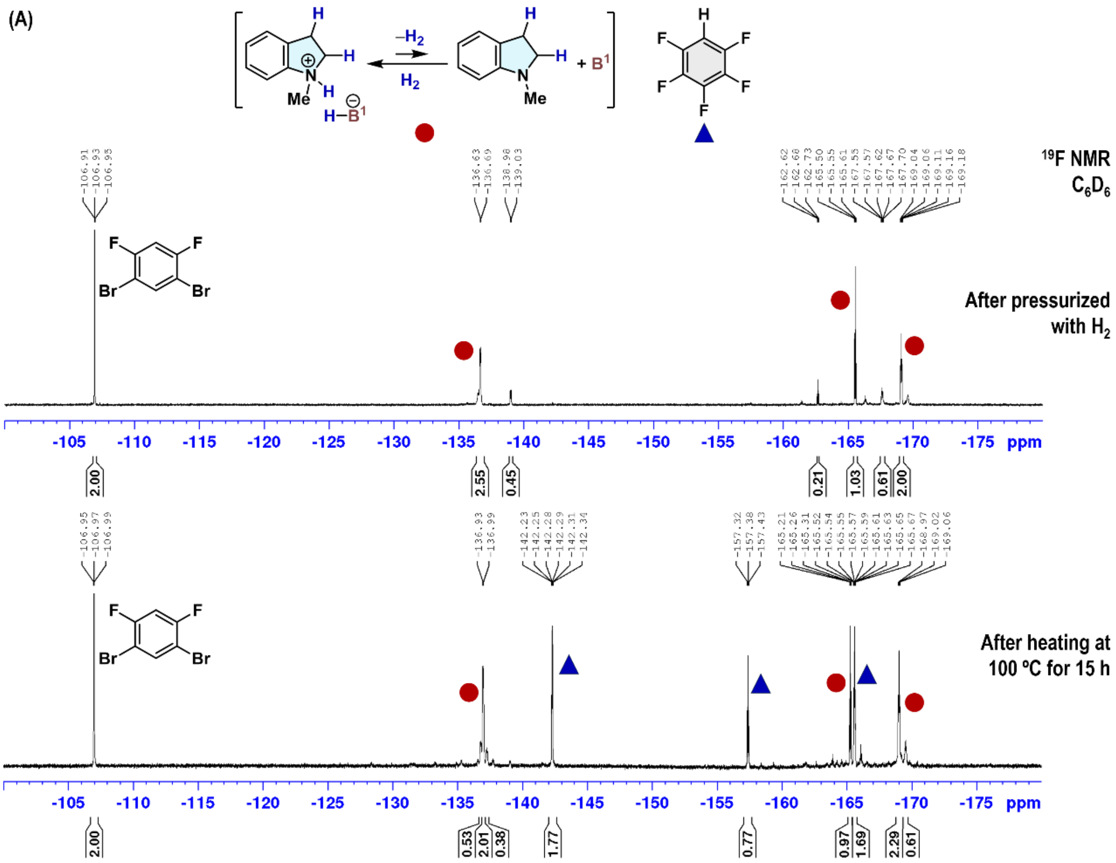
(A)
H
H
N
Me
H
H–B1
–H2
H2
H
H
N
Me
+ B1
H
F
F
F
F
F
19F NMR
C6D6
-106.91
-106.93
-106.95
-136.63
-136.69
-138.98
-139.03
-162.62
-162.68
-162.73
-165.50
-165.55
-165.61
-167.53
-167.57
-167.62
-167.67
-167.70
-169.04
-169.06
-169.11
-169.16
-169.18
F
F
Br
Br
After pressurized with H2
-105
-110
-115
-120
-125
-130
-135
-140
-145
-150
-155
-160
-165
-170
-175
ppm
2.00
2.55
0.45
0.21
1.03
0.61
2.00
-106.95
-106.97
-106.99
-136.93
-136.99
-142.23
-142.25
-142.28
-142.29
-142.31
-142.34
-157.32
-157.38
-157.43
-165.21
-165.26
-165.31
-165.52
-165.54
-165.55
-165.57
-165.59
-165.61
-165.63
-165.65
-165.67
-168.97
-169.02
-169.06
F
F
Br
Br
After heating at 100 °C for 15 h
-105
-110
-115
-120
-125
-130
-135
-140
-145
-150
-155
-160
-165
-170
-175
ppm
2.00
0.53
2.01
0.38
1.77
0.77
0.97
1.69
2.29
0.61

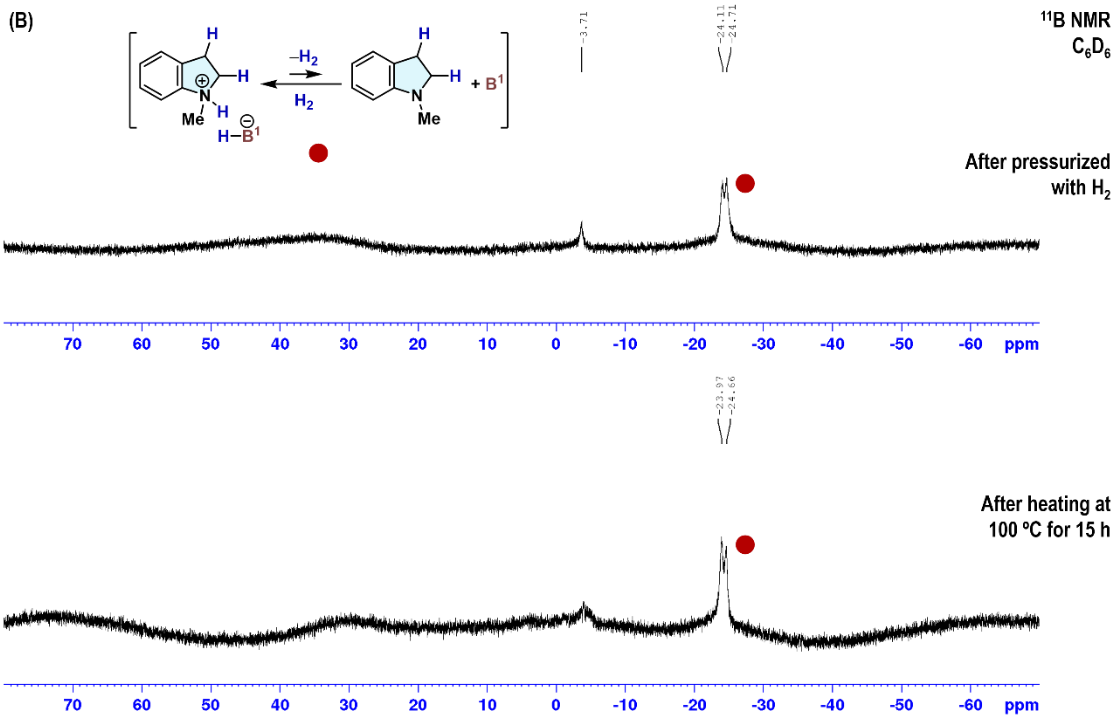
(B)
H
H
N
Me
H
H–B1
–H2
H2
H
H
N
Me
+ B1
11B NMR
C6D6
-3.71
-24.11
-24.71
After pressurized with H2
70
60
50
40
30
20
10
0
-10
-20
-30
-40
-50
-60
ppm
-23.97
-24.66
After heating at 100 °C for 15 h
70
60
50
40
30
20
10
0
-10
-20
-30
-40
-50
-60
ppm

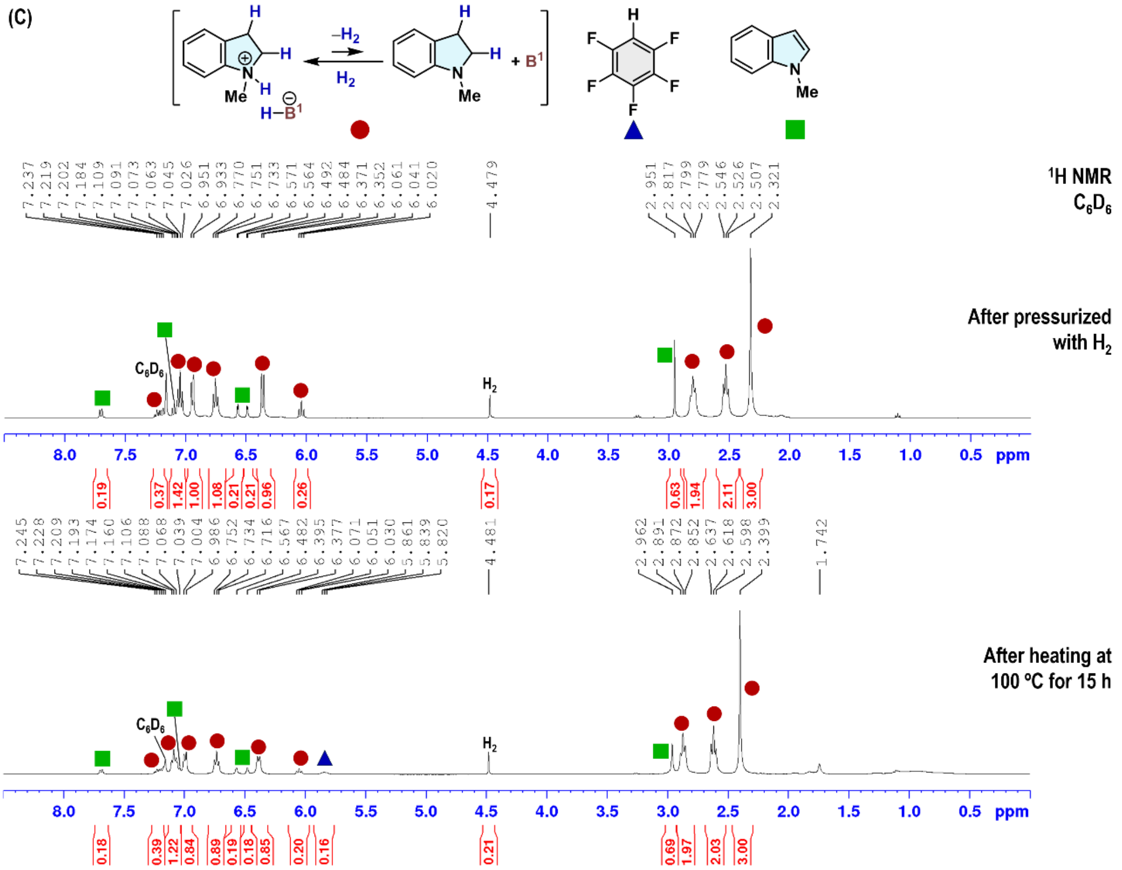

Figure 3.S6. Stoichiometric reaction between **B^1** and **2a** in the presence of H_2. (A) ^{19}F NMR spectra. (B) ^{11}B NMR spectra. (C) ^1H NMR spectra.

3.4.6. Scope of indoles

General: A 30 mL autoclave was charged with **1** (ca. 2.5 mmol) and **B^n** (n = 1 and/or 9; ca. 0.025 mmol; 1 mol%). Tetradecane or dodecane was added as an internal standard. Once sealed, the autoclave was pressurized with H_2 (20 atm) and heated at 100 °C for 16 h. After degassing at room temperature, the yield of **2** was determined by GC analysis.

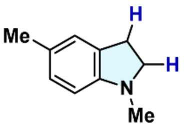

1,5-Dimethylindoline (2b): Followed by the general procedure, **1b** (369 mg; 2.54 mmol), **B^9** (17.8 mg; 0.0255 mmol), and tetradecane (244 mg; 1.23 mmol) were employed, giving **2b** in 93% GC yield. **^{1}H NMR** (400 MHz, $CDCl_3$): δ 6.94 (s, 1H, 4-CH), 6.91 (d, J = 8.0 Hz, 1H, 7-CH), 6.44 (d, J = 8.0 Hz, 1H, 6-CH), 3.26 (t, J = 8.0 Hz, 2H, 2-CH_2), 2.92 (t, J = 8.0 Hz, 2H, 3-CH_2), 2.74 (s, 3H, N-CH_3), 2.27 (s, 3H, 5-C-CH_3).[33]

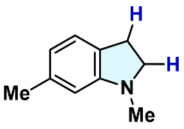

1,6-Dimethylindoline (2c): Followed by the general procedure, **1c** (360 mg; 2.48 mmol), **B^9** (17.5 mg; 0.0251 mmol), and tetradecane (236 mg; 1.19 mmol) were employed, giving **2c** in 96% GC yield. **^{1}H NMR** (400 MHz, $CDCl_3$): δ 6.89 (d, J = 7.2 Hz, 1H, 4-CH), 6.42 (d, J = 7.2 Hz, 1H, 5-CH), 6.26 (s, 1H, 7-CH), 3.20 (t, J = 8.0 Hz, 2H, 2-CH_2), 2.82 (t, J = 8.0 Hz, 2H, 3-CH_2), 2.67

(s, 3H, *N*-C*H*$_3$), 2.23 (s, 3H, 6-C-C*H*$_3$).[34]

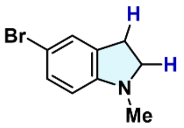

5-Bromo-1-methylindoline (2d): Followed by the general procedure, **1d** (574 mg; 2.73 mmol), **B**^{9} (17.5 mg; 0.0251 mmol), and tetradecane (238 mg; 1.20 mmol) were employed, giving **2d** in 96% GC yield. ^{1}**H NMR** (400 MHz, CDCl$_3$): δ 7.17–7.15 (m, 2H, 4-C*H*, 6-C*H*), 6.37 (d, J = 8.8 Hz 1H, 4-C*H*), 3.33 (t, J = 8.2 Hz, 2H, 2-C*H*$_2$), 2.93 (t, J = 8.2 Hz, 2H, 3-C*H*$_2$), 2.74 (s, 3H, *N*-C*H*$_3$).[14]

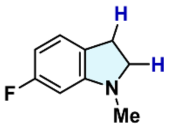

6-Fluoro-1-methylindoline (2e): Followed by the general procedure, **1e** (384 mg; 2.57 mmol), **B**^{9} (17.5 mg; 0.0251 mmol), and tetradecane (242 mg; 1.22 mmol) were employed, giving **2e** in 98% GC yield. ^{1}**H NMR** (400 MHz, CDCl$_3$): δ 6.96–6.93 (m, 1H, 4-C*H*), 6.34–6.29 (m, 1H, 5-C*H*), 6.16 (dd, $^3J_{H,F}$ = 10 Hz, $^4J_{H,H}$ = 2.0 Hz, 1H, 7-C*H*), 3.36 (t, J = 8.2 Hz, 2H, 2-C*H*$_2$), 2.90 (t, J = 8.2 Hz, 2H, 3-C*H*$_2$), 2.74 (s, 3H, *N*-C*H*$_3$).[34]

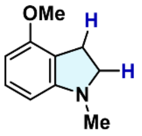

4-Methoxy-1-methylindoline (2f): Followed by the general procedure, **1f** (408 mg; 2.53 mmol), **B**^{9} (17.6 mg; 0.0252 mmol), and tetradecane (250 mg; 1.26 mmol) were employed, giving **2f** in 92% GC yield. ^{1}**H NMR** (400 MHz, CDCl$_3$): δ 7.08 (t, J = 8.0 Hz, 1H, 6-C*H*), 6.30 (d, J = 8.4 Hz, 1H, 7-C*H*), 6.20 (d, J = 7.6 Hz, 1H, 5-C*H*), 3.83 (s, 3H, *O*-C*H*$_3$), 3.32 (t, J = 8.4 Hz, 2H, 2-C*H*$_2$), 2.92 (t, J = 8.0 Hz, 2H, 3-C*H*$_2$), 2.76 (s, 3H, *N*-C*H*$_3$).[3]

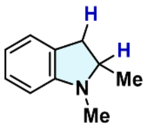

1,2-Dimethylindoline (2g): Followed by the general procedure, **1g** (364 mg; 2.51 mmol), **B**^{9} (17.6 mg; 0.0252 mmol), and dodecane (240 mg; 1.41 mmol) were employed, giving **2g** in 74% GC yield. ^{1}**H NMR** (400 MHz, CDCl$_3$): δ 7.16-7.09 (m, 2H, 4-C*H*, 6-C*H*), 6.72 (t, J = 7.2 Hz, 1H, 5-C*H*), 6.51 (d, J = 7.6 Hz, 1H, 7-C*H*), 3.48-3.42 (m, 1H, 2-C*H*$_2$), 3.16-3.10 (m, 1H, 3-C*H*$_2$), 2.77 (s, 3H, *N*-C*H*$_3$), 2.69-2.62 (m, 1H, 3-C*H*$_2$), 1.38 (d, J = 6.0 Hz, 3H, 2-C-C*H*$_3$).[35]

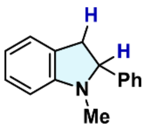

2-Phenyl-1-methylindoline (2h): Followed by the general procedure, **1h** (518 mg; 2.50 mmol), **B**^{1} (12.7 mg; 0.0248 mmol), and tetradecane (291 mg; 1.47 mmol) were employed, giving **2h** in 29% GC yield. ^{1}**H NMR** (400 MHz, CDCl$_3$): δ 7.37 (t, J = 8.0 Hz, 2H, 2-C-Ar-*H*), 7.26 (d, J = 8.0 Hz, 2H, 2-C-Ar-*H*), 7.16-7.21 (m, 2H, 4-C*H*, 7-C*H*), 7.10 (t, J = 7.6 Hz, 1H, 2-C-Ar-*H*), 6.99 (t, J = 7.2 Hz, 1H, 6-C*H*), 6.78 (t, J = 7.6 Hz, 1H, 5-C*H*), 3.98 (t, J = 8.4 Hz, 2H, 2-C*H*$_2$), 3.15 (t, J = 8.4 Hz, 2H, 3-C*H*$_2$).[36]

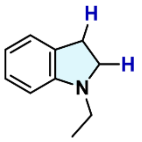

1-Ethylindoline (2i): Followed by the general procedure, **1i** (365 mg; 2.51 mmol), **B**^{9} (17.3 mg; 0.0248 mmol), and tetradecane (245 mg; 1.23 mmol) were employed, giving **2i** in 90% GC yield. ^{1}**H NMR** (400 MHz, CDCl$_3$): δ 6.98 (t, J = 7.8 Hz, 2H, 5-C*H*, 6-C*H*), 6.56 (d, J = 7.2 Hz, 1H, 7-C*H*), 6.40 (d, J = 7.6 Hz, 1H, 4-C*H*), 3.24 (t, J = 8.0 Hz, 2H, 2-C*H*), 3.06 (q, J = 7.2 Hz, 2H, *N*-C*H*$_2$-CH$_3$), 2.87 (t, J = 8.0 Hz, 2H, 3-C*H*), 1.11 (t, J = 7.2 Hz, 3H, *N*-CH$_2$-C*H*$_3$).[37]

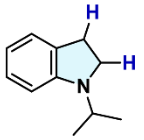

1-Isopropylindoline (2j): Followed by the general procedure, **1j** (413 mg; 2.59 mmol), **B**^{9} (17.6 mg; 0.0252 mmol), and tetradecane (242 mg; 1.22 mmol) were employed, giving **2j** in 78% GC yield. ^{1}**H NMR** (400 MHz, $CDCl_3$): δ 7.05-7.08 (m, 2H, 4-C*H*, 6-C*H*), 6.62 (t, *J* = 7.2 Hz, 1H, 5-C*H*), 6.45 (d, *J* = 8.0 Hz, 1H, 7-C*H*), 3.80-3.90 (m, 1H, *N*-C*H*), 3.36 (t, *J* = 8.4 Hz, 2H, 2-$C\mathit{H}_2$), 2.96 (t, *J* = 8.4 Hz, 2H, 3-$C\mathit{H}_2$), 1.18 (d, *J* = 6.8 Hz, 6H, *N*-C-$(C\mathit{H}_3)_2$).[38]

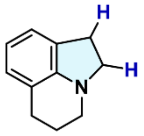

1,2,5,6-Tetrahydro-4H-pyrrolo[3,2,1-ij]quinoline (2k): Followed by the general procedure, **1k** (394 mg; 2.51 mmol), **B**^{9} (17.6 mg; 0.0252 mmol) and tetradecane (229 mg; 1.15 mmol) were employed, giving **2k** in 94% GC yield. ^{1}**H NMR** (400 MHz, $CDCl_3$): δ 6.96 (d, *J* = 7.2 Hz, 1H, 4-C*H*), 6.85 (d, *J* = 7.2 Hz, 1H, 6-C*H*), 6.65 (t, *J* = 7.2 Hz, 1H, 5-C*H*), 3.28 (t, *J* = 7.8 Hz, 2H, 2-$C\mathit{H}_2$), 3.01 (t, *J* = 5.2 Hz, 2H, *N*-$C\mathit{H}_2$), 2.93 (t, *J* = 7.8 Hz, 2H, 3-$C\mathit{H}_2$), 2.72 (t, *J* = 6.6 Hz, 2H, 7-C-$C\mathit{H}_2$), 2.12 (m, 2H, *N*-CH_2-$C\mathit{H}_2$).[39]

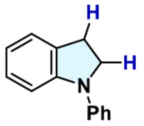

1-Phenylindoline (2l): Followed by the general procedure, **1l** (494 mg; 2.56 mmol), **B**^{1} (12.8 mg, 0.0250 mmol), **B**^{9} (17.7 mg; 0.0253 mmol) and tetradecane (250 mg; 1.26 mmol) were employed, giving **2l** in 94% GC yield. ^{1}**H NMR** (400 MHz, $CDCl_3$): δ 7.46 (d, *J* = 7.2 Hz, 2H, 2-C-Ar-*o*-H_2), 7.38 (t, *J* = 7.4 Hz, 2H, 2-C-Ar-*m*-H_2), 7.32 (d, *J* = 7.2 Hz, 1H, 2-C-Ar-*p*-*H*), 7.15 (t, *J* = 7.6 Hz, 1H, 5-C*H*), 7.08 (d, *J* = 7.2 Hz, 1H, 4-C*H*), 6.73 (t, *J* = 7.5 Hz, 1H, 5-C*H*), 6.54 (d, *J* = 8.0 Hz, 1H, 7-C*H*), 4.36 (dd, *J* = 11.2, 8.8 Hz, 1H, 3-$C\mathit{H}_2$), 3.33 (dd, *J* = 15.6, 8.8 Hz, 1H, 3-$C\mathit{H}_2$), 2.94 (dd, *J* = 15.6, 11.2 Hz, 1H, 2-$C\mathit{H}_2$), 2.62 (s, 3H, *N*-$C\mathit{H}_3$).[40]

I also explored the following Conditions 1-3 for the synthesis of **2l**;

Conditions 1: Followed by the general procedure, **1l** (506 mg; 2.62 mmol), **B**^{9} (35.0 mg; 0.0501 mmol; 2 mol%), **2a** (6.5 mg; 0.048 mmol; 2 mol%) and tetradecane (235 mg; 1.18 mmol) were employed, giving **2l** in 98% GC yield.

Conditions 2: Followed by the general procedure, **1l** (265 mg; 1.37 mmol), **B**^{9} (17.4 mg; 0.0249 mmol; 2 mol%) and tetradecane (242 mg; 1.22 mmol) were employed, giving **2l** in 15% GC yield. **Conditions 3:** **F**ollowed by the general procedure, **1l** (242 mg; 1.25 mmol), **B**^{1} (13.2 mg; 0.0258 mmol; 2 mol%) and tetradecane (229 mg; 1.15 mmol) were employed, giving **2l** in 87% GC yield.

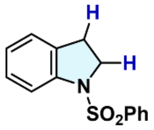

1-Phenylsulfonylindoline (2m): Followed by the general procedure, **1m** (644 mg; 2.50 mmol), **B**^{1} (13.0 mg; 0.0254 mmol) and tetradecane (240 mg; 1.21 mmol) were employed, giving **2m** in 47% GC yield. ^{1}**H NMR** (400 MHz, $CDCl_3$): δ 7.79 (d, *J* = 7.6 Hz, 2H, *S*-*o*-ArH_2), 7.65 (d, *J* = 8.0 Hz, 1H, *S*-*p*-Ar*H*), 7.55 (t, *J* = 7.2 Hz, 1H, 6-C*H*), 7.44 (t, *J* = 7.6 Hz, 2H, *S*-*m*-Ar*H*), 7.19 (d, *J* = 6.4 Hz, 1H, 4-C*H*), 7.08 (d, *J* = 7.2 Hz, 1H, 7-C*H*), 6.98 (t, *J* = 7.6 Hz, 1H, 5-$C\mathit{H}_3$), 3.93 (t, *J* = 8.4 Hz, 2H, 2-$C\mathit{H}_2$), 2.88 (t, *J* = 8.4 Hz, 2H, 3-$C\mathit{H}_2$).[41]

3.4.7. Theoretical studies

3.4.7.1. Computational details

The density functional theory (DFT) calculations were performed with Gaussian 16 (Revision C.01) software.[42] All the structures were optimized at the M06-2X level of theory with the Def2-SVP basis set.[43] Frequency calculations were performed to verify that intermediates have no imaginary frequency, whereas the transition state structures have only one imaginary frequency. The appropriateness of the connections between each reactant and product via the transition state was confirmed using intrinsic reaction coordinate (IRC).[44] Single-point energy calculations were carried out at M06-2X/Def2-TZVP/gas-phase level of theory.[45] The reported Gibbs free energies were calculated at 298.15 K. These calculations involve a certain margin of error.

3.4.7.2. Selected frontier molecular orbitals (FMOs) for [(*C3*-1a)···B^1]

Selected FMOs for **[(*C3*-1a)···B^1]** (from HOMO−2 to LUMO+3), calculated at M06-2X/Def2-TZVP//M06-2X/Def2-SVP level, are shown in Figure 3.S7.

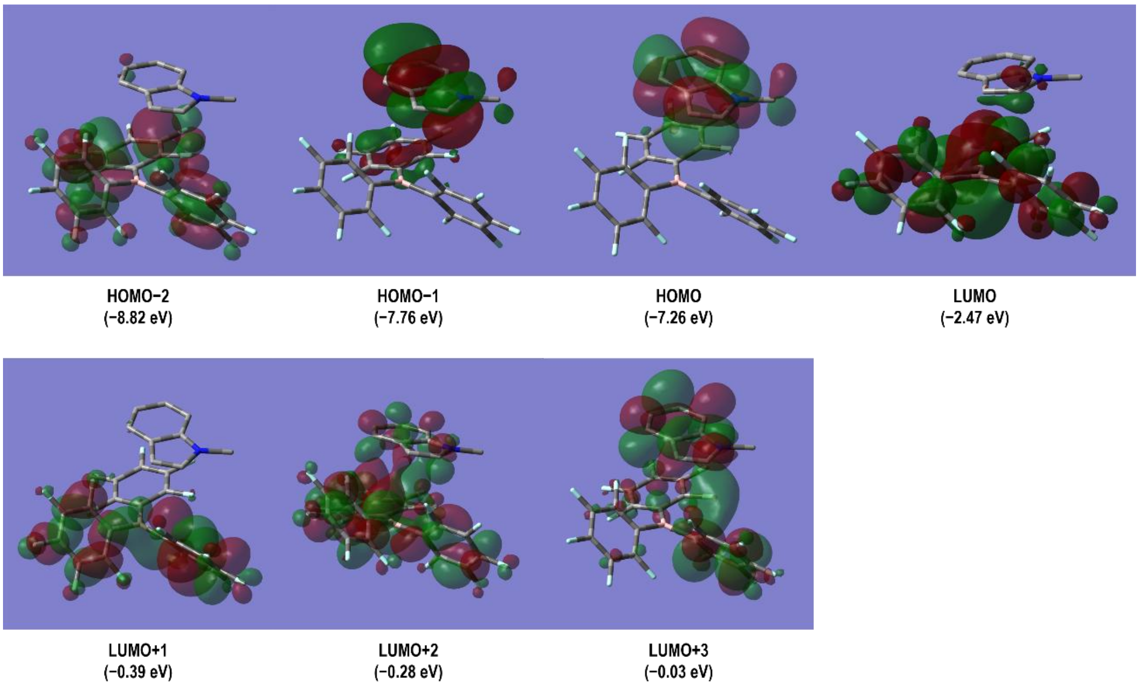

Figure 3.S7. Selected FMOs for **[(*C3*-1a)···B^1]**.

3.4.7.3. Plausible pathways for the reaction among 1a, B^1 and H$_2$

Plausible pathways for the reaction among **1a, B^1** and H$_2$ are shown in Figure 3.3C. The molecular structures of related compounds are summarized in Table 3.S2.

Table 3.S2. DFT-optimized structures in Figure 3.3C.

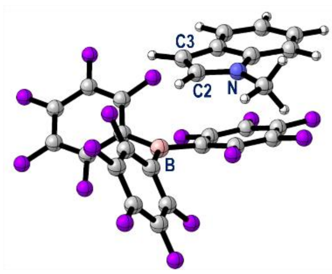 **[(*C3*-1a)···B^1]**	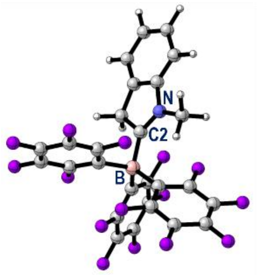 **(*C2*-1a)·B^1**	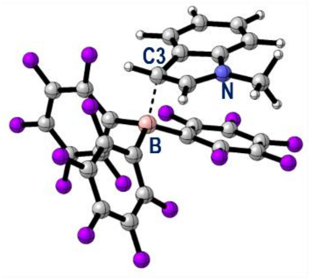 **(*C3*-1a)·B^1**
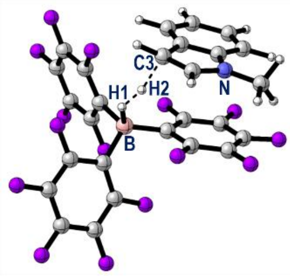 **TS10$_{(C3\text{-}B1)}$**	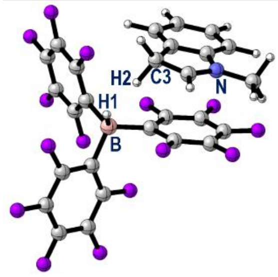 **[(*C3*-1a)–H][H–B^1]**	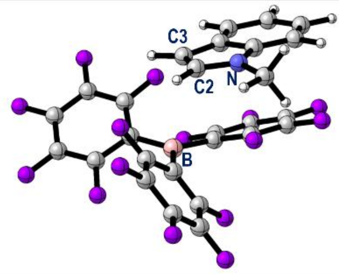 **[(*N*-1a)···B^1]**
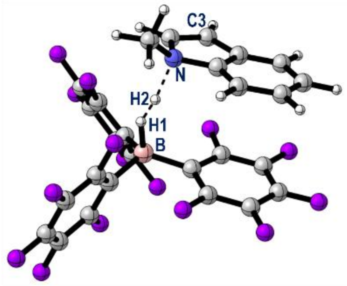 **TS10$_{(N\text{-}B1)}$**	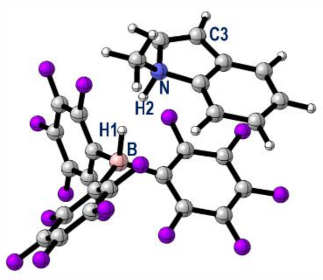 **[(*N*-1a)–H][H–B^1]**	

3.4.7.4. Plausible reaction mechanisms for the hydrogenation of 1a with B^9

Plausible reaction mechanisms for the hydrogenation of **1a** with **B^9** are shown in Figure 3.5. The molecular structures of related compounds are summarized in Table 3.S3.

Table 3.S3. DFT-optimized structures in Figure 3.5.

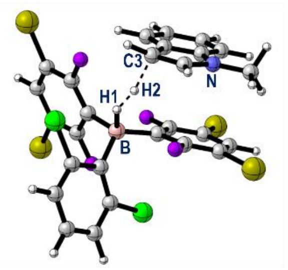 **TS10$_{(C3-B9)}$**	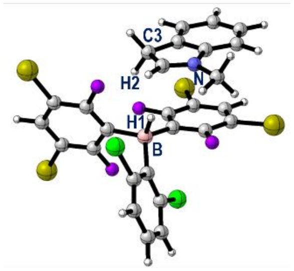 **[(*C3*-1a)–H][H–B^9]**	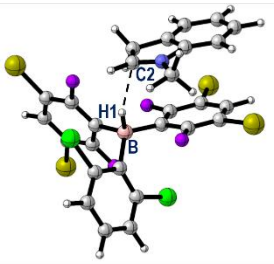 **TS11**
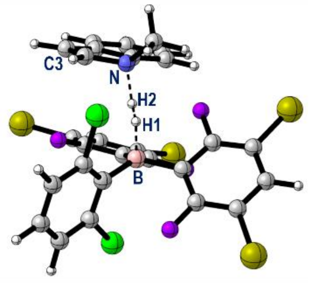 **TS10$_{(N-B9)}$**	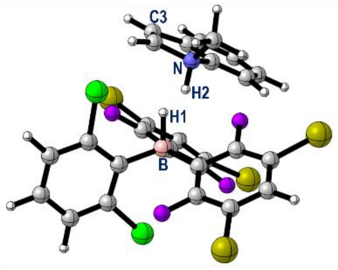 **[(*N*-1a)–H][H–B^9]**	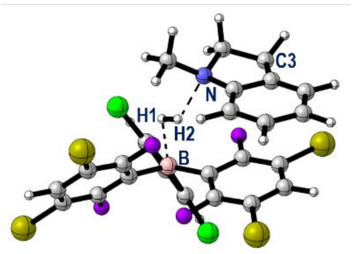 **TS12**
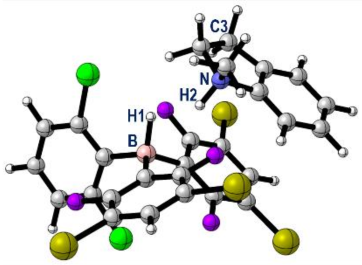 **[2a–H][H–B^9]**	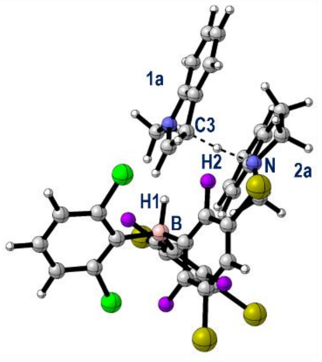 **TS13**	

3.5 References and notes

1. Wei, H.; Li, B.; Wang, N.; Ma, Y.; Yu, J.; Wang, X.; Su, J.; Liu, D. *ChemistryOpen* **2023**, *12*, e202200235.
2. Thakur, A.; Singh, A.; Kaur, N.; Ojha, R.; Nepali, K. *Bioorg. Chem.* **2020**, *94*, 103436.
3. Maiti, S.; Kim, J. S.; Kim, J. *New J. Chem.* **2024**, *48*, 3342.
4. Alvarez-Montoya, A.; Gillions, J. P.; Winfrey, L.; Hawker, R. R.; Singh, K.; Ortu, F.; Fu, Y.; Li, Y.; Pulis, A. P. *ACS Catal.* **2024**, *14*, 4856.
5. Wang, S.; Huang, H.; Bruneau, C.; Fischmeister, C. *ChemSusChem* **2019**, *12*, 2350.
6. Liu, C.; Wang, M.; Xu, Y.; Li, Y.; Liu, Q. *Angew. Chem., Int. Ed.* **2022**, *61*, 1.
7. Gunasekar, R.; Goodyear, R. L.; Proietti Silvestri, I.; Xiao, J. *Org. Biomol. Chem.* **2022**, *20*, 1794.
8. Chandrasekhar, S.; Basu, D.; Reddy, C. R. *Synthesis* **2007**, *10*, 1509.
9. Lam, J.; Szkop, K. M.; Mosaferi, E.; Stephan, D. W. *Chem. Soc. Rev.* **2019**, *48*, 3592.
10. Scott, D. J.; Fuchter, M. J.; Ashley, A. E. *Chem. Soc. Rev.* **2017**, *46*, 5689.
11. Stephan, D. W. *J. Am. Chem. Soc.* **2021**, *143*, 20002.
12. Stephan, D. W.; Greenberg, S.; Graham, T. W.; Chase, P.; Hastie, J. J.; Geier, S. J.; Farrell, J. M.; Brown, C. C.; Heiden, Z. M.; Welch, G. C.; Ullrich, M. *Inorg. Chem.* **2011**, *50*, 12338.
13. Tussing, S.; Paradies, J. *Dalton Trans.* **2016**, *45*, 6124.
14. Xu, Z. M.; Hu, Z.; Huang, Y.; Bao, S. J.; Niu, Z.; Lang, J. P.; Al-Enizi, A. M.; Nafady, A.; Ma, S. *J. Am. Chem. Soc.* **2023**, *145*, 14994.
15. We found the prices per 1 gram of **1a** and **2a** are $2.7 and $230 when purchasing from Sigma Aldrich. Also, the price of **2a** ($690/g) is higher than **1a** ($3.5/g) when purchasing from Tokyo Chemical Industry (TCI).
16. Focante, F.; Camurati, I.; Nanni, D.; Leardini, R.; Resconi, L. *Organometallics* **2004**, *23*, 5135.
17. Mahdi, T.; Heiden, Z. M.; Grimme, S.; Stephan, D. W. *J. Am. Chem. Soc.* **2012**, *134*, 4088.
18. Xu, Y.; Yang, Y.; Liu, Y.; Li, Z. H.; Wang, H. *Nat. Catal.* **2023**, *6*, 16.
19. Ullrich, M.; Lough, A. J.; Stephan, D. W. *J. Am. Chem. Soc.* **2009**, *131*, 52.
20. Greb, L.; Daniliuc, C. G.; Bergander, K.; Paradies, J. *Angew. Chem., Int. Ed.* **2013**, *52*, 5876.
21. Sakuraba, M.; Ogoshi, S.; Hoshimoto, Y. *Tetrahedron Chem* **2024**, *9*, 100059.
22. Dorkó, É.; Szabó, M.; Kótai, B.; Pápai, I.; Domján, A.; Soós, T. *Angew. Chem., Int. Ed.* **2017**, *56*, 9512.
23. Herrington, T. J.; Thom, A. J. W.; White, A. J. P.; Ashley, A. E. *Dalton Trans.* **2012**, *41*, 9019.
24. Hashimoto, T.; Asada, T.; Ogoshi, S.; Hoshimoto, Y. *Sci. Adv.* **2022**, *8*, eade0189.
25. Gyömöre, Á.; Bakos, M.; Földes, T.; Pápai, I.; Domján, A.; Soós, T. *ACS Catal.* **2015**, *5*, 5366.
26. Hisata, Y.; Washio, T.; Takizawa, S.; Ogoshi, S.; Hoshimoto, Y. *Nat. Commun.* **2024**, *15*, 3708.
27. Ashley, A. E.; Herrington, T. J.; Wildgoose, G. G.; Zaher, H.; Thompson, A. L.; Rees, N. H.; Krämer, T.; Öhare, D. *J. Am. Chem. Soc.* **2011**, *133*, 14727.
28. Dorkó, É.; Kótai, B.; Földes, T.; Gyömöre, Á.; Pápai, I.; Soós, T. *J. Organomet. Chem.* **2017**, *847*, 258.
29. Erös, G.; Nagy, K.; Mehdi, H.; Pápai, I.; Nagy, P.; Király, P.; Tárkányi, G.; Soós, T. *Chem. - A Eur. J.* **2012**, *18*, 574.

30. Sakuraba, M.; Morishita, T.; Hashimoto, T.; Ogoshi, S.; Hoshimoto, Y. *Synlett* **2023**, *34*, 2187.
31. Dong, Y.; Lan, M. F.; Lin, Y. Q.; Chen, L.; Wu, C. M.; Wang, Z. F.; Shi, Z. C.; Deng, G. W.; He, B. *J. Org. Chem.* **2024**, *89*, 6474.
32. Zhang, S.; Han, Y.; He, J.; Zhang, Y. *J. Org. Chem.* **2018**, *83*, 1377.
33. Kato, S.; Saga, Y.; Kojima, M.; Fuse, H.; Matsunaga, S.; Fukatsu, A.; Kondo, M.; Masaoka, S.; Kanai, M. *J. Am. Chem. Soc.* **2017**, *139*, 2204.
34. Han, Y.; Zhang, S.; He, J.; Zhang, Y. *J. Am. Chem. Soc.* **2017**, *139*, 739.
35. Li, W. D.; Zhu, D. Y.; Li, G.; Chen, J.; Xia, J. B. *Adv. Synth. Catal.* **2019**, *361*, 5098.
36. Pandey, G.; Tiwari, S. K.; Singh, B. *Tetrahedron Lett.* **2016**, *57*, 4480.
37. Gui, J.; Xie, H.; Jiang, H.; Zeng, W. *Org. Lett.* **2019**, *21*, 2804.
38. Johnston, J. N.; Plotkin, M. A.; Viswanathan, R.; Prabhakaran, E. N. *Org. Lett.* **2001**, *3*, 1009.
39. Mayer, R. J.; Hampel, N.; Mayer, P.; Ofial, A. R.; Mayr, H. *European J. Org. Chem.* **2019**, *2*, 412.
40. Xia, Q.; Tian, H.; Dong, J.; Qu, Y.; Li, L.; Song, H.; Liu, Y.; Wang, Q. *Chem. Eur. J.* **2018**, *24*, 9269.
41. Poeira, D. L.; Macara, J.; Faustino, H.; Coelho, J. A. S.; Gois, P. M. P.; Marques, M. M. B. *Euro. J. Org. Chem.* **2019**, *15*, 2695.
42. Gaussian 16, Revision C.01, Frisch, M. J.; Trucks, G. W.; Schlegel, H. B.; Scuseria, G. E.; Robb, M. A.; Cheeseman, J. R.; Scalmani, G.; Barone, V.; Petersson, G. A.; Nakatsuji, H.; Li, X.; Caricato, M.; Marenich, A. V.; Bloino, J.; Janesko, B. G.; Gomperts, R.; Mennucci, B.; Hratchian, H. P.; Ortiz, J. V.; Izmaylov, A. F.; Sonnenberg, J. L.; Williams-Young, D.; Ding, F.; Lipparini, F.; Egidi, F.; Goings, J.; Peng, B.; Petrone, A.; Henderson, T.; Ranasinghe, D.: Zakrzewski, V. G.; Gao, J.; Rega, N.; Zheng, G.; Liang, W.; Hada, M.; Ehara, M.; Toyota, K.; Fukuda, R.; Hasegawa, J.; Ishida, M.; Nakajima, T.; Honda, Y.; Kitao, O.; Nakai, H.; Vreven, T.; Throssell, K.; Montgomery Jr., J. A.; Peralta, J. E.; Ogliaro, F.; Bearpark, M. J.; Heyd, J. J.; Brothers, E. N.; Kudin, K. N.; Staroverov, V. N.; Keith, T. A.; Kobayashi, R.; Normand, J.; Raghavachari, K.; Rendell, A. P.; Burant, J. C.; Iyengar, S. S.; Tomasi, J.; Cossi, M.; Millam, J. M.; Klene, M.; Adamo, C.; Cammi, R.; Ochterski, J. W.; Martin, R. L.; Morokuma, K.; Farkas, O.; Foresman, J. B.; Fox, D. J. Gaussian, Inc., Wallingford CT, 2019.
43. Schäfer, A.; Horn, H.; Ahlrichs, R. *J. Chem. Phys.* **1992**, *97*, 2571.
44. Fukui, K. *Acc. Chem. Res.* **1981**, *14*, 363.
45. Schäfer, A.; Huber, C.; Ahlrichs, R. *J. Chem. Phys.* **1994**, *100*, 5829.

Conclusion

In this thesis, I have discussed the development of hydrogenation of *N*-heteroaromatics using crude or pure H_2. The key achievements in the thesis lies in the use of triarylborane catalysts with precisely designed boron-centered electrophilicity and steric hindrance around the boron atom. I found that the catalytic hydrogenation activity of triarylboranes toward *N*-heteroaromatics is primarily determined by the boron-centered electrophilicity and the intermolecular steric repulsion (front strain) between substituents at the *ortho*-positions relative to the boron atom and Lewis bases. Furthermore, the hydrogenation activity can be finely tuned through intramolecular steric repulsion (remote back strain) between substituents at the *meta*-positions relative to the boron atom, resulting in high catalytic performances.

In Chapter 1, a proof of concept for a H_2 purification technology based on LOHCs was demonstrated by establishing sequential hydrogenation of *N*-heteroaromatics using crude H_2/dehydrogenation of the hydrogenated products with the single triarylborane catalyst. I found that crude H_2 containing excess amounts of CO, CO_2, and CH_4 can also be applicable for this hydrogenation; thus, this technology can be expected to change the industrial value of crude H_2 containing substantial amounts of CO, CO_2, and CH_4, which can be produced from a variety of carbon resources such as biomass and industrial off-gases.

In Chapter 2, I elucidated the reaction mechanism of the hydrogenation of 2-methylquinoline using crude H_2 in the presence of triarylborane catalysts, as well as the irreversible decomposition mechanism of the triarylborane catalysts, employing the artificial force induced reaction (AFIR) method. The theoretical results suggested that olefinic π orbitals in the enamine intermediates are involved in the heterolytic cleavage of H_2.

In Chapter 3, I developed hydrogenation of *N*-substituted indoles using triarylborane catalysts and demonstrated that olefinic π orbitals are involved in the generation of FLPs. Furthermore, mechanistic studies revealed that the hydrogenation of indoles involves an olefin-to-nitrogen switching of Lewis bases in the critical H_2-cleavage steps; the initial H_2 activation is mediated by a frustrated Lewis pair (FLP) comprising the indole C3-carbon and boron atoms, while an FLP species comprising the indoline nitrogen and boron atoms promotes the subsequent H_2 activation leading to indoline.

Combined these results, I demonstrated several catalytic hydrogenation systems that were previously challenging to achieve using transition metal catalysts or existing organoboron catalysts based on the use of well-identified triarylboranes. These results pioneer highly chemoselective hydrogenation methods for unsaturated compounds under crude H_2 conditions. Moreover, they contribute to the establishment of highly efficient and environmentally friendly processes by bypassing purification steps in organic synthesis.

List of Publications

1. “Main Group Catalysis for H_2 Purification Based on Liquid Organic Hydrogen Carriers”
   Taiki Hashimoto, Takahiro Asada, Sensuke Ogoshi, Yoichi Hoshimoto
   Sci. Adv. **2022**, *8*, eade0189 (DOI: 10.1126/sciadv.ade0189).
2. “Elucidating multicomponent mechanisms on catalytic hydrogenation of 2-methylquinoline under crude H_2 conditions: a key H_2-cleavage process by a boron–olefin Lewis pair”
   Taiki Hashimoto, Yu Harabuchi, Sensuke Ogoshi, Satoshi Maeda, Yoichi Hoshimoto
   Bull. Chem. Soc. Jpn. **2024**, *Advance articles* (DOI: 10.1093/bulcsj/uoae145).
3. “Boosting Turnovers in Triarylborane-Catalyzed Hydrogenation of *N*-Substituted Indoles via Olefin-to-Nitrogen Switching of Lewis Bases for the FLP Generation”
   Taiki Hashimoto, Masakazu Tanigawa, Kimitaka Kambe, Sensuke Ogoshi, Yoichi Hoshimoto
   Precis. Chem. **2024**, *ASAP* (DOI: 10.1021/prechem.4c00090).

Supplementary Publications

1. “Remote Back Strain: A Strategy for Modulating the Reactivity of Triarylboranes”
   Mahiro Sakuraba, Taichi Morishita, Taiki Hashimoto, Sensuke Ogoshi, Yoichi Hoshimoto
   Synlett **2023**, *34*, 2187 (DOI:10.1055/a-2110-5359).
2. “Triarylborane Catalysis: From Hydrogenation of Unsaturated Molecules to H_2 Purification”
   Taichi Morishita, Yusei Hisata, Taiki Hashimoto, Sensuke Ogoshi, Yoichi Hoshimoto
   J. Synth. Org. Chem., Jpn. **2024**, *82*, 1097 (DOI: 10.5059/yukigoseikyokaishi.82.1097).